JOURNAL OF FLUID MECHANICS

VOLUME 7 PART 3

MARCH 1960

PUBLISHED BY

CAMBRIDGE UNIVERSITY PRESS

BENTLEY HOUSE, 200 EUSTON ROAD, LONDON, N.W.1

AMERICAN BRANCH: 32 EAST 57TH STREET, NEW YORK 22, N.Y.

Price 30*s.* (*U.S.A.* $5.00)

The JOURNAL OF FLUID MECHANICS exists for the publication of theoretical and experimental investigations of all aspects of the mechanics of fluids, and is issued in four parts per volume.

EDITOR

DR G. K. BATCHELOR

Department of Applied Mathematics and Theoretical Physics, University of Cambridge, Free School Lane, Cambridge, England

ASSISTANT EDITORS

DR T. B. BENJAMIN, DR I. PROUDMAN, DR P. G. SAFFMAN

Department of Applied Mathematics and Theoretical Physics, University of Cambridge, Free School Lane, Cambridge, England

ASSOCIATE EDITORS

PROF. G. F. CARRIER

Pierce Hall, Harvard University, Cambridge 38, *Massachusetts, U.S.A.*

DR W. C. GRIFFITH

Research and Development Laboratory, Missile Systems Division, Lockheed Aircraft Corporation, Palo Alto, California, U.S.A.

M. J. LIGHTHILL

Royal Aircraft Establishment, Farnborough, Hampshire, England

PROF. R. R. LONG

School of Engineering, The Johns Hopkins University, Baltimore 18, *Maryland, U.S.A.*

Authors wishing to have papers published in the JOURNAL should communicate them to any one of the persons named above, choosing one in their own country where possible.

Authors are urged to ensure that their papers are written clearly and attractively, in order that their work will be readily accessible to readers.

Manuscripts should be typed in double spacing on one side of the paper only, with references listed at the end in alphabetical order of authors. Drawings should be done on a large scale in Indian ink on tracing cloth or drawing paper, the lettering being shown clearly in pencil for reproduction by the printer; the list of captions should be typed at the end of the manuscript. Proofs of papers from overseas will usually be despatched to authors by airmail. There is no charge for publication. Authors are entitled to receive 50 offprints of a paper in the JOURNAL free of charge, and additional offprints can be purchased if ordered in advance.

SUBSCRIPTIONS

The subscription price for a volume of four parts is £5. 10*s*. net, post free, payable in advance; separate parts 30*s*. net, plus postage. Subscriptions may be sent to any bookseller, or to the Cambridge University Press, Bentley House, 200 Euston Road, London, N.W.1.

Subscribers in the United States should send their orders to the Cambridge University Press, American Branch, 32 East 57th Street, New York 22. The subscription price per volume is $18.50, post free, payable in advance; separate parts $5.00, plus postage.

Quotations for available back volumes and parts may be obtained on application to the Cambridge University Press.

Interaction of a shock wave with a mixing region

By N. RILEY
Department of Mathematics, University of Manchester

(Received 25 June 1959)

The interaction of a simple wave, in steady supersonic flow, with a two-dimensional mixing region is treated by applying Fourier analysis to the linearized equations of motion. From asymptotic forms for the Fourier transforms of physical quantities, for large wave-number, the dominant features of the resulting flow pattern are predicted; in particular it is found that a shock wave, incident on the mixing region, is reflected as a logarithmically infinite ridge of pressure. For two particular Mach-number distributions in the undisturbed flow, numerical solutions are obtained, showing greater detail than the results predicted by the asymptotic approach. A method is given whereby the linear theory may be improved to take into account some non-linear effects; and the reflected wave, for an incident shock wave, is then seen to consist of a shock wave, gradually diminishing in strength, followed by the main expansion wave.

1. Introduction

The problem of the interaction of a shock wave with a boundary layer has, over the past few years, received considerable attention from both experimental and theoretical workers. By contrast, the problem of the interaction of a shock wave with a mixing region has received scant attention. Perhaps the most common interaction of the latter type occurs when a supersonic jet emerges from a nozzle in which the pressure is less than atmospheric pressure, although an equally common but less obvious case is when a strong shock wave (i.e. strong enough to cause separation) interacts with a boundary layer. The separation point is then situated well upstream from the point of incidence of the initial shock which, consequently, is itself directly incident upon a layer of fluid in which the fluid velocity falls to zero, in the 'dead-air bubble', before the wall is reached, just as in a mixing region. The present problem can then perhaps also be considered as a special case of a shock-boundary-layer interaction. The main experimental results concerning interactions of shock waves with mixing regions are in the form of Schlieren photographs of supersonic jets, such as those taken at the Manchester University Fluid Motion Laboratory by Johannesen (1957). The difficulties in obtaining measurements by mechanical methods in these small regions are very great, owing to the relatively large disturbance created by any instrument which might be placed in the flow.

Important theoretical contributions to the problem of the interaction of a shock wave with a boundary layer have been made by Lighthill (1950, 1953). He considers an ideal fluid in which viscosity and heat conduction are neglected and

replaces the boundary layer by a shear layer in which the Mach number falls from its main stream value M_1 to zero (Lighthill 1950) at the wall, or to M_2 (Lighthill 1953) when an inner viscous sublayer is considered. The equations of plane steady flow are used and products of small quantities arising from small disturbances to the basic parallel flow are neglected. In the present problem, concerning the interaction of a shock wave with a mixing region, the same procedure is adopted, the mixing region being represented by a semi-infinite layer of vorticity in which the Mach number varies continuously from its main stream value M_1 to zero asymptotically at large distances from the main stream. The flow is assumed to be parallel everywhere. Owing to the absence of any solid boundary, there is no need to consider any inner viscous sublayer in this problem.

Having substituted this shear layer for the mixing region, it would hardly seem fair to refer to the mixing region as such, as in fact no mixing is taking place; consequently the 'mixing region' will be referred to as the 'non-uniform' region. The equations of motion are formulated in terms of derivatives $\partial/\partial s$ and $\partial/\partial n$ along and at right angles to the streamlines, with the flow direction and a suitably defined pressure coefficient as dependent variables depending only on the Mach-number distribution, and not on the separate velocity and temperature distributions. If the disturbances to the uniform parallel flow are small and if, in the undisturbed state, the fluid is flowing in a direction parallel to the x-axis, then to a first approximation the derivatives $\partial/\partial s$ and $\partial/\partial n$ may be replaced by $\partial/\partial x$ and $\partial/\partial y$ and the Mach-number distribution by its undisturbed value.

The Fourier transform of the pressure coefficient is defined and an ordinary differential equation which it satisfies is derived. Asymptotic solutions of this equation, with a general undisturbed Mach-number distribution, are obtained for large wave-number in the subsonic region, the solutions being continued across the sonic line by a method due to Langer (1931). In this way asymptotic forms of the Fourier transform of the pressure coefficient, reflected wave and flow direction are obtained, which in turn enable us to pick out the singularities in these quantities. It is thus shown that an incident wave in the form of a shock wave is reflected as a pressure ridge, as in Lighthill's boundary-layer theory.

Using a specific Mach-number distribution in the non-uniform region, it has been found possible to solve the equation for the Fourier transform of the pressure coefficient exactly. Using this solution it is not difficult to show that the upstream influence (i.e. the distance upstream which the disturbance penetrates) is only of the order of one layer thickness. The reflected wave for this Mach-number distribution has been calculated using numerical methods, analytical methods proving too intractable. When the incident wave is in the form of a shock wave the reflected wave is seen to consist of a very narrow region of compression followed by a broader region of expansion; photographic evidence in support of this is available. From the reflected wave for an incident shock, it is shown to be possible to calculate the reflected wave for an incident Prandtl–Meyer expansion fan which is found to consist of a slight further expansion followed by a region of compression. An interaction of the latter type occurs when a supersonic jet, in which the pressure is greater than atmospheric pressure, exhausts into the atmosphere.

In the linear theory, first approximations to the physical quantities are obtained, but the characteristic network is left unchanged as two sets of parallel lines. This is the fundamental failure of linear theory, since the characteristics along which the physical quantities are predicted are incorrectly placed. Several methods (Whitham 1952; Lighthill 1957; and Kantrowitz 1958) are available for obtaining a correctly modified first approximation to the flow pattern, and the method used here, anticipated by both Lighthill and Kantrowitz, is outlined in an appendix. The flow is assumed isentropic, which means that third-order terms due to entropy changes at the shock are neglected, so that any shock waves occurring must not be too strong. The mass flow in a given direction is examined and in the isentropic-flow theory this becomes multi-valued under a compressive disturbance. It is shown that a shock wave, inserted so as to leave the total mass flow unaltered, renders the mass flow single-valued though discontinuous and satisfies all the equations governing the complete flow pattern, under the isentropic-flow limitation. If we were to make the further assumption that products of small quantities are to be neglected, we should recover the method outlined by Whitham (1952). The resulting flow patterns, displayed graphically, show very clearly how the reflected expansion wave interacts with the adjacent shock wave, gradually weakening it.

2. Equations of motion

The equations of motion governing a perfect gas, with constant adiabatic index γ and zero viscosity and thermal conductivity, which flows in a steady two-dimensional pattern, are

$$\left.\begin{aligned} \frac{\partial}{\partial s}(\rho u)+\rho u\frac{\partial \theta}{\partial n}=0, \\ \rho u\frac{\partial u}{\partial s}=-\frac{\partial p}{\partial s}, \quad \rho u^2\frac{\partial \theta}{\partial s}=-\frac{\partial p}{\partial n}, \\ \frac{\partial p}{\partial s}=a^2\frac{\partial \rho}{\partial s}, \end{aligned}\right\} \tag{1}$$

expressing conservation of mass, momentum and entropy along a streamline, respectively. The derivatives $\partial/\partial s$ and $\partial/\partial n$ are derivatives along the streamlines and normal to them, respectively. The velocity is denoted by its magnitude u and direction θ which is the angle a streamline makes with some fixed direction, say the x-axis. The pressure p and density ρ are related to a the local velocity of sound by $a=(\gamma p/\rho)^{\frac{1}{2}}$. Elimination of $\partial u/\partial s$, $\partial \rho/\partial s$ between the first two and last of equations (1) gives

$$(1-M^2)\frac{\partial p}{\partial s}=\rho u^2\frac{\partial \theta}{\partial n}, \tag{2}$$

where $M=u/a$ is the local Mach number. If we now define a pressure coefficient $\phi=\log(p/p_1)^{1/\gamma}$, where p_1 is some constant pressure, then equation (2) and the third of equations (1) reduce to the simple form

$$\left.\begin{aligned} (1-M^2)\frac{\partial \phi}{\partial s}=M^2\frac{\partial \theta}{\partial n}, \\ \frac{\partial \phi}{\partial n}=-M^2\frac{\partial \theta}{\partial s}. \end{aligned}\right\} \tag{3}$$

Suppose the flow pattern consists of a basic parallel flow in the x-direction upon which is superimposed a small disturbance, then the streamlines will only be displaced by a small amount from their undisturbed state, and so to a first approximation we may take $\partial/\partial s = \partial/\partial x$ and $\partial/\partial n = \partial/\partial y$, giving

$$\left.\begin{aligned} \{1-M^2(y)\}\frac{\partial \varpi}{\partial x} &= M^2(y)\frac{\partial \theta}{\partial y}, \\ \frac{\partial \varpi}{\partial y} &= -M^2(y)\frac{\partial \theta}{\partial x}. \end{aligned}\right\} \tag{4}$$

If p_1 is taken to be the pressure in the basic flow then the pressure coefficient $\varpi = (p-p_1)/\gamma p_1$. In the basic flow we assume that the Mach number distribution $M(y)$ is a function of y only, continuous for all y and decreasing in $0 \geqslant y > -\infty$ with $M(y) \to 0$ as $y \to -\infty$ and $M(y) = M_1 > 1$ for $y \geqslant 0$. We see then that the distribution of pressure coefficient ϖ and the streamline pattern (deducible from θ) depend only on the distribution of Mach number $M(y)$ and not on the separate velocity and temperature distributions. The equation for ϖ obtained by eliminating θ from equations (4) is

$$\frac{\partial^2 \varpi}{\partial y^2} - 2\frac{M'(y)}{M(y)}\frac{\partial \varpi}{\partial y} + \{1-M^2(y)\}\frac{\partial^2 \varpi}{\partial x^2} = 0. \tag{5}$$

If the cause of the disturbance is taken as a simple plane wave incident on the non-uniform region from outside, then, by the theory of small disturbances to a uniform supersonic stream, ϖ must, in $y > 0$, take the form

$$\varpi = f(x+\beta y) + g(x-\beta y), \tag{6}$$

where f represents the incident wave, g the reflected wave, and $\beta = (M_1^2-1)^{\frac{1}{2}}$. The function g is what we particularly wish to determine in the present investigation.

The boundary condition at $y = 0$ is that the pressure field be continuous with the field given by (6); this may be written

$$\left(\beta\frac{\partial \varpi}{\partial x} + \frac{\partial \varpi}{\partial y}\right)_{y=0} = 2\beta f'(x), \tag{7}$$

providing that the derivatives are continuous across $y = 0$. Lighthill (1950) has shown that they will be so as long as $M(y)$ is continuous. To complete the formulation of the problem we need another boundary condition, and it would appear reasonable to take this as

$$(\varpi)_{y\to-\infty} \to 0. \tag{8}$$

Equation (5) must then be solved under conditions (7) and (8). When the pressure field has been determined the reflected wave can be derived from the equation

$$\left(\beta\frac{\partial \varpi}{\partial x} - \frac{\partial \varpi}{\partial y}\right)_{y=0} = 2\beta g'(x), \tag{9}$$

and the flow direction θ from the second of equations (4).

3. Fourier analysis

If $f(x)$ can be expressed as a Fourier integral

$$f(x) = \int_{-\infty}^{\infty} e^{ikx} F(k)\, dk, \tag{10}$$

then we shall seek solutions for ϖ, g and θ in the form

$$\varpi(x, y) = \int_{-\infty}^{\infty} e^{ikx} \Pi(k, y)\, dk, \tag{11}$$

$$g(x) = \int_{-\infty}^{\infty} e^{ikx} G(k)\, dk, \tag{12}$$

$$\theta(x, y) = \int_{-\infty}^{\infty} e^{ikx} H(k, y)\, dk. \tag{13}$$

If a substitution for ϖ, from (11), is made in equation (5), the following ordinary differential equation for Π is obtained:

$$\frac{d^2\Pi}{dy^2} - 2\frac{M'(y)}{M(y)}\frac{d\Pi}{dy} + k^2\{M^2(y) - 1\}\Pi = 0, \tag{14}$$

the boundary conditions (7) and (8) becoming

$$\Pi_y(k, 0) + ik\beta\Pi(k, 0) = 2\beta ikF(k), \tag{15}$$

$$\Pi(k, y) \to 0 \quad \text{as} \quad y \to -\infty. \tag{16}$$

For convenience, when model profiles are chosen, solutions of equation (14) are better expressed in terms of the basic solution $\Pi_0(k, y)$, where

$$\Pi_0(k, 0) = 1, \quad \Pi_0(k, y) \to 0 \quad \text{as} \quad y \to -\infty. \tag{17}$$

Then, to satisfy the boundary conditions (15) and (16), we must have

$$\Pi(k, y) = \frac{2\beta ikF(k)\Pi_0(k, y)}{\Pi_{0_y}(k, 0) + ik\beta\Pi_0(k, 0)}, \tag{18}$$

and from (9), (11), (12) and (18) the Fourier transform of the reflected wave is given as

$$\begin{aligned} G(k) &= [ik\beta\Pi(k, 0) - \Pi_y(k, 0)]/2\beta ik \\ &= -F(k)\frac{\Pi_{0_y}(k, 0) - ik\beta\Pi_0(k, 0)}{\Pi_{0_y}(k, 0) + ik\beta\Pi_0(k, 0)}. \end{aligned} \tag{19}$$

Also, we have the Fourier transform of the flow deflexion, from the second of equations (4) and equations (11), (13) and (18), given as

$$\begin{aligned} H(k, y) &= \frac{i}{kM^2(y)}\Pi_y(k, y) \\ &= -\frac{2\beta F(k)\Pi_{0_y}(k, y)}{M^2(y)\{\Pi_{0_y}(k, 0) + ik\beta\Pi_0(k, 0)\}}. \end{aligned} \tag{20}$$

Except for very special Mach-number distributions $M(y)$, equation (14) is very difficult to solve analytically. For the moment we shall confine ourselves to

approximate solutions of equation (14) for large values of the parameter k, for, by now, it is well known how the singularities of a Fourier integral can be deduced from the asymptotic behaviour of the integrand (see e.g. Lighthill 1958). The main features of the flow can be predicted in this way. Solutions for a particular form of $M(y)$ will be discussed in §5.

4. Asymptotic solutions

In order to estimate the asymptotic behaviour of $\Pi(k, y)$, we must refer to some of the results of a theory first fully developed by Langer (1931). The results which we shall need are set out briefly in appendix A; a more detailed summary is given by Lighthill (1950).

Considering now equation (14), we know from the 'W.B.K.' theory that asymptotic solutions as $|k| \to \infty$ must be a combination of the two forms

$$M(y)\{1-M^2(y)\}^{-\frac{1}{4}}\, e^{\pm iks}, \tag{21}$$

where

$$s = \int_{y_1}^{y} \{M^2(y)-1\}^{\frac{1}{2}}\, dy, \tag{22}$$

and $y = y_1$ is the sonic line in the undisturbed flow such that $M(y_1) = 1$. In the subsonic region, i.e. in the interval $-\infty < y < y_1$, we have $M(y) < 1$; hence $s = -i|s|$ from (22) and, from (21), any asymptotic solution as $|k| \to \infty$ must be a combination of

$$M(y)\{1-M^2(y)\}^{-\frac{1}{4}}\, e^{\pm k|s|}, \tag{23}$$

where $|s| \to \infty$ as $y \to -\infty$. Clearly then, to satisfy the second of conditions (17) we must take for the asymptotic form of $\Pi_0(k, y)$, as $|k| \to \infty$, in the subsonic region

$$\begin{aligned}\Pi_0(k, y) &\sim A_1 M(y)\{1-M^2(y)\}^{-\frac{1}{4}} \exp[-k|s| \operatorname{sgn} k] \\ &= A_1 M(y)\{1-M^2(y)\}^{-\frac{1}{4}}[H(k)\, e^{-k|s|} + H(-k)\, e^{k|s|}],\end{aligned} \tag{24}$$

where $\operatorname{sgn} k = k/|k|$ and $H(k) = 0$ for $k < 0$, $H(k) = 1$ for $k > 0$, and A_1 is, as yet, an arbitrary constant.

Writing $\Pi_0(k, y)$ as a combination $f_1(k)\, u_1(y) + f_2(k)\, u_2(y)$, where u_1 and u_2 are given in equation (62) by Langer's theory, enables us to determine $f_1(k)$ and $f_2(k)$ and hence continue the solution into the supersonic region $y > y_1$. Thus, since $s = -i|s|$,

$$f_1(k)\left(\frac{e^{k|s|}}{k^{\frac{1}{3}}} + \frac{e^{-k|s|}}{(-k)^{\frac{1}{3}}}\right) - f_2(k)\left(\frac{e^{k|s|}}{k^{\frac{2}{3}}} + \frac{e^{-k|s|}}{(-k)^{\frac{2}{3}}}\right) = A_1[H(k)\, e^{-k|s|} + H(-k)\, e^{k|s|}],$$

giving

$$\left.\begin{aligned} f_1(k) &= \frac{A_1}{\sqrt{3}}[H(k)\, k^{\frac{1}{3}} + H(-k)\,(-k)^{\frac{1}{3}}], \\ f_2(k) &= \frac{A_1}{\sqrt{3}}[H(k)\, k^{\frac{2}{3}} + H(-k)\,(-k)^{\frac{2}{3}}]. \end{aligned}\right\} \tag{25}$$

With $f_1(k)$, $f_2(k)$ given by (25), we have

$$f_1(k)\left(\frac{e^{iks}}{(ik)^{\frac{1}{3}}} + \frac{e^{-iks}}{(-ik)^{\frac{1}{3}}}\right) + f_2(k)\left(\frac{e^{iks}}{(ik)^{\frac{2}{3}}} + \frac{e^{-iks}}{(-ik)^{\frac{2}{3}}}\right) = 2A_1 \cos(ks - \tfrac{1}{4}\pi \operatorname{sgn} k), \tag{26}$$

giving, as the solution in the supersonic region, as $|k| \to \infty$,

$$\Pi_0(k, y) \sim \frac{M(y)\{M^2(y)-1\}^{-\frac{1}{4}} \cos(ks - \frac{1}{4}\pi \operatorname{sgn} k)}{M_1(M_1^2-1)^{-\frac{1}{4}} \cos(k\sigma - \frac{1}{4}\pi \operatorname{sgn} k)}, \tag{27}$$

where $\sigma = s(0) = \int_{y_1}^{0} \{M^2(y)-1\}^{\frac{1}{2}} dy$ and the arbitrary constant has been chosen to satisfy the first of conditions (17).

Now from (27) and (19) we have, retaining only those terms in Π_{0_y} which contain a factor k and discarding terms of lower order, as $|k| \to \infty$,

$$G(k) \sim F(k)\, e^{-2ik\sigma}\, i \operatorname{sgn} k. \tag{28}$$

And so, if the incident wave represents a simple discontinuity in pressure, of magnitude $\gamma p_1 \Delta$ on the characteristic $x + \beta y = 0$, so that

$$f(x+\beta y) = \tfrac{1}{2}\Delta[1 + \operatorname{sgn}(x+\beta y)], \tag{29}$$

we have, as $|k| \to \infty$,

$$F(k) \sim -\frac{i\Delta}{2\pi k} \tag{30}$$

giving, from (28),

$$G(k) \sim \frac{\Delta}{2\pi|k|}\, e^{-2ik\sigma}. \tag{31}$$

Equation (31) shows us that

$$g(x-\beta y) = -\frac{\Delta}{\pi} \log|x-\beta y - 2\sigma| + (\text{continuous function}), \tag{32}$$

indicating that the reflected wave possesses not a simple discontinuity but a logarithmic singularity on the characteristic $x - \beta y - 2\sigma = 0$. Although a positive logarithmic infinity of pressure is postulated in the reflected wave, this cannot be realized physically, and may be interpreted (see Lighthill 1950) as a pressure ridge, that is, as a rapid compression followed by a rapid expansion.

The reflexion of an incident wave of the form given by (29) can perhaps be seen more clearly by examining the pressure coefficient $\varpi(x, y)$ in the supersonic part of the non-uniform region $y_1 < y \leqslant 0$. From equations (18), (27) and (30), we have, as $|k| \to \infty$,

$$\Pi(k, y) \sim \frac{M(y)\{M^2(y)-1\}^{-\frac{1}{4}}}{M_1(M_1^2-1)^{-\frac{1}{4}}} \left[\left(\frac{-i\Delta}{2\pi k}\right) e^{ik(s-\sigma)} + \left(\frac{\Delta}{2\pi|k|}\right) e^{-ik(s+\sigma)}\right], \tag{33}$$

showing that $\varpi(x, y)$ has a discontinuity of magnitude

$$\frac{M(y)\{M^2(y)-1\}^{-\frac{1}{4}}}{M_1(M_1^2-1)^{-\frac{1}{4}}}\Delta \quad \text{on} \quad x = \sigma - s,$$

whilst

$$\varpi(x, y) + \frac{\Delta}{\pi} \frac{M(y)\{M^2(y)-1\}^{-\frac{1}{4}}}{M_1(M_1^2-1)^{-\frac{1}{4}}} \log|x-(\sigma+s)|$$

is continuous on $x = \sigma + s$. The incident wave then, on entering the non-uniform region at $(0, 0)$ is propagated along the characteristic with slope

$$dx/dy = -\{M^2(y)-1\}^{\frac{1}{2}},$$

that is along the line $x = \sigma - s$, until the sonic line $y = y_1$ is reached at $x = \sigma$; the wave is then reflected along the other characteristic through this point, $x = \sigma + s$, emerging from the non-uniform region at the point $(2\sigma, 0)$ and proceeding along the characteristic $x = \beta y + 2\sigma$ as we saw in (32). The singularity of the pressure coefficient ϖ on the sonic line itself may be estimated from equations (18), (25) and (64), since we know that $\Pi_0(k, y_1) \sim f_1(k)\, u_1(y_1) + f_2(k)\, u_2(y_1)$. In this way we see that $\varpi(x, y_1)$ possesses a singularity of the form

$$|x-\sigma|^{-\frac{1}{3}} \left(\operatorname{sgn}(x-\sigma) \cos\frac{5\pi}{12} + \sin\frac{5\pi}{12} \right). \tag{34}$$

It is worth noting here that if the incident wave $f(x)$ consists of one or more simple discontinuities in the pressure gradient, then no infinity of pressure in the reflected wave arises. This can be seen by observing that $\partial\varpi/\partial x$ satisfies the same differential equation and boundary condition, when $y \to -\infty$, as ϖ itself. Thus, if in the incident wave $\partial\varpi/\partial x$ has a discontinuity Δ_1, then the reflected wave will possess a region of logarithmically infinite pressure gradient. Again, if the incident wave possesses a discontinuity $-\Delta_1$ in $\partial\varpi/\partial x$ followed by one of Δ_1 representing a Prandtl–Meyer expansion, then the reflected wave has a region of large negative pressure gradient followed by one of large positive pressure gradient. Integration to find ϖ shows that a Prandtl–Meyer expansion is reflected as an expansion followed immediately by compression.

Although the flow direction is directly deducible from the second of equations (4), it is interesting to investigate it by methods similar to those developed above. Consider, first, the flow in the supersonic part of the non-uniform region when the incident wave is given by (29). In this region the asymptotic form of the Fourier transform of the flow deflexion, given by equations (20), (27) and (30), as $|k| \to \infty$, is

$$H(k, y) \sim \frac{(M_1^2-1)^{\frac{1}{4}} \{M^2(y)-1\}^{\frac{1}{4}}}{M_1 M(y)} \left(\frac{i\Delta}{2\pi k} e^{-ik(\sigma-s)} + \frac{\Delta}{2\pi|k|} e^{-ik(\sigma+s)} \right). \tag{35}$$

The first term in (35) indicates that on crossing the characteristic $x = \sigma - s$ (along which the incident wave lies) the flow is deflected by an amount

$$-\Delta \frac{(M_1^2-1)^{\frac{1}{4}} \{M^2(y)-1\}^{\frac{1}{4}}}{M_1 M(y)},$$

agreeing with the weak wave deflexion $-\Delta(M_1^2-1)^{\frac{1}{2}}/M_1^2$ at $y = 0$. The second term in (35) shows that, on crossing the characteristic $x = \sigma + s$, the flow is subjected to a logarithmically infinite deflexion, as may be expected when a logarithmically infinite pressure is involved.

In the subsonic region $y < y_1$, equations (20), (24) and (30) give us, as $|k| \to \infty$,

$$H(k, y) \sim \frac{(M_1^2-1)^{\frac{1}{4}} \{1-M^2(y)\}^{\frac{1}{4}}}{\sqrt{2}\, M_1 M(y)} \left[\frac{\Delta}{2\pi|k|} + \frac{i\Delta}{2\pi k} \right] e^{-|k||s|} e^{-ik\sigma}. \tag{36}$$

Neglecting the factor $e^{-|k||s|}$ for the moment, we see that the fluid is violently disturbed in the neighbourhood of $x = \sigma$, the point on the sonic line at which the incident wave is reflected, as we may have imagined. The effect of the factor $e^{-|k||s|}$ is merely to smooth out, over a distance of the order of $|s|$, the other features present.

Both equations (35) and (36) imply that the flow along the sonic line $y = y_1$ does not undergo any discontinuous change in direction. That this is so can be shown by examining the singularities of $\theta(x, y)$ along the sonic line. From equations (20) and (30) we have

$$H(k, y_1) = \frac{\Delta}{\pi k^2} \Pi_{0_y}(k, y_1) \cos(k\sigma - \tfrac{1}{4}\pi \operatorname{sgn} k) \exp[-ik\sigma + \tfrac{1}{4}\pi i \operatorname{sgn} k]. \quad (37)$$

Substituting for $\Pi_{0_y}(k, y_1)$ from (25) and (64) in (37), and performing the transformation, shows that on the sonic line $\theta(x, y)$ contains no singularity worse than

$$|x-\sigma|^{\frac{1}{3}} \left(\operatorname{sgn}(x-\sigma) \cos\frac{7\pi}{12} - \sin\frac{7\pi}{12}\right),$$

indicating that the flow along the sonic line suffers no discontinuous change in direction.

5. Solution with model profile

As we have seen, in § 4, it is possible to examine the main features of the flow by finding asymptotic forms, as $|k| \to \infty$, for the Fourier transforms of the reflected wave g, the pressure coefficient ϖ and the flow direction θ, and hence picking out the singularities in these quantities. This was achieved without specifying the Mach-number distribution $M(y)$ uniquely. We shall now, using a specific Mach-number distribution, examine the afore-mentioned quantities in more detail.

Let the Mach-number distribution in the non-uniform region be given by

$$M(y) = M_1 e^{Ay}, \quad (38)$$

where A is a positive constant. This satisfies the conditions imposed on $M(y)$ in § 2. Before substituting for $M(y)$ in equation (14) from (38), it is convenient in this case to transform the independent variable in (14) from y to $M(y)$. We then have

$$M'^2(y)\frac{d^2\Pi}{dM^2} + M''(y)\frac{d\Pi}{dM} - 2\frac{M'^2(y)}{M(y)}\frac{d\Pi}{dM} + k^2\{M^2(y)-1\}\Pi = 0, \quad (39)$$

the primes denoting differentiation with respect to y. Putting $M(y) = M_1 e^{Ay}$, equation (39) becomes

$$\Pi'' - \frac{1}{M}\Pi' + \frac{k^2}{A^2}\left(1 - \frac{1}{M^2}\right)\Pi = 0, \quad (40)$$

where the primes now denote differentiation with respect to M. If we now put

$$\Pi = z\,u(z), \quad (41)$$

where

$$z = Mk/A, \quad (42)$$

the equation satisfied by $u(z)$ is

$$z^2 u'' + zu' + \{z^2 - [1 + (k/A)^2]\}u = 0, \quad (43)$$

the primes denoting differentiation with respect to z. Equation (50) is Bessel's equation, and hence the solution of (40) satisfying conditions (17) is

$$\Pi_0(k, y) = C\, e^{Ay} J_{\sqrt{[1+(k/A)^2]}}(M_1 e^{Ay} k/A), \quad (44)$$

where

$$C = [J_{\sqrt{[1+(k/A)^2]}}(M_1 k/A)]^{-1}. \quad (45)$$

In the general case of an arbitrary Mach-number profile it has not been found possible to say anything about the upstream influence of the disturbance, i.e. how far upstream of the characteristic $x+\beta y = 0$, along which the incident wave lies, the disturbance in the non-uniform region penetrates. In the analagous problem of shock-wave-boundary-layer interaction, Lighthill (1953) has shown that, even for non-separating boundary layers, the upstream influence of a shock wave extends some tens of boundary-layer thicknesses ahead of the point of incidence. It will be shown that in the present case, when the Mach-number variation across the non-uniform region is given by equation (38), the upstream influence is negligible, as we may expect in the absence of a wall.

Since $f(x) = 0$ for $x < 0$, the transform $F(k) = (2\pi)^{-1}\int_{-\infty}^{\infty} e^{-ikx} f(x)\,dx$ is regular in the lower half-plane. Then the only singularities of $\Pi(k, y)$ are poles at the zeros of the denominator of equation (18). Hence, whenever $x < 0$, the function $\varpi(x, y)$ may by (11) be expressed as $-2\pi i$ times the sum of the residues of $\Pi(k, y)\, e^{ikx}$ at the zeros of the denominator of (18) in the lower half-plane. Since only the lower half-plane is to be considered it is convenient to put $k = -iK$, also, as it is unlikely that the upstream disturbance will be wavy, we shall confine ourselves to real and positive K.

Before proceeding further we shall now introduce a length δ, to be known as the 'mixing region thickness', such that at $y = -\delta$ the velocity has fallen to only 1 % of its free-stream value M_1. Thus,

$$M_1 e^{-A\delta} = 0{\cdot}01 M_1,$$

giving
$$A \simeq 4{\cdot}61/\delta. \tag{46}$$

Now, since
$$\varpi(x, y) = -2\pi i \sum_{n=1}^{\infty} R_n(y)\, e^{K_n x},$$

the smallest $K_n\,(= K_1, \text{say})$, will give an estimate of how far upstream the disturbance penetrates. Defining $\alpha = K_1/A$, equation (46) shows that

$$e^{K_1 x} = \exp\left[(4{\cdot}61\alpha/\delta)x\right], \tag{47}$$

and hence, if $\alpha \geqslant 1$, equation (47) shows that the disturbance upstream of the incident wave is effectively damped out within one 'mixing region thickness'. This means that to show the upstream influence is negligible is to show that no zeros of the denominator of equation (18) lie in the range $0 \leqslant K/A < 1$. We are concerned then with solutions of the equation

$$\Pi_{0_y}(-iK, 0) + K\beta\Pi_0(-iK, 0) = 0, \tag{48}$$

where $\Pi_0(k, y)$ is given by equation (44). On putting $k = -iK$, equation (44) becomes

$$\Pi_0 = C_1 e^{Ay} I_{\sqrt{[1-(K/A)^2]}}(M_1 e^{Ay} K/A), \tag{49}$$

where
$$C_1 = [I_{\sqrt{[1-(K/A)^2]}}(M_1 K/A)]^{-1}. \tag{50}$$

If we now put
$$[1-(K/A)^2]^{\frac{1}{2}} = \nu, \quad M_1 K/A = \eta, \tag{51}$$

substitution of (49) into (48) gives, as the equation to be solved,

$$1+\eta\frac{I'_\nu(\eta)}{I_\nu(\eta)}+\frac{\eta\beta}{M_1}=0, \tag{52}$$

or

$$1+\nu+\eta\frac{I_{\nu+1}(\eta)}{I_\nu(\eta)}+\frac{\eta\beta}{M_1}=0. \tag{53}$$

Now, as has been explained above, the object is not to obtain explicit solutions of equation (53) but is rather to obtain the negative result that no solution exists in the range $0 \leqslant K/A < 1$, i.e. in $0 \leqslant \eta < M_1$. It can be shown that

$$\frac{I_{\nu+1}(\eta)}{I_\nu(\eta)}=\eta^2\sum_{m=0}^{\infty}a_m\eta^{2m}\Big/\sum_{m=0}^{\infty}b_m\eta^{2m}, \tag{54}$$

where both $a_m, b_m > 0$; hence, in the range of η under consideration, the last three terms of (53) are never less than zero, and so equation (53) has no roots in this range. We may conclude that the upstream influence is negligibly small.

Although analytic solutions of equation (14) have been found when the Mach-number distribution is given by (38), it has not been found possible to integrate equation (12) analytically to obtain the reflected wave. However, using numerical methods in conjunction with a high-speed electronic computer, the form of the reflected wave, for a particular free-stream Mach number $M_1=\sqrt{2}$, has been found both when the incident wave is a simple discontinuity representing a shock wave and when the pressure gradient of the incident wave contains simple discontinuities representing a Prandtl–Meyer expansion fan. For an incident shock wave, the reflected wave was expressed, from (12) and (19), as

$$\Delta^{-1}g(x)+\tfrac{1}{2}=(2\pi)^{-1}\int_{-\infty}^{\infty}e^{i(k/A)Ax}\frac{i\Pi_{0Y}(k/A,0)+(k/A)\,\beta\Pi_0(k/A,0)}{\Pi_{0Y}(k/A,0)+i(k/A)\,\beta\Pi_0(k/A,0)}\frac{1}{k/A}\,d(k/A), \tag{55}$$

where $Y=Ay$ and $F(k)$ is, from (29), given by

$$F(k)=\frac{\Delta}{2}\left\{\delta(k)-\frac{i}{2\pi k}\right\}, \tag{56}$$

where $\delta(x)$ is the Dirac delta function such that $\delta(x)=0$, $x\neq 0$ and

$$\int_{-x_0}^{x_0}f(x)\,\delta(x)\,dx=f(0)\quad\text{for any } x_0>0.$$

The function $\Pi_{0Y}(k/A,0)$, occurring in (55), was obtained by numerically integrating (14) with the Mach-number distribution given by (38), taking $M_1=\sqrt{2}$. The reflected wave thus obtained is given in figure 1, where $\Delta^{-1}g(x)$ is plotted against Ax, showing the very narrow region of compression followed by a broader region of expansion, the overall drop in pressure being of magnitude $\gamma p_1\Delta$. In figure 2 the reflected wave, due to an incident shock wave, both for the Mach-number distribution given by (38) and for the distribution $M(y)=M_1e^{-A^2y^2}$ with $M_1=\sqrt{2}$, are compared by plotting $\Delta^{-1}g(x)$ against x/δ, where δ is the mixing region thickness. The comparison shows that the form of $M(y)$, beyond certain basic requirements, is not critical in determining the reflected wave. If the

incident wave is a Prandtl–Meyer expansion fan, represented by a discontinuity $-\gamma p_1 \Delta/l$ in the pressure gradient followed by a further discontinuity $\gamma p_1 \Delta/l$, where l is the length of the expansion and the overall drop in pressure is $\gamma p_1 \Delta$, then, as we have seen earlier, since $\partial\varpi/\partial x$ satisfies the same equation and boundary conditions as ϖ, the pressure gradient in the reflected wave is given as a linear combination of two reflected waves of the type shown in figure 1. The

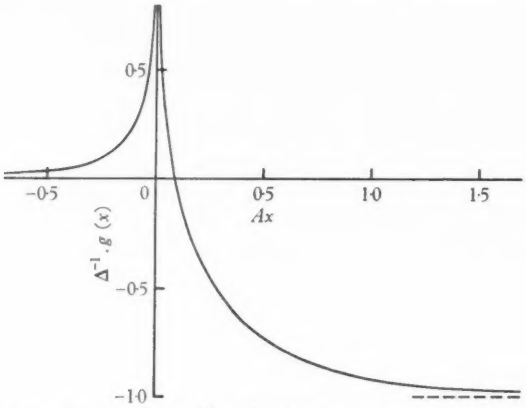

FIGURE 1. Reflected wave when the incident wave represents a shock wave.

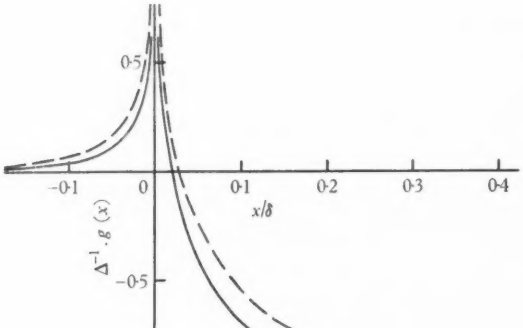

FIGURE 2. Comparison of the reflected wave due to an incident shock wave when (*a*) $M(y) = \sqrt{2}e^{Ay}$, ———; (*b*) $M(y) = \sqrt{2}e^{-A^2y^2}$, – – – –.

reflected wave is then obtained by simple integration. The reflected wave due to such an incident wave in the special case $Al = 1$ is shown in figure 3. This shows that there is, initially, a slight further drop in pressure followed by a sharp rise in pressure, the overall pressure rise being $\gamma p_1 \Delta$.

The Schlieren photograph shown in figure 4 (plate 1) is an example in which a plane shock wave, strong enough to cause separation, is incident on a boundary layer. The boundary layer is fully separated at the point where the incident shock

meets it, and the wave reflected there is seen to consist of a shock wave preceding a broad expansion wave. This shock wave loses its identity when it becomes coincident with the main reflected wave. Further Schlieren photographs (Johannesen 1957) show an axisymmetric jet emerging from a nozzle at a pressure less than atmospheric; in these the shock wave starting at the nozzle is incident on the mixing region and is reflected mainly as an expansion wave. On closer examination, however, remembering that we are looking through an axisymmetric jet, a thin dark line representing a narrow region of compression is seen immediately before the main expansion wave. Although the theory given above is for the two-dimensional case, we may expect the results, including the presence of such a region of compression, to hold qualitatively in the axisymmetric problem. These photographs do then provide evidence in favour of the theory given above.

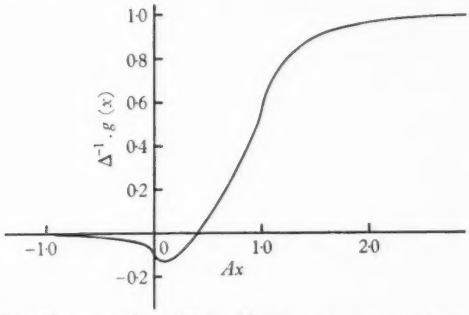

FIGURE 3. Reflected wave when the incident wave represents an expansion fan.

6. Improved linear theory

All the results obtained so far in preceding sections have been obtained using ordinary linearized theory; that is, in a uniform two-dimensional supersonic flow in which the two sets of characteristics are two sets of parallel straight lines, discontinuities to represent incident waves have been fitted on one or more of these characteristics pointing upstream, giving rise to a reflected wave situated along other characteristics pointing downstream, all the characteristics remaining unchanged. This failure of linear theory is fundamental, since regions in which shock waves occur are regions where the characteristics have run together and overlapped to form a limit line. The method by which we shall find the position of the shock wave in such a region is given in appendix B, which should be read in conjunction with the following discussion. For simplicity we shall only consider the flow around the reflected waves, shown in figures 1 and 3, and only in the region of uniform flow. The supersonic part of the non-uniform region will be very thin and errors introduced by ignoring it will only be significant at large distances from the non-uniform region. Furthermore, since all physical quantities have been obtained by neglecting products of small quantities, we shall here neglect such terms by using an approximation to $\tan(\mu+\theta)$, although the method outlined in appendix B allows products of small quantities to be retained.

Thus, taking

$$\varpi = \Delta \operatorname{sgn} f + g(x-\beta y), \tag{57}$$

where $\operatorname{sgn} f = +1$ if the incident wave represents a shock wave with pressure rise $\gamma p_1 \Delta$, and $\operatorname{sgn} f = -1$ if the incident wave represents a Prandtl–Meyer expansion with overall drop in pressure $\gamma p_1 \Delta$, we have, from (4),

$$\theta = \frac{1}{M_1^2} \int_x^\infty \frac{\partial \varpi}{\partial y} \, dx,$$

hence

$$\theta = \frac{\beta}{M_1^2} \{\Delta \operatorname{sgn} f + g(x - \beta y)\}. \tag{58}$$

Also, from Bernoulli's equation, neglecting products of small quantities, it can be shown that

$$\mu = \mu_\infty + \frac{(\gamma - 1) M_1^2 + 2}{2 M_1^2 (M_1^2 - 1)^{\frac{1}{2}}} \varpi. \tag{59}$$

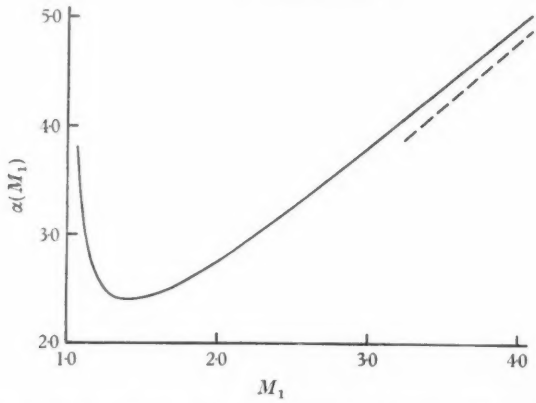

FIGURE 5. The coefficient $\alpha(M_1)$ occurring in equation (60) ($\gamma = 1{\cdot}4$).

Thus, along the correct characteristic $z(x, y) = \text{const.}$, we have from (58), (59) and (65)

$$\frac{dx}{dy} = \beta - \alpha\{\Delta \operatorname{sgn} f + g(z)\} \tag{60}$$

approximately, where $\alpha = \frac{1}{2}\beta^{-1}\{(\gamma - 1) M_1^2 + 2\} + \beta$ is shown in figure 5. If the value of z on a characteristic is taken as the value of $(x - \beta y)$ at the point where the characteristic meets the line $y = 0$, equation (60) can be integrated to give

$$x = \beta y - \alpha\{\Delta \operatorname{sgn} f + g(z)\} y + z. \tag{61}$$

Having found the characteristics, the mass-flow function $h(\mu)$ can be most easily determined along a line $x = \text{const.}$ by observing the value of μ at each point of the line where it is cut by a characteristic. Figures 6 and 7 show the mass flow function at different stations when the reflected wave is due to an incident shock and Prandtl–Meyer fan, respectively, with $\Delta = 0{\cdot}1$. In each case the shock wave is supposed to emerge from the non-uniform region at the point (0, 0). The associated flow patterns in figures 8 and 9 show very clearly the regions of compression, where the characteristics close together, and the regions of expansion where the characteristics spread out fanwise. It is important to note that now, in the reflected wave due to an incident shock wave, the only point where the pressure

is infinite is at (0, 0), elsewhere along the reflected shock the rise in pressure is finite, decreasing to zero under the influence of the neighbouring expansion fan. This removes the main peculiarity of the original theory, and makes what is left more satisfactory and credible.

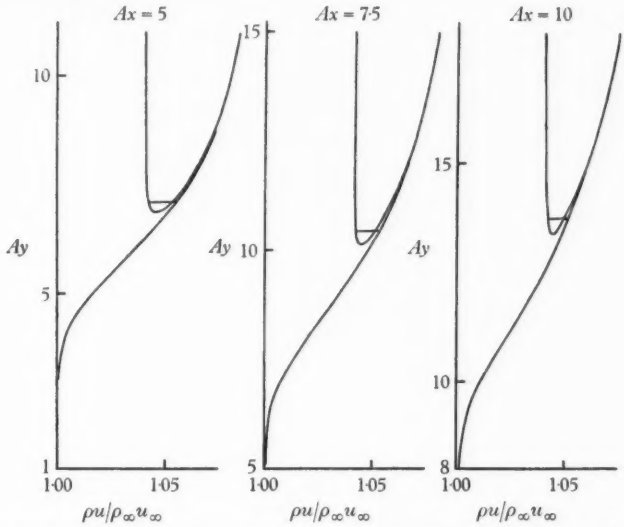

FIGURE 6. The mass flow at different stations when the incident wave is a shock wave. The horizontal line cutting off lobes of equal area indicates the position of the reflected shock wave ($M_1 = \sqrt{2}$, $\Delta = 0{\cdot}1$).

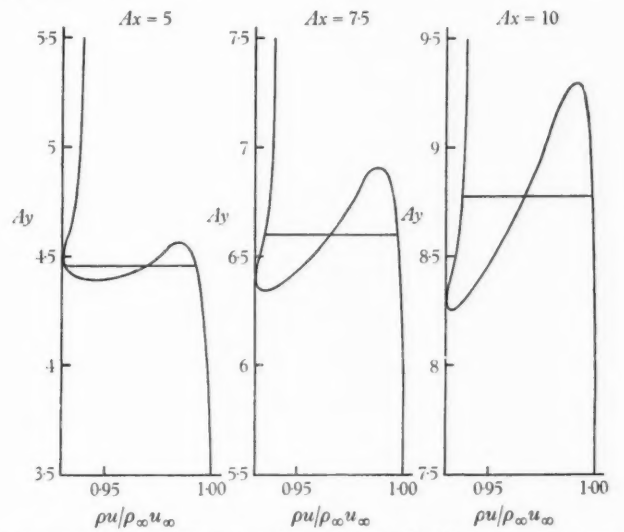

FIGURE 7. The mass flow at different stations when the incident wave is an expansion fan. The horizontal line cutting off lobes of equal area indicates the position of the reflected shock wave ($M_1 = \sqrt{2}$, $\Delta = 0{\cdot}1$).

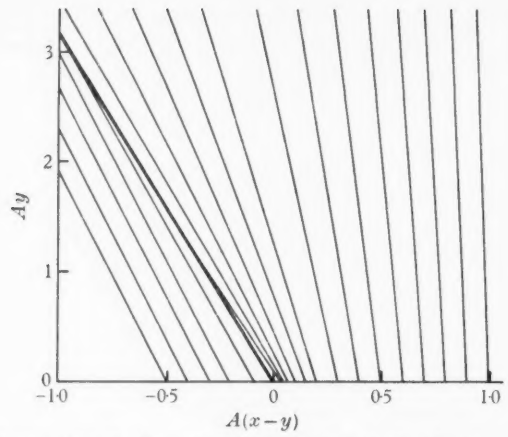

FIGURE 8. The flow pattern for the reflected wave when the incident wave is a shock wave. The shock wave in the reflected wave is indicated by the thicker line ($M_1 = \sqrt{2}$, $\Delta = 0{\cdot}1$).

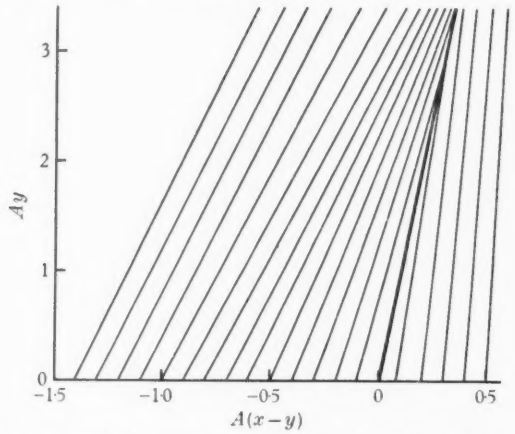

FIGURE 9. The flow pattern for the reflected wave when the incident wave is an expansion fan. The shock wave in the reflected wave is indicated by the thicker line ($M_1 = \sqrt{2}$, $\Delta = 0{\cdot}1$).

Appendix A

The results of Langer's theory used are briefly summarized here.

In the equation
$$\frac{d^2u}{dy^2} + p(y)\frac{du}{dy} + \{k^2q(y) + r(y)\}\,u = 0,$$
let $p(y)$, $q(y)$ and $r(y)$ be twice differentiable in $y_0 \leqslant y \leqslant y_2$. Let $q(y) < 0$ in $y_0 \leqslant y < y_1$ and $q(y) > 0$ in $y_1 < y \leqslant y_2$, while $q'(y_1) > 0$. Then two asymptotic solutions, valid in $y_0 \leqslant y \leqslant y_2$ as $|k| \to \infty$ for $y \neq y_1$ are

$$\left.\begin{aligned} u_1(y) &\sim \exp\left(-\frac{1}{2}\int_{y_1}^{y} p\,dy\right)\frac{|s|^{\frac{1}{6}}}{|q|^{\frac{1}{4}}}\left[\frac{e^{iks}}{(iks)^{\frac{1}{6}}} + \frac{e^{-iks}}{(-iks)^{\frac{1}{6}}}\right], \\ u_2(y) &\sim \exp\left(-\frac{1}{2}\int_{y_1}^{y} p\,dy\right)\frac{|s|^{\frac{2}{6}}}{|q|^{\frac{1}{4}}}\operatorname{sgn}(y-y_1)\left[\frac{e^{iks}}{(iks)^{\frac{2}{6}}} + \frac{e^{-iks}}{(-iks)^{\frac{2}{6}}}\right], \end{aligned}\right\} \tag{62}$$

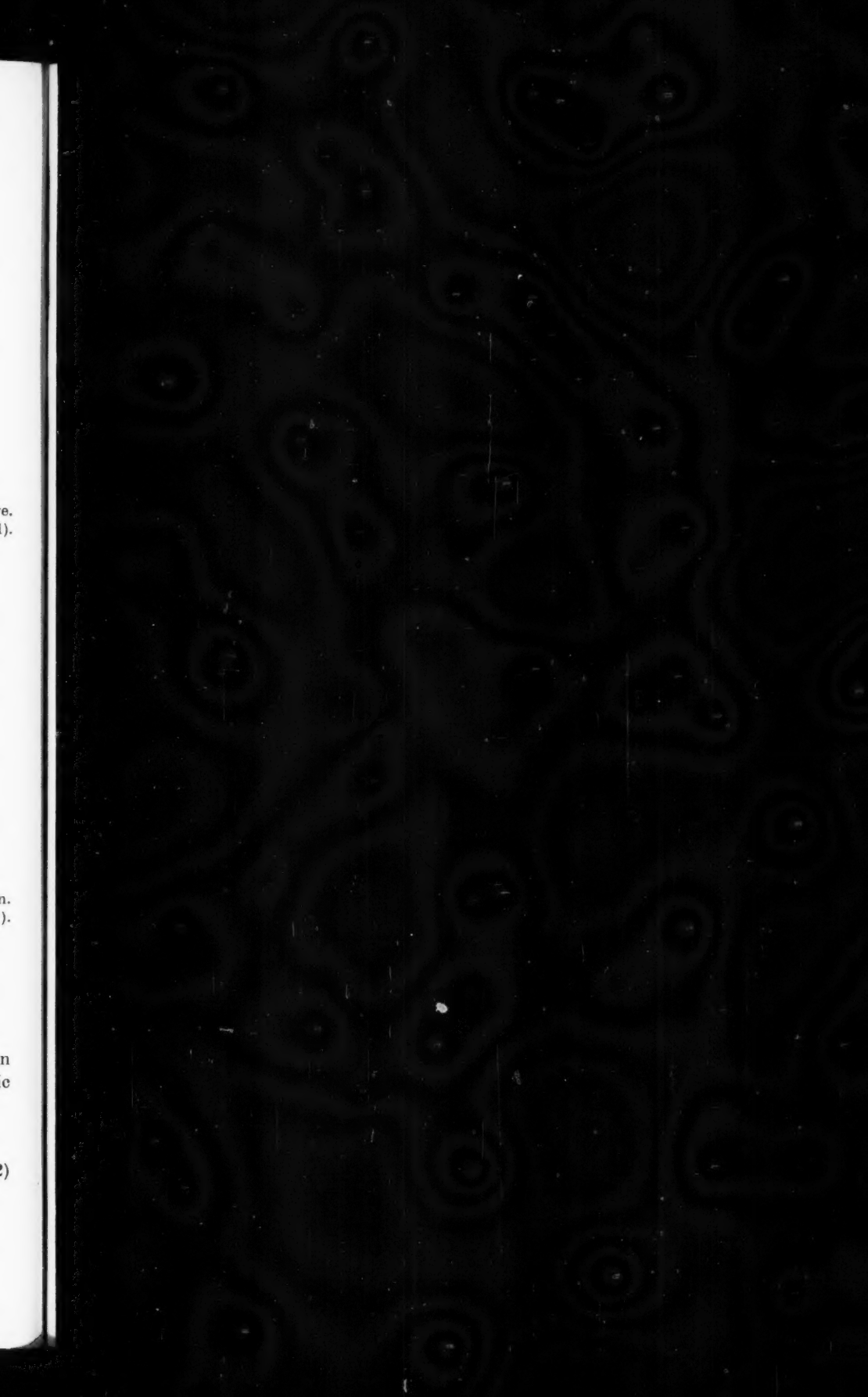

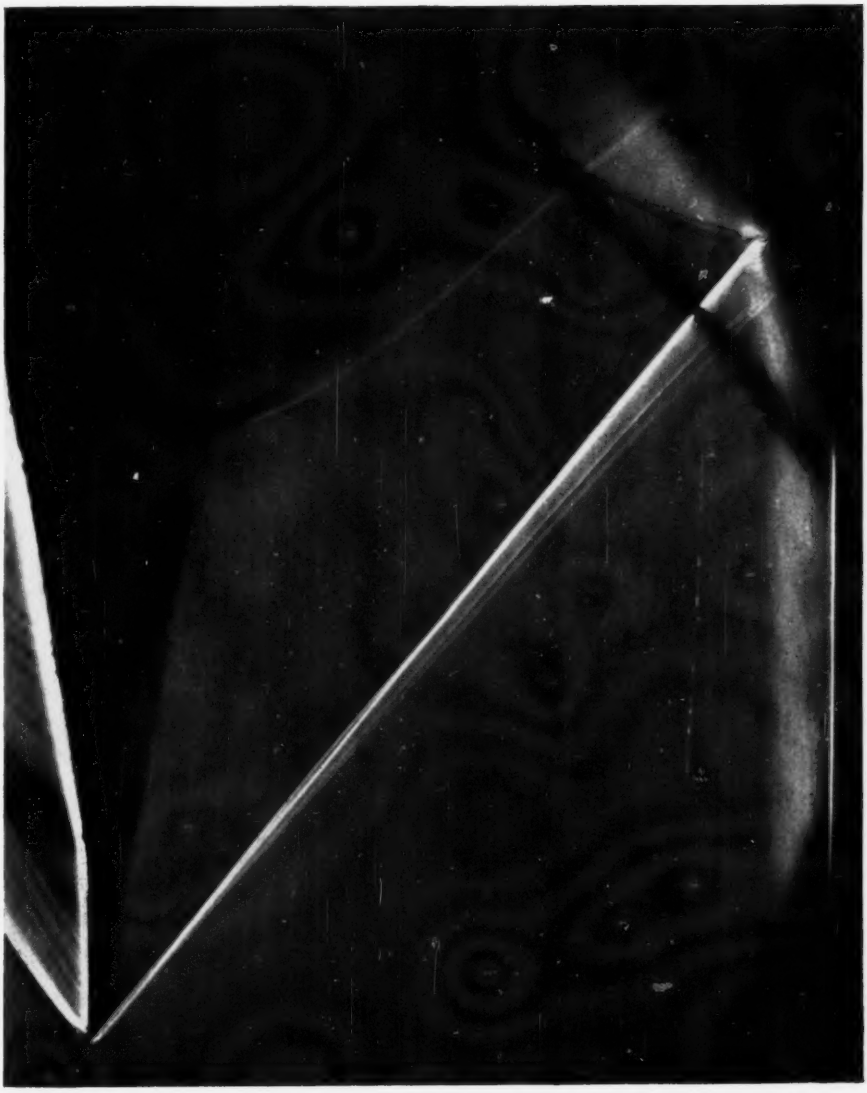

FIGURE 4 (plate 1). Shock wave incident on a two-dimensional boundary layer causing separation.

where
$$s = \int_{y_1}^{y} q^{\frac{1}{3}}\, dy. \tag{63}$$

When $y = y_1$

$$\left.\begin{aligned} u_1(y_1) &= \left(\frac{2}{3q'(y_1)}\right)^{\frac{1}{3}} \frac{2^{\frac{1}{3}}(2\pi)^{\frac{1}{3}}}{(-\frac{1}{3})!}, \quad u_1'(y_1) = 0, \\ u_2(y_1) &= 0, \quad u_2'(y_1) = (\tfrac{2}{3})^{\frac{1}{3}} \{q'(y_1)\}^{\frac{1}{3}} \frac{2^{-\frac{1}{3}}(2\pi)^{\frac{1}{3}}}{(\frac{1}{3})!}. \end{aligned}\right\} \tag{64}$$

If a special asymptotic solution is determined in either of these subintervals then it can be expressed in terms of u_1 and u_2 and hence extended into the other subinterval. In the theory of § 4, $y = y_1$ is seen to correspond to the sonic line and the method described here is used to extend solutions of (14) across this line.

Appendix B

The main fault that Whitham (1952) finds with linear theory is that although it gives a correct first approximation everywhere for any physical quantity on a characteristic, the characteristics themselves are incorrectly placed. From the physical quantities given by linear theory, Whitham calculates a first approximation to the correct characteristics, and, using the condition that when products of small quantities are negligible the shock bisects the pair of characteristics which meet it at any point, shows how the flow pattern can be completely determined. More refined methods of determining the flow pattern have been described by Lighthill (1957) and Kantrowitz (1958), and the method outlined below is foreshadowed by both these authors. The method, like Whitham's, can be criticized for assuming the discontinuous character of the solution in advance, but, since the only approximation to be made is that the flow is isentropic, the method is more accurate than Whitham's.

Assuming isentropic flow, we have that on the characteristics which point downstream in a two-dimensional flow

$$\frac{dy}{dx} = \tan(\mu + \theta), \tag{65}$$

where μ is the local Mach angle. Since, in isentropic flow, μ is constant along a characteristic and θ is a function of the Mach angle we can write (65) as

$$y - x\tan(\mu + \theta) = \text{const.} \tag{66}$$

Consider now the flux of mass parallel to the x-axis

$$\rho u/\rho_\infty u_\infty = \rho q \cos\theta/\rho_\infty q_\infty, \tag{67}$$

the subscript ∞ referring to some standard state of the flow. Now $\theta = f(\mu) - f(\mu_\infty)$ and $\rho q/\rho_\infty q_\infty = F(\mu, \mu_\infty)$ and so we may write (67) as

$$\rho u/\rho_\infty u_\infty = h(\mu, \mu_\infty), \tag{68}$$

and $h(\mu, \mu_\infty)$ will be known as the 'mass-flow function'. It may be shown that for a given μ_∞ the mass-flow function is an increasing function of μ, and when $\mu_\infty = \frac{1}{4}\pi$ figure 10 shows h as a function of μ.

Now, since on a characteristic

$$y - x\tan(\mu+\theta) = y_0 - x_0\tan(\mu+\theta), \tag{69}$$

it follows that

$$h(x,y) = h(x_0,y_0). \tag{70}$$

From (69) we may write equation (70) as

$$h(x,y) = h[x_0, y+(x_0-x)\tan(\mu+\theta)], \tag{71}$$

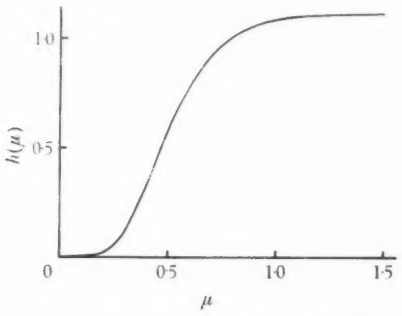

FIGURE 10. Mass flow function $h(\mu)$ when $\mu_\infty = \frac{1}{4}\pi$.

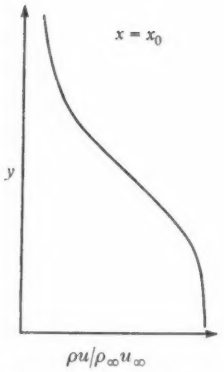

FIGURE 11. Typical mass-flow curve showing breakdown of uniqueness.

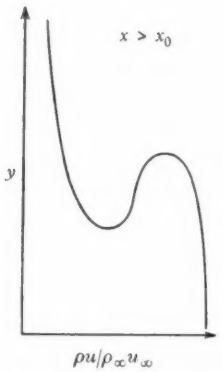

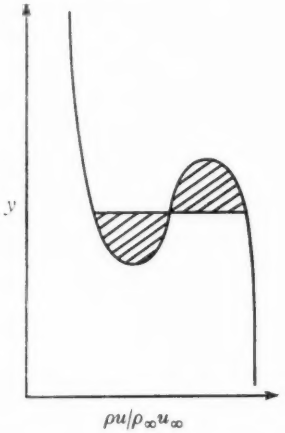

FIGURE 12. Typical non-unique mass-flow curve with horizontal line cutting off lobes of equal area indicating the position of the shock wave.

and so if the mass-flow function is known at any station x_0, for all y, then equation (71) enables us to find it at any other station x. Since μ is an increasing function of the pressure, equation (71) indicates that if a disturbance to the uniform flow is compressive, and if at x_0 the mass-flow function is a single-valued function of y, for some $x > x_0$ uniqueness breaks down and the mass-flow function becomes multi-valued as in figure 11. Obviously this state of affairs cannot exist physically, and a discontinuity representing a shock wave must be inserted on the mass-flow curve in order that the mass flow may remain single valued. Since

the area beneath the curve represents the mass flow, the discontinuity must be introduced so as to leave the total area under the curve constant, because the total mass flow cannot change as a result of the appearance of a shock wave. As shown in figure 12 this is achieved by letting the discontinuity cut off lobes of equal area on the mass-flow curve. The shock wave first develops where the tangent at the point of inflexion of the mass-flow curve becomes perpendicular to the y-axis under this shearing process.

Whitham's theory may be easily deduced from the above by noting that if we neglect products of small quantities then we can write

$$\tan(\mu+\theta) = \tan\mu_\infty + K(h-1), \tag{72}$$

and so, if the mass-flow function is known at any x, then, as equation (72) shows, it may be deduced at any other value of x by a simple linear shearing process. Since this shearing process conserves areas it may be noted that if, on the mass-flow function curve even when single-valued, lines are inserted cutting off equal area lobes on the curve then further downstream, each of these lines, in turn, will become perpendicular to the y-axis cutting off equal area lobes as we require. And so if, on a given mass-flow curve, lines are drawn cutting off lobes of equal area, then the complete flow pattern can be deduced since the pair of characteristics which pass through the points corresponding to the end-points of each line meet on the shock wave. This is, in effect, the rule given by Whitham (1952).

The author is indebted to Prof. M. J. Lighthill for his help and encouragement throughout the preparation of this paper, also to Dr N. H. Johannesen for permission to use the photograph shown in figure 4, plate 1.

REFERENCES

JOHANNESEN, N. H. 1957 Aero. Res. Counc., Lond., unpubl. rep. no. 18967.

KANTROWITZ, A. R. 1958 *Fundamentals of Gas Dynamics*, edited by H. W. Emmons. Princeton University Press.

LANGER, R. E. 1931 *Trans. Amer. Math. Soc.* **33**, 23.

LIGHTHILL, M. J. 1950 *Quart. J. Mech.* **3**, 303.

LIGHTHILL, M. J. 1953 *Proc. Roy. Soc.* A, **217**, 478.

LIGHTHILL, M. J. 1957 *Surveys in Mechanics.* The G. I. Taylor 70th Anniversary Volume, edited by G. K. Batchelor & R. M. Davies. Cambridge University Press.

LIGHTHILL, M. J. 1958 *Introduction to Fourier Analysis and Generalised Functions.* Cambridge University Press.

WHITHAM, G. B. 1952 *Commun. Pure Appl. Math.* **5**, 301.

Centrifugal waves

By O. M. PHILLIPS
Mechanical Engineering Department, The Johns Hopkins University, Baltimore, Maryland

(Received 10 June, 1959)

When a hollow circular cylinder with its axis horizontal is partially filled with water and rotated rapidly about its axis, an almost rigid-body motion results with an interior free surface. The motion is analysed assuming small perturbations to a rigid rotation, and a criterion is found for the stability of the motion. This is confirmed experimentally under varying conditions of water depth and angular velocity of the cylinder. The modes of oscillation (centrifugal waves) of the free surface are examined and a frequency equation deduced. Two particular modes are considered in detail, and satisfactory agreement is found with the frequencies observed.

1. Introduction

The term 'centrifugal waves' is a convenient one to describe the wave motion on the free surface of a rapidly rotating liquid, in which the equilibrium pressure distribution is determined primarily by the radial accelerations associated with the rotation. A simple apparatus in which the properties of these waves can be studied is shown in figure 1. A hollow circular transparent plastic cylinder C was supported by roller bearings B and mounted with its axis horizontal. The ends of the cylinder were closed except for a small hole H on the axis at one end through which water could be introduced slowly. The other end was coupled to a variable-speed motor, M.

When the cylinder is partially filled with water and rotated sufficiently rapidly, the water moves with almost rigid-body rotation about a central air core. The existence of the gravity field perpendicular to the axis and the presence of the free surface together impose a steady (time independent) perturbation on the truly rigid body motion, while for certain combinations of angular velocity and depth of water for a cylinder of given length, a variety of surface wave patterns are observed at the interface. These are most pronounced when the depth of water and speed of rotation are such that the half wavelength in the axial direction is an integral submultiple of the cylinder length. One particularly striking series of wave patterns is such that the free surface inside the rapidly rotating cylinder is stationary with respect to the observer. In another series, the wave crests are parallel to the cylinder axis and move circumferentially relative to the cylinder wall.

The wave frequencies and angular velocity of the cylinder were measured with a stroboscopic light. In a typical experiment, the empty cylinder was rotated at a constant angular velocity and water was introduced very slowly by means of

a thin tube passing through the hole H. As the depth of water increased slowly, the various modes of oscillation would build up and die away in turn, until, when the depth approached some critical value, the flow would become unstable and collapse suddenly.

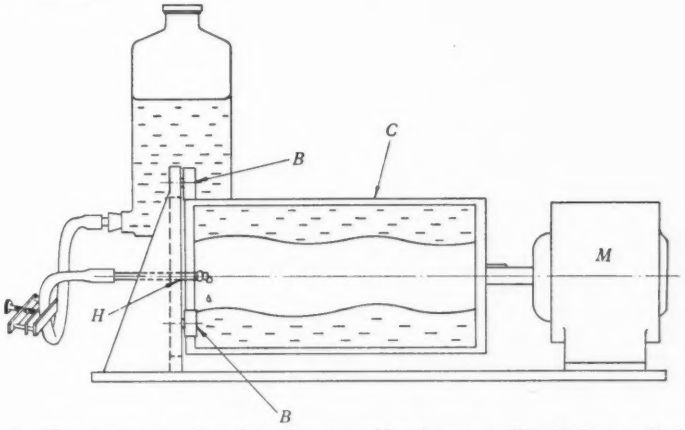

FIGURE 1. The apparatus for observing centrifugal waves. The hollow cylinder C is mounted on roller bearings B and driven by the motor M. Water is introduced through the small axial hole H.

In the following sections, a theory is developed to describe the various motions that can occur. At various points in the analysis, comparisons can be made with observations obtained in this way. Some of these phenomena were first observed by Mr L. Schaaf and Mr R. Drake, and detailed measurements were made with the able assistance of Mr E. C. Crist and Mr D. Meredith. I am also grateful to Mr W. G. Rose for the discussions we have had about this work.

2. The governing equations

Consider the motion inside a rotating circular cylinder of radius a with its axis horizontal, partially filled with a liquid of small viscosity, and suppose that the angular velocity Ω of the cylinder is sufficiently large that the motion of the fluid is almost a rigid-body rotation with a central air core.

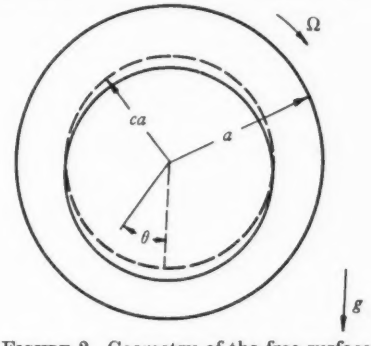

FIGURE 2. Geometry of the free surface.

The momentum and continuity equations for an inviscid fluid* are, expressed in cylindrical polar co-ordinates,

$$\left.\begin{aligned}
\frac{\partial u}{\partial t}+u\frac{\partial u}{\partial r}+\frac{v}{r}\frac{\partial u}{\partial \theta}+w\frac{\partial u}{\partial z}-\frac{v^2}{r} &= -\frac{1}{\rho}\frac{\partial p}{\partial r}+g\cos\theta,\\
\frac{\partial v}{\partial t}+u\frac{\partial v}{\partial r}+\frac{v}{r}\frac{\partial v}{\partial \theta}+w\frac{\partial v}{\partial z}+\frac{uv}{r} &= -\frac{1}{\rho r}\frac{\partial p}{\partial \theta}-g\sin\theta,\\
\frac{\partial w}{\partial t}+u\frac{\partial w}{\partial r}+\frac{v}{r}\frac{\partial w}{\partial \theta}+w\frac{\partial w}{\partial z} &= -\frac{1}{\rho}\frac{\partial p}{\partial z},\\
\frac{1}{r}\frac{\partial}{\partial r}(ru)+\frac{1}{r}\frac{\partial v}{\partial \theta}+\frac{\partial w}{\partial z} &= 0,
\end{aligned}\right\} \tag{2.1}$$

where u, v, w represent the velocity components in the directions r, θ, z, respectively, and the direction $\theta = 0$ is taken vertically downwards. If gravity were absent, the steady motion would be that of a rigid body, with

$$\left.\begin{aligned}
&u = 0, \quad v = \Omega r, \quad w = 0,\\
&p = \tfrac{1}{2}\rho\Omega^2(r^2-c^2a^2),
\end{aligned}\right\} \tag{2.2}$$

where a is the radius of the cylinder and ca ($0 < c < 1$) the radius of the cylindrical free surface. The presence of gravity, acting in a direction perpendicular to the axis, results in a steady perturbation on this rigid-body motion, and, as pointed out already, there may be in addition oscillatory wave disturbances. Therefore, writing

$$\eta = r/a,$$

let

$$\left.\begin{aligned}
u &= \Omega a(u_1+u_2),\\
v &= \Omega a(\eta+v_1+v_2),\\
w &= \Omega a w_2,
\end{aligned}\right\} \tag{2.3}$$

where u_1 and v_1 represent the steady (time-independent) disturbances, and u_2, v_2, w_2 the oscillating (wave) disturbances whose time average is zero. In the presence of gravity, the pressure distribution given by (2.2) is modified by a hydrostatic contribution and by the accompanying displacement of the free surface over which the pressure is constant. We therefore define quantities p_1, p_2 by

$$p = \tfrac{1}{2}\rho\Omega^2a^2\{(\eta^2-c^2)+p_1+p_2\}+\rho g a\eta\cos\theta, \tag{2.4}$$

where p_1 is time independent and the (time) mean value of p_2 is zero.

If the disturbances are sufficiently small (the nature of this requirement is discussed in more detail later), the dimensionless velocities $u_1, u_2, \ldots, w_2$ are small compared with η ($c \leqslant \eta < 1$) and when (2.3) and (2.4) are substituted into the

* The neglect of the viscous terms in (2.1) is discussed in § 3 below.

equations of motion (2.1), squares and products of the perturbations can be neglected. Thus

$$\left.\begin{aligned}
\frac{\partial u_2}{\partial \tau}+\frac{\partial}{\partial \theta}(u_1+u_2)-2(v_1+v_2) &= -\frac{1}{2}\frac{\partial}{\partial \eta}(p_1+p_2),\\
\frac{\partial v_2}{\partial \tau}+2(u_1+u_2)+\frac{\partial}{\partial \theta}(v_1+v_2) &= -\frac{1}{2\eta}\frac{\partial}{\partial \theta}(p_1+p_2),\\
\frac{\partial w_2}{\partial \tau}+\frac{\partial w_2}{\partial \theta} &= -\frac{1}{2}\frac{\partial}{\partial \zeta}(p_1+p_2),\\
\frac{1}{\eta}\frac{\partial}{\partial \eta}\{\eta(u_1+u_2)\}+\frac{1}{\eta}\frac{\partial}{\partial \theta}(v_1+v_2)+\frac{\partial w_2}{\partial \zeta} &= 0,
\end{aligned}\right\} \tag{2.5}$$

where $\tau = \Omega t$ and $\zeta = z/a$.

The equations that describe the steady disturbance to the rigid-body motion are obtained by taking the time average of (2.5):

$$\left.\begin{aligned}
\frac{\partial u_1}{\partial \theta}-2v_1 &= -\frac{1}{2}\frac{\partial p_1}{\partial \eta},\\
\frac{\partial v_1}{\partial \theta}+2u_1 &= -\frac{1}{2\eta}\frac{\partial p_1}{\partial \theta},\\
\frac{\partial p_1}{\partial \zeta} &= 0,\\
\frac{\partial}{\partial \eta}(\eta u_1)+\frac{\partial v_1}{\partial \theta} &= 0.
\end{aligned}\right\} \tag{2.6}$$

The equations for the wave motion are now found by subtracting the set (2.6) from the respective members of (2.5), giving

$$\left.\begin{aligned}
\frac{\partial u_2}{\partial \tau}+\frac{\partial u_2}{\partial \theta}-2v_2 &= -\frac{1}{2}\frac{\partial p_2}{\partial \eta},\\
\frac{\partial v_2}{\partial \tau}+\frac{\partial v_2}{\partial \theta}+2u_2 &= -\frac{1}{2\eta}\frac{\partial p_2}{\partial \theta},\\
\frac{\partial w_2}{\partial \tau}+\frac{\partial w_2}{\partial \theta} &= -\frac{1}{2}\frac{\partial p_2}{\partial \zeta},\\
\frac{1}{\eta}\frac{\partial}{\partial \eta}(\eta u_2)+\frac{1}{\eta}\frac{\partial v_2}{\partial \theta}+\frac{\partial w_2}{\partial \zeta} &= 0.
\end{aligned}\right\} \tag{2.7}$$

We now turn to consideration of the boundary conditions to be imposed on the sets of equations (2.6) and (2.7). Clearly, at the cylinder wall, both the steady and oscillatory parts of the normal velocity components must vanish, so that

$$u_1 = u_2 = 0 \quad \text{when} \quad \eta = 1. \tag{2.8}$$

Let the free surface, at which the pressure is constant, be given by

$$\eta = c+\delta_1(\theta)+\delta_2(\theta,\zeta,\tau), \tag{2.9}$$

where δ_1 and δ_2 represent dimensionless steady and oscillatory displacements, which are assumed to be small compared with the mean free-surface radius c. Substituting into (2.4) and taking the free-surface pressure as zero, we have

$$2c\frac{g}{\Omega^2 a}\cos\theta+2c(\delta_1+\delta_2)+p_1+p_2 = 0, \tag{2.10}$$

on $\eta = c$, correct to the first order in the infinitesimal wave displacements and to the first order in $g/\Omega^2 a$, the magnitude of the steady disturbance. Taking the mean and oscillating parts of (2.10), we obtain

$$p_1 + 2c\delta_1 = -2c\frac{g}{\Omega^2 a}\cos\theta \tag{2.11}$$

for the steady disturbance, and

$$p_2 + 2c\delta_2 = 0 \tag{2.12}$$

for the wave motion, both when $\eta = c$. The neglect of squares and products of order $(g/\Omega^2 a)^2$ in these boundary conditions is consistent with the neglect of the non-linear disturbance terms in the dynamical equations.

Finally, we have the kinematic boundary condition

$$u = \frac{D\delta}{Dt}$$

at the free surface, and since

$$\frac{D}{Dt} \simeq \frac{\partial}{\partial t} + \frac{\Omega r}{r}\frac{\partial}{\partial \theta},$$

we have

$$u_1 = \frac{\partial \delta_1}{\partial \theta} \tag{2.13}$$

and

$$u_2 = \frac{\partial \delta_2}{\partial \tau} + \frac{\partial \delta_2}{\partial \theta} \tag{2.14}$$

at $\eta = c$, for the steady and wave motions, respectively.

3. The steady disturbance

It is convenient to collect together from the previous section the equations describing the steady disturbance to the rigid body motion, set up by the gravity field. They are

$$\left.\begin{aligned} \frac{\partial u_1}{\partial \theta} - 2v_1 &= -\frac{1}{2}\frac{\partial p_1}{\partial \eta}, \\ \frac{\partial v_1}{\partial \theta} + 2u_1 &= -\frac{1}{2\eta}\frac{\partial p_1}{\partial \theta}, \\ \frac{\partial}{\partial \eta}(\eta u_1) + \frac{\partial v_1}{\partial \theta} &= 0, \end{aligned}\right\} \tag{3.1}$$

with the boundary conditions

$$u_1 = 0 \quad \text{at} \quad \eta = 1, \tag{3.2}$$

$$\left.\begin{aligned} p_1 + 2c\delta_1 &= -2c\frac{g}{\Omega^2 a}\cos\theta \\ u_1 &= \frac{\partial \delta_1}{\partial \theta} \end{aligned}\right\} \quad \text{at} \quad \eta = c. \tag{3.3}$$

The form of these equations suggests the substitutions

$$\begin{aligned} \delta_1 &= \Delta \cos\theta, \\ p_1 &= P(\eta)\cos\theta, \\ u_1 &= \chi(\eta)\sin\theta, \\ v_1 &= \phi(\eta)\cos\theta, \end{aligned}$$

so that

$$\left.\begin{aligned} \chi - 2\phi &= -\tfrac{1}{2}P', \\ -\phi + 2\chi &= \frac{1}{2\eta}P, \\ \chi + \eta\chi' - \phi &= 0, \end{aligned}\right\} \tag{3.4}$$

and

$$\left.\begin{aligned} \chi &= 0 \quad \text{at} \quad \eta = 1, \\ P + 2c\Delta &= -2c\frac{g}{\Omega^2 a} \quad \text{at} \quad \eta = c, \\ \chi + \Delta &= 0 \quad \text{at} \quad \eta = c, \end{aligned}\right\} \tag{3.5}$$

where the primes denote differentiation with respect to η.

Substituting for ϕ from the third equation of (3.4) into the other two, we have

$$-\chi - 2\eta\chi' = -\tfrac{1}{2}P',$$

$$\eta\chi + \eta^2\chi' = \tfrac{1}{2}P,$$

and on eliminating P,

$$\eta^2\chi'' + 3\eta\chi' = 0.$$

Thus

$$\chi = \frac{A}{\eta^2} + B,$$

where A and B are constants to be determined. The first equation of (3.5) gives $B = -A$, so that

$$\chi(\eta) = A\left(\frac{1}{\eta^2} - 1\right), \tag{3.6}$$

and from (3.4) it follows that

$$\phi(\eta) = -A\left(\frac{1}{\eta^2} + 1\right), \tag{3.7}$$

$$P(\eta) = 2A\eta\left(\frac{3}{\eta^2} - 1\right). \tag{3.8}$$

The boundary conditions at $\eta = c$ enable us to determine the constant A and the surface displacement Δ:

$$A = -\frac{c^2}{2}\frac{g}{\Omega^2 a}, \tag{3.9}$$

$$\Delta = \tfrac{1}{2}(1 - c^2)\frac{g}{\Omega^2 a}. \tag{3.10}$$

The steady gravity-induced disturbance is thus given by

$$\left.\begin{aligned} u_1 &= -\frac{c^2}{2}\frac{g}{\Omega^2 a}\left(\frac{1}{\eta^2} - 1\right)\sin\theta, \\ v_1 &= \frac{c^2}{2}\frac{g}{\Omega^2 a}\left(\frac{1}{\eta^2} + 1\right)\cos\theta, \\ p_1 &= -c^2\frac{g}{\Omega^2 a}\eta\left(\frac{3}{\eta^2} - 1\right)\cos\theta, \\ \delta_1 &= \frac{1}{2}\frac{g}{\Omega^2 a}(1 - c^2)\cos\theta. \end{aligned}\right\} \tag{3.11}$$

The vorticity of this perturbation is of course zero, since the basic flow has constant vorticity. A property of these solutions that is at first sight curious is that the central air core has its axis *below* the axis of the rotating cylinder. However, it can be seen readily that as the fluid moves from points $\theta = 0$ to $\theta = \pi$, it acquires potential energy at the expense of its kinetic energy. The circumferential velocity when $\theta = \pi$ is therefore less than when $\theta = 0$, so that by continuity the thickness of the layer must be greater.

The solutions (3.11) show that at the cylinder surface $\eta = 1$, the circumferential velocity perturbation $v_1 = c^2 g \cos\theta/\Omega^2 a$. If the liquid has viscosity ν, a boundary layer is formed of thickness $(2\nu/\Omega)^{\frac{1}{2}}$, since Ω is the frequency of the perturbation velocity at a fixed point on the rotating cylinder. In order that the above solutions be valid throughout most of the region occupied by the fluid, it is necessary that

$$(2\nu/\Omega)^{\frac{1}{2}} \ll a(1-c),$$

i.e.

$$\frac{\Omega a^2(1-c)^2}{\nu} \gg 2, \tag{3.12}$$

or that the Reynolds number of the layer be large. This condition is invalidated when $1-c$ is very small, and the fluid lies in a thin film inside the cylindrical wall.

In the plane $\theta = \pi$, the gravitational and centrifugal pressure gradients are of opposite sign, and a necessary condition for the stability of the flow is that the net radial pressure gradient be positive. In the absence of wave disturbances, we have from (2.4) and (3.11)

$$p_{\theta=\pi} = \tfrac{1}{2}\rho\Omega^2 a^2\left\{(\eta^2 - c^2) + \frac{g}{\Omega^2 a}c^2\left(\frac{3}{\eta} - \eta\right)\right\} - \rho g a\eta$$

$$= \tfrac{1}{2}\rho\Omega^2 a^2\left\{(\eta^2 - c^2) + \frac{g}{\Omega^2 a}\left[\frac{3c^2}{\eta} - (2+c^2)\,\eta\right]\right\},$$

so that a necessary condition for stability is that

$$\left(\frac{\partial p}{\partial \eta}\right)_{\theta=\pi} = \tfrac{1}{2}\rho\Omega^2 a^2\left\{2\eta - \frac{g}{\Omega^2 a}\left[\frac{3c^2}{\eta^2} + (2+c^2)\right]\right\} > 0, \tag{3.13}$$

for $c + \delta_1 \leqslant \eta \leqslant 1$. This condition is strictest when

$$\eta = c + \delta_1 = c - \frac{1}{2}\frac{g}{\Omega^2 a}(1-c^2),$$

from (3.11), so that we require

$$2c - \frac{g}{\Omega^2 a}(1-c^2) - \frac{g}{\Omega^2 a}(5+c^2) > 0,$$

approximately, or

$$\frac{\Omega^2 a}{g} > \frac{3}{c}. \tag{3.14}$$

This condition states that if the flow is to be stable, the value of $\Omega^2 a/g$ cannot be less than $3/c$ (except when $1-c$ is very small, and the flow is viscosity controlled). However, instability and collapse of the flow may occur at values of

$\Omega^2 a/g$ greater than $3/c$ if wave motions of large amplitude are present in addition. This lower limit is illustrated in figure 3, together with some experimental points giving measured values of c for collapse at various values of the parameter $\Omega^2 a/g$. It will be seen that the observational points all lie above the theoretical curve. As mentioned in the introduction, these points were obtained by holding the parameter $\Omega^2 a/g$ constant, and decreasing c from unity by the slow addition of water through the hole H. Values of c at collapse were closest to the theoretical value when $\Omega^2 a/g$ was such that, for the cylinder of given length, there

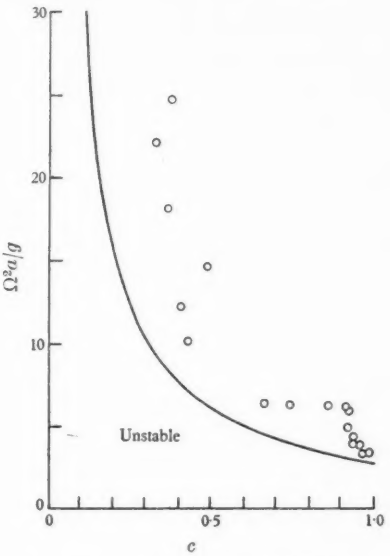

FIGURE 3. The stability condition.

were no large-amplitude wave modes present as c approached its critical value. If there were such waves present, as was usually the case, the collapse occurred prematurely at a larger value of c, because of a momentary unbalance induced by the waves. Near $c = 1$, it is likely that non-linear effects may be significant, since for marginal stability the parameter $\Omega^2 a/g$ is approximately 3, which is not an order of magnitude greater than unity.

It is perhaps worth noting that for a certain region above the curve shown in figure 3, the flow is metastable in the sense that for given values of $\Omega^2 a/g$ and c two types of flow are possible. The first is the almost rigid motion discussed here, and the second a 'collapsed' motion in which the water lies at the bottom of the cylinder and moves in a closed eddy with an almost plane, though tilted, free surface. To restore the almost rigid body motion after collapse, a considerably higher angular velocity of the cylinder is required.

4. The wave motion

The equations to be satisfied by the wave motion are conveniently rewritten here from §2. The momentum and continuity equations are

$$\left.\begin{aligned} \frac{\partial u_2}{\partial \tau}+\frac{\partial u_2}{\partial \theta}-2v_2 &= -\frac{1}{2}\frac{\partial p_2}{\partial \eta}, \\ \frac{\partial v_2}{\partial \tau}+\frac{\partial v_2}{\partial \theta}+2u_2 &= -\frac{1}{2\eta}\frac{\partial p_2}{\partial \theta}, \\ \frac{\partial w_2}{\partial \tau}+\frac{\partial w_2}{\partial \theta} &= -\frac{1}{2}\frac{\partial p_2}{\partial \zeta}, \\ \frac{1}{\eta}\frac{\partial}{\partial \eta}(\eta u_2)+\frac{1}{\eta}\frac{\partial v_2}{\partial \theta}+\frac{\partial w_2}{\partial \zeta} &= 0. \end{aligned}\right\} \tag{4.1}$$

The appropriate boundary conditions are

$$\left.\begin{aligned} u_2 &= 0 \quad \text{when} \quad \eta = 1, \\ \left.\begin{aligned} p_2+2c\delta_2 &= 0 \\ u_2 &= \frac{\partial \delta_2}{\partial \tau}+\frac{\partial \delta_2}{\partial \theta}, \end{aligned}\right\} & \quad \text{when} \quad \eta = c. \end{aligned}\right\} \tag{4.2}$$

Consider disturbances periodic in time and in the θ- and ζ-directions:

$$\left.\begin{aligned} u_2 &= \chi(\eta)\exp i(n\tau+k\zeta+l\theta), \\ v_2 &= \phi(\eta)\exp i(n\tau+k\zeta+l\theta), \\ w_2 &= \psi(\eta)\exp i(n\tau+k\zeta+l\theta), \\ p_2 &= P(\eta)\exp i(n\tau+k\zeta+l\theta), \\ \delta_2 &= \Delta\exp i(n\tau+k\zeta+l\theta), \end{aligned}\right\} \tag{4.3}$$

where l is an integer and no confusion need arise over the use of the same functional symbols, χ, ϕ, etc., that represented corresponding quantities in the analysis for the steady disturbance on the rigid-body motion.

With these substitutions, the governing equations become

$$\left.\begin{aligned} i(n+l)\chi-2\phi &= -\tfrac{1}{2}P', \\ i(n+l)\phi+2\chi &= -\frac{il}{2\eta}P, \\ i(n+l)\psi &= -\tfrac{1}{2}ikP, \\ \frac{\chi}{\eta}+\chi'+\frac{il}{\eta}\phi+ik\psi &= 0, \end{aligned}\right\} \tag{4.4}$$

with

$$\left.\begin{aligned} \chi &= 0 \quad \text{at} \quad \eta = 1, \\ P+2c\Delta &= 0 \quad \text{at} \quad \eta = c, \\ \chi &= i(n+l)\Delta \quad \text{at} \quad \eta = c. \end{aligned}\right\} \tag{4.5}$$

The equations (4.4) can be solved by substituting for ϕ, χ and ψ in the continuity equation, giving a single equation for P, namely

$$P'' + \frac{1}{\eta} P' + \left(\gamma^2 - \frac{l^2}{\eta^2}\right) P = 0, \tag{4.6}$$

where

$$\gamma^2 = \frac{k^2[4-(n+l)^2]}{(n+l)^2}. \tag{4.7}$$

Equation (4.6) is Bessel's equation and since l is integral, the solution is expressible (if $\gamma^2 > 0$) in terms of Bessel functions of the first and second kind,

$$P(\eta) = \alpha J_l(\gamma\eta) + \beta Y_l(\gamma\eta), \tag{4.8}$$

where α and β are constants whose ratio is to be determined.

The remainder of the solution is obtained readily. From the third of equations (4.4),

$$\psi(\eta) = -\frac{k}{2(n+l)} \{\alpha J_l(\gamma\eta) + \beta Y_l(\gamma\eta)\}, \tag{4.9}$$

while from the first two of this set,

$$\begin{aligned}\phi(\eta) = \frac{\gamma}{4[4-(n+l)^2]} &\{\alpha[(2+n+l) J_{l-1}(\gamma\eta) - (2-n-l) J_{l+1}(\gamma\eta)] \\ &+ \beta[(2+n+l) Y_{l-1}(\gamma\eta) - (2-n-l) Y_{l+1}(\gamma\eta)]\},\end{aligned} \tag{4.10}$$

$$\begin{aligned}\chi(\eta) = \frac{-i\gamma}{4[4-(n+l)^2]} &\{\alpha[(2+n+l) J_{l-1}(\gamma\eta) + (2-n-l) J_{l+1}(\gamma\eta)] \\ &+ \beta[(2+n+l) Y_{l-1}(\gamma\eta) + (2-n-l) Y_{l+1}(\gamma\eta)]\},\end{aligned} \tag{4.11}$$

where we have used the relations

$$\left.\begin{aligned}\frac{1}{\gamma}\frac{d}{d\eta} J_l(\gamma\eta) &= \frac{l}{\gamma\eta} J_l(\gamma\eta) - J_{l+1}(\gamma\eta), \\ \frac{2lJ_l(\gamma\eta)}{\gamma\eta} &= J_{l-1}(\gamma\eta) + J_{l+1}(\gamma\eta),\end{aligned}\right\} \tag{4.12}$$

and similar expressions for the Y-functions.

The ratio α/β is determined by the first of the boundary conditions (4.5), and from (4.11) we have immediately

$$\frac{\alpha}{\beta} = -\frac{(2+n+l) Y_{l-1}(\gamma) + (2-n-l) Y_{l+1}(\gamma)}{(2+n+l) J_{l-1}(\gamma) + (2-n-l) J_{l+1}(\gamma)}. \tag{4.13}$$

The second and third members of the set (4.5) determine the frequency equation $n = n(k, l, c)$. Eliminating Δ,

$$\chi + \frac{i(n+l)}{2c} P = 0 \quad \text{at} \quad \eta = c, \tag{4.14}$$

and substitution from the expressions above gives, after some algebra,

$$\begin{aligned}&\frac{\left(\frac{l+n}{l} - \frac{1}{2-n-l}\right) J_{l-1}(\gamma c) + \left(\frac{l+n}{l} - \frac{1}{2+n+l}\right) J_{l+1}(\gamma c)}{(2+n+l) J_{l-1}(\gamma) + (2-n-l) J_{l+1}(\gamma)} \\ &\quad = \frac{\left(\frac{l+n}{l} - \frac{1}{2-n-l}\right) Y_{l-1}(\gamma c) + \left(\frac{l+n}{l} - \frac{1}{2+n+l}\right) Y_{l+1}(\gamma c)}{(2+n+l) Y_{l-1}(\gamma) + (2-n-l) Y_{l+1}(\gamma)},\end{aligned} \tag{4.15}$$

an implicit relation between n, k, l and c.

Of the many possible wave motions, one of the most striking is the one specified by $l = 1$, $n = 0$. The free surface is stationary with respect to the observer and stands like a sinusoidally flexed transparent cylinder within the rapidly rotating outer case. With $l = 1$, $n = 0$ (4.15) reduces to

$$\{3Y_0(\gamma) + Y_2(\gamma)\}J_2(\gamma c) - \{3J_0(\gamma) + J_2(\gamma)\}Y_2(\gamma c) = 0, \tag{4.16}$$

where now $\gamma = k\sqrt{3}$. The allowable axial wave-numbers k for this wave mode are given by the roots of this equation and are illustrated as functions of c in figure 4. It is evident that k is multiple valued; an infinite number of wave-numbers k with

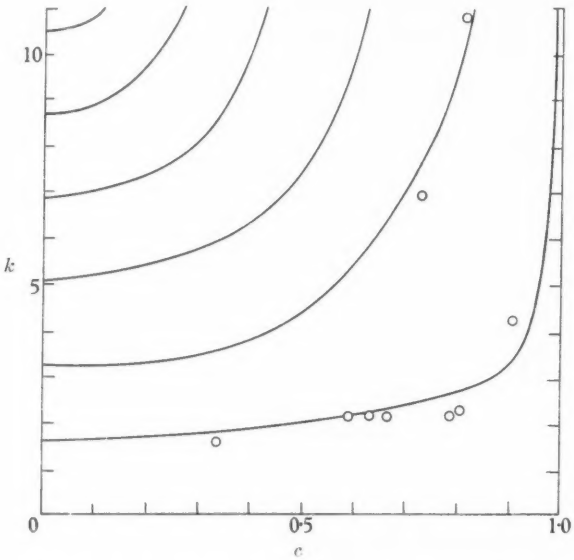

FIGURE 4. Allowable wave-numbers for stationary waves ($n = 0$) as a function of c.

$n = 0$ being possible for a given value of c. These waves were excited in the apparatus only when the wavelength was an integral submultiple of twice the cylinder length, so that only a few distinct modes of oscillation were observed. The agreement between the wave-numbers of the modes that were excited and the theoretical predictions are quite good, points being found near the two lowest branches of figure 4. For small values of c we have seen that the flow becomes unstable even for large values of $\Omega^2 a/g$, and the minimum attainable value of c for almost rigid body rotation in our apparatus was a little less than 0·4.

If $\gamma^2 < 0$, a similar frequency equation can be derived without difficulty, involving Bessel functions of purely imaginary argument. If $\gamma = 0$, that is, if either $k = 0$ or $(l+n)^2 = 4$, the above solutions become degenerate. The case $k = 0$ is more interesting physically since it represents a two-dimensional motion in which the crests are parallel to the cylinder axis and move in a circumferential direction.

When $\gamma = 0$, equation (4.6) reduces to

$$P'' + \frac{1}{\eta} P' - \frac{l^2}{\eta^2} P = 0,$$

whence

$$P(\eta) = A\eta^l + B\eta^{-l}, \tag{4.17}$$

where A and B are constants. If $k = 0$, we have immediately from (4.4),

$$\psi(\eta) = 0$$

$$\phi(\eta) = \frac{Al\eta^{l-1}}{2(2-n-l)} - \frac{Bl\eta^{-l-1}}{2(2+n+l)}, \tag{4.18}$$

$$\chi(\eta) = \frac{-iAl\eta^{l-1}}{2(2-n-l)} - \frac{iBl\eta^{-l-1}}{2(2+n+l)}. \tag{4.19}$$

The first boundary condition (4.5) requires

$$\frac{A}{B} = -\frac{2-n-l}{2+n+l},$$

so that

$$\left.\begin{aligned} P(\eta) &= \frac{A}{2-n-l}\{(2-n-l)\eta^l - (2+n+l)\eta^{-l}\}, \\ \phi(\eta) &= \frac{Al}{2(2-n-l)}\{\eta^{l-1} + \eta^{-l-1}\}, \\ \chi(\eta) &= \frac{-iAl}{2(2-n-l)}\{\eta^{l-1} - \eta^{-l-1}\}. \end{aligned}\right\} \tag{4.20}$$

The frequency equation follows from the boundary conditions at $\eta = c$. From (4.5),

$$\chi + \frac{i(n+l)}{2c} P = 0 \quad \text{at} \quad \eta = c,$$

whence, on substitution from (4.16),

$$n^2(1+c^{2l}) + 2n\{(1+l) - (1-l)c^{2l}\} + l\{(1+l) - (1-l)c^{2l}\} = 0. \tag{4.21}$$

This frequency equation can be obtained alternatively from (4.15) by a limiting process as $\gamma \to 0$, $(l+n)^2 \neq 4$. The roots of (4.21) are illustrated in figure 5 as functions of c for the case $l = 1$, which was the mode excited most readily in our apparatus. For a given value of c there are two possible wave frequencies, one greater and one less than the rotation frequency of the cylinder. The slow waves were observed most commonly, and their frequencies agreed well with the theoretical curve. The occurrence of these waves was often a prelude to premature collapse. On two occasions only were the high-frequency waves observed and both times they occurred in combination with one of the other modes. Presumably the high-frequency waves are more heavily damped by viscosity, and this may account for the relative difficulty in generating them.

It is interesting to notice that when $c = 1-\epsilon$, $\epsilon \ll 1$, equation (4.21) gives approximately

$$n = -l(1 \pm \epsilon^{\frac{1}{2}}),$$

where the relative signs of l and n determine the direction of wave motion. In a frame of reference rotating with the cylinder,

$$n = \mp l\epsilon^{\frac{1}{2}},$$

or in dimensional form, with frequency $\sigma = \Omega n$ and layer depth $d = \epsilon a$,

$$\sigma = \pm l\left(\frac{\Omega^2}{a}\right)^{\frac{1}{2}} d^{\frac{1}{2}}.$$

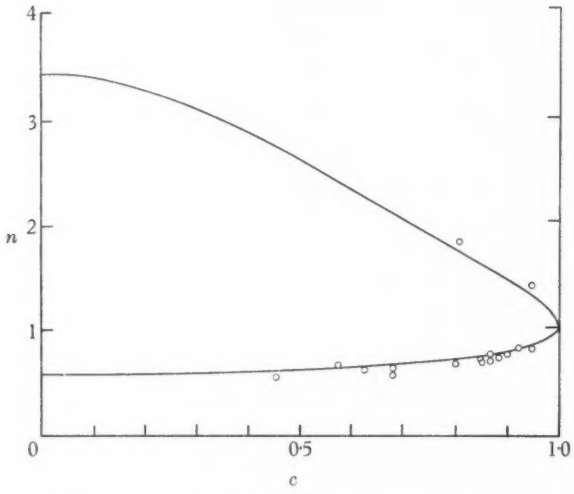

FIGURE 5. The frequency of circumferential waves with one node.

Since the wavelength $\lambda = 2\pi a/l$, and the wave velocity $V = \sigma\lambda/2\pi$, we have

$$V = (\Omega^2 a)^{\frac{1}{2}} d^{\frac{1}{2}}. \tag{4.22}$$

This is seen to be exactly analogous to the velocity of gravity waves under the long wave approximation ($\lambda \gg d$), where

$$V = g^{\frac{1}{2}} d^{\frac{1}{2}}.$$

The gravitational acceleration g is here replaced by the radial acceleration $\Omega^2 a$ in the rotating system.

This work was supported by the Office of Naval Research under contract Nonr 38(248).

The impact of a water wedge on a wall

By E. CUMBERBATCH†
Department of Mathematics, University of Manchester

(Received 22 June 1959)

1. Introduction

This paper is intended to give some indication of the impact forces of a water wave on a wall. The effect of gravity forces in the small time interval of impact considered will be small and is neglected. The shape of the wave before impact is considered to be a two-dimensional wedge which is assumed to strike a wall at right angles to its path. The wedge is assumed to be infinite in extent and to have a uniform translational velocity V before impact. The choice of a wedge shape enables the problem to be formulated in terms of similarity variables x/Vt, y/Vt, where the origin of the x, y plane is at the initial point of contact of the vertex of the wedge with the wall. The solution presented here can be easily adapted to the problem of an axi-symmetric cone of water striking a wall, but this is not pursued in the present paper.

A solution is obtained in §5 by suitably joining solutions valid at large and small distances from the wall. These solutions are obtained in §§3 and 4, respectively. The solution valid far from the wall may be regarded as an expansion beginning from the initial wedge shape. The solution valid near the wall may be regarded as an expansion beginning from a wedge having its axis along the wall and its vertex at the point of contact of the free surface with the wall. The method adopted in §5 of joining the solutions valid at large and small distances from the wall ensures continuity at the matching point of the slope and curvature of the free surface and the free surface potential. The condition of the conservation of mass is also satisfied.

A check on the method of solution is provided by the theorem that, for free surface problems with similarity, the arc length between fluid particles on the free surface is conserved. This theorem has been proved by Wagner (1932) and Garabedian (1953). The arc length of the solution obtained may be compared with the arc length of the wedge shape obtained in the absence of the wall. The difference between these arc lengths for the 22·2° and 45° semi-angle wedge examples computed is $0{\cdot}05Vt$ and $0{\cdot}26Vt$, respectively. It may therefore be inferred that the expansions and matching procedure used in this paper provide a reasonable description of the flow.

The solution valid far from the wall is obtained in §3 by assuming an expansion of the flow equations in this region. These equations are approximated to give four first-order non-linear equations which are reduced to two first-order equations, and a numerical solution is then obtained. Although the solution valid far from the wall may be inaccurate near the wall, it is used in §3 to

† At present at the California Institute of Technology, Pasadena, California.

provide a first estimate of the flow there. It is found that the wall condition of zero normal velocity cannot be satisfied at all points of the wall in this solution. However, by imposing a condition of zero total mass flow across the plane of flow, it is found that a moderate approximation to the wall condition is obtained. An estimate of the accuracy of the solution obtained in this way is provided by the condition of the conservation of mass. It is found that, of the mass displaced outside the oncoming wedge shape, 60 % is conserved for the 22·2° semi-angle wedge and 86 % for the 45° semi-angle wedge.

The solution valid near the wall is obtained in § 4, and is used to improve the description of the flow near the wall of the solution obtained in § 3. An expansion of the flow equations near the wall, similar to the expansion far from the wall but with the similarity variables interchanged, is assumed and the flow equations are again reduced to two first-order equations. This solution is then joined, in § 5, to the solution valid far from the wall. The conditions of continuity of the slope and curvature of the free surface at the matching point uniquely determine the matching of the solutions of the reduced equations. An arbitrary constant appears when the matched solution is completed in the physical plane, corresponding to an arbitrary position of the vertex of the wedge along the wall. This arbitrary constant is determined by imposing the condition of continuity of the potential on the free surface at the matching point. For a given angled wedge at infinity, the mass conservation condition is satisfied by choice of the angle at which the free surface meets the wall.

In the general problem of wave impact on a wall the total exchange of momentum with the wall up to a given time might be crudely estimated by supposing that all the fluid, which would have crossed the plane of the wall had the wall not been there, has lost all its momentum and the rest has lost none. The force on the wall could then be obtained by differentiation with respect to time. The analysis of this paper indicates that in two cases (wedges of semi-angles 45° and 22·2°) the force is greater than the value so obtained by factors 2·4 and 1·6, respectively.

2. Formulation

A two-dimensional wedge of water, incompressible and of density ρ, is taken to strike a flat wall at time $t = 0$ with velocity V. The axis of the wedge is perpendicular to the wall. The initial point of contact of the vertex of the wedge with the wall is taken as the origin of the x, y plane, with the y-axis along the axis of the wedge and the x-axis along the wall. The semi-angle of the wedge is taken to be $\tan^{-1} m_1$.

The problem is formulated in terms of a velocity potential $\Phi = \Phi(x, y, t)$ which, for an irrotational flow, satisfies Laplace's equation

$$\frac{\partial^2 \Phi}{\partial x^2} + \frac{\partial^2 \Phi}{\partial y^2} = 0 \tag{1}$$

at any time t. Bernoulli's theorem states that the quantity,

$$\frac{p}{\rho} + \frac{1}{2}\left(\frac{\partial \Phi}{\partial x}\right)^2 + \frac{1}{2}\left(\frac{\partial \Phi}{\partial y}\right)^2 + \frac{\partial \Phi}{\partial t}, \tag{2}$$

where p is the pressure at a point in the flow, depends only on the time. Boundary conditions of zero normal velocity at the wall $y = 0$ and on the line $x = 0$ are derived from the wall condition and from considerations of symmetry about the axis of the wedge, respectively. The flow far from the wall approximates to uniform translation given by

$$\frac{\partial \Phi}{\partial y} \sim -V, \quad \frac{\partial \Phi}{\partial x} \sim 0. \tag{3}$$

The potential has also to satisfy boundary conditions on the free surface $y = \eta(x, t)$, namely, that the pressure is a constant which is taken as zero, and that particles in the free surface remain there, which may be written as $(D/Dt)\,(y-\eta) = 0$. This second condition is expressed in terms of Φ as

$$\frac{\partial \Phi}{\partial y} = \frac{\partial \eta}{\partial t} + \frac{\partial \Phi}{\partial x}\frac{\partial \eta}{\partial x}. \tag{4}$$

The absence of a fundamental length in the formulation of the problem implies that a similarity solution is possible. Upon a transformation of the independent variables x, y, t to

$$\lambda = \frac{x}{tV}, \quad \mu = \frac{y}{tV}, \quad t_1 = t, \tag{5}$$

the assumption of a similarity solution implies that the dependent variables are functions of λ, μ and t_1 in the form

$$\Phi(x, y, t) = t_1 V^2 \phi(\lambda, \mu), \quad \eta(x, t) = t_1 V \xi(\lambda). \tag{6}$$

Equation (1) may be expressed in terms of the similarity variables to show that ϕ also satisfies Laplace's equation

$$\frac{\partial^2 \phi}{\partial \lambda^2} + \frac{\partial^2 \phi}{\partial \mu^2} = 0. \tag{7}$$

The boundary condition (4), valid on the free surface $\mu = \xi(\lambda)$, is transformed to

$$\frac{\partial \phi}{\partial \mu} = \mu - \lambda \frac{d\mu}{d\lambda} + \frac{\partial \phi}{\partial \lambda}\frac{d\mu}{d\lambda}. \tag{8}$$

Substitution of the free surface pressure condition, $p = 0$, in Bernoulli's theorem, (2), gives that on $\mu = \xi(\lambda)$

$$\left(\frac{\partial \phi}{\partial \lambda}\right)^2 + \left(\frac{\partial \phi}{\partial \mu}\right)^2 - 2\lambda \frac{\partial \phi}{\partial \lambda} - 2\mu \frac{\partial \phi}{\partial \mu} + 2\phi = C, \tag{9}$$

where C is a constant. Equation (3) for the flow far from the wall gives that

$$\frac{\partial \phi}{\partial \mu} \sim -1, \quad \frac{\partial \phi}{\partial \lambda} \sim 0, \tag{10}$$

as $\mu \to \infty$. Hence, for large μ

$$\phi \sim -\mu. \tag{11}$$

Substitution of the above values for ϕ and its derivatives far from the wall in equation (9) yields the value of C as unity provided the constant term in ϕ is taken to be zero. Similarly, equation (8) may be used to derive $\lambda(d\mu/d\lambda) \sim \mu+1$ for the asymptotic shape of the free surface. On integration this becomes

$$\lambda \sim m_1(\mu+1), \tag{12}$$

where $\tan^{-1} m_1$ is the semi-angle of the water wedge. This shows that for time $t > 0$, the free surface in the similarity plane is asymptotic to the wedge with vertex at $\mu = -1$ shown in figure 1. This wedge represents the position the original wedge would have reached in the absence of the wall.

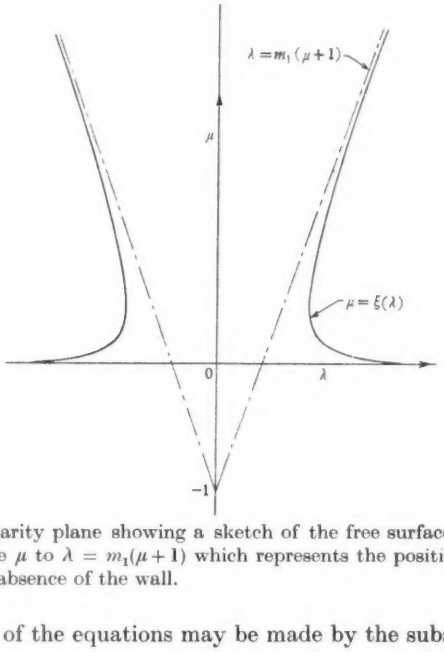

FIGURE 1. λ–μ similarity plane showing a sketch of the free surface $\mu = \xi(\lambda)$. The free surface tends at large μ to $\lambda = m_1(\mu+1)$ which represents the position the wedge would have reached in the absence of the wall.

A simplification of the equations may be made by the substitution

$$\psi(\lambda, \mu) = \phi(\lambda, \mu) - \tfrac{1}{2}(\lambda^2+\mu^2). \tag{13}$$

Equation (7) rewritten in terms of ψ is

$$\frac{\partial^2\psi}{\partial\lambda^2} + \frac{\partial^2\psi}{\partial\mu^2} = -2, \tag{14}$$

and the boundary conditions (8) and (9) on the free surface $\mu = \xi(\lambda)$ may be expressed as

$$\frac{d\mu}{d\lambda} = \frac{\partial\psi}{\partial\mu} \Big/ \frac{\partial\psi}{\partial\lambda}, \tag{15}$$

$$\left(\frac{\partial\psi}{\partial\lambda}\right)^2 + \left(\frac{\partial\psi}{\partial\mu}\right)^2 + 2\psi = 1, \tag{16}$$

respectively. The flow velocities may be written in terms of ψ as

$$\frac{\partial\Phi}{\partial x} = V\left(\frac{\partial\psi}{\partial\lambda}+\lambda\right), \quad \frac{\partial\Phi}{\partial y} = V\left(\frac{\partial\psi}{\partial\mu}+\mu\right). \tag{17}$$

The boundary conditions of zero normal velocity on $y = 0$ and $x = 0$ are thus

$$\left(\frac{\partial\psi}{\partial\mu}\right)_{\mu=0} = 0, \quad \left(\frac{\partial\psi}{\partial\lambda}\right)_{\lambda=0} = 0. \tag{18}$$

The flow equations (14)–(18), derived in terms of $\psi(\lambda, \mu)$, are used in the following sections where two solutions are derived which are used at large and small distances from the wall.

3. Solution at large distances from the wall

In this section the flow equations obtained in §2 are approximated in the region far from the wall. These equations are solved in the whole plane to provide a first approximation to the flow. It is seen that this solution is inadequate near the wall and the solution in this region is modified in later sections.

An expansion of the function $\psi(\lambda, \mu)$ defined in §2 is sought containing as its dominant term the wedge behaviour $\psi(\lambda, \mu) \sim -\frac{1}{2}\mu^2-\mu-\frac{1}{2}\lambda^2$ as $\mu \to \infty$, which is obtained from (11) and (13). The form

$$\psi(\lambda, \mu) = \psi_0(\mu)+\lambda^2\psi_1(\mu) \tag{19}$$

is assumed, where

$$\psi_0 \sim -\tfrac{1}{2}\mu^2-\mu, \quad \psi_1 \sim -\tfrac{1}{2}, \tag{20}$$

as $\mu \to \infty$. This form for ψ has the same λ dependence as the wedge solution at infinity. The form (19) satisfies the symmetrical boundary condition

$$(\partial\psi/\partial\lambda)_{\lambda=0} = 0,$$

but the wall condition

$$(\partial\psi/\partial\mu)_{\mu=0} = 0$$

is satisfied only if

$$\left(\frac{d\psi_0}{d\mu}\right)_{\mu=0} = \left(\frac{d\psi_1}{d\mu}\right)_{\mu=0} = 0. \tag{21}$$

A difficulty concerning this wall condition is encountered later in this section. On using the form (19) for ψ, the term independent of λ in the flow equation (14) is

$$\psi_0''+2\psi_1 = -2, \tag{22}$$

where the dash denotes differentiation with respect to μ. The boundary equations (15) and (16) for the free surface reduce to

$$\frac{d\mu}{d\lambda} = \frac{\psi_0'}{2\lambda\psi_1}, \tag{23}$$

$$2\psi_0+\psi_0'^2+\lambda^2(2\psi_0'\psi_1'+2\psi_1+4\psi_1^2) = 1, \tag{24}$$

where only the lowest powers of λ have been retained.

On making the substitution

$$\frac{d\psi_0}{d\mu} = \chi(\mu), \tag{25}$$

equation (22) reduces to the first-order equation

$$\frac{d\chi}{d\mu} = -2-2\psi_1, \tag{26}$$

and (23), (24) become

$$\frac{d\lambda}{d\mu} = \frac{2\lambda\psi_1}{\chi}, \tag{27}$$

$$\frac{d\psi_1}{d\mu} = \frac{1}{2\chi}\left(\frac{1-2\psi_0-\chi^2}{\lambda^2} - 2\psi_1 - 4\psi_1^2\right). \tag{28}$$

The independent variable μ is eliminated from equations (25), (26), (27) and (28) since it does not occur on the right-hand side of these equations. Dividing the equations (26), (27) and (28) by (25), the system reduces to

$$\frac{d\chi}{d\psi_0} = -\frac{2+2\psi_1}{\chi}, \tag{29}$$

$$\frac{d\lambda}{d\psi_0} = \frac{2\lambda\psi_1}{\chi^2}, \tag{30}$$

$$\frac{d\psi_1}{d\psi_0} = \frac{1}{2\chi^2}\left(\frac{1-2\psi_0-\chi^2}{\lambda^2} - 2\psi_1 - 4\psi_1^2\right), \tag{31}$$

where the functions λ, ψ_1 and χ are to be interpreted as functions of ψ_0. Throughout this paper the same symbol will be used to denote the same physical quantity.

Further reduction is accomplished by a transformation of the variables. The transformation corresponds to the extraction of the asymptotic wedge solution. The behaviour of ψ_0 and ψ_1 as $\mu \to \infty$ is given by (20). The behaviour of ψ_0 is rewritten in the form

$$\sqrt{(1-2\psi_0)} \sim 1+\mu. \tag{32}$$

The behaviour of $\chi = d\psi_0/d\mu$ as $\mu \to \infty$ follows as $\chi \sim -\sqrt{(1-2\psi_0)}$. The shape of the free surface as $\mu \to \infty$ is given by (12), which may be expressed, using (32), as $\lambda \sim m_1\sqrt{(1-2\psi_0)}$. New variables $f(\psi_0)$, $g(\psi_0)$, $z(\psi_0)$, are therefore defined by

$$\begin{aligned} \psi_1(\psi_0) &= -\tfrac{1}{2}f(\psi_0), \quad \lambda(\psi_0) = m_1\, g(\psi_0)\sqrt{(1-2\psi_0)}, \\ \chi(\psi_0) &= -z(\psi_0)\sqrt{(1-2\psi_0)}, \end{aligned} \tag{33}$$

where it follows, from the above, that as $\mu \to \infty$, f, g and z all tend to one.

Under the substitutions (33), equations (29), (30), (31) become

$$(1-2\psi_0)\frac{dz}{d\psi_0} = (f+z^2-2)/z. \tag{34}$$

$$(1-2\psi_0)\frac{dg}{d\psi_0} = g - gf/z^2, \tag{35}$$

$$(1-2\psi_0)\frac{df}{d\psi_0} = \left(f^2 - f + \frac{1}{m_1^2 g^2}(z^2-1)\right)\Big/ z^2. \tag{36}$$

Reduction to two equations follows immediately as the independent variable ψ_0 occurs only in the combination $d\psi_0/(1-2\psi_0)$ and may be eliminated.

Dividing equations (35) and (36) by (34), the following two first-order equations are obtained

$$\frac{dg}{dz} = \frac{g(f-z^2)}{z(2-f-z^2)}, \tag{37}$$

$$\frac{df}{dz} = \frac{g^2(f-f^2)+(1/m_1^2)(1-z^2)}{zg^2(2-f-z^2)}. \tag{38}$$

The equations (37), (38) are integrated numerically with the boundary conditions, $f = 1$, $g = 1$ at $z = 1$.

Numerical integration of equations (37), (38) requires the initial values of dg/dz, df/dz. As the functions on the right-hand side of (37), (38) are indeterminate at the starting point $z = 1$, an expansion

$$f = 1+f_0(z-1)+f_1(z-1)^2+f_2(z-1)^3+\ldots, \tag{39}$$

$$g = 1+g_0(z-1)+g_1(z-1)^2+g_2(z-1)^3+\ldots, \tag{40}$$

near the point $z = 1$ is assumed. This expansion is then substituted in equations (37), (38) to find the required values f_0, g_0. These are given by the equations

$$f_0 = \frac{1}{2}\left\{-1 \pm \sqrt{\left(1+\frac{8}{m_1^2}\right)}\right\}, \tag{41}$$

$$g_0 = (2-f_0)/(2+f_0). \tag{42}$$

Further coefficients in the expansions (39), (40) and details of the expansions used in the rest of this paper may be obtained from Cumberbatch (1958). Choice of the square-root sign to be taken in equation (41) for f_0 may be decided on inspection of the behaviour of equation (34) near $z = 1$. Substituting the expansion (39) in the right-hand side of (34) gives

$$(1-2\psi_0)\frac{dz}{d\psi_0} = (f_0+2)(z-1)+\ldots, \tag{43}$$

to the first power in $(z-1)$. Integration of (43) gives

$$\sqrt{(1-2\psi_0)} \sim (z-1)^{-1/(f_0+2)} \tag{44}$$

near $z = 1$. The value of $\sqrt{(1-2\psi_0)}$ as $\mu \to \infty$, which corresponds to $z \to 1$, may be deduced from (32) to be infinite, and it follows from (44) therefore that (f_0+2) is positive. This condition is satisfied by both signs of the square root in (41) for $m_1 > 1$, corresponding to a wedge of semi-angle greater than 45°, but is satisfied only by the positive square-root sign for $m_1 \leqslant 1$. Solutions for wedges of semi-angle greater than 45° are not considered in this paper.

The initial direction of integration from the point $z = 1$ for the solution of the reduced equations (37), (38) is deduced in the following manner from the assumption that the free surface expands away from the asymptotic wedge shape in the physical plane. The slope of the free surface is obtained from (27), using (33), as

$$\frac{d\mu}{d\lambda} = \frac{z}{m_1 fg}. \tag{45}$$

On using the expansions (39) and (40), this becomes

$$\frac{d\mu}{d\lambda} = \frac{1}{m_1}\{1+(1-f_0-g_0)(z-1)+\ldots\}. \tag{46}$$

The condition that the slope $d\mu/d\lambda$ increases along the free surface proceeding towards the wall from infinity implies that the initial direction of integration in the z-plane is chosen so that $(z-1)$ has the same sign as $(1-f_0-g_0)$. For the 45° and 22·2° semi-angle wedges computed, $(1-f_0-g_0)$ is negative and the initial direction of integration is z decreasing.

The integration should be terminated at a value of z corresponding to the wall conditions (21), which may be written in terms of the reduced variables, by using equations (25), (28) and (33), as

$$\frac{d\psi_0}{d\mu} = -z\sqrt{(1-2\psi_0)} = 0, \tag{47}$$

$$\frac{d\psi_1}{d\mu} = \frac{-1}{2m_1^2 z g^2\sqrt{(1-2\psi_0)}}\{1-z^2+m_1^2 g^2(f-f^2)\} = 0. \tag{48}$$

These conditions are not simultaneously satisfied. This is a weakness of the form of ψ, given by (19), assumed for this solution. A single condition of zero total mass flow across a plane at right angles to the flow is imposed instead. This condition may be obtained by integrating the normal velocity, given by (17), across the plane of the flow at $\mu = 0$, as

$$V\int_0^\lambda \left(\frac{\partial\psi}{\partial\mu}\right)_{\mu=0} d\lambda = V\left(\lambda\frac{d\psi_0}{d\mu}+\tfrac{1}{3}\lambda^3\frac{d\psi_1}{d\mu}\right) = 0. \tag{49}$$

Using the expressions in (47), (48) for $d\psi_0/d\mu$ and $d\psi_1/d\mu$, and equation (33) for λ, the condition (49) may be expressed in terms of the reduced variables as

$$1+5z^2+m_1^2 g^2(f-f^2) = 0. \tag{50}$$

Equations (37), (38) are integrated until values z_w, f_w, g_w are found which satisfy this condition. The wall is taken to be at the position in the physical plane corresponding to this point.

Numerical solutions to equations (37), (38) are obtained for the cases $m_1 = 1$ and $m_1 = 1/\sqrt{6}$, corresponding to wedges of semi-angle 45° and 22·2°, respectively. These solutions are displayed in figure 2. The numerical integration proceeds from the point $f = g = z = 1$ until the mass flow condition (50) is satisfied by values f_w, g_w, z_w. The values of z_w obtained are small, being $z_w = 0{\cdot}041$ and $z_w = 0{\cdot}126$ for the 45° and 22·2° wedges, respectively. The wall conditions (47) and (48) are therefore satisfied approximately as $d\psi_0/d\mu$ is zero when $z = 0$ and the vanishing of $d\psi_1/d\mu$ and the mass flow across $\mu = 0$ both reduce to $1+m_1^2 g^2(f-f^2) = 0$ when $z = 0$.

The solution in the physical plane is now deduced. Integration of (34) gives

$$\sqrt{(1-2\psi_0)} = k\exp\left(\int_{z_w}^{z}\frac{z\,dz}{2-f-z^2}\right), \tag{51}$$

where $k > 0$ is a constant. Equation (33) now gives λ in terms of z as

$$\lambda = m_1 k g(z)\exp\left(\int_{z_w}^{z}\frac{z\,dz}{2-f-z^2}\right). \tag{52}$$

Equations (25), (33) and (34) are used to determine $d\mu/dz$ as

$$\frac{d\mu}{dz} = \frac{\sqrt{(1-2\psi_0)}}{2-f-z^2}. \tag{53}$$

Using (51), integration of (53) gives

$$\mu = k\int_{z_w}^{z} \exp\left(\int_{z_w}^{z} \frac{z\,dz}{2-f-z^2}\right)\frac{dz}{2-f-z^2}, \tag{54}$$

where the constant of integration in this equation has been chosen to give $\mu = 0$ at the wall position $z = z_w$.

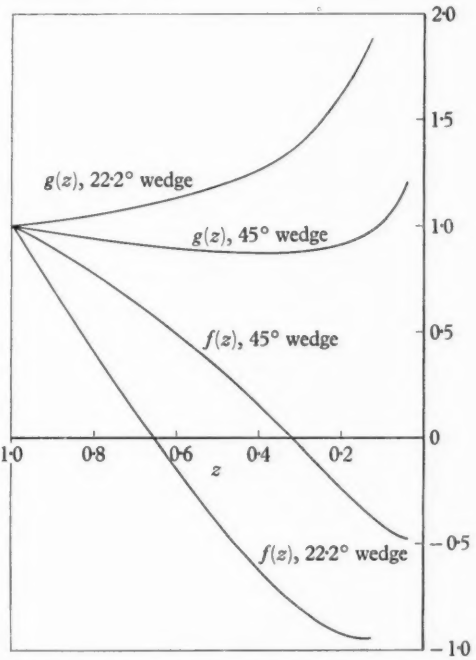

FIGURE 2. Numerical solutions to equations (37), (38) for wedges of semi-angle 45° and 22·2°. The equations are integrated from the point $f = g = z = 1$ until the mass flow condition (50) is satisfied at values $z = 0{\cdot}041$ and $z = 0{\cdot}126$, respectively.

The constant k is determined from the condition that the solution has the asymptotic wedge behaviour given by (32) at large distances, which may be expressed in terms of z, using (51) and (54), as

$$1 + k\int_{z_w}^{z} \exp\left(\int_{z_w}^{z} \frac{z\,dz}{2-f-z^2}\right)\frac{dz}{2-f-z^2} \sim k\exp\left(\int_{z_w}^{z} \frac{z\,dz}{2-f-z^2}\right) \quad \text{as} \quad z \to 1. \tag{55}$$

Since the integrals in (55) become infinite as $z \to 1$, k is to be found from the equation

$$\frac{1}{k} = \lim_{z\to 1}\left\{\exp\left(\int_{z_w}^{z} \frac{z\,dz}{2-f-z^2}\right) - \int_{z_w}^{z} \exp\left(\int_{z_w}^{z} \frac{z\,dz}{2-f-z^2}\right)\frac{dz}{2-f-z^2}\right\}. \tag{56}$$

Denoting by z^* a convenient point near $z = 1$, the integrals from z_w to z^* are taken outside the limit sign in (56). The integrals from z_w to z^* are evaluated by

numerical integration and the integrals from z^* to z under the limit sign are evaluated by expanding the integrand in powers of $(z-1)$ using the expansion (39). For the 45° and 22·2° semi-angle wedge solutions computed, the values of k are found to be 1·74 and 1·30, respectively.

Equations (52), (54) give the shape of the free surface in parametric form with z as the parameter. The free surface shapes are drawn in figure 3 for the two wedge examples computed. The flow quantities ψ_0 and ψ_1 are given as functions

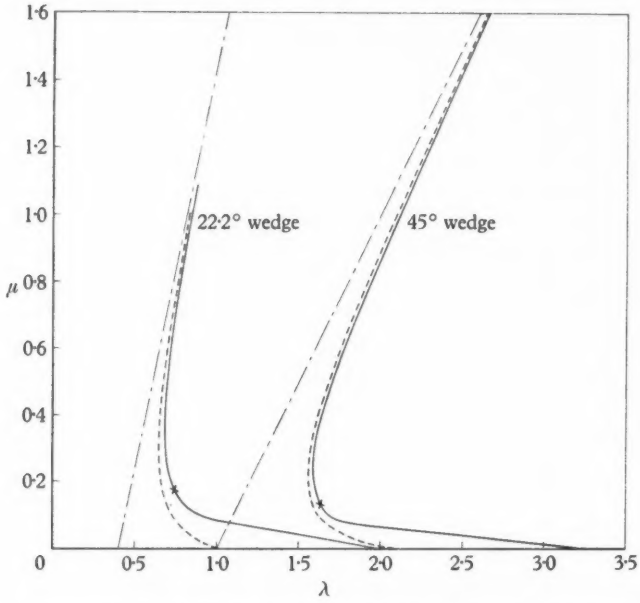

FIGURE 3. Free surface shapes for the matched solution derived in §5 for the 45° and 22·2° semi-angle wedges are shown by the solid lines, with the matching points indicated by a cross. Broken lines indicate the position these wedges would have reached in the absence of the wall and have their vertices at $\mu = -1$. The approximate solutions derived in §3 for these wedges are shown by dotted lines.

of z by equation (51) and $\psi_1 = -\frac{1}{2}f(z)$, respectively. As μ is given as a function of z by (54), the functions λ, ψ_0, ψ_1 and z are tabulated as functions of μ in tables 1 and 2 for the 45° and 22·2° semi-angle wedges, respectively. The value of $\psi = \psi_0(\mu) + \lambda^2\psi_1(\mu)$ on the free surface, ψ_F say, is given by the tables using the free surface λ given there. However, ψ can be evaluated at any point of the flow by using the appropriate value of λ.

The pressure on the wall due to the water wedge striking it is deduced as follows. The pressure at a point in the flow is given by Bernoulli's equation (2). Under the substitutions made in §2, the pressure coefficient $p/\frac{1}{2}\rho V^2$ may be derived in terms of the function $\psi(\lambda, \mu)$ as

$$\frac{p}{\frac{1}{2}\rho V^2} = 1 - 2\psi - \left(\frac{\partial\psi}{\partial\lambda}\right)^2 - \left(\frac{\partial\psi}{\partial\mu}\right)^2. \tag{57}$$

Using the form of ψ given by (19), this is written

$$\frac{p}{\frac{1}{2}\rho V^2} = 1 - 2\psi_0 - \psi_0'^2 - \lambda^2(2\psi_0'\psi_1' + 2\psi_1 + 4\psi_1^2), \tag{58}$$

again retaining only λ^2 terms. The pressure distribution (58) is therefore parabolic across planes at right angles to the flow. A more convenient form of (58) is derived by obtaining the terms in the bracket on the right-hand side from

μ	λ	ψ_0	ψ_1	ψ_F	z
0	2·09	−1·01	0·236	0·024	0·041
0·006	2·02	−1·01	0·235	−0·046	0·048
0·014	1·94	−1·01	0·231	−0·141	0·061
0·026	1·85	−1·01	0·222	−0·249	0·078
0·043	1·76	−1·01	0·205	−0·372	0·102
0·070	1·68	−1·02	0·175	−0·524	0·137
0·118	1·60	−1·03	0·115	−0·738	0·2
0·204	1·56	−1·07	0·015	−1·032	0·3
0·303	1·57	−1·13	−0·080	−1·330	0·4
0·422	1·63	−1·23	−0·168	−1·679	0·5
0·571	1·74	−1·40	−0·249	−2·157	0·6
0·773	1·89	−1·65	−0·322	−2·807	0·7
1·080	2·17	−2·18	−0·388	−4·009	0·8
1·701	2·74	−3·51	−0·447	−6·863	0·9

TABLE 1

TABLES 1 AND 2. Values of the free surface shape $\lambda(\mu)$, and the flow quantities $\psi_0(\mu)$, $\psi_1(\mu)$, $z(\mu)$ for the approximate solution derived in §3 for wedges of semi-angle 45° (table 1) and 22·2° (table 2). Values of $\psi = \psi_F$ along the free surface are also given.

μ	λ	ψ_0	ψ_1	ψ_F	z
0	1·000	−0·347	0·472	0·125	0·126
0·005	0·974	−0·348	0·474	0·102	0·136
0·010	0·948	−0·349	0·475	0·078	0·148
0·016	0·922	−0·350	0·474	0·053	0·161
0·022	0·896	−0·352	0·472	0·027	0·176
0·030	0·870	−0·354	0·467	0·001	0·193
0·039	0·845	−0·356	0·460	−0·027	0·212
0·048	0·820	−0·359	0·450	−0·056	0·233
0·060	0·794	−0·362	0·436	−0·087	0·257
0·073	0·770	−0·367	0·416	−0·120	0·285
0·088	0·746	−0·373	0·391	−0·156	0·317
0·107	0·722	−0·382	0·357	−0·196	0·355
0·131	0·700	−0·393	0·312	−0·241	0·4
0·159	0·680	−0·409	0·258	−0·282	0·45
0·189	0·666	−0·429	0·199	−0·341	0·5
0·223	0·655	−0·453	0·138	−0·394	0·55
0·260	0·649	−0·483	0·073	−0·452	0·6
0·302	0·647	−0·520	0·006	−0·523	0·65
0·350	0·648	−0·567	−0·063	−0·593	0·7
0·408	0·655	−0·630	−0·133	−0·687	0·75
0·481	0·669	−0·716	−0·205	−0·807	0·8
0·576	0·693	−0·843	−0·277	−0·976	0·85
0·719	0·736	−1·055	−0·351	−1·245	0·9
0·991	0·831	−1·530	−0·425	−1·824	0·95

TABLE 2. For explanation see table 1.

(24), which is valid only on the free surface, in terms of the λ co-ordinate of the free surface λ_F. Obtaining $\psi_0' = \chi$ from (33), the pressure distribution (58) is written as

$$\frac{p}{\frac{1}{2}\rho V^2} = (1-2\psi_0)(1-z^2)\left(1-\frac{\lambda^2}{\lambda_F^2}\right), \tag{59}$$

where the values of ψ_0, z and λ_F are given as functions of μ in tables 1 and 2 for the two wedge examples computed. The pressure distribution on the wall $\mu = 0$ is shown for these examples in figure 4.

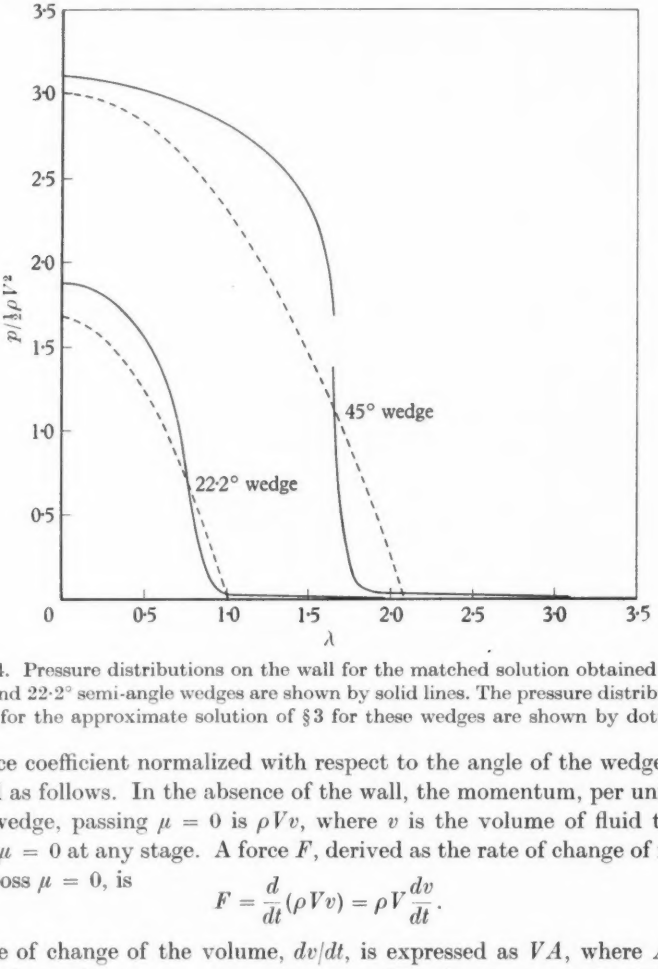

FIGURE 4. Pressure distributions on the wall for the matched solution obtained in §5 for the 45° and 22·2° semi-angle wedges are shown by solid lines. The pressure distributions on the wall for the approximate solution of §3 for these wedges are shown by dotted lines.

A force coefficient normalized with respect to the angle of the wedge is constructed as follows. In the absence of the wall, the momentum, per unit width of the wedge, passing $\mu = 0$ is $\rho V v$, where v is the volume of fluid that has crossed $\mu = 0$ at any stage. A force F, derived as the rate of change of momentum across $\mu = 0$, is

$$F = \frac{d}{dt}(\rho V v) = \rho V \frac{dv}{dt}.$$

The rate of change of the volume, dv/dt, is expressed as VA, where A is the area of the wedge at $\mu = 0$ at any stage. The force on a wall obstructing the flow of the wedge is the integral of the pressure over the wetted area A_w. A normalized force coefficient C_F is therefore defined as

$$C_F = \frac{1}{\rho V^2 A}\int_{A_w} p\,dA = \frac{1}{2m_1}\int_0^{\lambda_w} \frac{p}{\frac{1}{2}\rho V^2}\,d\lambda, \tag{60}$$

where λ_w is the point of contact of the free surface with the wall. The force coefficients obtained in this way for the 45° and 22·2° semi-angle wedges are $C_F = 2{\cdot}1$ and $C_F = 1{\cdot}4$, respectively.

An estimate of the accuracy of the solution obtained using the approximate equations (37), (38) is provided by the condition of the conservation of mass. In the absence of the wall the fluid occupies the wedge with vertex at $\mu = -1$, as shown in figure 1. The area of this portion of the wedge in $\mu < 0$ is $\frac{1}{2}m_1$. In a flow obstructed by the wall, therefore, the area of fluid lying between the free surface and the wedge $\lambda = m_1(\mu+1)$ is equal to $\frac{1}{2}m_1$ in an ideal solution. This area is

$$\int_0^\infty \{\lambda - m_1(\mu+1)\}\, d\mu. \tag{61}$$

Transforming to the reduced variables by obtaining the free surface λ from (52) and μ from (54), the area (61) is expressed as

$$m_1 k \int_{z_w}^{z} \left\{ kg(z) \exp\left(\int_{z_w}^{z} \frac{z\,dz}{2-f-z^2} \right) - 1 - k \int_{z_w}^{z} \exp\left(\int_{z_w}^{z} \frac{z\,dz}{2-f-z^2} \right) \frac{dz}{2-f-z^2} \right\} \times \exp\left(\int_{z_w}^{z} \frac{z\,dz}{2-f-z^2} \right) \frac{dz}{2-f-z^2}. \tag{62}$$

This integral is treated in a similar manner to the integral (56) defining k. It may be noted that the singular parts of the integrals in the curly bracket in (62) cancel due to the choice of k given in (56). For the 45° and 22·2° wedges, the integral (62) has the values 0·432 and 0·123 which are to be compared with the values of $\frac{1}{2}m_1$, namely, 0·5 and 0·204. These values imply that the solution obtained from the approximate equations (37), (38) valid at large distances from the wall is inadequate in predicting the flow near the wall. The simple λ^2 dependence assumed for ψ in (19) is unable to describe the slope of the free surface near the wall. A more accurate solution in this domain is desired. Such a solution is examined in the next section, and will allow a suitable matching with the solution valid at large distances from the wall.

4. Solution near the tip

In this section a solution is obtained which describes the flow in a region near the point of contact, λ_w, of the free surface with the wall. The solution is derived as the expansion beginning from the vertex of a wedge having its axis along the wall and its vertex at $\lambda = \lambda_w$. The semi-angle of this wedge is the angle between the tangent to the free surface at the point of contact and the wall, which is taken to be $\tan^{-1} m_2$. It is to be noted that the position (λ_w) and the angle of the wedge determined by m_2 are as yet arbitrary. In the next section it will be described how λ_w, m_2 may be determined to give a good matching of the solution of this section with the solution of §3 valid at large distances from the wall.

An expansion of $\psi(\lambda, \mu)$ in the form

$$\psi(\lambda, \mu) = \Psi_0(\lambda) + \mu^2 \Psi_1(\lambda) \tag{63}$$

is assumed near $\mu = 0$. This form satisfies the wall boundary condition $(\partial\psi/\partial\mu)_{\mu=0} = 0$. The expansion (63) is analogous to the expansion (19) used in §3, with the λ, μ axes interchanged. The equations resulting from the substitution of the expansion (63) in the flow equations are therefore obtained by analogy with equations (22)–(31), λ and μ being interchanged and capitals replacing small symbols for the dependent variables.

Reduction of the three equations corresponding to (29), (30) and (31) is effected by extracting the tip wedge solution. The slope of the free surface at the tip, λ_w, is $-m_2$ and hence

$$\mu \sim m_2(\lambda_w - \lambda) \quad \text{as} \quad \mu \to 0. \tag{64}$$

Corresponding to (20), the flow near the tip is given by

$$\Psi_0^* \sim \tfrac{1}{2} - \tfrac{1}{2}(\lambda_w - \lambda)^2, \quad \Psi_1^* \sim -\tfrac{1}{2}. \tag{65}$$

The behaviour of Ψ_0^* is rewritten as

$$\sqrt{(1 - 2\Psi_0^*)} \sim \lambda_w - \lambda \quad \text{as} \quad \mu \to 0. \tag{66}$$

New variables $F(\Psi_0^*)$, $G(\Psi_0^*)$ and $Z(\Psi_0^*)$ are defined by the equations

$$\begin{aligned} \Psi_1^*(\Psi_0^*) &= -\tfrac{1}{2}F(\Psi_0^*), \quad \mu(\Psi_0^*) = m_2\, G(\Psi_0^*)\sqrt{(1 - 2\Psi_0^*)}, \\ \mathrm{X}(\Psi_0^*) &= Z(\Psi_0^*)\,\sqrt{(1 - 2\Psi_0^*)}, \end{aligned} \tag{67}$$

where $\mathrm{X} = d\Psi_0^*/d\lambda$. It follows from (64), (65) and (66) that as $\mu \to 0$, F, G and Z all tend to one. A sign change occurring in the last equation in (67) contains the only difference from the analogous transformation (33). The equations (37), (38) are even in z and are not affected by a sign change in the last term in (33). The substitutions (67) therefore lead to equations which are identical with (37), (38) with F, G and Z replacing f, g and z, namely

$$\frac{dG}{dZ} = \frac{G(F - Z^2)}{Z(2 - F - Z^2)}, \tag{68}$$

$$\frac{dF}{dZ} = \frac{G(F - F^2) + (1/m_2^2)(1 - Z^2)}{ZG^2(2 - F - Z^2)}. \tag{69}$$

Initial values of dG/dZ and dF/dZ are determined by expansions of F and G analogous to (39), (40). Choice of the square root sign to be taken in the equation for $F_0 = (dF/dZ)_{Z=1}$, corresponding to (41), is decided from the behaviour near $Z = 1$ of the equation corresponding to (34). The value of $\sqrt{(1 - 2\Psi_0^*)}$ at the tip may be determined to be zero from (66). A negative value of $(F_0 + 2)$ is desired to satisfy this condition, and this is only attained when $m_2 < 1$ and by a choice of the negative square-root sign in the equation for F_0. The direction of integration from the point $Z = 1$ is deduced from the assumption that the required solution expands away from the tip wedge shape. The slope of the free surface is given by the equation corresponding to (27). Using the substitutions (67) this equation is expressed as

$$\frac{d\mu}{d\lambda} = -m_2 \frac{FG}{Z}. \tag{70}$$

Expanding near $Z = 1$,

$$\frac{d\mu}{d\lambda} = -m_2\{1-(1-F_0-G_0)(Z-1)+\ldots\}, \tag{71}$$

where $G_0 = (dG/dZ)_{Z=1}$. The direction of integration is chosen such that $(Z-1)$ has the opposite sign to $(1-F_0-G_0)$.

Equations (68), (69) may now be integrated numerically to provide the solution corresponding to the expansion away from the wedge $\mu = m_2(\lambda_w - \lambda)$. Numerical solutions of (68), (69) for the cases $m_2 = \frac{1}{19}, \frac{1}{12}$, corresponding to

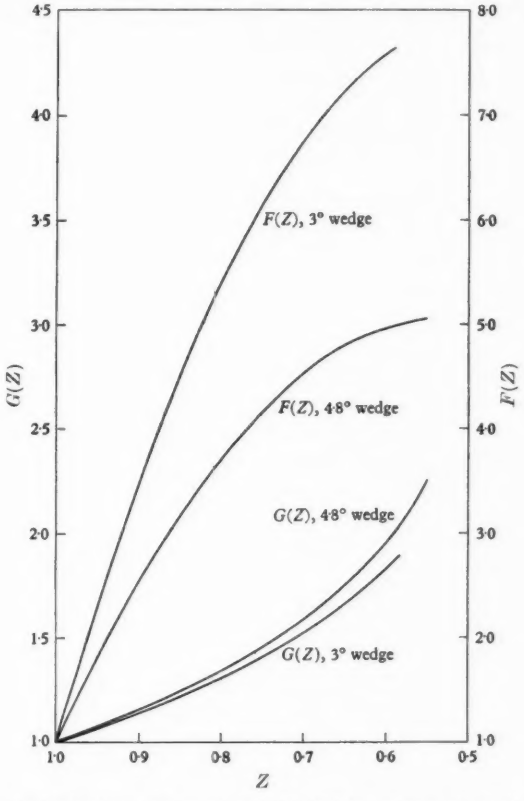

FIGURE 5. Numerical solutions to equations (68), (69) for wedges of semi-angle 3° and 4·8°.

wedges of semi-angle 3·0°, 4·8°, respectively, are shown in figure 5. The solution is valid in the tip of fluid near the point of contact of the free surface with the wall and is used to improve the accuracy near the wall of the solution obtained in § 3. The procedure for matching these solutions is discussed in § 5. The solution near the tip cannot be completed in the physical plane until the value of Z at the matching point is known. Denote this by Z_j.

Transformation to the physical plane of the solution of equations (68), (69) is inferred by analogy with equations (51), (52), rewritten with λ and μ inter-

changed, capitals replacing small symbols for the flow variables and Z_j replacing z_w as the lower limit of integration. Hence, using (51), $\sqrt{(1-2\Psi_0)}$ is given by

$$\sqrt{(1-2\Psi_0)} = K \exp\left(\int_{Z_j}^{Z} \frac{Z\,dZ}{2-F-Z^2}\right), \tag{72}$$

where $K > 0$ is a constant; and using the substitutions (67), it follows that

$$\mu = m_2 K G(Z) \exp\left(\int_{Z_j}^{Z} \frac{Z\,dZ}{2-F-Z^2}\right). \tag{73}$$

The equation for $d\lambda/dZ$ in the solution valid near the tip is derived by analogy with (53), but with a sign change resulting from the sign difference in the last equations of the substitutions (33) and (67). The equation for λ is

$$\lambda_w - \lambda = K \int_1^Z \exp\left(\int_{Z_j}^{Z} \frac{Z\,dZ}{2-F-Z^2}\right) \frac{dZ}{2-F-Z^2}, \tag{74}$$

where the constant of integration has been chosen so that $\lambda = \lambda_w$ at $\mu = 0$. An expansion is required to obtain the contribution near $Z = 1$ to the integral in (74) since the integrand is singular at $Z = 1$.

Equations (73), (74) give the free surface shape in parametric form for the solution valid near the tip. The function $\psi = \Psi_0(\lambda) + \mu^2 \Psi_1(\lambda)$ can now be determined at any point in the flow by using the appropriate value of μ and obtaining $\Psi_0(Z)$ from (72) and $\Psi_1(Z)$ from (67), Z being obtained in terms of λ from (74). This completes the formal description of the flow in the tip, but no numerical values can be given until the procedure for matching the tip flow with the solution in §3 is given in §5.

5. Matching of solutions

In this section, details are given of how the solutions derived in the previous sections may be joined together in as smooth a manner as possible. It is shown that a matching point exists at which the slope and curvature of the free surface are continuous, the function ψ is continuous along the free surface and the mass conservation law is satisfied. A check on the accuracy of the method used is provided by the condition that the arc length between particles in the free surface is conserved.

Presupposing that a matching point of the two solutions has been chosen and denoting this point by the suffix j, the solution at large distances from the wall is given by the solution derived in §3 with z_j replacing z_w, as it is not now intended to use this solution right up to the wall. The constant k occurring in §3 depends on the choice of z_w and therefore needs to be replaced by k' which depends on z_j. The value of λ at the matching point is given by (52) as

$$\lambda_j = m_1 k' g_j. \tag{75}$$

The formula for μ corresponding to (54) becomes

$$\mu = \mu_j + k' \int_{z_j}^{z} \exp\left(\int_{z_j}^{z} \frac{z\,dz}{2-f-z^2}\right) \frac{dz}{2-f-z^2}. \tag{76}$$

The condition that the solution at large distances from the wall has the asymptotic wedge behaviour given by (32) is expressed as

$$1+\mu_j+k'\int_{z_j}^{z}\exp\left(\int_{z_j}^{z}\frac{z\,dz}{2-f-z^2}\right)\frac{dz}{2-f-z^2}\sim k'\exp\left(\int_{z_j}^{z}\frac{z\,dz}{2-f-z^2}\right)\quad\text{as}\quad z\to 1. \tag{77}$$

This equation is used to find a relation between k' and μ_j by expressing it in the form corresponding to (56) with $(1/k')\,(1+\mu_j)$ replacing $1/k$ on the left-hand side and z_j replacing z_w as the lower limit in the integrals on the right-hand side. The limit as $z\to 1$ of these integrals is deduced by an expansion near $z=1$ in a similar manner to the derivation of k. Thus a given angle wedge at infinity is uniquely described up to any chosen join-up point μ_j.

The solution valid near the tip has been given in §4. The flow variables and the shape of the free surface are given there in terms of the constants m_2, λ_w, Z_j and K. The μ-co-ordinate of the matching point is deduced from (73) as

$$\mu_j = m_2 K G_j. \tag{78}$$

It is seen that the co-ordinates of the matching point λ_j, μ_j are given by (75) and (78) in terms of the constants k', K, m_2, z_j and Z_j. The condition (77) for the correct asymptotic wedge behaviour gives a relation between μ_j, k' and z_j. The value of λ at the wall, λ_w, is given by (74) on substituting $\lambda=\lambda_j$ and $Z=Z_j$, in terms of K, λ_j and Z_j. Thus there are four undetermined constants, which are taken to be K, m_2, z_j and Z_j.

The condition of the continuity at the matching point of the potential on the free surface is imposed. That is, the expansions $\psi_0(\mu)+\lambda^2\psi_1(\mu)$ and $\Psi_0(\lambda)+\mu^2\Psi_1(\lambda)$ are to have the same value at the matching point. The values at the matching point for the two expansions are deduced from the sets of equations (33), (51), (76) and (67), (72), (73), respectively, to give

$$1-k'^2-m_1^2k'^2f_jg_j^2 = 1-K^2-m_2^2K^2F_jG_j^2. \tag{79}$$

This equation is regarded as determining K, the positive value being taken, leaving the constants m_2, z_j, Z_j, still arbitrary.

The matching of the two solutions valid at large and small distances from the wall has now been effected in terms of the matching points z_j, Z_j of the reduced equations and m_2, the angle at which the free surface meets the wall. The method used in choosing z_j, Z_j will now be explained. Conditions of the continuity of slope and curvature of the free surface at the matching point of the two solutions are imposed. The slope of the free surface in terms of the reduced variables of the solutions valid at large distances from the wall and near the tip are given in (45) and (70) as

$$\frac{d\mu}{d\lambda}=\frac{z}{m_1fg}, \tag{80}$$

$$\frac{d\mu}{d\lambda}=-m_2\frac{FG}{Z}, \tag{81}$$

respectively. The second derivative of the free surface at a matching point for the two solutions may be deduced to be

$$\frac{d^2\mu}{d\lambda^2} = \frac{m_1}{k'gz^2}\left\{g^2(f^2-f)+\frac{1}{m_1^2}(1-z^2)\right\}, \tag{82}$$

$$\frac{d^2\mu}{d\lambda^2} = \frac{Z}{Km_2^2G^4F^3}\left\{G^2(F^2-F)+\frac{1}{m_2^2}(1-Z^2)\right\}. \tag{83}$$

By equating the expressions for the first and second derivatives, values of z_j, Z_j may be found at which continuity of the first and second derivatives of the free surface is satisfied. It is to be noticed that unfortunately the supplementary integrations involved in finding the constants of integration k', K have to be undertaken before the values of the second derivatives at each side of the matching point may be found. This makes the solution of (82), (83) numerically tedious. The procedure adopted to determine the z_j, Z_j which give the same value for the functions on the right-hand sides of equations (80), (81) and of (82), (83) is as follows. A first estimate of the slope of the free surface at the matching point is obtained by assuming that it is mid-way between the slope of the wedge at large distances and the slope of the free surface at the wall. Values of the matching points z_j, Z_j in the reduced planes of the solutions may then be determined from equations (80), (81). The supplementary integrations necessary to obtain k', K are then performed and values of the second derivative of the free surface at each side of the matching point are calculated from (82), (83). From these values a better estimate for the slope of the free surface at the matching point is obtained. In this way continuity of the first and second derivatives of the free surface at the matching point was achieved to three significant figures.

The solution is now determined apart from the value of m_2. The condition of the conservation of mass is satisfied by choice of m_2. In the λ, μ plane this condition may be seen to be the condition that the area contained between the free surface and wedge shape given by $\lambda = m_1(\mu+1)$ is equal to the area of the part of the wedge lying in the negative μ-plane. This condition may be stated as

$$\tfrac{1}{2}m_1 = \int_{\mu_j}^{\infty}\{\lambda - m_1(\mu+1)\}\,d\mu + \mu_j\lambda_j - \tfrac{1}{2}m_1\mu_j(2+\mu_j) + \int_{\lambda_j}^{\lambda_w}\mu\,d\lambda, \tag{84}$$

where the first integral on the right-hand side is the area outside the wedge in $\mu \geqslant \mu_j$, the other integral is the area outside the wedge in $\lambda \geqslant \lambda_j$ and the middle terms give the area of the part lying outside the wedge in the rectangle $0 \leqslant \lambda \leqslant \lambda_j$, $0 \leqslant \mu \leqslant \mu_j$. Transformation of the integrals in (84) to the reduced variables may be deduced for the first integral by use of equations (52) and (76), and for the second integral by use of (73), (74). After dividing by m_1, equation (84) may then be written

$$\begin{aligned}\tfrac{1}{2} = k'\int_{z_j}^{z}\Bigg\{&k'g(z)\exp\left(\int_{z_j}^{z}\frac{z\,dz}{2-f-z^2}\right)-\mu_j-1-k'\int_{z_j}^{z}\exp\left(\int_{zj}^{z}\frac{z\,dz}{2-f-z^2}\right)\frac{dz}{2-f-z^2}\Bigg\}\\ &\times\exp\left(\int_{z_j}^{z}\frac{z\,dz}{2-f-z^2}\right)\frac{dz}{2-f-z^2}+\frac{u_j\lambda_j}{m_1}-\tfrac{1}{2}\mu_j(2+\mu_j)\\ &-K^2\frac{m_2}{m_1}\int_{Z_j}^{1}G(Z)\exp\left(2\int_{Z_j}^{Z}\frac{Z\,dZ}{2-F-Z^2}\right)\frac{dZ}{2-F-Z^2}.\end{aligned} \tag{85}$$

The contribution near $z = 1$ to the first integral on the right-hand side is derived using the expansions (39), (40). An expansion near $Z = 1$ in the last integral in (85) is needed since the integrand becomes infinite at $Z = 1$. The integral may be obtained numerically up to $Z = Z^*$, a point near $Z = 1$. The integral is expanded between $Z = Z^*$ and $Z = 1$, using the expansions for F, G corresponding to those derived for f, g in §3.

μ	λ	Ψ_0	Ψ_1	ψ_F	Z
0	1·975	0·5	−0·5	0·5	1
0·080	1·026	0·050	−0·586	0·046	0·99
0·085	0·981	0·007	−0·671	−0·002	0·98
0·088	0·953	−0·020	−0·754	−0·025	0·97
0·091	0·934	−0·039	−0·835	−0·046	0·96
0·094	0·918	−0·055	−0·914	−0·063	0·95
0·096	0·904	−0·069	−0·991	−0·078	0·94
0·105	0·866	−0·108	−1·281	−0·122	0·90
0·114	0·837	−0·136	−1·540	−0·156	0·86
0·123	0·815	−0·157	−1·770	−0·184	0·82
0·133	0·796	−0·175	−1·969	−0·210	0·78
0·144	0·778	−0·191	−2·137	−0·235	0·74
0·157	0·762	−0·204	−2·275	−0·260	0·70
0·171	0·747	−0·217	−2·382	−0·287	0·66

TABLE 3(i)

μ	λ	ψ_0	ψ_1	ψ_F	z
0·171	0·747	−0·475	0·338	−0·287	0·374
0·186	0·734	−0·483	0·312	−0·315	0·4
0·215	0·714	−0·501	0·258	−0·369	0·45
0·247	0·698	−0·522	0·199	−0·425	0·5
0·282	0·688	−0·549	0·138	−0·484	0·55
0·321	0·681	−0·581	0·073	−0·547	0·6
0·365	0·678	−0·623	0·006	−0·620	0·65
0·416	0·680	−0·674	−0·063	−0·703	0·7
0·478	0·688	−0·744	−0·133	−0·806	0·75
0·553	0·702	−0·838	−0·205	−0·939	0·8
0·653	0·727	−0·978	−0·277	−1·124	0·85
0·803	0·772	−1·211	−0·351	−1·421	0·9
1·088	0·872	−1·734	−0·425	−2·058	0·95

TABLE 3(ii)

TABLES 3 AND 4. Values of the flow variables for the matched solution obtained in §5 for the 22·2° (table 3) and 45° (table 4) semi-angle wedges. The first half of each table is to be interpreted as giving Ψ_0, Ψ_1, Z and the free surface μ as functions of λ in the region $\lambda_j \leqslant \lambda \leqslant \lambda_w$ for the solution near the tip. The second half of each table is to be interpreted as giving ψ_0, ψ_1, z and the free surface λ as functions of μ in the region $\mu \geqslant \mu_j$ for the solution far from the wall. Values of $\psi = \psi_F$ on the free surface are given in both regions.

The following procedure to determine m_2 is used. A first estimate of the tip angle is given by the angle between the free surface and the wall at the point of contact obtained in the approximate solution in §3. The right-hand side of equation (85) is then evaluated for the matched solution obtained using this tip angle and this value then indicates a better value for the tip angle, an underestimate for the mass implying that a smaller tip angle is required.

A solution was obtained in the manner described above for 22·2° and 45° semi-angle wedges. The mass conservation condition was satisfied to two significant figures by a choice of the tip angles 4·8° and 3°, respectively. The slope and curvature of the free surface were matched to three significant figures. The

μ	λ	Ψ_0	Ψ_1	ψ_F	Z
0	3·201	0·5	−0·5	0·5	1
0·072	1·851	−0·410	−0·636	−0·413	0·99
0·075	1·813	−0·462	−0·768	−0·466	0·98
0·077	1·790	−0·493	−0·899	−0·498	0·97
0·079	1·773	−0·516	−1·026	−0·522	0·96
0·080	1·760	−0·534	−1·151	−0·541	0·95
0·082	1·749	−0·549	−1·273	−0·557	0·94
0·083	1·739	−0·562	−1·392	−0·571	0·93
0·085	1·731	−0·573	−1·509	−0·584	0·92
0·086	1·724	−0·583	−1·623	−0·595	0·91
0·088	1·717	−0·592	−1·735	−0·606	0·90
0·094	1·694	−0·622	−2·153	−0·641	0·86
0·100	1·676	−0·644	−2·528	−0·670	0·82
0·107	1·661	−0·662	−2·859	−0·695	0·78
0·115	1·648	−0·678	−3·145	−0·719	0·74
0·123	1·636	−0·692	−3·388	−0·743	0·70
0·133	1·625	−0·703	−3·585	−0·767	0·66
0·134	1·624	−0·704	−3·594	−0·768	0·658

TABLE 4(i)

μ	λ	ψ_0	ψ_1	ψ_F	z
0·134	1·624	−1·073	0·116	−0·768	0·199
0·135	1·623	−1·073	0·115	−0·770	0·2
0·176	1·593	−1·090	0·065	−0·925	0·25
0·221	1·581	−1·112	0·015	−1·075	0·3
0·269	1·583	−1·140	−0·033	−1·223	0·35
0·321	1·597	−1·176	−0·080	−1·380	0·4
0·378	1·621	−1·221	−0·125	−1·549	0·45
0·442	1·655	−1·277	−0·168	−1·737	0·5
0·512	1·700	−1·348	−0·210	−1·955	0·55
0·593	1·757	−1·438	−0·249	−2·207	0·6
0·686	1·829	−1·554	−0·287	−2·514	0·65
0·797	1·920	−1·709	−0·322	−2·895	0·7
0·932	2·037	−1·920	−0·356	−3·397	0·75
1·106	2·192	−2·226	−0·388	−4·090	0·8
1·345	2·414	−2·707	−0·418	−5·142	0·85
1·717	2·767	−3·584	−0·447	−7·007	0·9
2·484	3·504	−5·846	−0·474	−11·666	0·95

TABLE 4(ii). For explanation see legend to table 3.

values of z_j, Z_j, k', K were 0·374, 0·66, 1·40, 1·20 and 0·199, 0·658, 1·77, 1·55, for the 22·2° and 45° wedges, respectively. The co-ordinates λ_j, μ_j of the matching point were 0·747, 0·171 and 1·624, 0·134, respectively. The shape of the free surfaces for the solutions joined in this way is shown in figure 3, with the matching points indicated. Tables 3 and 4 give the values of the flow variables for the solutions matched, Ψ_0, Ψ_1 and Z being given as functions of λ for the flow in the region $\lambda_j \leqslant \lambda \leqslant \lambda_w$, and ψ_0, ψ_1 and z given as functions of μ for the flow in the region $\mu \geqslant \mu_j$. The corresponding free surface values of λ and μ are

given. The values of $\psi = \psi_F$ on the free surface are also given, using (19) or (63) in the appropriate regions of the flow and using the free surface values of λ, μ.

The flow in the rectangle bounded by the lines $\lambda = 0$, λ_j and $\mu = 0$, μ_j indicated as region III in figure 6 is not deduced in the solution presented above. The solution (19) at large distances from the wall is valid in the flow region I from $\mu = \mu_j$ to $\mu = \infty$ and the solution (63) near the wall is valid in region II bounded by the lines $\lambda = \lambda_j$ and $\lambda = \lambda_w$. However, the solution in region III

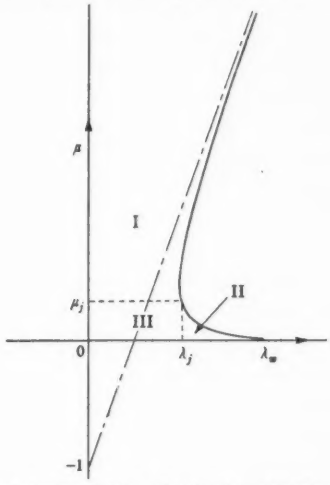

FIGURE 6. Sketch of the matched solution obtained in § 5. The solution far from the wall obtained in § 3 is valid in region I and the solution near the wall obtained in § 4 is valid in region II.

may be obtained by a relaxation method, using the appropriate solution (19) or (63) on the boundaries adjacent to region III, together with the boundary conditions (18) on the other two boundaries. The pressure distribution on the wall in the range $0 \leqslant \lambda \leqslant \lambda_j$ may then be determined from (57). The pressure distribution between the λ-co-ordinates, λ_j and λ_w, may be derived from the solution valid near the tip. The pressure coefficient $p/\frac{1}{2}\rho V^2$ on the wall $\mu = 0$ in this λ range may be deduced from equation (57), making the substitution (63) for ψ, as

$$\frac{p}{\frac{1}{2}\rho V^2} = 1 - 2\Psi_0 - \Psi_0'^2 = (1 - 2\Psi_0)(1 - Z^2) \tag{86}$$

in terms of the reduced variables, using (67). The pressure distribution on the wall over the whole range $0 \leqslant \lambda \leqslant \lambda_w$ obtained in this manner is shown in figure 4. In this description of the flow the pressure on the wall is discontinuous at $\lambda = \lambda_j$ due to its dependence on $d\psi/d\lambda$, which has not been matched between regions II and III of figure 4. For the 22·2° wedge this pressure jump is indiscernible, but for the 45° wedge the jump in $p/\frac{1}{2}\rho V^2$ is 0·321—about 10 % of the total variation along the wall. The force coefficient (60) using this pressure distribution has the values 2·4 and 1·6 for the 45° and 22·2° semi-angle wedges, respectively.

The condition of the conservation of arc length along the free surface is used

to provide a check on the accuracy of the solution obtained by the matching procedure described above. The theorem that the arc length of the free surface in a two-dimensional similarity flow is conserved was discovered independently by Wagner and Garabedian. The arc length conservation condition is formulated in the λ, μ similarity plane by relating the arc length of the free surface for the solution obtained to the arc length of the free surface of the wedge shape $\lambda = m_1(\mu+1)$ obtained in the absence of the wall. Since these arc lengths are infinite the condition is derived using a technique similar to the one involved in finding k from (55). Let μ^* be the μ-co-ordinate corresponding to z^*. The parts of the arc lengths to be compared in the range from μ^* to infinity are collected together and an expansion found for their difference. The arc length condition is therefore put in the form

$$(\mu^*+1)\sqrt{(1+m_1^2)} = \int_{\mu^*}^{\infty}\left\{\sqrt{\left[1+\left(\frac{d\lambda}{d\mu}\right)^2\right]}-\sqrt{(1+m_1^2)}\right\}d\mu+\int_{\mu_j}^{\mu^*}\sqrt{\left\{1+\left(\frac{d\lambda}{d\mu}\right)^2\right\}}\,d\mu + \int_{\lambda_j}^{\lambda_w}\sqrt{\left\{1+\left(\frac{d\mu}{d\lambda}\right)^2\right\}}\,d\lambda, \quad (87)$$

where the arc lengths in the range μ^* to infinity of the solution and the wedge are to be found in the first integral on the right-hand side. The remainder of the arc length of the wedge is on the left-hand side and the remainder of the arc length of the solution is given in the last two integrals on the right-hand side which represent the contributions from the two sides of the matching point. Equation (87) is obtained in terms of the reduced variables, using (45) for $d\lambda/d\mu$ and (76) for $d\mu/dz$ for the solution between infinity and μ_j, and using (70) for $d\mu/d\lambda$ and (74) for $d\lambda/dZ$ for the solution between λ_j and λ_w to give

$$\begin{aligned}(\mu^*+1)\sqrt{(1+m_1^2)} = {} & k'\int_{z^*}^{1}\left\{\sqrt{\left(1+\frac{m_1^2f^2g^2}{z^2}\right)}-\sqrt{(1+m_1^2)}\right\}\exp\left(\int_{z_j}^{z}\frac{z\,dz}{2-f-z^2}\right)\frac{dz}{2-f-z^2}\\ & +k'\int_{z_j}^{z^*}\sqrt{\left(1+\frac{m_1^2f^2g^2}{z^2}\right)}\exp\left(\int_{z_j}^{z}\frac{z\,dz}{2-f-z^2}\right)\frac{dz}{2-f-z^2}\\ & -K\int_{Z_j}^{1}\sqrt{\left(1+\frac{m_2^2F^2G^2}{Z^2}\right)}\exp\left(\int_{Z_j}^{Z}\frac{Z\,dZ}{2-F-Z^2}\right)\frac{dZ}{2-F-Z^2}. \quad (88)\end{aligned}$$

Expansions are needed in the first and last terms on the right-hand side of (88). The arc lengths evaluated for the matched solutions for the 45° and 22·2° semi-angle wedges were underestimates of $0{\cdot}26Vt$ and $0{\cdot}05Vt$, respectively. (The approximate method of §3 gave underestimates of 2·2 and 0·7.) The matching procedure described above therefore gives a satisfactorily close approximation.

The author wishes to express his great appreciation for many useful discussions with Prof. M. J. Lighthill and Dr R. F. Chisnell. The author also wishes to thank Mrs R. Grant for preparing the manuscript. The work was carried out while the author held a Department of Scientific and Industrial Research maintenance grant.

REFERENCES

Cumberbatch, E. 1958 Ph.D. Thesis, Manchester University.
Garabedian, P. R. 1953 *Commun. Pure Appl. Math.* **6**, 157.
Wagner H. 1932 *Z. angew. Math. Mech.* **12**, 193.

Temperature fluctuations in the atmospheric boundary layer

By C. H. B. PRIESTLEY

C.S.I.R.O. Division of Meteorological Physics, Aspendale, Victoria, Australia

(Received 24 June 1959)

A systematic analysis is made of published measurements of the magnitude of temperature fluctuations in the atmospheric boundary layer. These cover a wide range of height, wind speed, and thermal stratification. Within appropriate ranges of the variables, there is evidence for the existence of a dominantly forced convection régime, and also one wherein the predictions of the similarity theory of free convection are fairly closely approached. Subject to the limitations set by the recording systems used, regression relations are obtained for the magnitude of the fluctuations in terms of height and vertical temperature gradient or heat flux.

1. Introduction

Townsend (1959) has made a study of the temperature fluctuations in a laboratory chamber, heated at the bottom. Defining a length scale z_0, in terms of the upward heat flux H and thermometric conductivity κ, by

$$z_0 = \left(\frac{\rho c_p T \kappa^3}{gH}\right)^{\frac{1}{4}},$$

Townsend finds that the root mean square temperature fluctuation, σ_T, rises to a maximum value near $z/z_0 = 3$, and from $z/z_0 = 6$ to 90 decreases with height according to the relation

$$\frac{\sigma_T}{T\theta_0} = 1{\cdot}6\left(\frac{z}{z_0}\right)^{-0{\cdot}6}. \tag{1}$$

θ_0 is a scale of logarithmic temperature defined by

$$\theta_0^4 = \frac{1}{\kappa g}\left(\frac{H}{\rho c_p \bar{T}}\right)^3,$$

and the other symbols have their usual meaning.

We shall here, similarly, seek to relate appropriately normalized forms of σ_T and z in an analysis of the considerable body of published measurements in the atmospheric boundary layer, under conditions of both heating and cooling from below. However, the typical values of H by day are from 10 to 20 mW cm^{-2}, at times larger, whence $z_0 \approx 0{\cdot}12$ cm. Townsend's results therefore correspond to the lowest 10 cm or so of the atmosphere and, for this reason alone, need not resemble the behaviour at the commonly used heights between 25 cm and 30 m.

Moreover, and more basically, the typical atmospheric condition includes some mean horizontal motion, implying the existence at sufficiently low levels of a régime of effectively forced convection. With the near-boundary condition so radically altered, there is less reason to expect the explicit appearance of molecular quantities, such as κ, in the relationships. Rather, the main purpose of the analysis is changed to that of determining the depth of the effectively forced convection layer and also, by day, how rapidly the transition takes place to a dominantly free convection régime which generally exists at sufficient height. This is truly free convection in that the motions transporting the heat originate from buoyancy, so that wind speed and wind shear no longer appear in the relationships: nevertheless, the presence of these elements, and the difference in conditions below the free convection layer, may give rise to properties substantially different from those of free convection in otherwise perfectly still air.

An analysis of measurements of H (Priestley 1955; Taylor 1956) has suggested that for practical purposes one extreme form of relationship gives way to the other within a rather narrow (twofold or so) range in heights, and there is some evidence that the same holds for the form of the temperature-height profile (Webb 1958). We do not necessarily expect the same limits to apply for the transition of σ_T, since the spectra are known to be dissimilar in that fluctuations of the higher frequencies contribute relatively more to σ_T than to H.

2. Data

Measurements of σ_T were made by Swinbank (1955) at heights from 1·5 to 30 m, over a wide range of degrees of unstable thermal stratification, but avoiding the lightest winds. The limiting factor in frequency response was the recording galvanometer of 2·3 second free period. Taylor (1956, 1958) took further measurements using essentially the same equipment and height range, but selecting the conditions of strongest heating with light wind, generally less than 2 m sec^{-1} at 2 m height. Cramer, Gill and Record of the Massachusetts Institute of Technology measured σ_T during the Great Plains Turbulence Field Programme (Lettau & Davidson 1957) from 1·5 to 12 m, using a galvanometer of 1·1 second free period. Though non-selective in intent, this material (hereafter referred to as M.I.T. data) was in fact mainly confined to conditions of strong wind, averaging 7–8 m sec^{-1} at 2 m during the daytime. Where these sets of data overlapped, no significant separation was found between them, and accordingly the whole is treated herein as one more or less homogeneous body.

When the responsiveness of the overall sensing-recording system is substantially increased, fluctuations of higher frequency are detected, and a correspondingly larger value of σ_T is obtained. Concurrently with the M.I.T. measurements, Stewart and Kassander of Iowa State College (I.S.C. hereafter) recorded σ_T from 0·25 to 8 m height on magnetic tape with a modulator designed to yield a flat amplitude versus frequency response characteristic from zero to 15 c/s (Lettau & Davidson, pp. 206–15). The sensing device was a bead thermistor whose lag time was found to vary in an approximately exponential manner between 0·5 sec at zero wind speed and 0·1 sec in a 5 m sec^{-1} wind. This latter speed was approached throughout and usually exceeded (except at the lower

levels during some of the night-time runs). For reasons stated above, the analysis of I.S.C. data has been kept distinct from the remainder.

Details of the procedures used in analysis are described in the Appendix.

3. Variation of σ_T with height in unstable stratification

In the case of potential temperature decreasing with height, it proves useful, as a preliminary analysis, to consider purely the variation of σ_T with height without requiring σ_T to be normalized. We seek to fit a relation of the form

$$\sigma_T \propto z^{-p}. \tag{2}$$

The simultaneous or near-simultaneous measurement of σ_T at any pair of heights will then determine a single value of p (which will be presumed to refer to the geometric mean of the two heights). In this way, over 400 individual values of p were obtained from the I.S.C. data and over 200 from the other material.

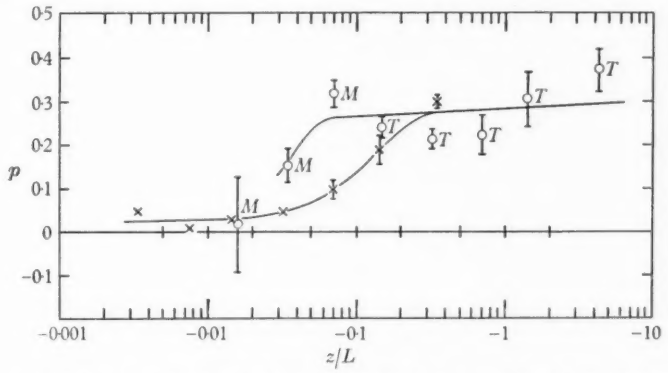

FIGURE 1. Index p as a function of z/L. Marks on the $p = 0$ line show the ranges into which values are grouped. × denotes I.S.C., ○ other data (T = Taylor, M = M.I.T. preponderating). Where no standard error lengths are indicated, this was less than 0·01.

p may be expected to depend on the relative strength of mechanical and convective processes and hence on the ratio z/L, where L is the Obukhov length defined as

$$L = -\frac{c_p \rho T u_*^3}{kgH}. \tag{3}$$

u_* is the friction velocity $(\tau/\rho)^{\frac{1}{2}}$, τ the shearing stress, and k von Karman's constant. The values of p have accordingly been grouped in ranges of z/L, and the mean of each group and its standard deviation are shown in figure 1. The symbols M and T denote that either the M.I.T. or the Taylor data contributed the majority of determinations in the group indicated; in no case did the Swinbank data contribute more than a minority.

In interpretation, we must note that $p = 0$ in forced convection while in free convection, subject to the principles of similarity with the assumption that molecular effects are not explicitly important, $p = \frac{1}{3}$ (Priestley 1954). In the I.S.C. data, mechanically generated fluctuations appear to be dominant up to

$z/|L| \approx 0{\cdot}05$. The régime is close enough to fully forced convection to expect useful working relationships to be obtainable therefrom, though it may be more strictly correct to speak of dominantly forced or quasi-forced convection, corresponding, for example, to the log-linear wind or temperature profile form of Monin & Obukhov (1954) at these small values of $z/|L|$. Above $z/|L| \approx 0{\cdot}05$, there is a relatively rapid change until, shortly above 0·1, the results become indistinguishable from those obtained with the less responsive equipment. These latter, on the other hand, display from as low as $z/|L| = 0{\cdot}05$ a rather strong tendency for dominance by buoyancy-induced effects. What is here perhaps no more than an indication that the transition is largely concentrated within the range 0·02–0·05 becomes stronger when set against earlier, and almost entirely independent, evidence of the transition in the régime of heat flux within the same limits.

4. Absolute value of σ_T in unstable stratification

The absolute analysis of σ_T has been carried out within the framework of the relation

$$\sigma_T/(z\theta')_{z_1} = \phi(z, L), \tag{4}$$

where ϕ is the function which requires to be discovered. θ' is written for $|\partial\theta/\partial z|$, the magnitude of the potential temperature gradient, and z_1 is a fixed height at which θ' was relatively accurately known in all instances, 1·5 m in fact being selected. Ideally it would have been preferable to divide σ_T by $z\theta'$ measured at the same height, or at some height which was a constant multiple or fraction χ of L or, equivalently to the latter, divide it by

$$T_* = H/(\rho c_p k u_*).$$

In any of these alternative analyses the right-hand side would be expected, on similarity theory, to be a function of the ratio z/L rather than of the two variables separately. For reasons appertaining to the data, as discussed briefly in the Appendix, these forms of analysis were not practicable without introducing undesirable corruption. However, the limiting forms of such relationships can be readily derived from the limiting forms of (4) and will be given below.

The results are displayed in figure 2 as a diagram of $\log\{\sigma_T/(z\theta')_{1{\cdot}5}\}$ against $\log z$, the data being divided into groups with similar values of L. As is foreshadowed in figure 1 and known from other evidence (see e.g. Priestley 1959), the forced fluctuations are of generally shorter period than the free fluctuations, and the more responsive I.S.C. system will record much of the former which the other data will miss. The two sets of data may be clearly distinguished in figure 2, and will be discussed separately in what follows.

The following extreme forms of (4) may readily be verified:

(i) When z and z_1 both lie within the forced convection régime,

$$\sigma_T/(z\theta')_{z_1} = \text{constant}, a.$$

(ii) When z lies in, but z_1 above, the forced convection régime,

$$\sigma_T/(z\theta')_{z_1} = \text{constant}, a'.$$

a' will depend on z_1/L but will always be greater than a.

(iii) When z and z_1 both lie within the free convection régime then, on the similarity theory,

$$\sigma_T/(z\theta')_{z_1} = b(z/z_1)^{-\frac{1}{3}},$$

where b is a constant.

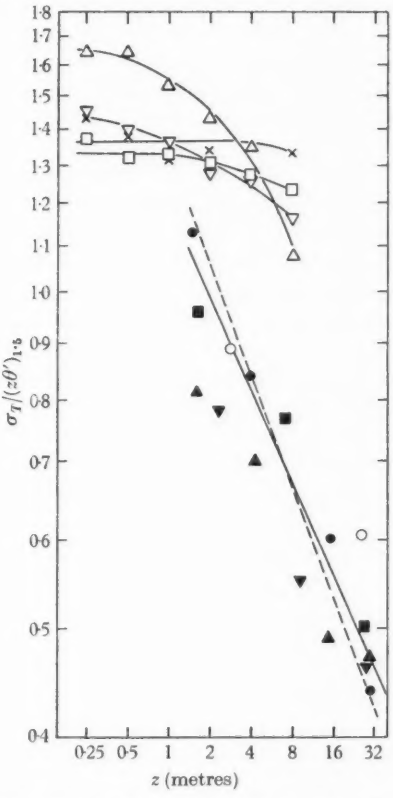

FIGURE 2. Normalized temperature fluctuations as a function of z and L. Designation of points, for I.S.C. data, is as follows: △, $|L| \leqslant 60$ m (average 45 m); ▽, $60 < |L| \leqslant 100$; □, $100 < |L| \leqslant 150$; ×, $150 < |L|$ (average 225 m). For other data: ●, $|L| \leqslant 15$ m (average 8·3 m); ○, $15 < |L| \leqslant 30$; ▲, $30 < |L| \leqslant 60$; ▼, $60 < |L| \leqslant 100$; ■, $100 < |L|$ (average 210 m). Each point represents the mean of at least seven individual determinations, the average being eight for the I.S.C. data (186 determinations) and thirteen for the less homogeneous material of the other data (202 determinations). The full and broken straight regression lines correspond to equations (6) and (7), respectively, of the text: other lines are drawn by eye to fit the four categories of the I.S.C. data.

(iv) When z lies in, but z_1 below, the free convection régime,

$$\sigma_T/(z\theta')_{z_1} = b'(z/z_1)^{-\frac{1}{3}},$$

where b' depends on z_1/L but will always be greater than b.

The upper set of curves in figure 2, corresponding to the I.S.C. data, shows separation of the profiles according to the magnitude of L, and the ranges within which the predictions (i) and (ii) are approached serve to confirm $z/|L| \approx 0{\cdot}02$ as

effectively the limit of fully forced convection. Any conclusions as to numerical magnitudes are subject to the limitation imposed by the response times of the recording instruments, but with this reservation the relation for forced convection may be written as

$$\sigma_T = 1{\cdot}4z\,|\partial\theta/\partial z|. \tag{5}$$

The need for a standard height has disappeared because of the constancy of $z\theta'$ through the layer in question. Using the familiar equation $H = \rho c_p K\,|\partial\theta/\partial z|$, where $K = ku_* z$, equivalent forms of (5) are seen to be

$$\sigma_T/T_* = \sigma_T/(z\theta')_{\chi L} = 1{\cdot}4,$$

so long as the level χL is in the same régime.

The points from the other data in figure 2 show no systematic separation according to the magnitude of L. This in itself is an indication of dominance by one or other of the two extreme régimes and the pattern of results, backed by what has gone before, points to free convection in this instance. The two mechanisms are of course to a large extent coexistent and forced fluctuations will occur in the overlapping region, and at even larger values of $z/|L|$; but the less responsive equipment fails to register their finer structure. Nor is it proved that all the free fluctuations are fully registered, though it appears likely on internal and other evidence that this is approximately true. In making any further comparison between the two sets of points, note should be taken of the range of L as well as of z.

For the 'other' data, in the lower part of figure 2, regression coefficients were calculated between $\log\{\sigma_T/(z\theta')_{1{\cdot}5}\}$ and $\log z$ excluding, for reasons evident from figure 1, those points for which $z/|L| < 0{\cdot}05$, and weighting the remainder according to the number of individual contributing values. The result obtained was

$$\sigma_T/(z\theta')_{1{\cdot}5} = 1{\cdot}19z^{-0{\cdot}28} = 1{\cdot}07(z/1{\cdot}5)^{-0{\cdot}28}, \tag{6}$$

where z is measured in metres. This is shown by the full line in the diagram. The broken line shows the best fit when the index is constrained to the value $-\frac{1}{3}$, the regression then being

$$\sigma_T/(z\theta')_{1{\cdot}5} = 1{\cdot}34z^{-\frac{1}{3}} = 1{\cdot}20(z/1{\cdot}5)^{-\frac{1}{3}}. \tag{7}$$

In the similarity theory of free convection, the temperature profile is given by $\theta' \propto z^{-\frac{1}{3}}$, and where this holds (7) is equivalent to a more basic form of relationship

$$\sigma_T = 1{\cdot}2z\,|\partial\theta/\partial z|, \tag{8}$$

in which the need for a standard height as intermediary has again been eliminated. The formal similarity between (5) and (8) is interesting. Whether it portrays a physical similarity or conceals a physical difference is possibly a matter for debate, but it certainly suggests that an analysis carried through in terms of $\sigma_T/z\theta'$, instead of $\sigma_T/(z\theta')_{z_1}$, had it been practicable, would have proved considerably less illuminating.

An alternative form of (8), which portrays the height-variation explicitly, may be obtained from the heat flux relation of similarity theory, namely

$$H = h\rho c_p (g/T)^{\frac{1}{2}} z^2\,|\partial\theta/\partial z|^{\frac{1}{2}},$$

where h is the free convection constant whose value is about 0·9 (Priestley 1959). This leads immediately to

$$\sigma_T/T_* = 1{\cdot}2k^{\frac{1}{3}}h^{-\frac{2}{3}}|z/L|^{-\frac{1}{3}} \approx 0{\cdot}4|z/L|^{-\frac{1}{3}}.$$

5. Inversion conditions

The analysis of σ_T in stable stratifications is confined to the I.S.C. and M.I.T. material, Taylor's studies having included no such cases and Swinbank's only a few of more uncertain quality. Winds ranged between 3 and 9·5 m sec^{-1} at 8 m, and between 1 and 5·5 m sec^{-1} at 0·5 m.

The means for obtaining L, as described in the Appendix for unstable conditions, are no longer available. Instead, we shall make direct use of Ri′ as tabulated by Lettau & Davidson and defined as

$$\mathrm{Ri}' = \frac{\Sigma \mathrm{Ri}(z_i)}{\Sigma z_i},$$

where $\mathrm{Ri}(z_i)$ was obtained from the profile measurements at a number (up to 5) of heights z_i more or less proportionately spaced from 0·8 to 8 m. Since $\mathrm{Ri}' = 1/L$ in fully forced convection, and may be expected to behave in a closely sympathetic fashion elsewhere, $z\,\mathrm{Ri}'$ is a valid substitute for z/L in the search for universal relationships.

The I.S.C. data was first grouped in ranges of Ri′ and it was found that, in each group, σ_T increased slowly with height. The rate of increase corresponded to a p in (2) of between $-0{\cdot}01$ and $-0{\cdot}05$ resembling, with change of sign, the behaviour towards the left in figure 1. It was accordingly considered suitable to make the absolute analysis of σ_T in the same terms as that of the previous section, save that the fixed height z_1 was here chosen as 65 cm in order to permit $(z\theta')_{z_1}$ to be read off directly from the published data (see Appendix). The slow variation of σ_T with height permitted values to be estimated where these were occasionally missing from one or two levels, so rendering the material homogeneous.

The average (geometric mean) values of $\sigma_T/(z\theta')_{0{\cdot}65}$ were then obtained in ranges of $z\,\mathrm{Ri}'$ and the results are shown in table 1, I.S.C. and M.I.T. data being treated separately. The first value of the I.S.C. data appears anomalous, probably because both σ_T and θ' are relatively most inaccurate in this range, and the use of occasional spuriously low values of θ' may have biased the quotient in the sense indicated. Otherwise, below $z\,\mathrm{Ri}' \approx 0{\cdot}1$ there is no significant departure from the overall mean value of 1·33 and, by analogy with the unstable case, we may infer the existence of a dominantly forced convection régime wherein

$$\sigma_T = 1{\cdot}33z\left|\frac{\partial\theta}{\partial z}\right|. \tag{9}$$

Within the accuracy of determination there is no significant difference between the constants in (9) and (5).

Above $z\,\mathrm{Ri}' \approx 0{\cdot}1$ the suppressive influence of stability enters, and this begins to take effect on the longer-period fluctuations (M.I.T. data) at much

smaller values of $z\,\mathrm{Ri}'$. Here the decrease to about one-third in a 20-fold range in $z\,\mathrm{Ri}'$ appears sharper than the corresponding decrease in the unstable condition. Moreover, the two are to be further distinguished by the fact that $z\theta'$ typically increases with height in the more stable conditions, so that a relationship of the form (8) is here no longer even remotely applicable.

Range	$z\,\mathrm{Ri}' \leqslant 0{\cdot}002$	$0{\cdot}002 < z\,\mathrm{Ri}' \leqslant 0{\cdot}005$	$0{\cdot}005 < z\,\mathrm{Ri}' \leqslant 0{\cdot}01$	$0{\cdot}01 < z\,\mathrm{Ri}' \leqslant 0{\cdot}02$	$0{\cdot}02 < z\,\mathrm{Ri}' \leqslant 0{\cdot}05$	$0{\cdot}05 < z\,\mathrm{Ri}' \leqslant 0{\cdot}1$	$0{\cdot}1 < z\,\mathrm{Ri}' \leqslant 0{\cdot}2$	$0{\cdot}2 < z\,\mathrm{Ri}'$
I.S.C. data								
No. of observations	21	36	35	35	41	27	10	5
Av. $\sigma_T/(z\theta')_{0{\cdot}65}$	1·73	1·43	1·25	1·31	1·34	1·26	1·04	0·87
M.I.T. data								
No. of observations	—	—	13	24	42	33	15	13
Av. $\sigma_T/(z\theta')_{0{\cdot}65}$	—	—	0·96	0·95	0·77	0·63	0·51	0·30

TABLE 1. $\sigma_T/(z\theta')_{0{\cdot}65}$ as a function of $z\,\mathrm{Ri}'$.

6. Conclusions

It has been seen that a considerable body of data on temperature fluctuations is available from the atmospheric boundary layer, but its definitive interpretation is limited by the responsiveness of the recording systems used. Subject to this limitation, quite well-defined regression relations have been obtained. From the more responsive equipment, the total intensity σ_T follows a régime of dominantly forced convection up to $z/|L| = 0{\cdot}05$ to $0{\cdot}1$ on either side of neutral conditions. Above these levels, the effects of stratification make themselves felt quite rapidly. However, the longer-period fluctuations, which alone are recorded by the less responsive equipment, are subject to strong thermal influence above $z/|L| \approx 0{\cdot}02$ on either side of neutral conditions, and in unstable conditions above $z/|L| \approx 0{\cdot}05$ obey a relationship not very different from the predictions of the similarity theory of free convection. These in part consolidate the views previously arrived at from the study of heat-flux measurements in unstable conditions. To the extent that further interest exists in the fluctuations *per se*, a more complete exploration is called for with equipment responding to periods even shorter than 0·1 sec, combined with some form of spectral analysis.

Appendix. Details of the analysis

The analysis was restricted to occasions when conditions were steady, as far as could be determined from the data. In particular, runs made at or near the times of cross-over between stable and unstable stratifications were excluded whenever there was evidence that one or other of these conditions were not maintained throughout the relevant range of heights.

Before analysis, certain amendments were made to the data as published. Two values of σ_T published by Taylor (1958) were subsequently found to be in error: in run 2 of 1 February 1956, σ_T was 0·60 and 0·55 °C at 1·5 and 4 m, respectively.

The gradient of potential temperature at 1·5 m, reported in Swinbank's and Taylor's papers, had been derived by an objective smoothing (as described in the former) of the measured data at $\frac{1}{2}$, 1, 2 and 8 m. In a few instances where this might have introduced some error owing to the incidence of vanishing gradients below 8 m in strongly unstable situations (Webb 1958), the gradient was recalculated using only $\frac{1}{2}$, 1 and 2 m. For the Great Plains data, $z\theta'_{1\cdot5}$ was taken as the value given in Table 7.3*b* of Lettau & Davidson. It is seen that this

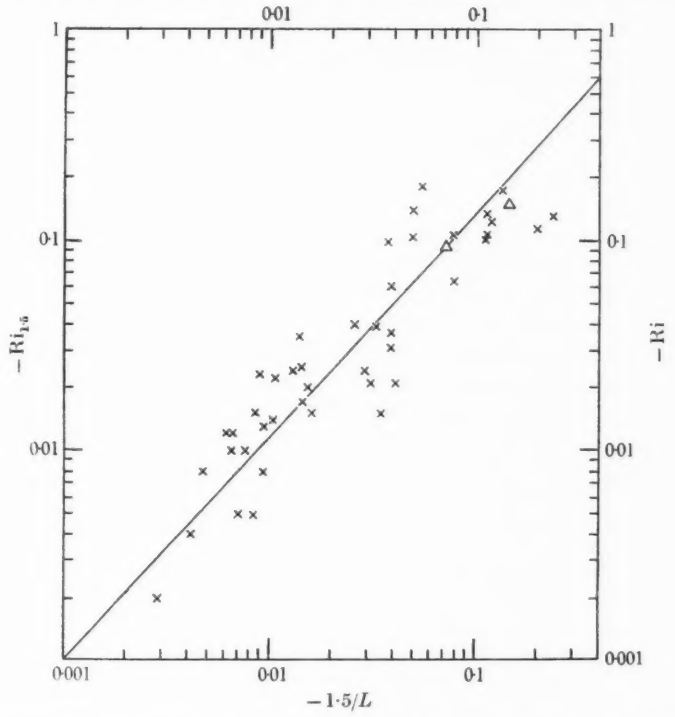

FIGURE 3. $\mathrm{Ri}_{1\cdot5}$ versus $1\cdot5/L$ from Swinbank's measurements (L in metres). Triangles denote values obtained by Rider.

is actually a weighted mean of gradients between 82 and 39 cm and between 160 and 40 cm, and applies to a level of about 65 cm. In general, this identification was justified because of the strong winds and rather modest temperature gradients, but in the one case (1235 on 8 September 1953) when conditions were sufficiently unstable to invalidate it, $z\theta'_{1\cdot5}$ was interpolated from the original temperature data using all measurements between 0·5 and 4 m inclusive.

Acceptable measured values of L were available only in Swinbank's material. Here, although both H and τ were biased to some extent by the responsiveness of the recorder, the resulting underestimation was common to both so that L should be rather more accurate than its numerator or denominator separately. Flux measurements at higher levels were notably less reliable than at the lower

levels (4 m and below) and the latter only were used, these being assumed to apply to a proximate high level run provided the interval was less than $\frac{1}{2}$ hour and the $\mathrm{Ri}_{1\cdot5}$ did not change by more than $\frac{1}{3}$ of the prior value.† Where these conditions were not satisfied, the high level σ_T was not included in the material.

For the Great Plains and Taylor's data, in unstable conditions, L was obtained as follows. Figure 3 shows values of $-\mathrm{Ri}_{1\cdot5}$ reported by Swinbank plotted against the corresponding value of $-1{\cdot}5/L$ obtained from the low-level H and τ measurements. Two points are also shown as obtained by Rider (1954). This allows the straight line as drawn, or its prolongation, to be used as a basis for obtaining L from $\mathrm{Ri}_{1\cdot5}$, which was always available either directly or from Ri′ as tabulated by Lettau & Davidson. It is to be noted that L has been used only as a grouping parameter, or as divisor of z, for quantities which are never more than slowly varying functions of z. Modest errors in L will therefore not substantially affect the conclusions.

Coming finally to the choice of equation (4) as the framework of the absolute analysis it may be seen that T_*, as an alternative divisor of σ_T, could have been inferred with an accuracy comparable with that of L. However, errors acceptable in the divisor of z would have been much more serious in the divisor of the less accurately known, and much slower varying, quantity σ_T. Of other possible divisors, $z\theta'$ at the same height as σ_T was not always available, and its individual measurement would anyway be subject to increasing relative inaccuracy at the greater heights. Similar considerations forbade the use of $z\theta'$ at χL, however χ might be chosen, since $|L|$ ranged from 2 m to several hundred metres.

REFERENCES

Lettau, H. H. & Davidson, B. 1957 *Exploring the Atmosphere's First Mile.* London: Pergamon Press.

Monin, A. S. & Obukhov, A. M. 1954 *U.S.S.R. Acad. Sci.*, Geophys. Inst. no. 24, 28 pp.

Priestley, C. H. B. 1954 *Aust. J. Phys.* **7**, 176.

Priestley, C. H. B. 1955 *Quart. J. Roy. Met. Soc.* **81**, 139.

Priestley, C. H. B. 1959 *Turbulent Transfer in the Lower Atmosphere.* Chicago University Press.

Rider, N. E. 1954 *Phil. Trans.* A, **246**, 481.

Schmidt, W. 1941 *Z. angew. Math. Mech.* **21**, 265, 351.

Swinbank, W. C. 1955 *C.S.I.R.O. Div. Met. Phys., Tech. Paper no.* 2.

Taylor, R. J. 1956 *Quart. J. R. Met. Soc.* **82**, 89.

Taylor, R. J. 1958 *Aust. J. Phys.* **11**, 168.

Townsend, A. A. 1959 *J. Fluid Mech.* **5**, 209.

Webb, E. K. 1958 *Quart. J. R. Met. Soc.* **84**, 118.

† The same criterion for steadiness was applied to Swinbank's data for accepting values σ_T from two successive runs for comparison through equation (2).

An experiment on the stability of hypersonic laminar boundary layers

By ANTHONY DEMETRIADES

Guggenheim Aeronautical Laboratory, California Institute of Technology
Pasadena, California

(Received 24 June 1959)

An experimental investigation of the hydrodynamic stability of the laminar hypersonic boundary layer was carried out with the aid of a hot-wire anemometer. The case investigated was that of a flat surface at zero angle of attack and no heat transfer.

The streamwise amplitude variation of both natural disturbances and of disturbances artificially excited with a siren mechanism was studied. In both cases it was found that such small fluctuations amplify for certain ranges of frequency and Reynolds number R_θ, and damp for others. The demarcation boundaries for the amplification (instability) zone were found to resemble the corresponding limits of boundary-layer instability at lower speeds. A 'line of maximum amplification' of disturbances was also found. The amplification rates and hence the degree of selectivity of the hypersonic layer were found, however, to be considerably lower than those at the lower speeds. The disturbances selected by the layer for maximum amplification have a wavelength which was estimated to be about twenty times the boundary-layer thickness δ.

I. Introduction

The problem of transition of a fluid flow to turbulence has for a long time attracted the attention and toil of both theoreticians and experimentalists. At hypersonic speeds the problem of transition is one of pressing importance, since the differences in skin friction and heat transfer between laminar and turbulent flow are large enough to alter radically the performance of, say, a hypersonic aircraft or a long-range missile.

Of the various hypotheses put forth to describe the mechanism of transition, one which has been steadily gaining ground is the small-disturbance hypothesis. It states that within some range of the mean-flow parameters, certain infinitesimal disturbances found in the laminar part of the flow (whether wake, jet, or boundary layer) amplify as they progress downstream and eventually break up into the random pattern that we identify as turbulence. The small-disturbance theory itself does not deal with the problem of turbulence; it merely examines whether and how disturbances amplify and damp in the laminar flow, and is therefore a theory of hydrodynamic stability.

The stability of parallel flows was treated by Rayleigh (1880), Prandtl & Tietjens (1925), Heisenberg (1924), and Tollmien & Schlichting (1930). Recently

the stability of the boundary layer of a compressible fluid with heat transfer was investigated by Lees & Lin (1946), Lees (1947), and Dunn & Lin (1955). The small-disturbance theory of boundary-layer flows enjoyed its first success with the classic experiments of Schubauer & Skramstad (1948), and of Liepmann (1943), which showed the existence of the laminar waves of Tollmien and Schlichting and which verified, both qualitatively and quantitatively, many of the prominent features of the theory. Recently, Laufer & Vrebalovich (1956), in studying the flow over a flat plate at a Mach number of about 2, obtained data similar to that obtained by Schubauer & Skramstad at low speeds.

At hypersonic speeds the large temperature differences existing across the boundary layer bring to the foreground some hitherto unsettled points in the analysis of the stability problem.* The present experiment (Demetriades 1958) was undertaken in order to provide an understanding of the stability of the hypersonic layer, and, more specifically, to see whether there exist ranges of the defining parameters where small disturbances damp or amplify, to obtain information on the bounds of these ranges, and to study the manner of amplification or damping. For this purpose the experiment was limited to the simple case of a smooth flat plate at zero heat transfer and zero pressure gradient.

2. Technique and equipment

The downstream progress of a small disturbance

$$Q' = q(y)\, e^{i\alpha(x-ct)}$$

in a laminar boundary layer will be arrested or enhanced depending on whether c_i, the imaginary part of the propagation velocity c, is negative or positive. When c_i is zero the disturbance is neutral and, for a fixed Mach number, the small-disturbance theory produces a unique relationship between wave-number α and Reynolds number R_θ, based on momentum thickness. This relationship divides the (α, R_θ) plane into a stable and an unstable region.

Consideration of the (α, R_θ) plane suggests a suitable experimental technique. If one measures the root-mean-square amplitude of a particular disturbance at successive streamwise positions in the boundary layer, one should be able to identify the extrema in this amplitude variation with points falling on the dividing curve. In fact, the primary aim of this investigation was to see whether these extrema defined a unique locus at a hypersonic Mach number.

In addition to studying the streamwise history of a disturbance of a given frequency, a second obvious method is to study the energy spectrum of disturbances at a preselected, fixed point in the layer. This approach is particularly tempting, since the small-disturbance theory in this case predicts energy concentrations in certain portions of the spectrum and since these peaks have been easy to observe at the lower flow velocities (Schubauer & Skramstad 1948; Liepmann 1943). In order to apply these two methods, an instrument capable of temporal and spatial measurements on a minute scale is required. Such

* A theoretical study of the stability of the hypersonic laminar boundary layer has been undertaken by E. Reshotko and L. Lees at the Guggenheim Aeronautical Laboratory, California Institute of Technology.

an instrument is the hot-wire anemometer. The applicability and reliability of this instrument in high-speed flows has been demonstrated by many workers, notable Kovasznay (1954), Morkovin (1956), and Laufer & McClellan (1955). Calibration of the anemometer or resolution of its output into components due to velocity, density or temperature fluctuations is unnecessary here since the stability boundaries remain unaltered when different types of disturbances are considered.

The present investigation was carried out in Leg 1 of the GALCIT hypersonic wind tunnel. Two different flat-plate models were used. The survey plate used to study the stability of natural fluctuations was 26 in. long, had a sharp leading edge and smooth finish, and was aligned within the test rhombus at zero incidence (cf. figure 1). The siren plate was almost identical to the survey plate externally but contained a mechanism for producing fluctuations of controllable

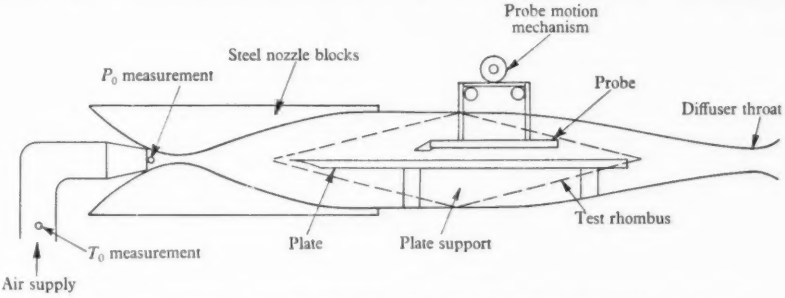

FIGURE 1. Schematic diagram of GALCIT Leg 1 hypersonic tunnel test section showing flat plate and probe installation.

amplitude and frequency. A 4 in. diameter thin brass siren disk imbedded under the surface had sixty regularly spaced holes drilled along its circumference, while another seven small slits 0·060 × 0·028 in. were drilled along a straight line 1·75 in. downstream from the leading edge, in a cover-plate emplaced over the disk. The seven slits were spaced so that they were either in complete coincidence or in complete anti-coincidence with the holes in the siren disk as the latter rotated underneath; an air pulse was therefore injected into the flat-plate boundary layer for each 6° of disk rotation. By regulating the speed of a motor driving the disk, frequencies from about 1 up to about 40 kc/s were attainable.

The hot-wire anemometer probe is pictured in figure 1. The probe can be moved vertically above the plate surface, as well as in a stream-wise direction, providing the hot wire with two degrees of freedom. The hot-wire element was soft-soldered on the tips of two heat-treated sewing needles which were, in turn, cemented in grooves on the detachable probe head. The probe head is 'plugged in' to a socket in the front of the probe strut through which pass a pair of co-axial cables, with very small diameter, maintaining electrical connexion with the electronic apparatus. The wire was operated at constant current drawn from five 45 V cells in series. The instrumentation included a pre-amplifier with a maximum gain of about 3200, a compensating amplifier to correct for the thermal lag of the wire, and band-pass filtering apparatus. The magnitude of the r.m.s.

voltage was measured with a vacuum thermocouple in series with a 92 Ω microammeter. A display-type wave analyser was also found to be very useful in this work. Energy spectra were recorded with a harmonic wave analyser and a thermocouple-microammeter combination.

Platinum-rhodium wires of 0·0001 in. diameter measuring from 0·02 to 0·03 in. in length were used exclusively in this work. The wires were always held normal to the flow direction and parallel to the plate surface, so that they were sensitive to the u' (streamwise) perturbation velocity component. It was found expedient to anneal and prestretch the wire in the hypersonic stream itself; thus treated some wires were used for several tens of hours without any appreciable changes in electrical characteristics or any visible deterioration. No severe strain-gauge effects (Morkovin 1956) were encountered. Table 1 presents some of the pertinent operating conditions of the hot wire.

Material	Platinum 90% Rhodium 10%
Diameter	0·0001 in.
Length	0·02–0·03 in.
Aspect ratio	200–300
Mach number	5·8
Wire Reynolds number Re_d (free-stream conditions)	Order of 1
Wire Nusselt number Nu_d (free-stream conditions)	Order of 0·1
Resistance (equilibrium) R_e	30–40 Ω
Total pressure	28–75 p.s.i.g.
Total temperature	225 °F
Dynamic loading	0·8–1·6 p.s.i.
Error in sensitivity coefficients due to 'end effects'	5–10%
Time constant	$0{\cdot}2\text{–}1 \times 10^{-3}$ sec
Maximum current through wire	About 10 mA

TABLE 1. Typical operating conditions for the hot-wire anemometer.

The laminar boundary layer over the survey flat-plate at zero incidence at $M = 5{\cdot}8$ was studied in some detail by Korkegi (1954) and also by McMahon (1958) and the author. Laminar boundary-layer profiles obtained by using a total-pressure tube yielded the layer thickness δ and the momentum thickness θ along the centreline of the plate. A series of such profiles taken along the centreline of the survey plate disclosed that boundary layer similarity is definitely preserved. The boundary-layer growth over the siren plate was also measured with flow conditions simulating those under which the presently described experiment was carried out. The agreement between these measurements and the measurements in the boundary layer on the survey plate was good. The range of R_θ varied between 350 and 2050.

The free-stream turbulence was also investigated in the region of interest, namely, in the region of the test section which would be normally occupied by the flat-plate boundary layer. The absolute level of the turbulence was measured

at a distance of 17·5 in. from the nozzle throat. The data yielded values of the order of 0·4 % in both the mass flux and the temperature fluctuation in the range 0–100 kc/s, with little variation due to the tunnel supply pressure. Thus the free-stream disturbance energy contained in a narrow frequency band (say, between 20 and 25 kc/s) was one, or possibly two, orders of magnitude smaller than the allowable level for purposes of this experiment.

3. Measurements of the natural fluctuations

The growth or decay of fluctuations which exist naturally in the laminar boundary layer was measured on the survey plate by moving the hot wire along the layer at chosen constant values of y/δ. The hot-wire output at a series of selected frequencies was recorded with the aid of the harmonic wave analyser and the vacuum thermocouple-microammeter combination. Keeping y/δ constant as the hot wire was moved streamwise in increments of x was relatively simple, since the wire resistance R_w is a function only of y/δ. As the probe was moved downstream by steps it was also raised slightly each time, so that the

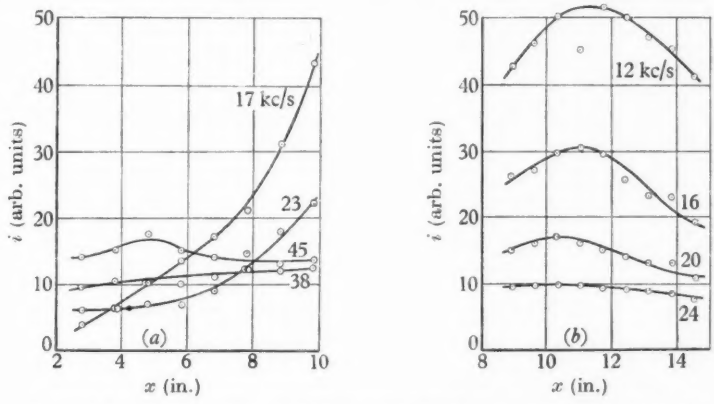

FIGURE 2. Typical variation of hot-wire output intensity due to natural fluctuations. (*a*) $P_0 = 35$ p.s.i.g.; (*b*) $P_0 = 45$ p.s.i.g.

resistance-measuring galvanometer was again balanced at the previously set value of R_w. Some typical data, taken at values of y/δ ranging from 0·7 to 0·9, are singled out and shown in figure 2. The abcissa of these graphs is the distance of the wire from the leading edge of the plate; the ordinate is the microammeter reading, which is proportional to the mean-square voltage fluctuation $\overline{(\Delta e')^2}$ and thence to the square of the fluctuation amplitudes, that is to the fluctuation energy. Figure 2(*a*) shows the appearance of a maximum at a frequency of 45 kc/s, and figure 2(*b*) a sequence of such maxima. The x-values at which these maxima occurred, when used in conjunction with the tunnel-flow parameters and the local boundary-layer momentum thickness, gave points in the plot of the non-dimensional frequency $\beta_r \nu_\infty / U_\infty^2$ versus the Reynolds number R_θ; here β_r is proportional to the disturbance frequency, and ν_∞ and U_∞ the kinematic viscosity and fluid velocity, respectively, in the free stream.

These points fell, within some scatter, on a line which should thus be the upper neutral branch of the boundary-layer stability diagram; this line will not be presented here, however, since it generally agreed with the branch found by means of the more reliable artificial-fluctuation method. Since no consistent appearance of minima was observed, the lower neutral branch was not discernible for the natural fluctuations.

As pointed out earlier, the amplitude spectrum of the natural fluctuations should exhibit a maximum when measured at any streamwise location in the boundary layer. In searching for this property in the hypersonic boundary layer the survey flat plate was again employed, and the wire-output spectrum was recorded for various combinations R_θ and y/δ. After prolonged measurements at various ranges of output frequency and Reynolds number a series of energy peaks were discovered in the intervals from 0 to 10 kc/s in frequency and 800–2000 in R_θ. The data are shown in figure 3.

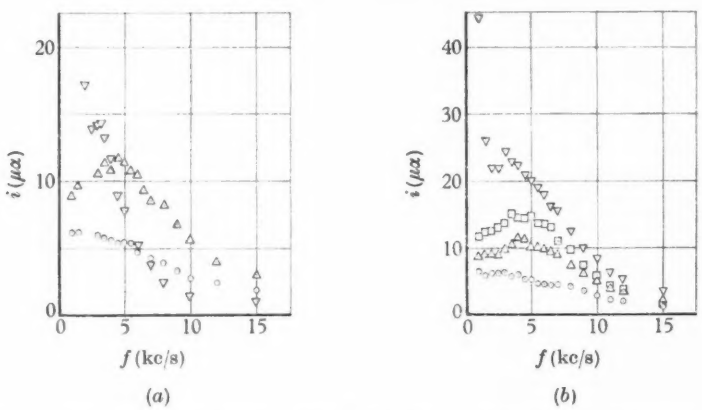

FIGURE 3. Hot-wire mean-square output spectra in the laminar boundary layer, $M = 5{\cdot}8$, $T_0 = 225$ °F. (*a*) $P_0 = 28$ p.s.i.g.; ⊙, $x = 9{\cdot}2$ in.; △, $x = 11{\cdot}8$ in.; ▽, $x = 16{\cdot}5$ in. (*b*) $P_0 = 35$ p.s.i.g.; ⊙, $x = 9{\cdot}2$ in.; △, $x = 11{\cdot}5$ in.; □, $x = 14{\cdot}0$ in.; ▽, $x = 16{\cdot}5$ in.

By far the most interesting feature of the energy spectra of figure 3 is the absence of any completely predominant energy peak corresponding to the data for incompressible flow obtained by Schubauer & Skramstad (1948). The energy peak is barely discernible for $R_\theta = 880$, although this lower limit is presumably strongly dependent on the free-stream turbulence level and other characteristics of the experimental environment. For larger values of x (or R_θ) the relative magnitude of the peak increases, but certainly not in a manner permitting it, for example, to be viewed on an oscilloscope without band-pass filtering. At the largest x-values attainable with the hot-wire probe traverse the peak is finally obscured by an abrupt increase of the energy contained from 0 to 2 kc/s in the spectrum. Figure 4 presents the points defined by the frequency-at-maximum-amplitude of curves such as those given in figure 3. The two solid curves on figure 4 are the neutral branches discussed in §4.

A final point of interest concerns the value of y/δ at which the measurements just described were carried out. More specifically, one is interested in finding out how the amplitude peak, at the fluctuation frequency that the boundary layer has selected for maximum amplification at some R_θ, changes with y/δ. For this purpose the wire was held at some constant R_θ and was traversed across the boundary layer from the solid surface toward the free stream in steps of about $\frac{1}{5}\delta$ each; at each step the energy spectrum was recorded. Very near the plate there is no peak in the spectrum. As the wire is raised through the layer the peak, in this case at about 2·8 kc/s, appears, becomes most prominent for values of y/δ between 0·6 and 1, persists briefly in the free stream and finally disappears for $y/\delta = 1{\cdot}34$.

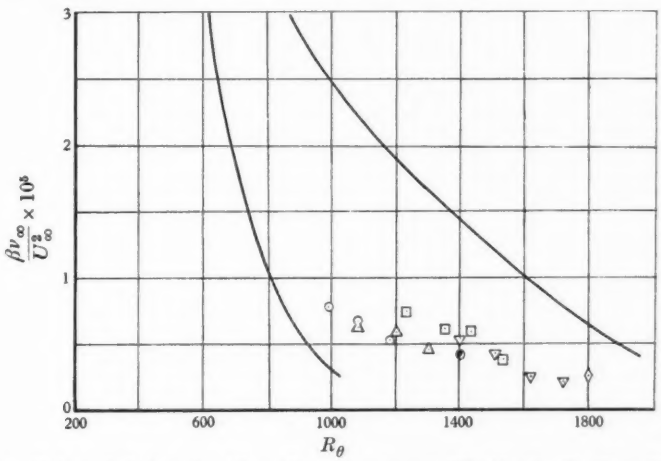

FIGURE 4. Points defining the 'line of maximum amplification'. ⊙, $P_0 = 28$ p.s.i.g.; △, $P_0 = 35$ p.s.i.g.; ◐, $P_0 = 40$ p.s.i.g.; ⊡, $P_0 = 45$ p.s.i.g.; ▽, $P_0 = 55$ p.s.i.g.; ◇, $P_0 = 60$ p.s.ig.

At the conclusion of the work with the natural fluctuations encouraging evidence had been accumulated to the effect that the laminar hypersonic boundary layer observed, at least in a general way, the stability rules of the small-disturbance theory. A demarcation boundary between an unstable and a stable region had been found and characteristic fluctuations at selected frequencies had also been found and their dependence on R_θ ascertained (figure 4). The amplification rates that had been found, however, were quite low and it was suspected that natural causes such as the free-stream turbulence might have been concealing the detailed features of the stability diagram, particularly the lower neutral branch. For this reason the study of disturbances injected with the 'siren' mechanism described in the next section was undertaken.

4. Measurement of the artificial fluctuations

In utilizing the siren plate for the measurement of artificial fluctuations, care was taken to see that the amount of air injected did not cause premature transition. For very small injection rates it was almost impossible to detect the

induced fluctuation downstream of the slits. As the injection rate increased the energy peak corresponding to the siren frequency appeared and increased in magnitude. When some critical injection rate was reached the peak magnitude increased no further, but an abrupt large increase of the wire output was noted over the entire frequency range; raising the injection rate further had no significant effect on the mean-square level of the wire output. This critical injection rate was, therefore, the one at which the layer became turbulent at the

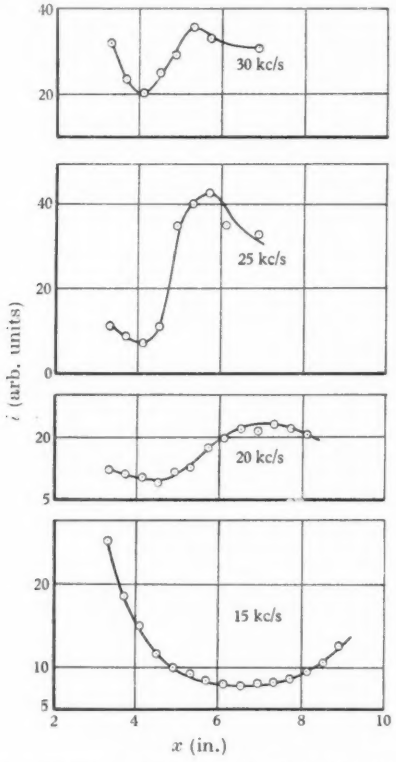

FIGURE 5. Typical hot-wire output variations due to artificial fluctuations. $P_0 = 30$ p.s.i.g.;

location of the wire. Knowledge of this rate enabled one to choose an injection rate appropriate for taking data and thus to estimate, even though roughly, the comparative magnitude of the fluctuation amplitudes. Generally, data were taken at all subcritical rates, the guiding consideration being the appearance and clarity of the energy peak at the siren frequency. All artificial fluctuation data were taken by using the band-pass filter to suppress signals at all frequencies below and above that of the siren.

The results of the constant-frequency surveys appear in figures 5 and 6. The value of y/δ was maintained constant for each survey using the method described in the previous section. Figure 5 shows typical surveys at constant frequency exhibiting extrema in the amplitude variation. In almost all cases

the variation of the location of the extrema (maxima or minima) with fluctuation frequency is apparent. As a rule the signals were very weak for y/δ much smaller than unity and disappeared rapidly once the probe was moved into the free stream.

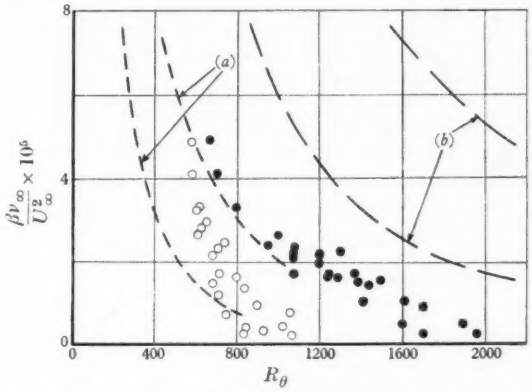

FIGURE 6. Experimentally determined upper neutral branch (solid circles) and lower branch (open circles) at $M = 5{\cdot}8$. (*a*) $M = 2{\cdot}16$ (Laufer & Vrebalovitch; (*b*) $M \simeq 0$ (Schubauer & Skramstad).

The results of the artificial-fluctuation study are plotted in figure 6 in the usual non-dimensional frequency plot, where they are also compared with similar findings at lower Mach numbers. It is apparent that the general shape of the region of instability is preserved throughout the range of Mach numbers from 0 to 5·8. Another consistent trend appears to be the gradual decrease, with increasing Mach number, of the area enclosed by the neutral stability boundaries, at least above a certain low non-dimensional frequency. The scatter of the data in figure 6 is of undetermined origin. No systematic effect of the supply pressure P_0 on the scatter was observed, nor did there seem to be an effect of y/δ and hence also of the wire sensitivity. The effect of the air injection rate, on the other hand, is difficult to estimate properly since it may be significant in two independent ways, namely, by affecting the fluctuation amplitude and also by changing the boundary-layer thickness. Both these effects are thought to be small.

By far the most remarkable feature of the work with the artificial fluctuations was that it made possible the discovery of the lower neutral branch. It is thought that the inability to discover the lower branch for the natural fluctuations lies mainly in the interference caused by the free-stream turbulence level. In order to substantiate this conjecture, a comparison was made of the hot-wire signal in the boundary layer a few inches downstream of the leading edge of the survey plate, and the signal obtained at the same geometrical position but with the plate removed from the wind tunnel: these two signals were found to be of about the same magnitude, both quite smaller than signals obtained with the siren mechanism operating. In fact, an insight into all the differences between the natural-fluctuation and the artificial-fluctuation data could be gained by considering the role of the free-stream turbulence.

5. The critical layer

One of the features of the theory of boundary-layer stability is that the phase velocity c_r of the laminar fluctuations is such that, for fluctuations which are 'subsonic' relative to the free stream,

$$1-(1/M_\infty) < (c_r/U_\infty) < 1,$$

so that for $M_\infty = 5{\cdot}8$ we have

$$0{\cdot}828 < (c_r/U_\infty) < 1.$$

The point in the boundary layer where c_r is equal to the local air velocity is called the critical point and the surface locus of these points over the flat plate is called the critical layer. In the present instance it was assumed that

$$c_r = 0{\cdot}9U_\infty = \text{constant},$$

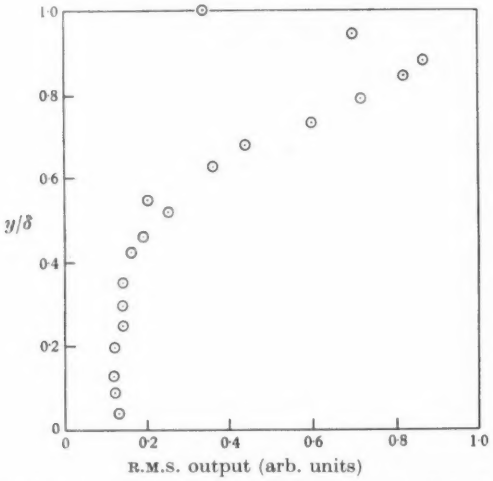

FIGURE 7. Variation, across the laminar boundary layer, of the hot-wire output integrated over all frequencies. $R_\theta \approx 1400$.

which implies a maximum probable error of less than 10 %. Using this approximation to c_r, we can now compute the fluctuation wavelengths to the same degree of accuracy with the aid of the relation

$$\alpha_\theta = \frac{2\pi\theta}{\lambda} = \frac{R_\theta}{c_r/U_\infty}\left(\frac{\beta_r \nu_\infty}{U_\infty^2}\right) = 1{\cdot}11R_\theta\left(\frac{\beta_r \nu_\infty}{U_\infty^2}\right),$$

where θ is the momentum thickness of the boundary layer. The result is shown on figure 8, with the theoretical computations for $M = 0$ and $M = 1{\cdot}3$ from Lees (1947) also shown for comparison. With the aid of figure 4 we also observe that the fluctuations receiving maximum amplification in the range from $R_\theta = 1000$ to 2000 have an α_θ of about 0·01. Since there is a difference of a factor of about 30 between θ and the boundary-layer thickness δ, the corresponding wavelengths are of the order of 20δ, or from 3 to 6 in.

The location of the critical layer was also discovered independently. Keeping the current constant, the hot wire was traversed across the boundary layer and

the change in the root-mean-square output, integrated over all frequencies was recorded. It was immediately noticed that the output increased rapidly as the wire approached the edge of the layer, came to a maximum at $y/\delta \doteqdot 0{\cdot}9$ and then decreased to some constant value in the free stream, as shown on figure 7. This energy concentration could not be explained on the basis of any assumed structural vibrations of the probe support or the plate model itself, and it was

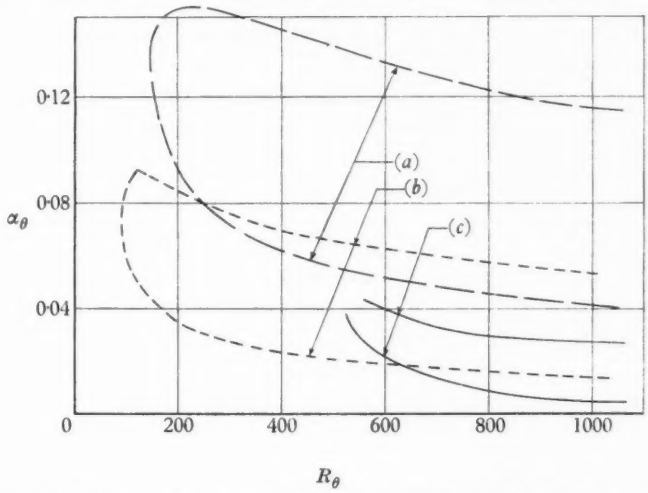

FIGURE 8. Wave-number α_θ *vs.* R_θ for neutral stability of the boundary layer. (*a*) $M \simeq 0$ (Blasius flow); (*b*) $M = 1{\cdot}3$ (Lees); (*c*) $M = 5{\cdot}8$ (present data).

concluded that it was due to the cumulative effect of the maximum in the amplitude distribution factor $q(y)$ of the various fluctuations, and therefore that the value of y/δ at which this prominence appeared gave the position of the critical layer.* From Korkegi (1954) we can further deduce that at $y/\delta = 0{\cdot}9$ the local flow velocity is about $0{\cdot}98U_\infty$, which is within the expected 10 % error in the assumption $c_r = 0{\cdot}9U_\infty$.

6. Conclusions

The laminar boundary layer growing over a flat plate at zero incidence in a hypersonic air stream has been investigated with the aid of a hot-wire anemometer. The main purpose of the investigation has been to see whether the hypersonic layer is hydrodynamically stable or unstable to small disturbances in the flow variables. The following results have been obtained:

1. For certain ranges of the flow conditions and the frequency of the small fluctuations the boundary layer is stable, while for all other ranges of the same parameters it is unstable, in a manner resembling the theoretically and experimentally ascertained stability of boundary-layer flows at lower speeds.

* Recent computations by E. Reshotko at this laboratory have shown that, at Mach numbers of the order of 5, a strong concentration of the temperature fluctuation amplitude $q(y)$ occurs at the critical layer. Since the hot wire is most sensitive to the temperature fluctuation at the edge of the layer, it is inferred that the peak of figure 7 is due mostly to temperature fluctuations and thus marks the location of the critical layer.

2. The amplication rates observed are much lower than those observed at low speeds. Similarly, the characteristic fluctuations selected by the laminar layer for maximum amplification have a broad band width and hence are more difficult to detect than those at the lower speeds.

3. The wavelengths of these characteristic fluctuations are at least one order of magnitude larger than the local boundary-layer thickness δ.

The author is indebted to Prof. Lester Lees for guidance and encouragement received throughout this work and to Dr John Laufer of the Jet Propulsion Laboratory, California Institute of Technology, whose advice and suggestions proved invaluable. The author also acknowledges with appreciation the assistance of the GALCIT staff and experimental shop, and the generous support of the Office, Chief of Ordnance, and the Office of Ordnance Research, U.S. Army.

REFERENCES

DEMETRIADES, A. 1958 An experimental investigation of the stability of the laminar hypersonic boundary layer. *GALCIT Hypersonic Research Project, Memorandum*, no. 43.

DUNN, D. W. & LIN, C. C. 1955 On the stability of the laminar boundary layer in a compressible fluid. *J. Aero. Sci.* **22**, no. 7, 455–77.

HEISENBERG, W. 1924 *Ann. Phys.* **74**, 577–627.

KORKEGI, R. H. 1954 Transition studies and skin friction measurements on an insulated flat plate at a hypersonic Mach number. *GALCIT Hypersonic Wind Tunnel Memorandum*, no. 17.

KOVASZNAY, L. S. G. 1954 Turbulence measurements. Article in Princeton Series *Handbook on High-Speed Aerodynamics and Jet Propulsion*, **9**, 213–76. New Jersey: Princeton.

LAUFER, J. & MCCLELLAN, R. 1953 Measurements of heat transfer from fine wires in supersonic flows. *External Publication, Jet Propulsion Laboratory*. California Institute of Technology, Pasadena, California, no. 315.

LAUFER, J. & VREBALOVICH, T. 1956 Experiments on the instability of a supersonic boundary-layer. *External Publication, Jet Propulsion Laboratory*. California Institute of Technology, Pasadena, California, no. 350.

LEES, L. & LIN, C. C. 1946 Investigations of the stability of the laminar boundary-layer in a compressible fluid. *NACA TN* 1115. Washington, D.C.

LEES, L. 1947 The stability of the laminar boundary layer in a compressible fluid. *NACA Report 876*. Washington, D.C.

LIEPMANN, H. W. 1943 Investigations on laminar boundary layer stability and transition on curved boundaries. *NACA ACR* no. 3H30. Washington, D.C.

MCMAHON, H. M. 1958 An experimental study of the effect of mass injection at the stagnation point of a blunt body. *GALCIT, Hypersonic Research Project, Memorandum*, no. 42.

MORKOVIN, M. V. 1956 Fluctuations and hot wire anemometry in compressible flows. *AGARDograph*, no. 24, *NATO, AGARD*.

RAYLEIGH, LORD *Scientific Papers*. Vol. 1, pp. 474–87 (1880); vol. 3, pp. 17–23 (1887); vol. 3, pp. 575–84 (1892); vol. 4, pp. 203–9 (1895); vol. 6, p. 917 (1913). Cambridge University Press.

RESHOTKO, E. 1959 (Private communication.)

SCHUBAUER, G. B. & SKRAMSTAD, H. K. 1948 Laminar boundary layer oscillations and transition on a flat plate. *NACA TR* 909, Washington, D.C.

TIETJENS, O. 1925 *Z. angew. Math. Mech.* **5**, 200–17.

TOLLMIEN, W. 1930 *Proceedings of the 3rd International Congress on Applied Mechanics. Stockholm*, vol. 1, pp. 105–8.

Measurements of the effect of molecular diffusivity in turbulent diffusion

By WILLIAM R. MICKELSEN

National Aeronautics and Space Administration, Lewis Research Center, Cleveland, Ohio, U.S.A.

(Received 2 June 1959)

Townsend (1954) has shown that turbulent vorticity may rotate and strain a diffusion wake, thereby increasing the contribution of molecular diffusion to the total mean dispersion over short diffusion times. To test whether any such effect occurs at longer diffusion times, the lateral dispersion of both helium and of carbon dioxide in air were measured downstream from a continuous point source in the turbulence produced by a grid in a wind tunnel. The data show that, for long diffusion times, accelerated molecular diffusion is negligible, so that molecular diffusion makes only an independent contribution to the total dispersion.

1. Introduction

The turbulent diffusion of quantities such as mass and heat can be characterized by the mean-square displacement of fluid particles from their original position as a function of time. Taylor (1922) has shown that the mean-square displacement $\overline{Y^2}$, in a given direction, and due to homogeneous turbulence is

$$\overline{Y^2} = 2\overline{v^2}\int_0^t\int_0^{t'} R\,dt'\,dt'', \tag{1}$$

where the Lagrangian correlation coefficient $\overline{v^2}R(t''-t_0) = \overline{v_0 v_{t''}}$ is an average of the product of the turbulent velocities of a fluid particle at time zero and at a later time t''. Experiment has shown that lateral concentration profiles downstream from a continuous point source are of Gaussian form (Batchelor & Townsend (1956) discuss some theoretical reasons for this), i.e.

$$C = C_0 \exp(-r^2/2D^2), \tag{2}$$

where C is the concentration at radius r from the diffusion wake centre, and C_0 is the concentration at the wake centre. The total mean lateral dispersion D^2 has often been assumed to be merely the sum of contributions due to the turbulent and molecular diffusion, in which case

$$D^2 = \overline{Y^2} + 2\alpha t, \tag{3}$$

where α is the molecular diffusion coefficient.

Townsend (1954) has shown that for short diffusion times

$$D^2 = \overline{Y^2} + 2\alpha t(1 + \tfrac{14}{15}\overline{\omega^2}t^2 + \text{higher order terms}), \tag{4}$$

where $\boldsymbol{\omega}$ is the vorticity of the turbulent motion, and the higher order terms constitute the rest of an alternating series of very complex terms which are negligible for small times. The difference between equations (3) and (4) arises from consideration of the rotation and strain of the instantaneous diffusion wake caused by the turbulent vorticity, which acts to increase the rate of molecular diffusion and thereby increases the lateral dispersion observed by concentration measurements. Townsend (1954), and Batchelor & Townsend (1956), have suggested that an effect such as that expressed by the terms in t^3, t^5, etc., in equation (4) might hold for longer diffusion times than those investigated by Townsend (1954); in that event, interpretation of diffusion experiments would be affected by the value of the molecular diffusivity. If the total dispersion is in fact influenced by interaction between molecular conduction and turbulent convection at large values of t, then many previous experiments (such as the experimental comparison of Eulerian and Lagrangian correlation coefficients by Mickelsen (1955)) would be in serious doubt.

As noted by Townsend (1954), equation (4) may be expressed in terms of the Prandtl or Schmidt numbers when applied to the decaying turbulent field downstream of grids; for, on neglecting the higher order terms, we have

$$\frac{D^2}{x_0 M} = \frac{\overline{Y^2}}{x_0 M} + \frac{2\alpha t}{x_0 M} + \frac{14}{15A}\frac{\alpha}{\nu}\left(\frac{x-x_0}{x_0}\right)^3\left(\frac{x_0}{x}\right)^2 \tag{5}$$

(in which the normalization is due to Batchelor (1952)), where x_0 is the distance from the virtual source of turbulence to the source of diffusion, $x-x_0$ is the distance downstream from the source of diffusion, M is the mesh length of the turbulence generating grid, A is approximately 135 for Townsend's (1954) turbulent field, and ν is the kinematic viscosity of air. From equation (5), it is evident that the value of the Prandtl number ν/α for the diffusion of heat in air, and of the Schmidt number ν/α for the diffusion of another gas in air, should markedly affect the total dispersion at the small values of t for which the relation (5) is a valid approximation. The present experiment was performed to test the suggestion that $D^2-2\alpha t$ would depend on ν/α at longer diffusion times than those investigated by Townsend (1954). The experiment essentially consisted of comparing the mean lateral dispersion D^2 of two gases of widely different molecular diffusivities, and hence Schmidt numbers, in the same flowing turbulent field previously used by Townsend (1954).

2. The experiment

The experiment was carried out in the wind tunnel in the Cavendish Laboratory in which Townsend (1954) originally observed the accelerated molecular diffusion of heat downstream from a line source. The wind tunnel, injector, and sampling apparatus of the present experiment are shown in figure 1. Helium and carbon dioxide were used for the diffusing gas because of (*a*) the wide difference in their molecular diffusivities (for helium $\alpha = 0{\cdot}725\,\mathrm{cm^2/s}$; for carbon dioxide $\alpha = 0{\cdot}167\,\mathrm{cm^2/s}$; both at 80 °F and 1 atm.), and (*b*) the convenience in measuring their concentrations with the katharometer (thermal conductivity bridge). The gas was injected into the turbulent air stream through a small tube of 0·8 mm

outside diameter (2 mm for the large mesh grid data), as shown in figure 1. Helium was always injected at stream velocity, but it was necessary to inject the carbon dioxide at four or five times the stream velocity in order to obtain concentrations high enough for accurate measurement. Several concentration profiles were measured at $(x-x_0)/x_0 = 0{\cdot}1$, with the high injection velocity, and with injection at stream velocity. The negligible difference in these profiles indicated that the injector, even with the high injection velocity used for carbon dioxide, was closely simulating a point source.

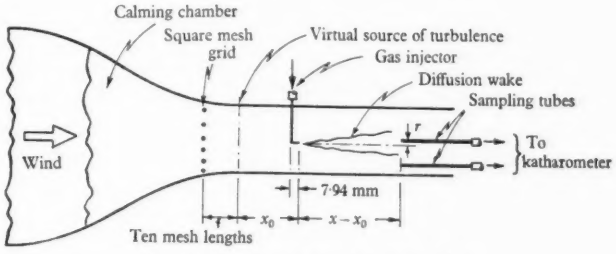

FIGURE 1. Experimental apparatus.

Concentrations of gas downstream from the injector were measured by continuously drawing samples through the katharometer from both the diffusion wake and from the pure air outside the wake. The sampling tubes were 0·6 mm inside diameter, and the sampling rate was at stream velocity. The concentration profiles were found to be as in equation (2), which enabled the mean dispersion D^2 to be determined graphically.

3. Results

Concentration measurements were made at a number of axial stations downstream from the injector, using two widely different grid meshes at a fixed wind speed of 640 cm/sec. The total contribution $D^2-2\alpha t$ to the dispersion due directly and indirectly to the turbulence was determined from these data, and is shown in figure 2. The dispersion and axial distance have been normalized as in (5) to account for the decrease in turbulence intensity and increase in turbulence scale with distance downstream. Estimates indicated that the turbulent wake from the cylindrical injector was small compared with the turbulence generated by the grid, and this is borne out by the good agreement between the gas diffusion data and Townsend's (1954) data for diffusion of heat from a line source which was small enough to leave no wake.

To indicate what trends would be expected if accelerated molecular diffusion were appreciable, values of $(D^2-2\alpha t)/x_0 M$ for helium, carbon dioxide, and heat were calculated from (5) (which is of course valid only for small t), and are shown as dashed lines in figure 2. These calculations were made by using Townsend's (1954) value for turbulence intensity at $(x-x_0)/x_0 = 0{\cdot}1$, and by assuming that Townsend's data for longer diffusion times (shown by the solid line) represented the turbulent mean-square displacement $\overline{Y^2}/x_0 M$.

It is evident from figure 2 that, at least within experimental error, equation (3) adequately describes the total dispersion for the diffusion times and turbulent field used in the present experiment and that accelerated molecular diffusion does not make a significant contribution. Whether these results may be generalized to all situations is still open to some question which might be answered by further

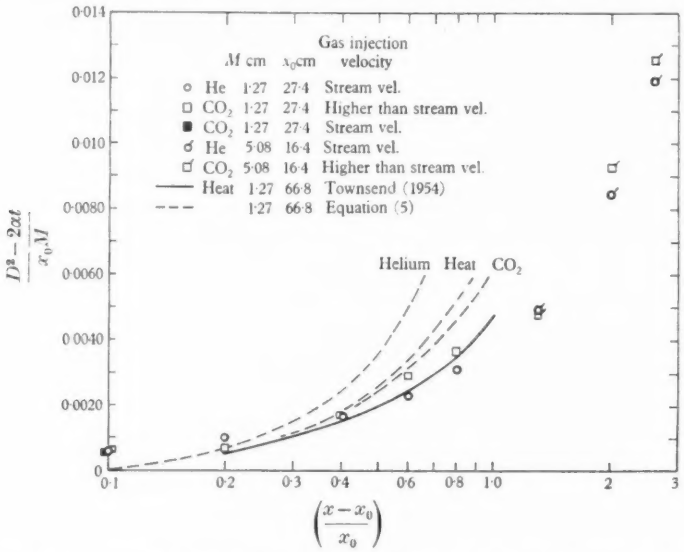

FIGURE 2. Comparison of turbulent dispersion of helium and carbon dioxide.

experiment. It is possible that Townsend's accelerated molecular diffusion does not obtain in cases where the diffusion wake has been sufficiently broken up, as it is when the diffusion time is large.

This work was carried out in the Cavendish Laboratory, University of Cambridge, during study under a Rockefeller Public Service Award.

The author is greatly indebted to the counsel of Dr A. A. Townsend and Dr G. K. Batchelor before and during the course of the experiment. The Cambridge Instrument Company was most helpful in the loan of the katharometer.

REFERENCES

BATCHELOR, G. K. 1952 *Proc. Camb. Phil. Soc.* **48**, 345.

BATCHELOR, G. K. & TOWNSEND, A. A. 1956 Article in *Surveys in Mechanics*, p. 352. Cambridge University Press.

MICKELSEN, W. R. 1955 *Nat. Adv. Comm. Aero. Tech. Note* 3570.

TAYLOR, G. I. 1922 *Proc. Lond. Math. Soc.* (2), **20**, 196.

TOWNSEND, A. A. 1954 *Proc. Roy. Soc.* A, **224**, 487.

An empirical torque relation for supercritical flow between rotating cylinders

By R. J. DONNELLY AND N. J. SIMON
Institute for the Study of Metals and Department of Physics,
The University of Chicago, Chicago, Illinois

(Received 16 July 1959)

An empirical relationship for the torque transmitted by fluid friction to an outer cylinder as a function of the angular velocity of the inner cylinder has been obtained by analysis of experimental data published by Wendt, Taylor and Donnelly. With one exception it is found that the torque G has the functional form

$$G = a\Omega_1^{-1} + b\Omega_1^{1\cdot36},$$

where Ω_1 is the angular velocity of the inner cylinder and a and b are constants determined from the data. The formula applies to a range of values of Ω_1 above the onset of instability extending to about 10 times the critical angular velocity. The experiments also show that the finite amplitude analysis recently advanced by Stuart gives the correct variation of torque over a short range above the critical speed. At speeds well beyond critical it is found that G varies approximately as $\Omega_1^{1\cdot5}$, and that the variation of torque with gap width can be expressed as a simple power law with exponent about 0·31. In an appendix Dr G. K. Batchelor shows that these latter relations are consistent with the supposition that the flow is steady and consists of inviscid cores surrounded by boundary layers.

1. Introduction

The study of the flow of a viscous liquid between rotating cylinders has been a very important and fruitful area of investigation in fluid mechanics. Linear stability theory has had its greatest success in the prediction of the onset of instability in this geometry. It is natural, therefore, to try to obtain a description of the unstable flow as a means of studying the transition to turbulence.

Experimentally, two techniques commonly used are the observation of dye traces in the fluid and the measurement of the torque transmitted to one cylinder as a function of the angular velocity of the other. The first of these is well suited to the observation of flow patterns up to the onset of instability, but is of less value as the motions of the fluid become more rapid and complicated. Suspensions of fine particles such as aluminium pigment (cf. Schultz-Grunow & Hein 1956) overcome some of the difficulties. The torque method, while applied so far only to the case where one cylinder is at rest, has the advantage that the results can be compared quantitatively with theory.

Recently Stuart (1958) has advanced an analysis which enabled him to calculate the relationship between the torque on the outer cylinder and the angular

velocity of the inner cylinder, if the two cylinders have nearly equal radii. He has compared his results with measurements by Taylor (1936). Since increasing attention is being given to finite amplitude problems, we have analyzed all the available published torque measurements of this kind in order to provide a basis for comparison with theory. The results may also provide some guide as to the selection of suitable assumptions for calculations.

2. Theoretical relations

When the flow is laminar the torque G transmitted to the outer cylinder as a function of the rate of rotation of the inner cylinder Ω_1 is

$$G = \frac{4\pi\eta R_1^2 R_2^2 h \Omega_1}{R_2^2 - R_1^2}. \tag{1}$$

Here η is the viscosity of the fluid, R_1 and R_2 are the radii of the cylinders ($R_2 > R_1$) and h is the length of the outer cylinder. Equation (1) is exact and forms the basis for the absolute determination of viscosity. At speeds near the onset of instability, small deviations from (1) possibly due to the finite length of the cylinders or incorrect alignment may be observed (Donnelly 1958).

The validity of (1) is limited by the onset of instability in the laminar flow with formation of vortices as described first by Taylor (1923). The value of Ω_1 at which instability begins, which we shall call Ω_c, is calculated from the critical Taylor number. For the case of a 'narrow gap' the Taylor number (Chandrasekhar 1954) is defined as

$$T = \frac{4R_1^2 d^4}{R_2^2 - R_1^2}\left(\frac{\Omega_1}{\nu}\right)^2 \quad (d \ll r_0), \tag{2}$$

where

$$d = R_2 - R_1, \tag{3}$$

$$r_0 = \tfrac{1}{2}(R_1 + R_2), \tag{4}$$

$\nu\,(=\eta/\rho)$ is the kinematic viscosity of the liquid and ρ is the density. The critical Taylor number here is

$$T_c = 3{\cdot}390 \times 10^3. \tag{5}$$

It should be emphasized that in all these formulae we assume that the outer cylinder is at rest. Another approximation, used by Stuart in the calculations quoted below, is

$$T = R_1 d^3 (\Omega_1/\nu)^2, \tag{6}$$

$$T_c = 1{\cdot}708 \times 10^3. \tag{7}$$

In the limit $d \to 0$ the expressions (2) and (6) are identical (except for a factor 2) and the values of Ω_c calculated from the critical numbers are very close.

When the gap between cylinders is finite a different analysis of the stability problem is required (Chandrasekhar 1958). Numerical calculations have been given only for the case of $R_1/R_2 = \frac{1}{2}$. Here the appropriate Taylor number is

$$T = \tfrac{64}{9} R_1^4 \left(\frac{\Omega_1}{\nu}\right)^2 \quad (R_1/R_2 = \tfrac{1}{2}) \tag{8}$$

and

$$T_c = 3{\cdot}310 \times 10^4. \tag{9}$$

A calculation of the torque for values of Ω beyond Ω_c has been made by Stuart (1958) on the basis of a finite amplitude theory. His result may be written

$$G = 2\pi R_1^2 h\eta \left|\frac{\partial \bar{v}}{\partial r}\right|_{r=R_1}, \tag{10}$$

where

$$\left|\frac{\partial \bar{v}}{\partial r}\right|_{r=R_1} = \frac{\Omega_1 r_0}{d}\left[1+\mathscr{D}\left(1-\frac{T_c}{T}\right)\right] \quad (d \ll r_0,\ T-T_c \to 0). \tag{11}$$

T and T_c are given in (6) and (7) and $\mathscr{D}$ is a constant which follows from the formulae given on p. 18 of Stuart's paper. In the notation of that paper

$$\mathscr{D} = \left\{\int_{-\frac{1}{2}}^{\frac{1}{2}} Z^2 d\zeta \left(\int_{-\frac{1}{2}}^{\frac{1}{2}} Z\, d\zeta\right)^{-2} - 1\right\}^{-1} = 1{\cdot}4472. \tag{12}$$

For purposes of comparison with experiment we may rewrite (10) and (11) in the form

$$G = a\Omega_1^{-1} + b\Omega_1 \quad (\Omega_1 > \Omega_c), \tag{13}$$

where

$$a = -(2\pi R_1 h\eta r_0 \nu^2)(\mathscr{D}T_c)/d^4 \tag{14}$$

and

$$b = (2\pi R_1^2 h\eta r_0)(1+\mathscr{D})/d. \tag{15}$$

As suggested by (11), Stuart's analysis is valid for the 'narrow gap' geometry and is not expected to hold for values of T much above T_c.

From dimensional considerations one can see that the general expression for the torque must be of the form

$$G/\rho h\Omega_1^2 R_1^4 \propto f(R, d/R_1) \tag{16}$$

provided only the inner cylinder rotates. Here the Reynolds number is defined as

$$R = \Omega_1 R_1 d/\nu. \tag{17}$$

Dr G. K. Batchelor shows in an appendix to this paper that a prediction for the form of the function f can be made for speeds well above critical using the 'inviscid-core-and-boundary-layer' model of the flow (Batchelor 1956). The result of such an argument leads to

$$G/\rho h\Omega_1^2 R_1^4 \propto R^{-\frac{1}{2}}(d/R_1)^{\frac{1}{4}}. \tag{18}$$

In §§3–5 we shall discuss the variation of torque with angular velocity. In §6 we shall consider the evidence for the variation of torque with gap width at high speeds.

3. Reduction of the data

Torque measurements of the type we are discussing have been reported by Wendt (1933), Taylor (1936) and Donnelly (1958). Since the first two authors did not publish tables of measurements, we have photographed and enlarged the graphs and taken the data from them with calipers. Due to mechanical limitations of the apparatus several fluids must be used to determine a complete (G, Ω_1)-curve. Dynamical similarity requires that for any given pair of radii $G/\rho\Omega_1^2$ must be a function of Ω_1/ν. It is customary to calculate these quantities (or equivalent dimensionless parameters) for each fluid and combine them on a single curve.

On such a graph the laminar flow line starts at the upper left and extends to the lower right. The data leave this line at the critical speed (see figure 1).

For theoretical purposes the different fluids are of little interest, so that the empirical relations below have been quoted for the fluid of greatest viscosity. From the discussion above we see that if two fluids are measured at the same value of Ω_1/ν in the same apparatus, the same value of $G/\rho\Omega_1^2$ is obtained. We can then convert the torque data from liquid 2 to the equivalent for liquid 1 by the relation

$$G_1 = \left(\frac{\rho_1 \nu_1^2}{\rho_2 \nu_2^2}\right) G_2. \tag{19}$$

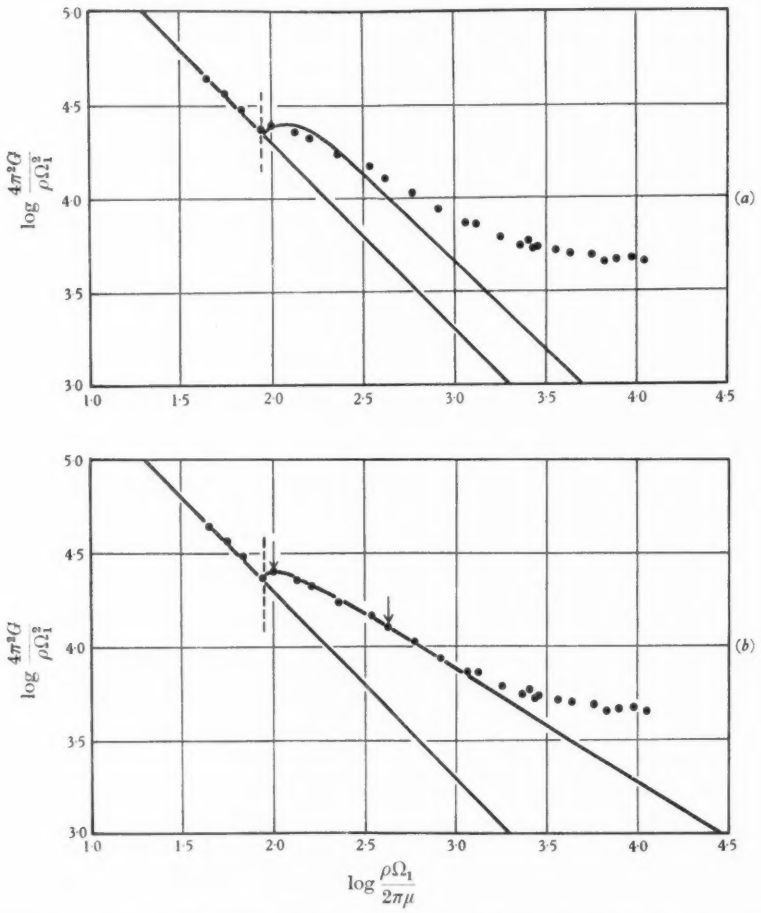

FIGURE 1. (*a*) After Taylor (1936, Fig. 2). $R_2 = 4{\cdot}05$ cm, $R_1 = 3{\cdot}94$ cm, $\nu = 0{\cdot}131$, $\rho = 1{\cdot}171$. The dashed line corresponds to the calculated value of Ω_c. The solid line corresponds to $G = -3{\cdot}71 \times 10^8 \Omega_1^{-1} + 1{\cdot}12 \times 10^5 \Omega_1$, calculated from Stuart's formula. (*b*) Data as in (*a*). The solid line corresponds to $G = -1{\cdot}21 \times 10^8\ \Omega_1^{-1} + 1{\cdot}59 \times 10^4\ \Omega_1^{1{\cdot}36}$, fitted empirically.

The notation and constants of the experiments are listed below.

(*a*) *Measurements of Taylor*

G = measured torque in g cm^2 sec^{-2};
ρ = density of fluid in g/cm^3 = 1·171 g/cm^3;
ν = 0·131 cm^2/sec;
h = 84·4 cm.

Taylor made measurements with R_2 = 4·05 cm and inner cylinders of the following sizes:

R_1 = 3·94 (figure 1), 3·89 (figure 2), 3·83, 3·74, 3·68, 3·59, 3·45 and 3·20 cm.

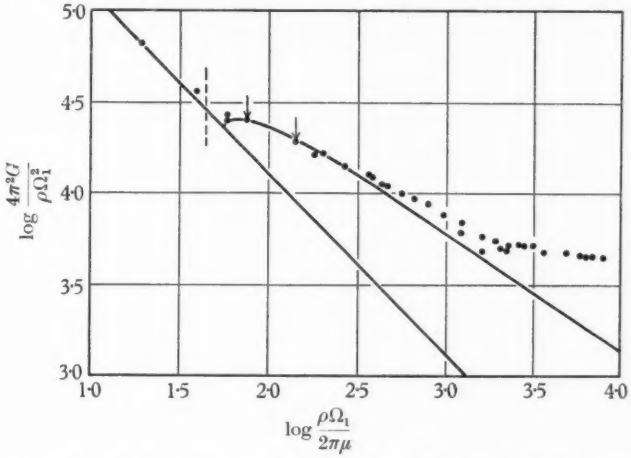

FIGURE 2. After Taylor (1936, Fig. 3). R_1 = 3·89 cm, R_2 = 4·05 cm, ν = 0·131, ρ = 1·171. The curve corresponds to $G = -4{\cdot}41 \times 10^7\, \Omega_1^{-1} + 1{\cdot}28 \times 10^4\, \Omega_1^{1{\cdot}36}$.

(*b*) *Measurements of Wendt*

R_2 = 14·70 cm;
R_1 = 13·75 cm (figure 3), 12·50 cm (figure 4), 10·00 cm (figure 5);
$\lambda = \tau_i/\frac{1}{2}\rho\Omega_1^2 R_1^2 = G/\pi h\rho\Omega_1^2 R_1^4$, where τ_i is the stress on the inner cylinder.

As Wendt did not list the viscosity of his liquids, which were pure water and glycerine–water solutions, we have reduced his data by defining

$$\mathrm{T} = \tau_i/\tfrac{1}{2}\rho\nu^2, \quad U = \Omega_1 R_1/\nu, \tag{20}$$

so that $\lambda = \mathrm{T}/U^2$. Thus T is proportional to the torque and U is proportional to Ω_1 (for constant ν, R_1 and R_2).

(*c*) *Measurements of Donnelly*

G = torque in dyne cm;
$h = 4{\cdot}998 \pm 0{\cdot}0003$ cm;
$R_2 = 2{\cdot}00023 \pm 0{\cdot}0001$ cm;
$R_1 = 1{\cdot}89936 \pm 0{\cdot}0001$ cm in figures 6 and 7,
$= 0{\cdot}99963 \pm 0{\cdot}0001$ cm in figures 8 and 9;

$\nu = 5{\cdot}796 \times 10^{-3}$ in figures 6 and 7,
$= 1{\cdot}226 \times 10^{-1}$ in figures 8 and 9;
$\rho = 1{\cdot}585\,\mathrm{g/cm^3}$ in figures 6 and 7,
$= 0{\cdot}8404\,\mathrm{g/cm^3}$ in figures 8 and 9.

The original data are presented in tables 1 and 2. G is given as a function of the Reynolds number R and (19) has been used to convert all the data to the equivalent torque for the liquid of greatest kinematic viscosity.

G (dyne cm)	R	G (dyne cm)	R	G (dyne cm)	R
13·0	20·8	108	174	292	297
14·2	22·9	113	181	328	318
16·3	26·3	116	183	382	346
18·5	30·0	120	185	547	431
21·5	34·7	124	188	597	452
25·9	41·6	127	189	633	470
32·2	51·9	130	190	641	482
43·0	69·2	134	192	755	549
64·5	104	140	195	786	568
72·1	116	147	200	924	634
76·2	122	151	204	1090	710
80·8	129	160	210	1330	825
82·2	138	173	219	1580	920
92·9	149	183	231	1858	1026
100	160	220	254	2209	1165
104	167	256	276		

TABLE 1. Torque measurements as a function of Reynolds number ($R_1 = 1{\cdot}9$ cm, $R_2 = 2{\cdot}0$ cm, $h = 5{\cdot}0$ cm, $\nu = 5{\cdot}796 \times 10^{-3}$ cm²/sec, $\rho = 1{\cdot}585$ g/cm³, $R = \Omega_1 R_1 d/\nu$)

G (dyne cm)	R	G (dyne cm)	R	G (dyne cm)	R
10·8	10·2	70·4	65·5	180	121
12·1	11·4	71·4	66·6	198	127
13·6	12·8	72·5	67·4	240	149
15·5	14·6	72·9	67·8	283	167
18·1	17·1	73·6	68·2	345	192
21·8	20·5	74·9	69·1	808	360
27·2	25·6	76·7	70·2	1430	541
36·2	34·1	82·0	73·0	1710	619
45·4	42·7	86·5	75·3	2150	722
54·5	51·1	93·4	78·8	2680	867
57·4	53·9	106	85·1	2830	901
60·6	56·9	116	92·7	3690	1050
64·0	60·1	126	94·8	5450	1440
68·3	63·9	146	107	8990	2040

TABLE 2. Torque measurements as a function of Reynolds number ($R_1 = 1{\cdot}0$ cm, $R_2 = 2{\cdot}0$ cm, $h = 5{\cdot}0$ cm, $\nu = 0{\cdot}1226$ cm²/sec, $\rho = 0{\cdot}8404$ g/cm³, $R = \Omega_1 R_1 d/\nu = \Omega_1 R_1^2/\nu$)

4. The variation of torque with angular velocity

From the discussion in §2 we see that the torque can be computed by (1) up to a known Ω_c. Above Ω_c, Stuart's equation (13) can be used. A comparison of (13) with Taylor's data is shown in figure 1*a*. From (14) and (15) and the dimensions in §3 we find

$$a = -3{\cdot}71 \times 10^8, \quad b = 1{\cdot}12 \times 10^5.$$

The fit as $T - T_c \to 0$ is quite accurate, the dominant term being that in Ω_1^{-1}. This is the expected range of validity of the theory. At higher speeds (13) is dominated by the linear term and the curve becomes parallel to the laminar flow line. A comparison with data of Donnelly may be seen in figure 7.

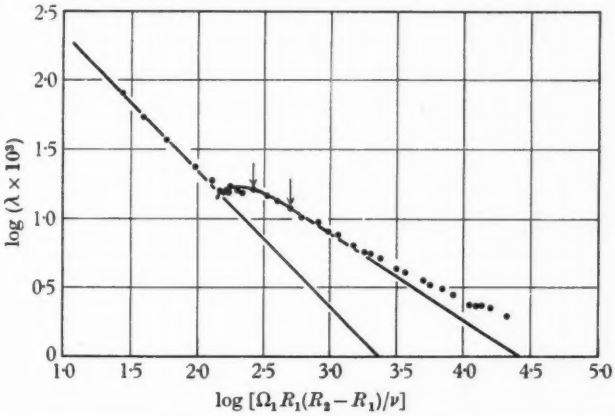

FIGURE 3. After Wendt (1933, Abb. 13). $R_1 = 13{\cdot}75$ cm, $R_2 = 14{\cdot}70$ cm. The curve corresponds to $T = -4{\cdot}46 \times 10^4 U^{-1} + 0{\cdot}650 U^{1{\cdot}36}$.

An examination of figure 1*a* shows that the data for $\Omega \gg \Omega_c$ follow a straight line, but with a higher power of Ω_1. Figure 1*b* shows the result of assuming that the torque relation has the form

$$G = a\Omega_1^{-1} + b\Omega_1^n \quad (\Omega > \Omega_c), \tag{21}$$

with $n = 1{\cdot}36$. The constants a and b have been determined by the points marked with arrows. It can be seen that (21) fits the data within experimental error in the range $1{\cdot}9 < \log(\rho\Omega_1/2\pi\mu) < 3{\cdot}1$, or over a factor of 16 above Ω_c. Since $T \propto \Omega_1^2$, this corresponds to agreement over a range of about $256T_c$. The value of n in (21) appears to be the same for all the experiments, as will be shown below. Therefore we will use the form

$$G = a\Omega_1^{-1} + b\Omega_1^{1{\cdot}36} \quad (\Omega_1 > \Omega_c) \tag{22}$$

for all the data.

A second measurement by Taylor is shown in figure 2. The solid line is calculated from (22) and the marked points. It holds within experimental error over the range $1{\cdot}75 < \log\rho\Omega_1/2\pi\mu < 2{\cdot}5$, or up to values of Ω near $6\Omega_c$. The deviation at $\log(\rho\Omega_1/2\pi\mu) = 3{\cdot}0$ amounts to 20 %.

The data of Wendt are shown in figures 3–5. As explained in §3 we have used T and U instead of G and Ω_1 in (22). The solid line represents the data in figure 3 over the range $2{\cdot}2 < \log R < 3{\cdot}3$, or up to values of Ω near $13\Omega_c$. The deviation at $\log R = 4{\cdot}0$ is 35 % from the empirical curve.

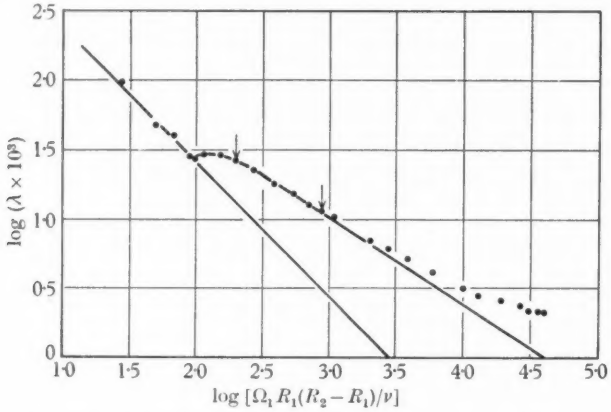

FIGURE 4. After Wendt (1933, Abb. 13). $R_1 = 12{\cdot}50$ cm, $R_2 = 14{\cdot}70$ cm. The curve corresponds to $\mathrm{T} = -1{\cdot}60 \times 10^3 U^{-1} + 0{\cdot}506 U^{1{\cdot}36}$.

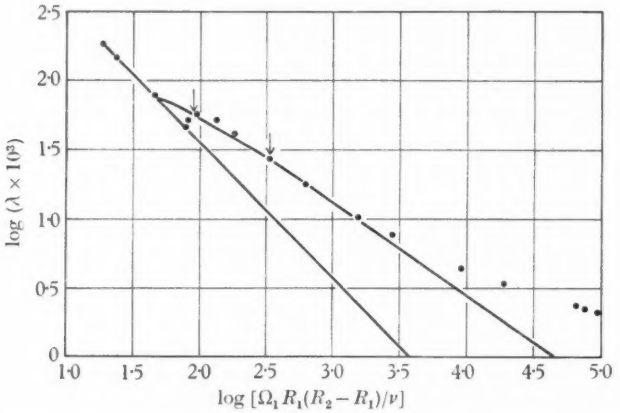

FIGURE 5. After Wendt (1933, Abb. 13). $R_1 = 10{\cdot}00$ cm, $R_2 = 14{\cdot}70$ cm. The form given by (22) will not represent this data accurately. The curve shown is

$$\mathrm{T} = -15U^{-1} + 0{\cdot}387U^{1{\cdot}36}.$$

In figure 4 the empirical curve fits over even a wider range: $2{\cdot}0 < \log R < 3{\cdot}3$, or up to $\Omega = 20\Omega_c$. The deviation at $\log R = 4{\cdot}0$ is 35% from the solid line.

The relation (22) is less successful for Wendt's widest gap arrangement, shown in figure 5. The curve may be made to fit either the beginning portion or the straight line portion of the measurements (as shown), but not both. There is a possibility that (22) breaks down for wide gap geometries. However, a comparison

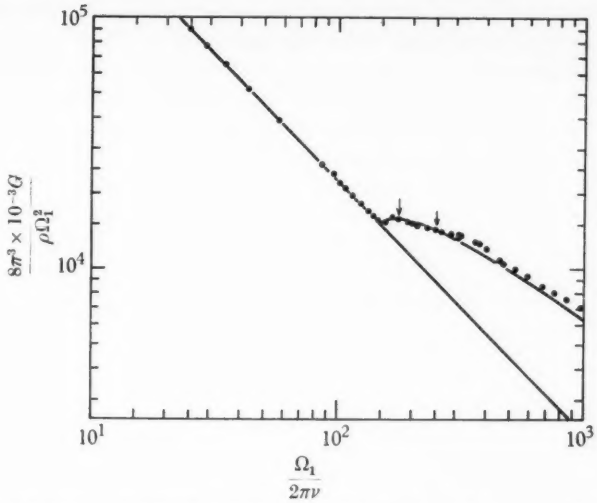

FIGURE 6. After Donnelly (1958, Fig. 5). $R_1 = 1{\cdot}9$ cm, $R_2 = 2{\cdot}0$ cm, $\nu = 5{\cdot}796 \times 10^{-3}$, $\rho = 1{\cdot}585$. The curve corresponds to $G = -254\,\Omega_1^{-1} + 16{\cdot}0\,\Omega_1^{1{\cdot}36}$.

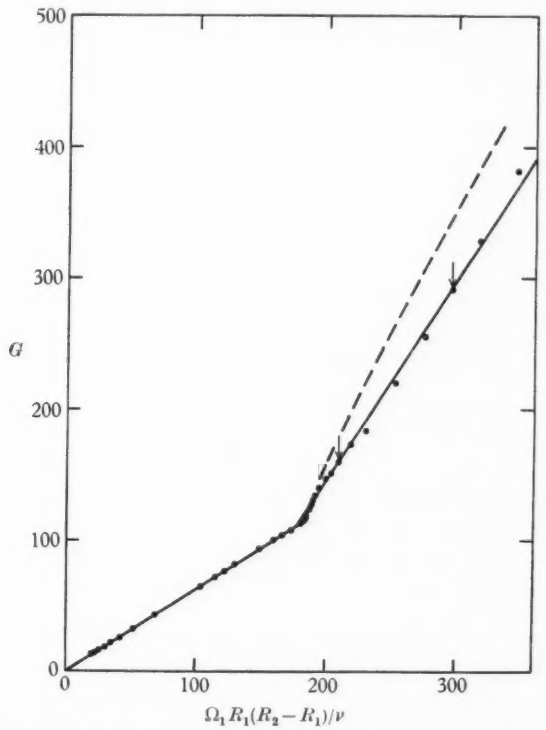

FIGURE 7. Plot of torque as a function of Reynolds number of the data in figure 6 and table 1. The dashed line corresponds to $G = -857\,\Omega_1^{-1} + 49{\cdot}2\,\Omega_1$, calculated from Stuart's formula.

of figures 6 and 8 which represent narrow and wide gap measurements shows that both follow (22).

The measurements of Donnelly are shown in figure 6 for the case $R_1 = 1{\cdot}9$ cm, $R_2 = 2{\cdot}0$ cm. The solid line is seen to fit the data fairly closely over the whole range, or to $7\Omega_c$. The detailed nature of the observations seem to indicate reproducible features which are not followed by the curve. In order to illustrate more clearly the nature of these deviations a linear plot of the original data near $\Omega = \Omega_c$, taken from table 1, is shown in figure 7. One can seen that the deviations from the curve are less than 3% in this range. It should be noticed that Wendt's data in figure 3 also show such deviations near Ω_c in a similar case: $d = 0{\cdot}0667\, r_0$ for figure 3 and $d = 0{\cdot}0513\, r_0$ for figures 6 and 7.

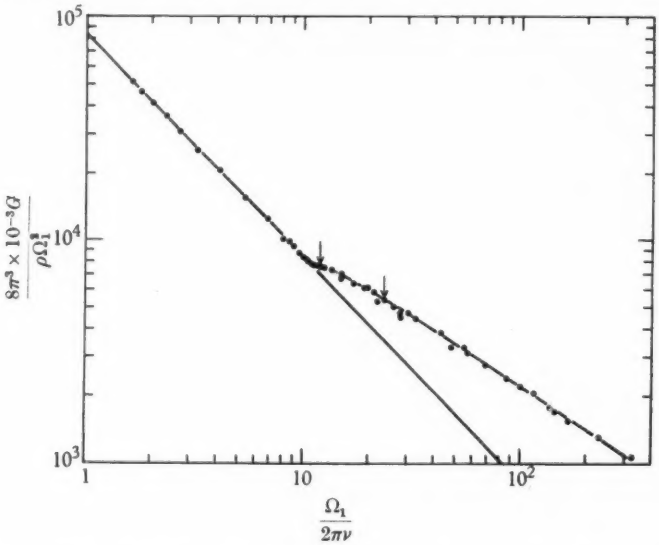

FIGURE 8. After Donnelly (1958, Fig. 8). $R_1 = 1{\cdot}0$ cm, $R_2 = 2{\cdot}0$ cm, $\nu = 0{\cdot}1226$, $\rho = 0{\cdot}8404$. The curve shown is $G = -104\,\Omega_1^{-1} + 4{\cdot}70\,\Omega_1^{1{\cdot}364}$.

We have calculated Stuart's torque relation (13) for this case and find

$$a = -857, \quad b = 49{\cdot}2.$$

This is plotted as a dashed line in figure 7. The calculated curve agrees with experiment very closely near the critical value (which is its intended range). The experimental critical point agrees with that calculated from (2) and (5) or (6) and (7) within 1%. At $\Omega_1 R_1 d/\nu = 300$ the calculated torque is about 20% too high.

Figure 8 shows measurements for the case $R_1 = 1{\cdot}0$ cm, $R_2 = 2{\cdot}0$ cm. Here (22) appears to represent the data within experimental error over the entire range of measurements, i.e. to $30\,\Omega_c$ or $900\,T_c$. The experimental data are given in table 2, and the fit near Ω_c is displayed on a linear scale in figure 9. The experimental value of Ω_c agrees with the value calculated from (8) and (9) to within $\frac{1}{2}$%.

We have made some studies to determine the experimental limits of the exponent n in (21). Wendt has suggested $n = 1{\cdot}5$ in his paper (cf. §6). We have tried several curves with $n = 1{\cdot}5$ and conclude that this represents the upper limit of the exponent for a close representation of the data in the range of interest here. The value $n = 1{\cdot}36$, which was determined from figure 8, appears to be the best compromise for all the measurements illustrated here, and at the same time

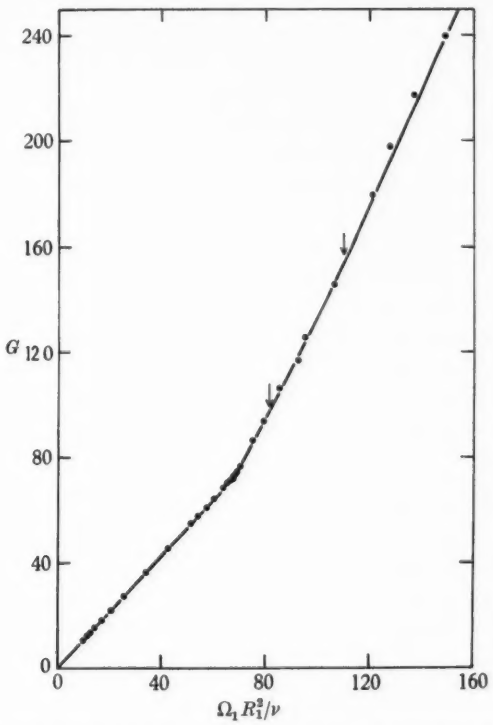

FIGURE 9. Plot of torque as a function of Reynolds number of the data in figure 8 and table 2.

Author	Figure	Range of approximation		Deviation from data	
Taylor	1*b*	$16 \times \Omega_c$	$256 \times T_c$	40 % at	$40 \times \Omega_c$
	2	6	36	20	18
Wendt	3	13	169	35	64
	4	20	400	35	100
	5	Fails	—	—	—
Donnelly	6	7*	49	8	7
	8	30	900	0	30

* Total range measured. Data deviates on both sides of curve: see §4.

TABLE 3. Range of validity of the empirical relation (22)

to be very near the lower limit of n. We may say that the experiments give $\frac{4}{3} < n < \frac{3}{2}$ with the smaller value somewhat closer to the best compromise. The range of validity is summarized in table 3.

5. Discussion

The experiments shown in figures 1*a* and 7 confirm the validity of the torque relation (13) given by Stuart over its intended range: $T \to T_c$ from above and $d \ll r_0$. The mechanism proposed by Stuart accounts for the general variation of torque even though detailed numerical agreement is limited to a short range above the critical Taylor number. The experimental evidence suggests that a relation of the form given in (22), which is a modification of Stuart's calculated equation, is suitable over quite a wide range of conditions. The fact that the exponent 1·36 in (22) is found to be almost independent of the gap width suggests that an understanding of the limiting case $d \to 0$ should be relevant to the more general problem.

Landau (1944) has advanced the interesting suggestion that instability may lead to a stable secondary flow, which after a certain increase in velocity would become unstable in turn and be replaced by a still more complex flow. This would continue until eventually the flow is sufficiently disordered as to be considered turbulent. The torque measurements do not appear to show any significant departure from (22) until $T \geqslant 100\,T_c$ and then the points leave the empirical curve fairly slowly. Nothing appears to be as clearly marked as the first instability (cf. Donnelly 1958, Figs. 4, 7). On the other hand, the torques are averaged over considerable fluctuations in the range above Ω_c, which makes it difficult to measure with the precision which one can obtain below Ω_c. Torque measurements alone are not likely to be sufficient to explore the transition to turbulence. Schultz-Grunow and Hein have compared their finite amplitude experiments with Wendt's torque data. They show that at certain Reynolds numbers the regular cells which form after instability begins are perturbed by tangential waves and eventually change their spacing. These details can be correlated with details in the torque measurements.

We have explored the range above Ω_c in figure 8 (which is quite regular) with a visual technique similar to that of Schultz-Grunow and Hein, as well as with ink traces. The wide gap apparatus of Donnelly & Fultz (1960) was used. Here we find that the cell spacing continues to be regular up to speeds corresponding to the limit of measurements in figure 8. The motions in the cells, however, show features which would have to be reported in more detail than can be done at present (see Donnelly & Fultz 1960).

6. The variation of torque with gap width

The variation of G with gap width is, of course, completely specified for laminar flow by (1). The dependence of G upon gap width just above Ω_c is not immediately clear, but for higher values of Ω_1 appears to show significant regularities. For purposes of analysis we might assume, following (16), that the form for G is

$$G/\rho h \Omega_1^2 R_1^4 \propto R^{-l}(d/R_1)^m. \tag{23}$$

From (17), (21), (22) and (23) we see that $l = 2 - n \doteqdot 0{\cdot}64$.

If we plot $\log(G/\rho h\Omega_1^2 R_1^4)$ as a function of $\log R$ and if the proportionality constant in (23) is independent of geometry, then curves corresponding to different values of d/R_1 will be equally spaced for all values of R (provided we avoid the region near Ω_c). A particularly striking example of this is given by the measurements

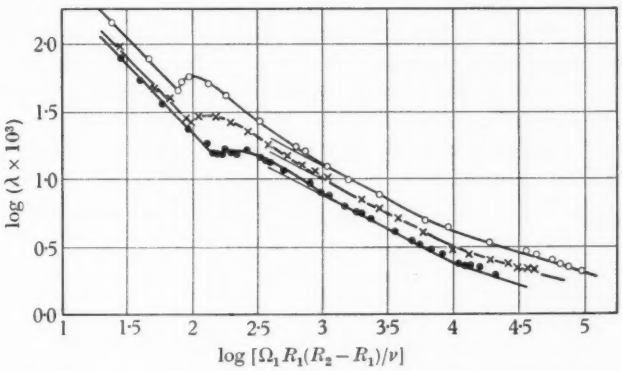

FIGURE 10. Reproduction of Abb. 13 of Wendt's paper. The solid lines represent the empirical equations (24) given by Wendt (1933). $R_2 - R_1$: ○, 4·70 cm; ×, 2·20 cm; ●, 0·95 cm.

of Wendt shown in figure 10. Wendt has drawn the straight lines according to the empirical formulae

$$\lambda = 0{\cdot}46\left[\frac{(R_2-R_1)R_2}{R_1^2}\right]^{\frac{1}{4}} R^{-0{\cdot}5} \quad (4\times10^2 < R < 10^4), \tag{24a}$$

$$\lambda = 0{\cdot}073\left[\frac{(R_2-R_1)R_2}{R_1^2}\right]^{\frac{1}{4}} R^{-0{\cdot}3} \quad (R > 10^4). \tag{24b}$$

We see that (24*a*) implies a variation of torque with Reynolds number similar to what we have proposed in § 4 for $\Omega \gg \Omega_c$ (i.e. $n = 1{\cdot}5$ in (21)). From an inspection of figures 2–5 it can be seen that $n = 1{\cdot}5$ ($l = 0{\cdot}5$) is probably a better choice in this high speed region than $n = 1{\cdot}36$ which was chosen for the best fit closer to Ω_c. This, of course, is the sort of limitation one expects in a purely empirical analysis. It is also interesting to notice from figure 10 and equation 24*b* that the curves are still approximately equally spaced after the bend in the torque curves at $R = 10^4$.

The value of m can be determined from measurements on figure 10 by measuring the distance between any two curves, denoted a and b.

$$\log\lambda_b - \log\lambda_a = m\log[(d/R_1)_b/(d/R_1)_a]. \tag{25}$$

We can also follow Wendt's suggestion given in (24) that dR_2/R_1^2 is the correct parameter and define m' from

$$\log\lambda_b - \log\lambda_a = m'\log[(dR_2/R_1^2)_b/(dR_2/R_1^2)]. \tag{26}$$

Results of such calculations are shown in table 4. They show that for $\log R > 3{\cdot}0$ the values of m (or m') are roughly constant, and that m is not very sensitive to a change in comparison between sets of curves with a ratio $(d/R_1)_b/(d/R_1)_a$ of 2·55 to 6·80.

The measurements by Donnelly can be used again for a comparison between large and small gap widths: $(d/R_1)_b/(d/R_1)_a = 18{\cdot}8$. Beginning with the data in tables 1 and 2 we have computed the quantity

$$\Lambda = G/\rho\Omega_1^2 R_1^4 = G(d/\nu)^2/\rho R^2 R_1^2, \tag{27}$$

and found the ratio Λ_b/Λ_a as a function of R. Here Λ_b refers to the narrow gap measurements. Values of m and m' are compiled as before and the results are given in table 5. We see that over the range $400 < R < 1200$ a constant value of $m = 0{\cdot}35$ will describe the data. Furthermore, the value of m is not much changed from values in table 4 for smaller gap-width ratios.

(*a*) Comparison of Wendt's curves in figure 10 for gap widths 0·95 and 2·20 cm

log R	log λ_b/λ_a	m	m'
2·5	0·148	0·36	0·33
3·0	0·123	0·30	0·28
3·5	0·121	0·30	0·27
4·0	0·121	0·30	0·27
4·5	0·121	0·30	0·27

(*b*) Comparison of curves in figure 10 for gap widths 0·95 and 4·70 cm

2·5	0·277	0·33	0·30
3·0	0·212	0·26	0·23
3·5	0·220	0·26	0·24
4·0	0·224	0·27	0·24
4·5	0·227	0·27	0·24

TABLE 4

R	Λ_b/Λ_a	m	m'
200	0·271	0·45	0·36
300	0·311	0·40	0·33
400	0·342	0·37	0·30
500	0·355	0·35	0·29
600	0·343	0·36	0·30
700	0·348	0·36	0·29
800	0·353	0·35	0·29
900	0·353	0·35	0·29
1000	0·357	0·37	0·29
1100	0·358	0·35	0·29
1200	0·357	0·35	0·29

TABLE 5. Comparison of Donnelly's measurements for gap widths 0·1 and 1·0 cm

Taylor's measurements are not as conclusive as the other experiments on this particular point. His curves extend to higher Reynolds numbers and are not always parallel. This can be seen in Fig. 10 of Taylor's paper (1936) on which are plotted $G/(\rho\Omega_1^2 R_1^2 R_2^2)$ *vs* R for a series of 8 different inner cylinders. We have calculated values of Λ as in (27) for several of Taylor's curves excluding the highest speeds. The results for m are summarized in table 6. We see that, up to log $R = 4$, the values of m are fairly constant and do not vary very much with change in gap width. An exception is seen in table 6*c*, where two wide gap cases

are compared and m is considerably lower. However, the curves lie so close that the error in this determination could be rather large.

We conclude that (23) will represent approximately the data in the speed range considered. The value of m is about $0{\cdot}32 \pm 0{\cdot}05$ and is not very sensitive to the ratio of gap widths being compared. Wendt's suggestion that $(dR_2/R_1^2)^{m'}$ should replace $(d/R_1)^m$ in (23) does not seem to lead to much improvement, as seen in tables 4–6. The results of this section are consistent with the relation (18) proposed by Batchelor, in which the value of m is 0·25.

(*a*) Comparison of Taylor's measurements for gap widths 0·16 and 0·46 cm

log R	log Λ_b/Λ_a	m	m'
3·1	0·166	0·34	0·31
3·3	0·173	0·35	0·33
3·5	0·173	0·35	0·33
3·7	0·180	0·37	0·34
3·8	0·184	0·37	0·35

(*b*) Comparison for gap widths 0·16 and 0·85 cm

3·3	0·262	0·32	0·29
3·5	0·255	0·31	0·28
3·7	0·266	0·33	0·30
3·8	0·272	0·34	0·30

(*c*) Comparison for gap widths 0·60 and 0·85 cm

3·3	0·048	0·26	0·22
3·5	0·038	0·21	0·18
3·8	0·041	0·22	0·19
4·0	0·042	0·23	0·19

TABLE 6

7. Conclusions

We have analysed the results of a number of measurements of the torque transmitted to an outer cylinder as a function of the angular velocity of the inner cylinder. The results show that the analysis of Stuart (1958) gives the correct variation of torque for a short range above the critical speed. With one exception (figure 5) we find that the functional form

$$G = a\Omega_1^{-1} + b\Omega_1^n \quad (\tfrac{4}{3} < n < \tfrac{3}{2})$$

describes the measurements over a range of about ten times the critical velocity. Details of the range of validity of this equation are given in table 3. The exponent n is not sensitive to the width of the gap between cylinders. A good compromise value appears to be $n = 1{\cdot}36$ for the range indicated in table 3 and $n = 1{\cdot}5$ at higher speeds. When measurements are pushed far enough the empirical relation breaks down.

For speeds well beyond critical it is possible also to describe the variation of torque with gap by

$$G/(\rho h \Omega_1^2 R_1^4) \propto R^{-l}(d/R_1)^m,$$

where $l = 2 - n \doteqdot 0{\cdot}5$ and $m \doteqdot 0{\cdot}31$. This is in fair agreement with the formula (18) obtained by Batchelor (see the appendix).

The authors are indebted to Dr J. T. Stuart for supplying the numerical result in (12) and for discussions of his theory. We owe to Dr G. K. Batchelor the suggestion that we investigate the variation of torque with gap width at high speeds. Dr G. Veronis has assisted us with discussions and suggestions on the manuscript.

The research described here has been supported, in part, by a grant (NSF G-3489) from the National Science Foundation. One of us (R. J. D.) is indebted to the Alfred P. Sloan Foundation for a Research Fellowship.

Appendix

A theoretical model of the flow at speeds far above the critical

By G. K. Batchelor (University of Cambridge)

After Dr Donnelly and Miss Simon had prepared their paper for publication, I noticed that the empirical relation between torque G and angular velocity Ω_1 at speeds well above the critical (viz. that $G \propto \Omega_1^n$ where n is about 1·5) is in accord with a prediction based on a simple theoretical model of the flow. This theoretical model also gives a prediction of the dependence of G on the size of the gap between the cylinders at speeds well above the critical; and it seems from further analysis of the available data by Donnelly and Simon, now incorporated in the paper, that the theoretical and observed relationships are again in fair agreement. It therefore seems worthwhile to record here the basis of the theoretical results.

It is supposed, first, that the flow between the two cylinders is steady, even though the angular velocity of the inner cylinder is far above the critical value. This steady flow will presumably have a cellular form, with the same axial wavelength as at speeds just above the critical although certainly not with the same velocity distribution, and the streamlines will lie on closed surfaces of revolution. When the angular velocity Ω_1 is large enough, the Reynolds number of the motion in an axial plane will be large compared with unity, and the whole flow will consist of regions in which viscous forces are negligible and thin layers in which viscous forces are significant. The distribution of vorticity in the inviscid core of flow systems of this kind has been investigated (Batchelor 1956), but no use of the detailed form of the velocity or vorticity distributions will be made here. For the present purpose (which is to predict the functional dependence of torque on angular velocity Ω_1 and gap d, without bothering about the numerical value of constants of proportionality) it is sufficient to assume a flow in the axial plane of the kind sketched in figure 11. In this figure δ represents the general magnitude of the thickness of the boundary layer round the outside of the inviscid core of one cell, and we shall write v for the velocity (in the axial plane) at the outer edge of this inviscid core.

We now estimate δ and v in terms of d and Ω_1. One relation is obtained by assuming the usual parabolic growth of a boundary layer with distance. The boundary layer under discussion is closed, and its thickness increases over part of its length and decreases over the remainder (the decrease occurring because the centrifugal force accelerates the fluid in the boundary layer over the horizontal parts of its length), but the general magnitude of the thickness will presumably be

the same as if the layer had increased in thickness over a path of length of order d under the action of an external stream velocity of order v. Thus we have

$$\frac{\delta}{d} \sim \left(\frac{dv}{\nu}\right)^{-\frac{1}{2}}. \tag{A 1}$$

A second relation follows from the balance in the boundary layer between the driving centrifugal force and the retarding viscous force. Fluid very close to the inner cylinder is acted on by centrifugal force $\Omega_1^2 R_1$, whereas fluid close to the stationary outer cylinder is subject to no centrifugal force. The general magnitude

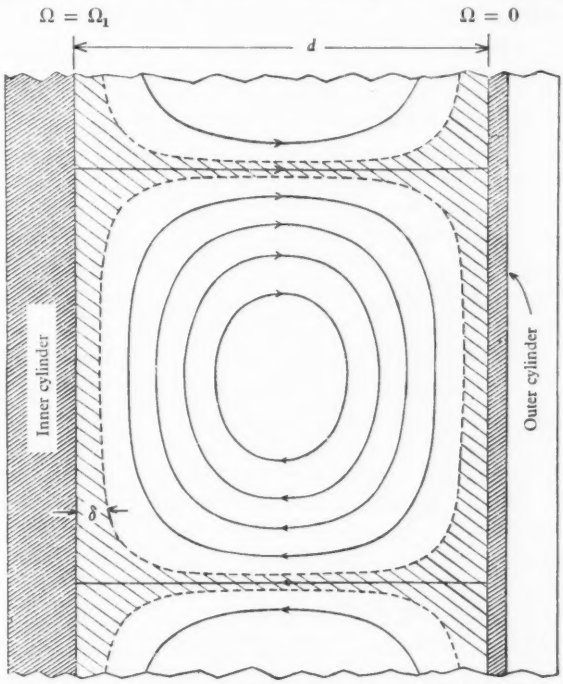

FIGURE 11. Sketch of the flow (in an axial plane) assumed in the theoretical argument. The lightly shaded area represents the boundary layer region in which viscous forces are significant.

of the centrifugal force acting on fluid throughout the boundary layer is thus $\Omega_1^2 R_1$, whereas that of the viscous force per unit mass, in the direction of flow in the axial plane, is $\nu v/\delta^2$. Hence

$$\Omega_1^2 R_1 \sim \nu v/\delta^2. \tag{A 2}$$

The relations (A 1) and (A 2) together give

$$v \sim \Omega_1 (dR_1)^{\frac{1}{2}}, \quad \delta \sim d^{\frac{1}{4}} \nu^{\frac{1}{2}} / \Omega_1^{\frac{1}{2}} R_1^{\frac{1}{4}}. \tag{A 3}$$

The corresponding Reynolds number of the axial boundary-layer flow is thus

$$\frac{v\delta}{\nu} \sim \left(\frac{\Omega_1 R_1 d}{\nu}\right)^{\frac{1}{2}} \left(\frac{d}{R_1}\right)^{\frac{1}{4}},$$

and this is the number which must be large compared with unity for the analysis to be applicable. This requirement was certainly satisfied in some of the experiments described in the paper; for instance, in Donnelly's (1958) experiments with the smaller of his two inner cylinders, $d/R_1 = 1{\cdot}0$ and the Reynolds number $\Omega_1 R_1 d/\nu$ ranged up to about 2000.

The torque G acting on a length h of the inner cylinder can now be determined from the fact that the azimuthal velocity of the fluid drops from $\Omega_1 R_1$ at the cylinder to some value representative of the core conditions in a distance δ. The distribution of angular velocity Ω in the inviscid core is such (Batchelor 1956) as to make the circulation about the inner cylinder uniform (i.e. $\Omega \propto r^{-2}$) and equal to some value intermediate between $2\pi\Omega_1 R_1^2$ and zero, so that Ω must change by an appreciable fraction of its value across the boundary layer. Hence

$$\begin{aligned} G &\sim hR_1^2 \times \text{viscous stress at cylinder} \\ &\sim hR_1^2\left(\frac{\mu\Omega_1 R_1}{\delta}\right) \\ &\sim h\rho\Omega_1^2 R_1^4\left(\frac{\nu}{\Omega_1 R_1 d}\right)^{\frac{1}{2}}\left(\frac{d}{R_1}\right)^{\frac{1}{2}}, \end{aligned} \tag{A 4}$$

which is the relation (18) quoted in the paper. It is to be noted that this relation is an asymptotic one, holding more closely as the Reynolds number of the flow increases. It seems reasonable to infer, from the agreement between (A 4) and some of the observations discussed in the paper, that a flow of the type sketched in figure 11 does in fact occur under the conditions of these same observations.

REFERENCES

Batchelor, G. K. 1956 *J. Fluid Mech.* **1**, 177.

Chandrasekhar, S. 1954 *Mathematica*, **1**, 5.

Chandrasekhar, S. 1958 *Proc. Roy. Soc.* A, **246**, 301.

Donnelly, R. J. 1958 *Proc. Roy. Soc.* A, **246**, 312.

Donnelly, R. J. & Fultz, D. 1960 *Proc. Roy. Soc.* A (to be published).

Landau, L. 1944 *C.R. Acad. Sci. U.S.S.R.* **44**, 311.

Schultz-Grunow, F. & Hein, H. 1956 *Z. Flugwiss.* **4**, p. 28.

Stuart, J. T. 1958 *J. Fluid Mech.* **4**, 1.

Taylor, G. I. 1923 *Phil. Trans.* A, **223**, 289.

Taylor, G. I. 1936 *Proc. Roy. Soc.* A, **157**, 546.

Wendt, F. 1933 *Ingen.-Arch.* **4**, 577.

A comparison between buoyant vortex rings and vortex pairs

By J. S. TURNER
Mechanics of Fluids Department, University of Manchester

(Received 25 June 1959)

In this paper it is shown how earlier results for buoyant vortex rings may be extended to describe the corresponding two-dimensional case, which arises in the theory of bent-over plumes. It is again assumed that in uniform surroundings the circulation remains constant while the buoyancy acts to increase the momentum of the pair. The behaviour in two dimensions is quite different from that in three, however; a buoyant vortex ring spreads linearly with height, whereas a buoyant pair spreads exponentially with height, or linearly with time (and therefore, in a bent-over plume, linearly with distance downwind).

The theory has been extended to describe the rise of buoyant rings and pairs through stably stratified surroundings having a linear density gradient. The behaviour near the maximum height reached is found to depend critically in both cases on the relative rates at which the circulation and the momentum fall to zero. If these reach zero together, the rings or pairs will steadily increase in size and come to rest at a finite height and with a finite radius. If the circulation is non-zero when the momentum vanishes, the radius begins to decrease soon after the buoyancy becomes zero, and the vortices will therefore tend to break up suddenly and mix into their surroundings. There is a considerable increase in the final height which should be attained by vortex rings or bent-over plumes if the initial circulation is increased; it is suggested that releasing smoke intermittently, rather than continuously, at high velocity might be a means of increasing the effective height of chimneys in calm conditions. When the circulation reaches zero before the momentum does, the solutions indicate that the radius becomes very large near the level of zero buoyancy.

1. Introduction

In a previous paper (Morton, Taylor & Turner (1956), which will be referred to hereafter as I), the properties of an isolated mass of buoyant fluid released from rest in stratified surroundings were investigated, with the object of obtaining results which could be applied to the atmosphere. It was later shown (Turner (1957), to be referred to as II) how the motion in such a 'buoyant cloud' can be considered as a particular case of a buoyant vortex ring. The more general theory deals with the situation in which an arbitrary amount of vorticity is injected into the ring as it is formed, and the behaviour is found to be altered greatly by this extra vorticity. The buoyant cloud corresponds to the case in which the only circulation is produced by the buoyancy, during the initial

acceleration from rest; thereafter the cloud spreads linearly with height in uniform surroundings, but at a larger angle than a buoyant ring containing the same total buoyancy and more vorticity.

At the time the above work was done, there was no reason to suppose that the corresponding two-dimensional problem would have a real physical significance, although the line source of buoyancy released continuously has been treated in the literature (e.g. Rouse, Yih & Humphreys 1952). Recently, however, Scorer (1958) has followed up his earlier work on 'thermals' (the name he has adopted for what we have called 'buoyant clouds') by suggesting that the behaviour of plumes of smoke when they have been bent over by a cross-wind and become nearly horizontal, can conveniently be discussed in terms of a line source of buoyancy. It is in fact sometimes observed that a plume of smoke bent over in this way tends to split sideways into two concentrated regions with a clear space between them, and the effect is clearly shown in the photograph obtained in a laboratory channel (figure 1, plate 1), which will be discussed in more detail in §2.1. The flow in planes perpendicular to the axis of the plume is very like that in a vortex pair, with a region of greater than the mean velocity of rise in the centre and a slower region on each side. The behaviour of a short length of such a plume as it is swept downstream should be similar to that from a two-dimensional source developing in time, and Scorer has initiated experiments to study this simplified problem in the laboratory.

In this paper it will be shown that an extension of the ideas developed for vortex rings may again be used to obtain an understanding of the two-dimensional case. There are, however, certain important differences, both when one considers the generation of the motion and the subsequent rate of spread. The first purpose of this paper will therefore be to derive corresponding results to those obtained for buoyant vortex rings in uniform surroundings, and to point out where the two cases differ physically. The attempts at extension to vortex pairs in a stratified ambient fluid have also led to a more complete understanding of the vortex rings in this case, and in the second part of this paper we shall discuss the different types of behaviour which can be obtained, particularly near the maximum height reached by the rings or pairs.

2. Motion in uniform surroundings

2.1. *Buoyant vortex rings*

The assumptions and results of II will be summarized in this section, but some familiarity with the earlier papers will be assumed when comparisons are made.

The basic assumption is that in uniform surroundings, the circulation K in a buoyant vortex ring remains constant, while the buoyancy acts to increase the momentum of the mass of fluid moving with the ring. This idea may be justified as follows. It is clear that an increase of momentum implies an increase in the radius of the ring, and therefore the addition of external fluid. It is observed that at least some (and sometimes all) of the added fluid is drawn up the centre from behind, thereby tending to concentrate the buoyant fluid in a ring, even in cases where it has been uniformly distributed to start with. Thus a

circuit may be taken round the vorticity-containing region which lies completely in irrotational fluid of constant density; that is, K must be constant. It is also implied that any turbulent motion is much less important than the large-scale circulation.

If we neglect the effect of small density differences in the inertia terms, the momentum P is given by

$$P = \pi\rho K R^2, \tag{1}$$

where R is the 'mean radius' of the ring. Hence the equation balancing the buoyancy force with the rate of change of momentum is

$$\frac{dP}{dt} = \pi\rho K \frac{dR^2}{dt} = gW(\rho - \rho')$$

or

$$\frac{dR^2}{dt} = \frac{F}{\pi K}. \tag{2}$$

Here the total buoyancy ρF is defined by

$$F = \frac{gW(\rho - \rho')}{\rho}, \tag{3}$$

where W is the volume of buoyant fluid, of density ρ', and ρ is the density of the surroundings. In uniform surroundings F is constant, and equation (2) may be integrated to give

$$R^2 - R_0^2 = \frac{Ft}{\pi K}. \tag{4}$$

In order to proceed further we need to make some assumption about the vorticity distribution in the moving mass, since the velocity V of a vortex ring is critically dependent on the size of the vorticity-containing region. If we assume that the distribution remains *similar* at all heights, we have

$$\left.\begin{aligned} V &= cK/R, \\ \text{and hence} \qquad R &= \alpha x = \frac{F}{2\pi c K^2} x, \end{aligned}\right\} \tag{5}$$

where x is the height above a virtual source and c and α are constants. In terms of the distance h between states R_0 and R, time t apart, we may obtain the form

$$t = \left(\frac{h^2}{4\pi c^2 K^3}\right) F + \frac{hR_0}{cK}. \tag{6}$$

Thus, for a given circulation, *increasing* the buoyancy gives a *lower* velocity, i.e. a longer time to reach a given height.

2.2. *Buoyant vortex pairs*

When there is no density difference in the fluid through which a vortex pair is travelling, then we know (Lamb 1932, §155) that the velocity V and the momentum per unit length P' are given by

$$V = \frac{K}{4\pi R}, \tag{7}$$

and

$$P' = 2\rho K R, \tag{8}$$

where $2R$ is the separation of the pair and K is the circulation round one line vortex. The (irrotational) fluid motion accompanying the pair has an oval cross-section with semi-axes $2{\cdot}09R$ and $1{\cdot}73R$; this shape, unlike the corresponding one for the vortex ring, is independent of the size of the region containing the vorticity, provided this is small compared with R. The velocity is also independent of this distribution, a fact which makes the two-dimensional analysis possible with one assumption less than was required in three dimensions. (With widely distributed vorticity, one might of course have to make some similarity assumption, and use a different constant in equation (7).)

We may again make the assertion that the circulation K is constant, and for the same reasons; an increase in momentum implies a separation of the pair. Suppose that the pair contains a volume Q per unit length of fluid of density ρ'. Then, neglecting density differences except in the buoyancy term, we have

$$\frac{dP'}{dt} = 2\rho K\frac{dR}{dt} = gQ(\rho-\rho')$$

or

$$\frac{dR}{dt} = \frac{F'}{2K}, \tag{9}$$

where the buoyancy $\rho F'$ per unit length is defined by

$$F' = \frac{gQ(\rho-\rho')}{\rho}. \tag{10}$$

In uniform surroundings F' is constant, and (9) may be integrated to give

$$R-R_0 = F't/2K, \tag{11}$$

where $2R_0$ and $2R$ are the initial and final separations, and t is the elapsed time. The increase of radius is *linear* with time, or, referring to the suggested application to the bent-over plume, linear with distance downwind; the corresponding theoretical and experimental result in three dimensions (equation (4)) is that R^2 increases linearly with time.

At this point it is interesting to refer to figure 1 (plate 1), which shows a plan view of a bent-over plume in a 10×5 cm Perspex water channel. In this case the velocity of the water was about 3 cm/sec and the initial density difference of the order of $\frac{1}{10}$ %. This photograph was produced for illustration only, and should not be examined quantitatively, since the velocity across the channel was not uniform; but the splitting is clearly shown, and the spread appears to be nearly linear with distance.

In the two-dimensional case, using (7) and (9) with *no* extra assumption, one arrives at the following explicit expression for radius in terms of distance:

$$\frac{R}{R_0} = \exp\left(\frac{2\pi F'}{K^2}h\right), \tag{12}$$

where h is the height between states R_0 and R. This exponential increase of separation with height is very different from the linear spread of vortex rings predicted by equation (5).

It also follows that in the two-dimensional case,

$$t = \frac{2KR_0}{F'}\left[\exp\left(\frac{2\pi F'}{K^2}\,h\right) - 1\right]. \tag{13}$$

This shows that, again, increasing the buoyancy for a given circulation reduces the rate of rise, because the pair spreads faster. An obvious extension of (13) leads to a prediction of the path of the centre of the plume as it is swept downwind at a known velocity; this can of course only be applied while the motion is dominated by the buoyancy and not by the turbulence in the surroundings.

Using (11) and (12), one could determine F'/K and F'/K^2 experimentally and hence in principle find F' and K. If F' is known (and in the laboratory the volume and density of fluid released usually would be measured), then one relation is sufficient to determine K.

2.3. *The generation of the circulation*

So far it has been assumed that F' and K may be specified separately, which is so when extra momentum is given to the fluid initially. The most important case, however, is that in which a mass of buoyant fluid is released from rest, and the only circulation is that generated soon after the release by the action of the buoyancy before non-buoyant fluid has been drawn up the centre. This is what in three dimensions we have called a 'buoyant cloud', and it is in the comparison of this with the corresponding case for the line source that the contrast between the two- and three-dimensional solutions may most clearly be brought out.

In three dimensions, the mean half-angle of spread for the cloud was found in II to be $\alpha \doteqdot 0{\cdot}18$, in agreement with Woodward (1959), and corresponding to particular values of F/K^2 and c in (5). Such a relation is to be expected on dimensional grounds, since F and K^2 have the same physical dimensions, and it is not easy to see how the scale could matter, whatever the exact mechanism of generation of vorticity might be. In two dimensions, on the other hand, a non-dimensional constant cannot be formed from F' and K alone, since F' is the buoyancy *per unit length*. Another length must enter the problem, and one might suggest the dimensionally correct form

$$\frac{F'R_0}{K^2} = \text{const.} = \frac{d}{2\pi}, \tag{14}$$

where $2R_0$ is the separation of the vortex pair just after the circulation has become established, as the first relation to try when interpreting observations. With this assumption, it follows from (12) that the shape of the region swept out by the pair as it rises will always be the same when it is made non-dimensional with the initial separation:

i.e.
$$\frac{R}{R_0} = \exp\left(\frac{dh}{R_0}\right), \tag{15}$$

where d, the same constant as in (14), should be obtainable by experiment. It should be noted, however, that two-dimensional experiments will be much more sensitive to the presence of walls in a laboratory tank; the rate of spread is

likely to be underestimated and the region swept out will appear more nearly wedge shaped if $2R$ approaches half the total width of the tank.

The dimensional necessity for the appearance of a length in the equations together with F' and K also helps us to understand why the spread in two dimensions is not linear with height, as it was in three dimensions. Since $F'h/K^2$ is non-dimensional, all we can say using purely dimensional reasoning is that the radius must be some function of this group, multiplied by the initial radius. The nature of this functional dependence must be determined by a complete solution such as we have given; whereas in three dimensions, since F/K^2 is the relevant non-dimensional group and this does not involve a length, we are led immediately to the result that R varies linearly with h.

3. Motion in a stably stratified fluid with constant density gradient

3.1. *Buoyant vortex rings*

Provided the analysis is restricted to the case where the extreme (potential) density differences over the region considered are small compared to some chosen reference density, say ρ_1 at the height of the source, then many of the relations obtained for a uniform fluid are again valid for the rise of a buoyant vortex ring through a stratified fluid which is at rest. We have

$$\left.\begin{aligned} P = \pi\rho_1 K R^2, \quad \frac{dP}{dt} = \rho_1 F \\ \text{and} \qquad V = \frac{dx}{dt} = \frac{cK}{R}. \end{aligned}\right\} \tag{16}$$

An additional equation, obtained in II, describes the conservation of density deficiency; for a constant stable density gradient defined by $G = -(g/\rho_1)\,(d\rho/dx)$, it may be put in the form

$$\frac{dF}{dt} = -qGR^3\frac{dx}{dt}, \tag{17}$$

where q is a constant which will depend on the *shape* of the volume moving with the ring.

Some general remarks based on dimensional reasoning were made in II about the dependence of the final height on the initial buoyancy and circulation F_0 and K_0 and on G, but no solution of (16) and (17) was attempted. In I, Morton obtained a solution which, although it was based on slightly different reasoning and does not introduced K explicitly, corresponds to a particular relation between F_0 and K_0^3. This point will be brought out more clearly in the following, where we obtain the more general solution.

In order to do this, we require an equation describing the variation of K. The vorticity equation in a medium of varying density becomes

$$\frac{dK}{dt} = -\oint\frac{dp}{\rho},$$

where the integration is taken round a circuit containing one of the line vortices. Let us suppose that at any instant the fluid up the centre of the ring over a

depth comparable with R has been drawn from a denser level distant sR below the ring (where s is a constant), and that the density of the surroundings has not been changed by the passage of the ring. The vorticity equation then becomes

$$\frac{dK}{dt} = -\frac{\Delta\rho}{\rho} gR = -sR^2G. \tag{18}$$

That this is a reasonable assumption to make may be seen by referring to the diagrams obtained by Woodward (1959), who examined the motion inside thermals in detail, and her results will later be used to evaluate the constants s and q. (Her figures incidentally give further support to our assumption that external fluid is drawn up the centre, not only in vortex rings in which the buoyant fluid is very concentrated near a ring, but also in buoyant clouds where this assumption is less obviously valid.) The form of (18) also agrees with the solution given in I, as of course it must on purely dimensional grounds.

Equations (16), (17) and (18) may be put into a more convenient non-dimensional form by making the transformations

$$\left.\begin{aligned} t &= \left(\frac{\pi}{qc}\right)^{\frac{1}{2}} G^{-\frac{1}{2}}\tau, \quad F = F_v f, \\ \frac{P}{\rho_1} &= \left(\frac{\pi}{qc}\right)^{\frac{1}{2}} F_v G^{-\frac{1}{2}} p, \quad K = \left(\frac{2s}{qc}\right)^{\frac{1}{2}} F_v^{\frac{1}{2}} k, \\ R &= (2\pi s)^{-\frac{1}{4}} F_v^{\frac{1}{4}} G^{-\frac{1}{4}} r, \quad x = q^{-1}(2\pi s)^{\frac{3}{4}} F_v^{\frac{1}{4}} G^{-\frac{1}{4}} \xi, \end{aligned}\right\} \tag{19}$$

where τ, f, p, k, r and ξ are non-dimensional functions, and F_v is the buoyancy at a virtual origin, to be defined later. The equations become

$$\left.\begin{aligned} p &= kr^2, && (a) \\ \frac{dp}{d\tau} &= f, && (b) \\ v &= \frac{d\xi}{d\tau} = \frac{k}{r}, && (c) \\ \frac{df}{d\tau} &= -r^3\frac{d\xi}{d\tau}, && (d) \\ 2\frac{dk}{d\tau} &= -r^2. && (e) \end{aligned}\right\} \tag{20}$$

From (20) we see that $d^2p/d\tau^2 = -p$; this has the solution $p = p_0\cos\tau + f_0\sin\tau$, and hence $f = f_0\cos\tau - p_0\sin\tau$, using (20) (*b*).

If the origin of τ is chosen in order to make $p = 0$ and $F = F_v$ (i.e. $f = 1$) there, we have finally

$$\left.\begin{aligned} p &= \sin(\tau+\tau_v) = \sin\tau_1, \\ f &= \cos(\tau+\tau_v) = \cos\tau_1. \end{aligned}\right\} \tag{21}$$

Given f_0 and p_0, this choice may always be made by taking a virtual origin at time $\tau_v = \tan^{-1}(p_0/f_0)$ earlier than the actual origin of time. Note that this (non-dimensional) interval will depend, through (19), on F_0, P_0 and also the density gradient G.

Using (21), we may now obtain easily from (20) the explicit solutions

$$k = [\cos\tau_1 + b]^{\frac{1}{2}}, \tag{22}$$

where b is a constant of integration related to k_v, the value of k at the virtual origin, by

$$k_v^2 = (b+1); \tag{23}$$

also

$$r = \frac{(\sin\tau_1)^{\frac{1}{2}}}{(\cos\tau_1 + b)^{\frac{1}{4}}} \tag{24}$$

and

$$\frac{d\xi}{d\tau} = \frac{(\cos\tau_1 + b)^{\frac{3}{4}}}{(\sin\tau_1)^{\frac{1}{2}}}. \tag{25}$$

The form of solution will depend on the value we assign to b, and the various possibilities will be discussed in turn.

The case $b = 1$

First of all we may note that $b = 1$ corresponds to the situation in which $k = 0$ when $\tau_1 = \pi$, i.e. when $p = 0$; the momentum and the circulation then fall to zero together. When this value of the constant is substituted in (24) and (25), they take the simpler form

$$r = (1 - \cos\tau_1)^{\frac{1}{4}} \tag{24a}$$

and

$$\frac{d\xi}{d\tau} = \frac{\sin\tau_1}{(1-\cos\tau_1)^{\frac{3}{4}}}. \tag{25a}$$

This last equation may be integrated to give

$$\xi = 4(1-\cos\tau_1)^{\frac{1}{4}} = 4r. \tag{26}$$

This is precisely the form of solution obtained in I up to the level where the velocity first vanishes, and it clearly leads to a linear increase of radius with distance, as is the case in uniform surroundings. (It is interesting to note, without giving the proof here, that the spread is also linear in an *unstable* linear density gradient, provided the same value of k_v is chosen.) The variation of the other non-dimensional quantities with τ_1 is shown in figure 2.

The case $b > 1$

If $b > 1$, implying that the initial circulation is large enough for k to be non-zero when $p = 0$, the solutions take the form shown in figure 3, which has been calculated for illustration with the particular value $b = 1{\cdot}5$. It is seen that the distance travelled remains finite, although the velocity near the virtual origin and at the maximum height is infinite. This results from the fact that r decreases to zero soon after the buoyancy vanishes, which is shown more clearly in figure 5, where r is plotted against ξ. The spread below this level is again nearly linear.

It is unlikely that the *loss* of fluid from the region moving with the ring can take place in an ordered, smooth manner, and in any case there is an excess of

vorticity in the moving region. The obvious physical prediction to be made from figure 3 is that above a certain level, a buoyant vortex ring in stratified surroundings will suddenly collapse and mix with the environment. This effect was in fact noted in the experiments reported in II, but it was there attributed (probably wrongly) to the unstable layering within the structure of the ring, due to the successive addition of layers of fluid of decreasing density.

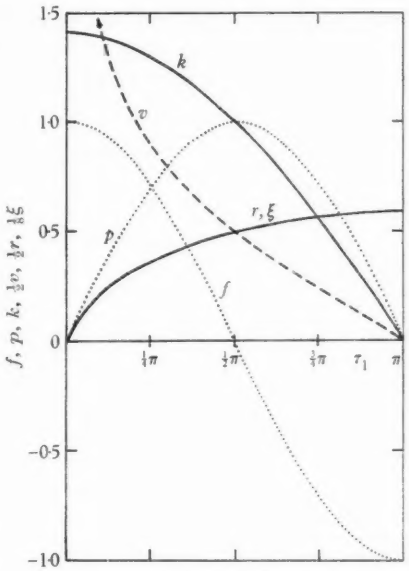

FIGURE 2

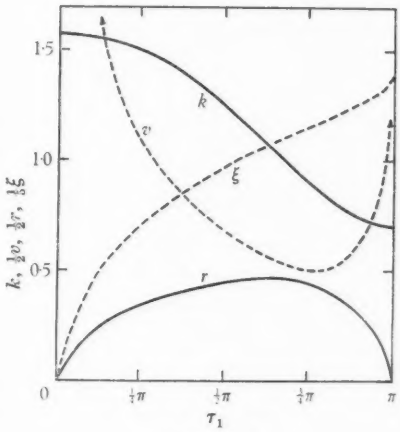

FIGURE 3

FIGURE 2. The non-dimensional solution for a buoyant vortex ring rising through stably stratified surroundings. The initial vorticity is such that the momentum and circulation fall to zero together, i.e. the constant $b = 1$.

FIGURE 3. The non-dimensional solution for a buoyant vortex ring rising through stably stratified surroundings: $b = 1{\cdot}5$, so that the circulation is non-zero when the momentum vanishes.

Note that when b is large, the value of ξ reached before the ring breaks up is, from (25), approximately proportional to $b^{\frac{3}{4}}$, so that using (27) it follows that the maximum height is proportional to $F_v^{-\frac{1}{4}} K_v^{\frac{3}{4}} G^{-\frac{1}{4}}$. This agrees with the prediction made using a dimensional argument in II, and shows again that there can be a considerable increase in the height attained in stable surroundings by a mass having a given buoyancy if it is given extra vorticity (or, equivalently, extra momentum) when it is released. The intermittent release of smoke at a high velocity might be worth considering as a method of increasing the effective height of chimneys, particularly in the very calm, stable conditions when smog is most liable to form; it has been shown on the other hand (Morton 1959) that increasing the momentum of a continuous source under these conditions tends to reduce the final height slightly.

The case $b < 1$

In exactly the same way, when $b = 0{\cdot}5$ (corresponding to the case in which the circulation falls to zero before the momentum does), we can obtain the solutions set out in figure 4. With this assumption, the radius starts increasing linearly, but becomes very large near the maximum height, as is shown in figure 5. The physical reality of this last solution is in some doubt, however, since the least circulation possible for a given buoyancy is that corresponding to the 'buoyant cloud'. In the next section we shall investigate this point further by comparing the buoyant cloud with the condition implied by the 'critical' value of $b = 1$.

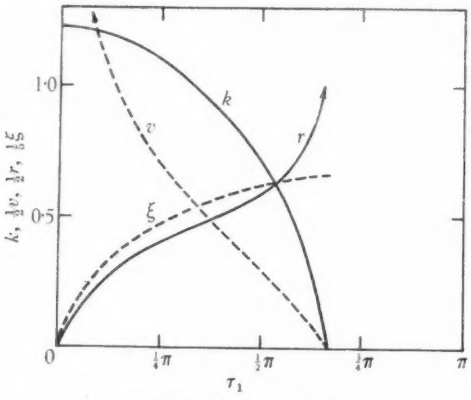

FIGURE 4. The non-dimensional solution for a buoyant vortex ring rising through stably stratified surroundings: $b = 0{\cdot}5$, and the circulation falls to zero before the momentum does.

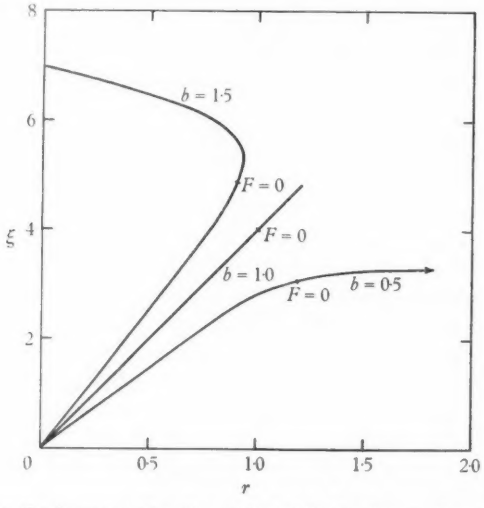

FIGURE 5. Showing the increase of radius with height for buoyant vortex rings in stratified surroundings. The spread is linear for $b = 1$; for $b > 1$ the radius decreases to zero just above the level of zero buoyancy, and for $b < 1$ the radius becomes large at this level.

3.2. *The meaning of the critical condition* $b = 1$

Using (19), equation (23) may be rewritten in the dimensional form

$$\frac{K_v^2}{F_v} = \left(\frac{2s}{qc}\right)(b+1). \tag{27}$$

Putting $b = 1$, and using (5), the half-angle of spread corresponding to the critical case is seen to be

$$\alpha_c = \frac{q}{8\pi s}. \tag{28}$$

Thus, we must now make numerical estimates of the geometrical factors q and s. The shapes and streamlines within thermals which Woodward (1959) has published immediately allow us to evaluate the volume in terms of R as we have defined it, and hence show that q is about 13. In order to obtain a precise value for s, we would need to know the variation of density through the centre of the thermal and in its wake; but by examining Woodward's diagrams showing the distortion of initially horizontal layers in a uniform ambient fluid, we can say that s must be about 3.

Inserting these constants in (28) gives the value $\alpha_c = 0{\cdot}17$. This is very close to the half-angle of spread for the buoyant cloud which was discussed in §2.3, and it suggests that it is *not* possible to realize physically the solution for $b < 1$. The agreement between the two values is in fact so close that it is tempting to seek a physical reason why they might be identical. It is difficult, however, to convince oneself that there is an exact parallel between the processes of generation of vorticity in a cloud starting from rest in uniform surroundings and the destruction of vorticity as the cloud is brought to rest in a density gradient. It is worth remarking that *dimensionally* the two problems are the same, since the density gradient does not enter into the condition specifying the critical value of b except through the (small) differences between the values of K and F at the real and virtual sources. This is not so for the pair vortex, as will be shown in the next section.

3.3. *Buoyant vortex pairs*

The development of the theory for a vortex pair will proceed in a parallel form to that given above for vortex rings, and with the same assumptions except of course for the obvious modifications necessary in two dimensions. For conciseness we will proceed directly to the non-dimensional set of equations in the variables τ, f', p', k, r and ξ which are related to the physical variables by

$$\left.\begin{aligned} t &= \left(\frac{8\pi}{q'}\right)^{\frac{1}{2}} G^{-\frac{1}{2}}\tau, \quad F' = F'_v f', \\ \frac{P'}{\rho_1} &= \left(\frac{8\pi}{q'}\right)^{\frac{1}{2}} F'_v G^{-\frac{1}{2}} p', \quad K = \left(\frac{8\pi}{q'}\right)^{\frac{1}{2}} \left(\frac{3s'}{8}\right)^{\frac{1}{3}} F'^{\frac{2}{3}}_v G^{-\frac{1}{3}} k, \\ R &= (3s')^{-\frac{1}{3}} F'^{\frac{1}{3}}_v G^{-\frac{1}{3}} r, \quad x = (3s')^{\frac{2}{3}} (q')^{-1} F'^{\frac{1}{3}}_v G^{-\frac{1}{3}} \xi. \end{aligned}\right\} \tag{29}$$

Here q' and s' are new constants corresponding to q and s for the vortex ring. The governing equations become

$$\left.\begin{aligned} p' &= kr, \quad \frac{dp'}{d\tau} = f', \quad \frac{d\xi}{d\tau} = \frac{k}{r}, \\ \frac{df'}{d\tau} &= -r^2\frac{d\xi}{d\tau}, \quad \frac{3}{2}\frac{dk}{d\tau} = -r^2. \end{aligned}\right\} \tag{30}$$

The solution for p' and f' may be obtained in a form similar to that for the vortex ring

$$p' = \sin(\tau+\tau_v) = \sin\tau_1, \quad f' = \cos(\tau+\tau_v) = \cos\tau_1, \tag{31}$$

where the virtual origin of τ has been chosen at a time $\tau_v = \tan^{-1}(p_0'/f_0')$ earlier than the actual origin, in order to make $p' = 0$ when $f' = 1$. This time will again depend on G as well as on F_0 and P_0.

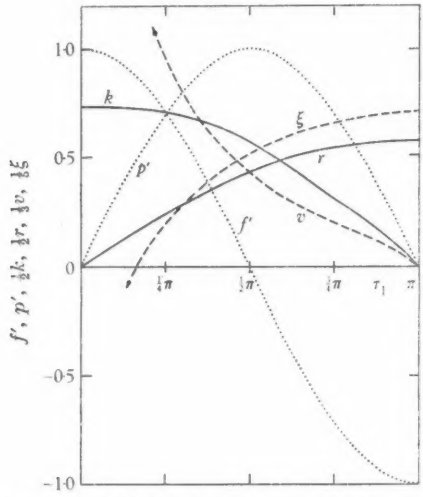

FIGURE 6. The non-dimensional solution for a buoyant vortex pair in a stably stratified fluid: $k_v^3 = \pi$, so that the circulation and momentum fall to zero together.

Using (31) in (30), k may now be expressed as

$$k = (\sin\tau_1\cos\tau_1 - \tau_1 + k_v^3)^{\frac{1}{3}}, \tag{32}$$

where k_v is the value of k at the virtual origin. Also

$$r = \frac{\sin\tau_1}{(\sin\tau_1\cos\tau_1 - \tau_1 + k_v^3)^{\frac{1}{3}}} \tag{33}$$

and

$$\frac{d\xi}{d\tau} = \frac{(\sin\tau_1\cos\tau_1 - \tau_1 + k_v^3)^{\frac{2}{3}}}{\sin\tau_1}. \tag{34}$$

It is again convenient to distinguish a 'critical' case, such that $k = 0$ when $p = 0$, or when $\tau_1 = \pi$. This occurs when $k_v^3 = \pi$; and the solution with this value of the constant is shown in figure 6. The integration of (34), which has been carried out numerically, must be started at an arbitrary value of τ_1, since the virtual origin is at $\xi = -\infty$ (as it is for a pair vortex in a uniform ambient

fluid). The pair, however, comes to rest at a finite height above the real origin, with a finite radius, as is shown more clearly in figure 9.

As examples of the other forms of solution possible, we have taken the cases $k_v^3 = 4$ and $k_v^3 = 2$. When $k_v^3 > \pi$, and there is excess vorticity in the pair, the solution (figure 7) indicates that the radius begins to decrease soon after the

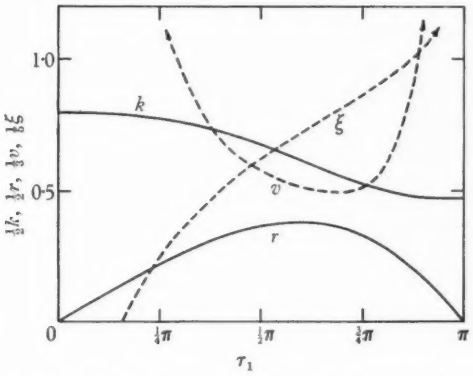

FIGURE 7. The non-dimensional solution for a buoyant vortex pair in a stably stratified fluid: $k_v^3 = 4$.

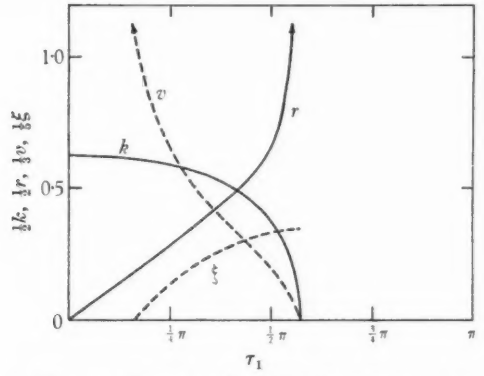

FIGURE 8. The non-dimensional solution for a buoyant vortex pair in a stably stratified fluid: $k_v^3 = 2$.

buoyancy vanishes; the velocity and distance travelled become infinite (in contrast to the corresponding vortex ring solution which gave zero radius at a finite height). Again we would suggest that physically this implies that such a buoyant pair would become unstable and suddenly mix with its surroundings at a certain height.

When k_v^3 is less than the critical value π, the radius becomes large at a finite height (figure 8). The different forms of the relation between radius and height are again shown in figure 9.

It should be noted that there is an important difference between the 'critical' conditions for vortex rings and vortex pairs. We saw in the last section that it is

meaningful to look for at least a numerical relation between the conditions in a buoyant cloud and the critical state, since these both depend only on K_v and F_v which will be little different from K_0 and F_0. For the pair vortex, however, the distribution of vorticity established through the action of buoyancy forces depends also on a length scale (equation (14)), whereas the critical condition depends explicitly on the density gradient in the surroundings (equation (29)).

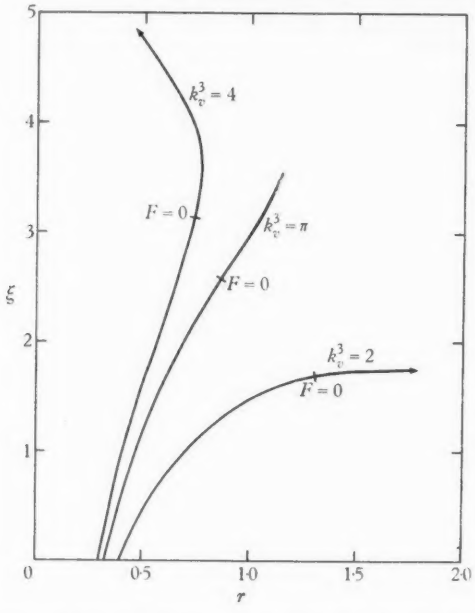

FIGURE 9. The increase of radius of buoyant vortex pairs in stably stratified surroundings as a function of height, starting from the height corresponding to $r_1 = 0{\cdot}5$. When $k_v^3 = \pi$, the pair comes to rest at a finite height and radius; when $k_v^3 > \pi$, the radius decreases soon after the buoyancy vanishes, but only becomes zero at an infinite height; and when $k_v^3 < \pi$, the radius becomes infinite near the level of zero buoyancy.

Even if experiments were available to allow us to evaluate q' and s' (and none have so far been reported), the size and the density gradient would have to be known before the appropriate solution could be applied. It seems possible in this case that all three types of solution may correspond to physical reality under some atmospheric and initial conditions.

REFERENCES

LAMB, H. 1932 *Hydrodynamics*, 6th ed. Cambridge University Press.
MORTON, B. R., TAYLOR, G. I. & TURNER, J. S. 1956 *Proc. Roy. Soc.* A, **234**, 1.
MORTON, B. R. 1959 *J. Fluid Mech.* **5**, 151.
ROUSE, H., YIH, C. S. & HUMPHREYS, H. W. 1952 *Tellus*, **4**, 201.
SCORER, R. S. 1958 *Natural Aerodynamics*. London: Pergamon Press.
TURNER, J. S. 1957 *Proc. Roy. Soc.* A, **239**, 61.
WOODWARD, B. 1959 *Quart. J. R. Met. Soc.* **85**, 144.

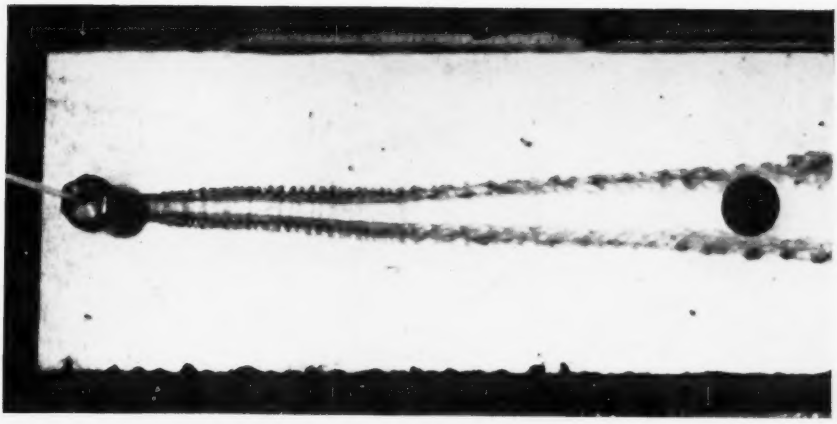

FIGURE 1 (plate 1). Photograph showing a plan view of a bent-over, buoyant plume. Note how it splits sideways into two line vortices, which spread nearly linearly with distance. The photograph was taken through the larger face of a 10 cm × 5 cm water channel; the bolt heads are spaced at 20 cm intervals. The water velocity was about 3 cm/sec, and the rate of release of buoyant fluid through a 1·5 mm tube was adjusted so that the plume bent over near the centre of the channel.

(*Facing p.* 432)

The stability of free boundary layers between two uniform streams

By T. TATSUMI AND K. GOTOH
Department of Physics, Faculty of Science, University of Kyoto, Japan

(Received 3 July 1959)

Hydrodynamic stability of free boundary-layer flows is treated in general. It is found that the situations at low Reynolds numbers are universal for all velocity profiles of free boundary-layer type. Curves of constant amplification are calculated as far as $O(R^3)$. In particular, the asymptotic form of the neutral curves for $R \doteqdot 0$ is found to be $\alpha = R/(4\sqrt{3})$, so that the critical Reynolds numbers of these flows are identically zero. The phase velocity of the disturbance is also found to be zero, for all disturbances, up to the second approximation.

A method of normalizing the velocity profiles is suggested, and existing results for the stability of various profiles at large Reynolds numbers are discussed from a new point of view.

1. Introduction

It has recently become recognized that the problem of hydrodynamic stability for unbounded laminar flows is considerably different from that for bounded flows. For instance, it has been found that a plane laminar jet in an infinite fluid is highly unstable, and its critical Reynolds number is about 4 (Tatsumi & Kakutani 1958; Howard 1959) in contrast with the value 420 for the boundary layer along a flat plate and 6000 for plane Poiseuille flow. The mathematical behaviour of the eigen-solutions in the neighbourhood of the critical Reynolds number is also quite different for unbounded and bounded flows. In the latter, the solutions are sensitive to the second spatial derivative of the velocity profile, while in the former they may be expressed in terms of definite integrals of the profile, and so are largely independent of its detailed structure.

This difference seems to be particularly marked in the case of free boundary-layer flows between two uniform streams, since, according to Esch (1957), a simple piecewise linear profile of free boundary-layer type has zero critical Reynolds number, which means that the flow is always unstable. The stability of a realistic velocity profile of free boundary-layer type was first investigated by Lessen (1950). However, since he employed a method of analysis which is effective only for large Reynolds numbers, no result was given for the critical Reynolds number, which was supposed to be very low. Even in the region of large Reynolds number which was covered by the analyses of both Lessen and Esch, the behaviour of the respective curves of neutral stability is not identical. According to Lessen's result, the range of the wave-number α corresponding to instability decreases monotonically with decreasing Reynolds number R. On the other hand, Esch's

neutral curve of $\alpha(R)$ shows a curious kink at about $R = 10$ giving there a widest wave-number range of instability. This result clearly contradicts the general belief regarding the stability of unbounded flows that viscosity always acts on the disturbance as a stabilizing factor.

In order to clarify these points, we attempt in this paper to discuss the stability of free boundary-layer flows in general, that is, assuming no particular form of the velocity profile. The mathematical method employed here is the same as that developed by Tatsumi & Kakutani for treating a plane laminar jet at low Reynolds numbers (Tatsumi & Kakutani 1958; this paper will be referred to hereafter as I).

The asymptotic behaviour of the neutral curve and the distribution of the amplification factor in the (α, R)-plane are obtained for small values of α and R, and they are found to be *universal* for all flows of this type, if the profiles are normalized with respect to some appropriate characteristic length. Among the universal properties of free boundary-layer flows at *small* Reynolds numbers, the following two may be noted: (i) the critical Reynolds numbers of these flows are zero, and (ii) the phase velocities of all disturbances are identically zero.

If the velocity profiles are normalized so as to make their stability properties at low Reynolds numbers universal, they generally show different behaviour for larger Reynolds numbers. The above-mentioned difference between the high-R branches of Lessen's and Esch's neutral curves is therefore easily accountable from this point of view. It may be concluded in general that we cannot use a rough approximation to a velocity profile for investigating its stability at larger Reynolds numbers.

2. Formulation of the problem

Let $U(y)$ be the velocity profile of a steady plane parallel flow, taking the x-axis of Cartesian co-ordinates along the direction of the flow. In stability problems of plane flow, Squire's theorem (1933) guarantees that we need only consider two-dimensional disturbances, provided they are smaller in order of magnitude than the velocity of the undisturbed flow.

Two-dimensional disturbance velocities (u, v) may be expressed in terms of the stream function $\psi(x, y, t)$ as

$$u = \frac{\partial \psi}{\partial y}, \quad v = -\frac{\partial \psi}{\partial x}. \tag{2.1}$$

In particular, we consider here a harmonic component

$$\psi = \phi(y) \exp\{i\alpha(x - ct)\}, \tag{2.2}$$

where $\alpha\,(>0)$ represents the wave-number in the x-direction, $\mathscr{R}(c) \equiv c_r$ the phase velocity, and $\alpha\mathscr{I}(c) \equiv \alpha c_i$ the amplification factor of the disturbance. According as c_i takes positive, zero or negative values, we have an amplified, neutral or damped disturbance respectively.

Substituting (2.1) and (2.2) into the equations of motion and neglecting the non-linear terms with respect to ϕ, we obtain the Orr–Sommerfeld equation

$$\phi^{\mathrm{iv}} - 2\alpha^2\phi'' + \alpha^4\phi = i\alpha R\{(U - c)(\phi'' - \alpha^2\phi) - U''\phi\}, \tag{2.3}$$

where dashes denote the differentiation with respect to y, and all quantities are made non-dimensional using the characteristic velocity U_0, scale l, and Reynolds number $R = U_0 l/\nu$. In the following, U_0 is so chosen as to make

$$U(\infty) = 1, \quad U(-\infty) = -1, \tag{2.4}$$

and l will be specified later.

Now we divide the whole space into two regions (I) where $y > 0$, and (II) where $y < 0$, and define $U_j(y)$ $(j = \text{I}, \text{II})$ by

$$\left.\begin{aligned} U_{\text{I}}(y) &= U(y) - U(\infty) = U(y) - 1, \\ U_{\text{II}}(y) &= U(y) - U(-\infty) = U(y) + 1. \end{aligned}\right\} \tag{2.5}$$

Then equation (2.3) may be written, for the regions I and II, as

$$(D^2 - \alpha^2)(D^2 - \beta_j^2)\phi = i\alpha R\{U_j(D^2 - \alpha^2) - U_j''\}\phi, \tag{2.6}$$

where

$$D \equiv d/dy, \quad \beta_{\text{I}}^2 = \alpha^2 - i\alpha R(c-1), \quad \beta_{\text{II}}^2 = \alpha^2 - i\alpha R(c+1), \quad \mathscr{R}(\beta_j) > 0.$$

In the region (I), U_{I} and U_{I}'' on the right-hand side of equation (2.6) decrease with increasing y, and in the region (II) the same is true for U_{II} and U_{II}'' with increasing $-y$. Thus, the premises for expanding the solution ϕ in power series of αR, which was explored in § 5 of I, are satisfied in each region separately, and we can express ϕ_j in the form

$$\phi_j(y) = \sum_{n=0}^{\infty} (i\alpha R)^n \phi_j^{(n)}(y; \alpha, \beta_j), \tag{2.7}$$

where the ϕ_j's are the solutions of the following equations:

$$\left.\begin{aligned} &(D^2 - \alpha^2)(D^2 - \beta_j^2)\phi_j^{(0)} = 0, \\ &(D^2 - \alpha^2)(D^2 - \beta_j^2)\phi_j^{(n)} = \{U_j(D^2 - \alpha^2) - U_j''\}\phi_j^{(n-1)} \quad (n \geqslant 1). \end{aligned}\right\} \tag{2.8}$$

The uniform convergence of the series (2.7) can be easily verified, by extending the proof given in § 5 of I, for those velocity profiles in which U_{I} and U_{II} tend to zero as, or more rapidly than, $e^{\mp my}$ for $y \to \pm\infty$ respectively, and provided that $\alpha < m$, $\mathscr{R}(\beta_j) < m$. The above conditions for $U(y)$ are usually satisfied if the boundary-layer approximation is valid for the basic flow. For, in that case, the stream function, denoted by f, must satisfy

$$2f''' + ff'' = 0,$$

and asymptotically

$$U(y) = f'(y) \propto \frac{1}{y} e^{-my^2} + \text{const.}, \quad \text{or} \quad e^{\mp my} + \text{const.},$$

according as $f'(\pm\infty)\,[= U(\pm\infty)] \neq 0$ or $f'(\pm\infty)\,[= U(\pm\infty)] = 0$ respectively.

The boundary condition for the disturbance is that the component velocities must vanish at $y = \pm\infty$, that is,

$$\phi'(\pm\infty) = \alpha\phi(\pm\infty) = 0. \tag{2.9}$$

3. Equation for eigenvalues

Equations (2.8) permit four independent solutions for each ϕ_j, but two of them must always be rejected by the condition (2.9). Thus we have the solutions

$$\left.\begin{aligned} \phi_{\mathrm{I}} &= C_1\phi_{\mathrm{I}1}+C_2\phi_{\mathrm{I}2} \quad \text{for} \quad y>0, \\ \phi_{\mathrm{II}} &= C_3\phi_{\mathrm{II}1}+C_4\phi_{\mathrm{II}2} \quad \text{for} \quad y<0, \end{aligned}\right\} \tag{3.1}$$

where the C's are numerical constants, and $\phi_{jk}(j=\mathrm{I},\mathrm{II};\ k=1,2)$ are given by

$$\phi_{jk} = \sum_{n=0}^{\infty} (i\alpha R)^n \phi_{jk}^{(n)}(y;\alpha,\beta_j), \tag{3.2}$$

with
$$\phi_{\mathrm{I}1}^{(0)} = e^{-\alpha y}, \quad \phi_{\mathrm{I}2}^{(0)} = e^{-\beta_{\mathrm{I}} y}, \quad \phi_{\mathrm{II}1}^{(0)} = e^{\alpha y}, \quad \phi_{\mathrm{II}2}^{(0)} = e^{\beta_{\mathrm{II}} y}, \tag{3.3}$$

and

$$\phi_{jk}^{(n)} = \frac{1}{\alpha^2-\beta_j^2}\left[e^{-\alpha y}\int_{\pm\infty}^{y} U_j e^{\alpha y}(D+\alpha)\phi_{jk}^{(n-1)}\,dy + e^{\alpha y}\int_{\pm\infty}^{y} U_j e^{-\alpha y}(D-\alpha)\phi_{jk}^{(n-1)}\,dy\right.$$
$$\left. - e^{-\beta_j y}\int_{\pm\infty}^{y} U_j e^{\beta_j y}\left(D+\frac{\alpha^2+\beta_j^2}{2\beta_j}\right)\phi_{jk}^{(n-1)}\,dy - e^{\beta_j y}\int_{\pm\infty}^{y} U_j e^{-\beta_j y}\left(D-\frac{\alpha^2+\beta_j^2}{2\beta_j}\right)\phi_{jk}^{(n-1)}\,dy\right] \tag{3.4}$$

$$(j=\mathrm{I},\mathrm{II}, \quad k=1,2, \quad n\geqslant 1),$$

where $\pm\infty$ in the integrals must be taken as $+\infty$ and $-\infty$ for $j=\mathrm{I}$ and II respectively.

In order to obtain the complete solution ϕ of (2.3) throughout $-\infty<y<\infty$, we have to connect ϕ_{I} and ϕ_{II} analytically at $y=0$. This is done by putting

$$\left.\begin{aligned} &\phi_{\mathrm{I}}(0)=\phi_{\mathrm{II}}(0), \quad \phi_{\mathrm{I}}'(0)=\phi_{\mathrm{II}}'(0), \\ &\phi_{\mathrm{I}}''(0)=\phi_{\mathrm{II}}''(0), \quad \phi_{\mathrm{I}}'''(0)=\phi_{\mathrm{II}}'''(0), \end{aligned}\right\} \tag{3.5}$$

equality of all other higher derivatives being then automatically satisfied through these conditions and equation (2.3). Substituting (3.1) into (3.5), we have the following condition for all C's not to vanish:

$$E \equiv \begin{vmatrix} \phi_{\mathrm{I}1}(0) & \phi_{\mathrm{I}2}(0) & \phi_{\mathrm{II}1}(0) & \phi_{\mathrm{II}2}(0) \\ \phi_{\mathrm{I}1}'(0) & \phi_{\mathrm{I}2}'(0) & \phi_{\mathrm{II}1}'(0) & \phi_{\mathrm{II}2}'(0) \\ \phi_{\mathrm{I}1}''(0) & \phi_{\mathrm{I}2}''(0) & \phi_{\mathrm{II}1}''(0) & \phi_{\mathrm{II}2}''(0) \\ \phi_{\mathrm{I}1}'''(0) & \phi_{\mathrm{I}2}'''(0) & \phi_{\mathrm{II}1}'''(0) & \phi_{\mathrm{II}2}'''(0) \end{vmatrix} = 0. \tag{3.6}$$

This equation gives a relationship between eigenvalues of α, R and c. For real values of c it defines α as a function of R, which may be shown graphically in the (α, R)-plane as the neutral curve.

4. Eigenvalue problem for small α and R

Equation (3.6), with (3.2), (3.3) and (3.4) substituted, can be expanded into powers of $i\alpha R$ as follows:

$$E \equiv \sum_{m=0}^{\infty}\sum_{n=0}^{\infty}\sum_{p=0}^{\infty}\sum_{q=0}^{\infty} (i\alpha R)^{m+n+p+q} E_{mnpq} = 0, \tag{4.1}$$

where

$$E_{mnpq} = \begin{vmatrix} I_{\mathrm{I}1}^{(m)} - J_{\mathrm{I}1}^{(m)} & I_{\mathrm{I}2}^{(n)} - J_{\mathrm{I}2}^{(n)} & I_{\mathrm{II}1}^{(p)} - J_{\mathrm{II}1}^{(p)} \\ \alpha M_{\mathrm{I}1}^{(m)} - \beta_{\mathrm{I}} N_{\mathrm{I}1}^{(m)} & \alpha M_{\mathrm{I}2}^{(n)} - \beta_{\mathrm{I}} N_{\mathrm{I}2}^{(n)} & \alpha M_{\mathrm{II}1}^{(p)} - \beta_{\mathrm{II}} N_{\mathrm{II}1}^{(p)} \\ (\alpha^2 - \beta_{\mathrm{I}}^2) J_{\mathrm{I}1}^{(m)} & (\alpha^2 - \beta_{\mathrm{I}}^2) J_{\mathrm{I}2}^{(n)} & (\alpha^2 - \beta_{\mathrm{II}}^2) J_{\mathrm{II}1}^{(p)} - 2i\alpha R(I_{\mathrm{II}1}^{(p)} - J_{\mathrm{II}1}^{(p)}) \\ \beta_{\mathrm{I}}(\alpha^2 - \beta_{\mathrm{I}}^2) N_{\mathrm{I}1}^{(m)} & \beta_{\mathrm{I}}(\alpha^2 - \beta_{\mathrm{I}}^2) N_{\mathrm{I}2}^{(n)} & \beta_{\mathrm{II}}(\alpha^2 - \beta_{\mathrm{II}}^2) N_{\mathrm{II}1}^{(p)} + 2i\alpha R(\alpha M_{\mathrm{II}1}^{(p)} - \beta_{\mathrm{II}} N_{\mathrm{II}1}^{(p)}) \end{vmatrix}$$

$$\begin{vmatrix} I_{\mathrm{II}2}^{(q)} - J_{\mathrm{II}2}^{(q)} \\ \alpha M_{\mathrm{II}2}^{(q)} - \beta_{\mathrm{II}} N_{\mathrm{II}2}^{(q)} \\ (\alpha^2 - \beta_{\mathrm{II}}^2) J_{\mathrm{II}2}^{(q)} - 2i\alpha R(I_{\mathrm{II}2}^{(q)} - J_{\mathrm{II}2}^{(q)}) \\ \beta_{\mathrm{II}}(\alpha^2 - \beta_{\mathrm{II}}^2) N_{\mathrm{II}2}^{(q)} + 2i\alpha R(\alpha M_{\mathrm{II}2}^{(q)} - \beta_{\mathrm{II}} N_{\mathrm{II}2}^{(q)}) \end{vmatrix} \tag{4.2}$$

with
$$\left.\begin{aligned} I_{j1}^{(0)} &= 1, & I_{j2}^{(0)} &= 0, & J_{j1}^{(0)} &= 0, & J_{j2}^{(0)} &= -1, \\ M_{j1}^{(0)} &= (-1)^j, & M_{j2}^{(0)} &= 0, & N_{j1}^{(0)} &= 0, & N_{j2}^{(0)} &= (-1)^{j+1}, \end{aligned}\right\} \tag{4.3}$$

and

$$\left.\begin{aligned} I_{jk}^{(n)} &= \frac{2}{\beta_j^2 - \alpha^2} \int_0^{\pm\infty} U_j(y) \{\cosh(\alpha y) D + \alpha \sinh(\alpha y)\} \phi_{jk}^{(n-1)}(y)\, dy, \\ J_{jk}^{(n)} &= \frac{2}{\beta_j^2 - \alpha^2} \int_0^{\pm\infty} U_j(y) \left\{\cosh(\beta_j y) D + \frac{\alpha^2 + \beta_j^2}{2\beta_j} \sinh(\beta_j y)\right\} \phi_{jk}^{(n-1)}(y)\, dy, \\ M_{jk}^{(n)} &= \frac{-2}{\beta_j^2 - \alpha^2} \int_0^{\pm\infty} U_j(y) \{\sinh(\alpha y) D + \alpha \cosh(\alpha y)\} \phi_{jk}^{(n-1)}(y)\, dy, \\ N_{jk}^{(n)} &= \frac{-2}{\beta_j^2 - \alpha^2} \int_0^{\pm\infty} U_j(y) \left\{\sinh(\beta_j y) D + \frac{\alpha^2 + \beta_j^2}{2\beta_j} \cosh(\beta_j y)\right\} \phi_{jk}^{(n-1)}(y)\, dy \quad (n \geqslant 1). \end{aligned}\right\} \tag{4.4}$$

In principle we can calculate $\alpha(R, c)$ for any value of R by solving equation (4.1), so far as the conditions $\alpha < m$, $\mathscr{R}\{\beta_j\} < m$ $(j = \mathrm{I}, \mathrm{II})$ are satisfied. In practice however, the computation becomes laborious for large R, for then we have to take more and more terms in order to obtain accurate solutions. Here we shall restrict ourselves to the study of equation (4.1) in the region of small α and R. Then, expanding E_{mnpq} again into powers of α and β_j, and retaining only first few terms, we obtain the following equation for eigenvalues:

$$E = \{1 + \tfrac{1}{2}(\beta_{\mathrm{I}} - \beta_{\mathrm{II}})(V_{\mathrm{I}} - V_{\mathrm{II}}) + \tfrac{1}{8}(\beta_{\mathrm{I}} - \beta_{\mathrm{II}})^2 (V_{\mathrm{I}} - V_{\mathrm{II}})^2\} \times \{2\alpha(\alpha - \beta_{\mathrm{I}})(\beta_{\mathrm{II}} - \alpha)(\beta_{\mathrm{I}} + \beta_{\mathrm{II}})\} F = 0, \tag{4.5}$$

with
$$\left.\begin{aligned} F &= \{\beta_{\mathrm{I}}^2 + \beta_{\mathrm{II}}^2 - \beta_{\mathrm{I}}\beta_{\mathrm{II}} + \alpha(\beta_{\mathrm{I}} + \beta_{\mathrm{II}}) + \alpha^2\} \\ &\quad - \tfrac{1}{2}(\beta_{\mathrm{I}} - \beta_{\mathrm{II}})^2 [\{\beta_{\mathrm{I}}^2 + \beta_{\mathrm{II}}^2 - \beta_{\mathrm{I}}\beta_{\mathrm{II}} + \alpha(\beta_{\mathrm{I}} + \beta_{\mathrm{II}}) + \alpha^2\} \\ &\quad + (\beta_{\mathrm{I}} + \beta_{\mathrm{II}})(\beta_{\mathrm{I}} + \beta_{\mathrm{II}} - 2\alpha)] [W_{\mathrm{I}} - W_{\mathrm{II}} + \tfrac{1}{4}(V_{\mathrm{I}} - V_{\mathrm{II}})^2] + O(\alpha^5, \beta_j^5), \\ V_{\mathrm{I}} &= \int_0^{\infty} U_{\mathrm{I}}\, dy, \quad V_{\mathrm{II}} = \int_0^{-\infty} U_{\mathrm{II}}\, dy, \\ W_{\mathrm{I}} &= \int_0^{\infty} y U_{\mathrm{I}}\, dy, \quad W_{\mathrm{II}} = \int_0^{-\infty} y U_{\mathrm{II}}\, dy, \end{aligned}\right\} \tag{4.6}$$

where use is made of the relationship $\beta_{\mathrm{I}}^2 - \beta_{\mathrm{II}}^2 = 2i\alpha R$.

The first factor of the right-hand side of (4.5) comes from arbitrariness in the choice of the origin of y, and does not affect the eigenvalue problem. In fact, if we choose $y = 0$ so as to make $V_{\mathrm{I}} = V_{\mathrm{II}}$, this factor becomes unity. The second factor, put equal to zero, gives only a trivial solution: $R = 0$ and $\alpha = 0$. Thus the true eigenvalue equation must be

$$F = 0, \tag{4.7}$$

in which it is confirmed, as a matter of course, that the factor

$$[W_{\mathrm{I}} - W_{\mathrm{II}} + \tfrac{1}{4}(V_{\mathrm{I}} - V_{\mathrm{II}})^2]$$

is independent of the choice of the origin of y.

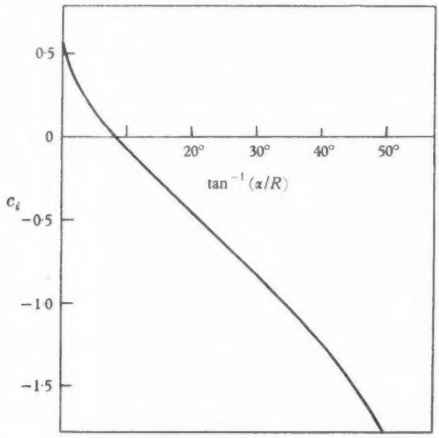

FIGURE 1. Distribution of c_i for small α and R.

As the first approximation, we take the equation

$$\beta_{\mathrm{I}}^2 + \beta_{\mathrm{II}}^2 - \beta_{\mathrm{I}}\beta_{\mathrm{II}} + \alpha(\beta_{\mathrm{I}} + \beta_{\mathrm{II}}) + \alpha^2 = 0, \tag{4.8}$$

the solution of which is given, under the conditions $\alpha > 0$, $\alpha R > 0$, $\mathscr{R}\{\beta_j\} > 0$ $(j = \mathrm{I}, \mathrm{II})$, by

$$\left.\begin{aligned} \alpha &= \frac{(1-\sqrt{3}\,c_i)^2}{4(\sqrt{3}-c_i)}\,R, \\ c_r &= 0. \end{aligned}\right\} \tag{4.9}$$

From (4.9) we obtain the distribution of the amplification factor c_i over the (α, R)-plane as shown in figure 1. Putting $c_i = 0$ in (4.9), we have the asymptotic neutral curve for small R

$$\alpha = \frac{R}{4\sqrt{3}}, \tag{4.10}$$

which agrees with the result obtained by Esch (1957) for a piecewise linear profile. It should be noted that the results (4.9) and (4.10) apply universally to all velocity profiles of the free boundary-layer type, that is, those profiles in which $U(\infty)$ and $U(-\infty)$ have a finite difference.

The second-approximate solution of (4.7) may be obtained by perturbation of the first approximation as

$$\left.\begin{aligned}\alpha &= \frac{(1-\sqrt{3}\,c_i)^2}{4(\sqrt{3}-c_i)}\,R\left\{1-\frac{(1-3c_i^2)\,(7-2\sqrt{3}\,c_i+c_i^2)}{4\sqrt{3}(\sqrt{3}-c_i)^3}\,(W_{\mathrm{I}}-W_{\mathrm{II}})\,R^2+O(R^3)\right\},\\ c_r &= 0.\end{aligned}\right\} \tag{4.11}$$

Thus, for the neutral curve,

$$\alpha = \frac{R}{4\sqrt{3}}\{1-\tfrac{7}{360}(W_{\mathrm{I}}-W_{\mathrm{II}})\,R^2+O(R^3)\}. \tag{4.12}$$

5. Discussion

It may be seen from (4.11) that the velocity profile $U(y)$ enters the problem only through the factor $W_{\mathrm{I}}-W_{\mathrm{II}}$. As we have left the characteristic length l unspecified, we have now the liberty of choosing l so as to make

$$W_{\mathrm{II}}-W_{\mathrm{I}} = 1. \tag{5.1}$$

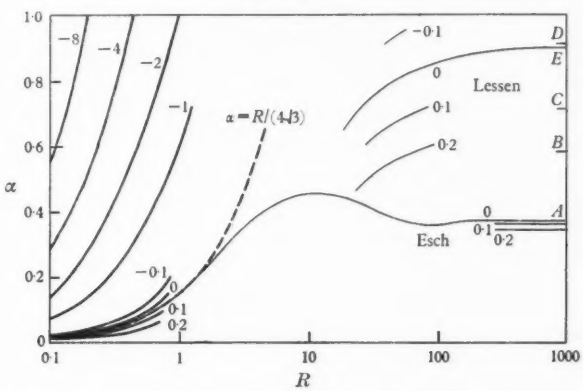

FIGURE 2. Curve of constant c_i. Numbers attached to the curves denote values of c_i.

With this choice of the characteristic length, the asymptotic behaviour of the curves of constant c_i becomes universal up to $O(R^3)$. These curves (including the neutral curve) calculated from (4.11) and (4.12) are shown in figure 2.

Figure 2 also shows the results obtained by Lessen (1950) and Esch (1957) for the asymptotic branch of the neutral curve at higher Reynolds numbers, their velocity profiles being normalized as to satisfy the condition (5.1). As is clearly seen from figure 2, the solutions cease to be universal for Reynolds numbers which are not small, and the neutral curves have different limiting values of wavenumber, α_s say, for infinite Reynolds number. It is of course possible to choose l so as to make the high Reynolds number branches of any two neutral curves coincide, but then the situation at small Reynolds numbers is no longer unique. Since the condition (5.1) gives an absolute rule for determining l which is valid not only for a given pair of profiles but also for all possible profiles of free boundary-layer type, it seems most meaningful to adopt this condition for normalizing the velocity profiles.

As the neutral curves of Lessen's and Esch's profiles show a common feature that α does not change appreciably with R for larger values of R, the same trend may be expected to hold for other profiles, and high Reynolds number branches of their neutral curves may be well approximated by $\alpha = \text{const.} = \alpha_s$. Thus it may be concluded that if we want to investigate the stability problem of a free boundary-layer flow using some approximate velocity profile, the profile must be such that it gives α_s close to that of the exact profile. The limiting wavenumber α_s has been calculated for a number of typical velocity profiles, and its numerical values are tabulated in table 1 and marked in figure 2. It may be seen from table 1 that the profile $U(y) = \tanh ky$ gives the closest approximation to Lessen's profile which was obtained by solving the boundary-layer equation numerically.

	Antisymmetric profile	α_s
A	$\begin{cases} 0 < ky < 1,\ U = ky; \\ 1 < ky,\ U = 1;\ k = 1/\sqrt{3} \end{cases}$	0·37
B	$\begin{cases} 0 < 2ky < 1,\ U = ky; \\ 1 < 2ky < 3,\ U = (2ky+1)/4; \\ 3 < 2ky,\ U = 1;\ k = \sqrt{7}/4 \end{cases}$	0·58
C	$U = 2\,\mathrm{erf}\,ky - 1,\ k = 1/\sqrt{2}$	0·71
D	$U = \tanh ky,\ k = \pi/2\sqrt{3}$	0·91
	Asymmetric profile	
E	Numerical solution (Lessen)	0·90

TABLE 1

Equation (4.11) also shows that the relation $c_r = 0$ holds up to the second approximation. In a general co-ordinate system which is free from the condition (2.4), this relation may be expressed as

$$c_r = \tfrac{1}{2}\{U(\infty) + U(-\infty)\}. \tag{5.2}$$

It is unlikely, however, that (5.2) is universally valid for all Reynolds numbers and profiles, and if not it must fail to be satisfied at some higher stage of approximation. If the velocity profile is antisymmetric with respect to y, $c_r = 0$ follows from the uniqueness of ϕ for given α and R. Since $U(-y) = -U(y)$ for this profile, we have, replacing y by $-y$ in the Orr–Sommerfeld equation (2.3),

$$\begin{aligned}\phi^{\mathrm{iv}}(-y) - 2\alpha^2\phi''(-y) + \alpha^4\phi(-y) \\ = -i\alpha R[(U+c)\{\phi''(-y) - \alpha^2\phi(-y)\} - U''\phi(-y)].\end{aligned} \tag{5.3}$$

If we put $\chi(y) \equiv \overline{\phi}(-y)$, the equation for $\chi(y)$ is written, taking the complex conjugate of (5.3), as

$$\chi^{\mathrm{iv}} - 2\alpha^2\chi'' + \alpha^4\chi = i\alpha R\{(U+\bar{c})(\chi'' - \alpha^2\chi) - U''\chi\}. \tag{5.4}$$

Equation (5.4) for $\chi(y)$ is identical with equation (2.3) for $\phi(y)$, and therefore if the latter has a unique solution for given α and R, the eigen-solutions χ and ϕ must be equal, and so are the eigenvalues c and $-\bar{c}$, thus giving that $c_r = 0$. But so far nothing is known about the uniqueness of this eigenvalue problem.

One of the essential weaknesses in applying the usual procedure of hydrodynamic stability theory to low Reynolds number flows seems to lie in its fundamental assumption that the undisturbed flow is, at least approximately, parallel. This assumption is generally satisfied when Reynolds number of the flow is sufficiently large, but it becomes difficult at small Reynolds numbers to maintain parallel flows unless some body force is applied from outside. Therefore, without such external forces, the results obtained by treating the flows as essentially parallel become unrealistic for small Reynolds numbers, and they should only be accepted with these reservations in mind.

The authors wish to express their cordial thanks to Prof. S. Tomotika for his interest to this work. During the course of this work the authors have been in receipt of a grant-in-aid for fundamental scientific research from the Ministry of Education of Japan.

REFERENCES

Esch, R. E. 1957 *J. Fluid Mech.* **3**, 289.

Howard, L. N. 1959 *J. Math. Phys.* **37**, 283.

Lessen, M. 1950 *Rep. Nat. Adv. Comm. Aero., Wash.* no. 979.

Squire, H. B. 1933 *Proc. Roy. Soc.* A, **142**, 621.

Tatsumi, T. & Kakutani, T. 1958 *J. Fluid Mech.* **4**, 261.

A note on fluctuating heat transfer at small Péclet numbers

By C. R. ILLINGWORTH
Department of Mathematics, University of Manchester

(Received 29 June 1959)

1. Introduction

The hot-wire anemometer, used for recording speed variations in turbulent flow, involves in its working principle the unsteady heat transfer from a hot fixed surface to a fluctuating air stream moving past the surface. If the wire is maintained at a constant (high) temperature, the rate of loss of heat from the wire changes with the velocity of the incident stream, and the compensating rate of gain of heat, produced by the Joule heating effect of the electric current, changes correspondingly. The accompanying change of current can be measured, and used to calculate the varying velocity of the air stream. The hot wire may have a diameter as low as 10^{-4} in. and the Reynolds number of the flow is then of the order of 0·05 for each ft. per sec of velocity. With low velocities, of the order of 10 or 20 ft./sec, the flow past the wire is in the range of small Reynolds number, and the exact equations of flow may be approximated by simpler equations in the manner of Oseen's theory (Lamb 1932). The approximate equations are not easy to solve when the flow is compressible, as it will be in the presence of the large temperature differences imposed by the heat of the wire. If, however, the temperature differences are assumed to be small, the approximate energy equation is no longer linked with the equations of continuity and momentum, and it may be solved without knowledge of the velocity field. The purpose of this note is to give the solution for the temperature field when a warm circular cylinder or a warm sphere is held at rest in a fluctuating stream.

2. The temperature equation

The energy equation from which we start may be written as

$$\rho \frac{D}{Dt}(c_p T) = \operatorname{div}(\lambda \operatorname{grad} T), \tag{1}$$

where t is the time, ρ the density, T the temperature, c_p the specific heat at constant pressure, and λ the thermal conductivity. This equation differs from the exact energy equation, for a compressible fluid, in the omission of the rate of working of the pressure forces and the rate of heat production through the action of viscosity. The weights of these omitted terms are in the ratio M^2: $(\chi - 1)$ compared with the terms retained, where M is the Mach number of the free stream and χ is T_w/T_∞, the ratio of the temperatures of the obstacle and the free stream. In quoting (1) we have assumed that $M^2 \ll (\chi - 1)$, and we now go further and

assume also that $\chi - 1 \ll 1$ so that temperature differences in the flow are small. This allows us to neglect density variations and to regard λ as a constant, so that (1) becomes

$$\frac{DT}{Dt} = \kappa \nabla^2 T, \tag{2}$$

where κ is the thermometric conductivity. If the stream is slow moving, (2) can be replaced by the Oseen-type equation

$$\left(\frac{\partial}{\partial t} + U_\infty \frac{\partial}{\partial x}\right) T = \kappa \nabla^2 T, \tag{3}$$

in which U_∞ is the velocity of the free stream and x is the Cartesian co-ordinate in the direction of U_∞. In this equation, the convection term $\mathbf{v}.\mathrm{grad}\, T$ from (2) has been replaced by its form at infinity; if it is omitted altogether, on the grounds that $\mathbf{v}$ and $\mathrm{grad}\, T$ are both small, the Stokes-type equation

$$\frac{\partial T}{\partial t} = \kappa \nabla^2 T \tag{4}$$

is obtained, but this yields a solution for a circular cylinder that cannot satisfy the boundary condition at infinity.

We may notice at this point that if we introduce non-dimensional variables

$$\tilde{t} = \omega t, \quad \tilde{x} = Px/l, \tag{5}$$

in which ω is a representative frequency in the fluctuating motion, l is a representative length, and P is the Péclet number Ul/κ, where U is a representative velocity, then (3) becomes

$$\frac{\omega\kappa}{U^2}\frac{\partial T}{\partial \tilde{t}} + \frac{U_\infty}{U}\frac{\partial T}{\partial \tilde{x}} = \tilde{\nabla}^2 T. \tag{6}$$

This shows that (3) stands as the appropriate form of the energy equation provided $\omega\kappa/U^2$ is $O(1)$, but that if ω is very small the term $\partial T/\partial t$ can be omitted (the quasi-steady case), and if ω is very large the term $U_\infty \partial T/\partial x$ is negligible so that the equation reduces to Stokes's form. If we denote the Reynolds number Ul/ν by R, and the Prandtl number by σ, the Péclet number P is σR. For air, with $\sigma = 0{\cdot}72$, smallness of the Reynolds number implies smallness of the Péclet number, but, as (5) and (6) indicate, it is the Péclet number and not the Reynolds number which is the fundamental parameter in this problem.

We shall now assume that the free stream is fluctuating in simple harmonic motion about a mean value U with a small amplitude and an angular frequency ω, so that

$$U_\infty = U(1 + \epsilon e^{i\omega t}), \tag{7}$$

where $\epsilon \ll 1$. If the temperature is expressed in terms of a function f by the relation

$$T = T_\infty[1 + (\chi - 1)f], \tag{8}$$

equation (3) becomes

$$\frac{\partial f}{\partial t} + U(1 + \epsilon e^{i\omega t})\frac{\partial f}{\partial x} = \kappa \nabla^2 f, \tag{9}$$

and f must satisfy the boundary conditions: $f = 1$ on the obstacle, $f \to 0$ at infinity.

It is appropriate to write

$$f = f_0 + \epsilon e^{i\omega t} f_1, \tag{10}$$

where f_0, f_1 satisfy

$$\left(\nabla^2 - 2k\frac{\partial}{\partial x}\right) f_0 = 0, \tag{11}$$

$$\left(\nabla^2 - 2k\frac{\partial}{\partial x} - \frac{i\omega}{\kappa}\right) f_1 = 2k\frac{\partial f_0}{\partial x}, \tag{12}$$

in which $k = U/2\kappa$. Finally, with the substitutions

$$f_0 = e^{kx} g_0, \quad f_1 = e^{kx} g_1,$$

equations (11) and (12) reduce to

$$(\nabla^2 - k^2) g_0 = 0, \tag{13}$$

$$[\nabla^2 - (k^2 + i\omega/\kappa)] g_1 = 2k\left(\frac{\partial g_0}{\partial x} + k g_0\right), \tag{14}$$

with the boundary conditions:

$$g_0 = e^{-kx}, \quad g_1 = 0, \quad \text{on the obstacle,} \tag{15}$$

$$g_0 \to 0, \quad g_1 \to 0, \quad \text{at infinity.} \tag{16}$$

3. Circular cylinder

In plane polar co-ordinates r, θ, the appropriate solution of (13) is

$$g_0 = \sum_{m=0}^{\infty} a_m K_m(s) \cos m\theta, \tag{17}$$

where the a_m are constants to be determined, K_m is a Bessel function in the usual notation (Watson 1944) and $s = kr$. The function g_0 must be a single-valued even function of θ that vanishes for large r. From the boundary condition (15),

$$\sum_{m=0}^{\infty} a_m K_m(s_0) \cos m\theta = e^{-s_0 \cos\theta}, \tag{18}$$

where $s_0 = ka$, and a is the radius of the cylinder; and since

$$e^{-s\cos\theta} = I_0(s) + 2\sum_{m=0}^{\infty} (-1)^m I_m(s) \cos m\theta,$$

it follows that

$$a_m = \begin{cases} I_0(s_0)/K_0(s_0) & (m = 0), \\ 2(-1)^m I_m(s_0)/K_m(s_0) & (m \geqslant 1). \end{cases} \tag{19}$$

Equation (14) in polar co-ordinates is

$$(\nabla^2 - \alpha^2 k^2) g_1 = 2k^2\left[\cos\theta\frac{\partial g_0}{\partial s} - \frac{\sin\theta}{s}\frac{\partial g_0}{\partial \theta} + g_0\right]$$

$$= 2k^2 \sum_{m=0}^{\infty} A_m K_m(s) \cos m\theta, \tag{20}$$

where

$$A_m = \begin{cases} \dfrac{1}{s_0 K_0(s_0) K_1(s_0)} & (m = 0), \\ \dfrac{2(-1)^{m+1} K_m'(s_0)}{s_0 K_{m-1}(s_0) K_m(s_0) K_{m+1}(s_0)} & (m \geqslant 1). \end{cases} \tag{21}$$

Also

$$\alpha^2 = 1 + \frac{i\omega}{k^2\kappa} = 1 + \frac{4ih}{P}, \tag{22}$$

in which h is the frequency parameter $\omega l/U$; in the present case, $l = 2a$. The required solution of (20), vanishing at $s = s_0$ and $s = \infty$, is

$$g_1 = \frac{iP}{2h} \sum_{m=0}^{\infty} A_m \left[K_m(s) - \frac{K_m(s_0)}{K_m(\alpha s_0)} K_m(\alpha s) \right] \cos m\theta. \tag{23}$$

Since $$e^{s\cos\theta} \cos m\theta = I_m(s) + \sum_{n=1}^{\infty} [I_{m-n}(s) + I_{m+n}(s)] \cos n\theta,$$

we obtain $$f_0 = \sum_{m=0}^{\infty} \sum_{n=0}^{\infty} a_m F_{mn}(s, s) \cos n\theta, \tag{24}$$

where $$F_{mn}(\xi, \eta) = \begin{cases} K_m(\xi)\, I_m(\eta) & (n = 0), \\ K_m(\xi)\, [I_{m-n}(\eta) + I_{m+n}(\eta)] & (n \geqslant 1), \end{cases} \tag{25}$$

and $$f_1 = \frac{iP}{2h} \sum_{m=0}^{\infty} \sum_{n=0}^{\infty} A_m \left[F_{mn}(s, s) - \frac{K_m(s_0)}{K_m(\alpha s_0)} F_{mn}(\alpha s, s) \right] \cos n\theta. \tag{26}$$

This completes the required solution for the temperature distribution.

It remains to determine the fluctuating heat transfer from the cylinder to the stream. The total heat flux per unit length from the cylinder is

$$Q = -\int_0^{2\pi} \lambda \left(\frac{\partial T}{\partial r} \right)_{r=a} a\, d\theta,$$

and the corresponding Nusselt number, defined as

$$C_q = \frac{Q}{2\pi a [\lambda (T_w - T_\infty)/2a]},$$

is given by $$C_q = -\frac{ka}{\pi} \int_0^{2\pi} \left(\frac{\partial f}{\partial s} \right)_{s=s_0} d\theta.$$

It follows that $$C_q = C_{q0} + \epsilon\, e^{i\omega t} C_{q1}, \tag{27}$$

where $$C_{q0} = 2 \left[\frac{I_0(s_0)}{K_0(s_0)} + 2 \sum_{m=1}^{\infty} (-1)^m \frac{I_m(s_0)}{K_m(s_0)} \right], \tag{28}$$

and $$C_{q1} = -\frac{iP^2}{4h} \sum_{m=0}^{\infty} A_m K_m(s_0)\, I_m(s_0) \left[\frac{K'_m(s_0)}{K_m(s_0)} - \frac{\alpha K'_m(\alpha s_0)}{K_m(\alpha s_0)} \right]. \tag{29}$$

These expressions are, however, in a more general form than the Oseen approximation warrants, for the approximation is only valid if P, which is equal to $4s_0$, is small. Accordingly, we replace the Bessel functions by their series expansions for small values of the argument. If we write

$$\beta = \frac{P}{8} \quad \text{and} \quad L(\beta) = [\ln(\beta^{-1}) - \gamma]^{-1}, \tag{30}$$

where γ is Euler's constant, we obtain from (21)

$$A_0 = L(\beta) + [2 - L^2(\beta)]\, \beta^2 + O(\beta^4),$$
$$A_1 = -L(\beta) - [4 - L^2(\beta)]\, \beta^2 + O(\beta^4),$$
$$A_2 = 2\beta^2 + O(\beta^4),$$
$$A_n = O(\beta^{2n-2}) \quad \text{for} \quad n \geqslant 3.$$

It follows from (28) and (29), when terms $O(\beta^4)$ are neglected, that

$$C_{q0} = 2\{L(\beta) - [4 + L^2(\beta)]\beta^2\}, \tag{31}$$

$$C_{q1} = i\frac{8\beta}{h}\left\{L(\beta) - L(\alpha\beta) + \left[\alpha^2 L^2(\alpha\beta) - L^2(\beta) + 2\left(\alpha^2\frac{L(\beta)}{L(\alpha\beta)} - \frac{L(\alpha\beta)}{L(\beta)}\right) + \frac{ih}{\beta}(L(\alpha\beta)+1)\right]\beta^2\right\}. \tag{32}$$

In quoting these formulae we must remember that they would be modified if the second approximation to the convection term $\mathbf{v}.\mathrm{grad}\,T$ in (2) were used instead of the first approximation $U_\infty(\partial/\partial x)$ shown in (3). To introduce the second approximation would require the calculation of the fluctuating velocity field according to Oseen's equations. Recent work improving the Oseen theory for the velocity field in steady flow past a circular cylinder (Kaplun 1957) suggests that the

$\beta(=\frac{1}{8}P)$	0·01	0·02	0·04	0·06	0·08	0·10
C^*_{q1}	0·123	0·180	0·287	0·400	0·527	0·672
β	0·12	0·14	0·16	0·18	0·20	—
C^*_{q1}	0·840	1·037	1·269	1·545	1·877	—

TABLE 1

$4h/P$	0·1		0·2		0·4		0·6		0·8		1·0	
β	m	$\delta°$	m	$\delta°$	m	$\delta°$	m	$\delta°$	m	$\delta°$	m	$\delta°$
0·01	0·998	2·15	0·994	4·27	0·977	8·31	0·952	11·97	0·923	15·20	0·892	18·00
0·02	0·999	2·00	0·994	3·97	0·978	7·73	0·955	11·14	0·928	14·13	0·899	16·74
0·04	0·999	1·78	0·995	3·53	0·980	6·86	0·959	9·87	0·934	12·50	0·907	14·77
0·06	0·999	1·58	0·995	3·14	0·982	6·09	0·962	8·75	0·939	11·06	0·914	13·03
0·08	0·999	1·39	0·996	2·76	0·983	5·38	0·965	7·67	0·943	9·66	0·920	11·33
0·10	0·999	1·20	0·996	2·38	0·984	4·61	0·967	6·57	0·947	8·24	0·925	9·62
0·12	0·999	1·01	0·996	1·99	0·985	3·84	0·969	5·44	0·950	6·76	0·930	7·81
0·14	0·999	0·86	0·996	1·58	0·986	3·02	0·971	4·24	0·953	5·20	0·933	5·90
0·16	0·999	0·58	0·996	1·14	0·987	2·16	0·972	2·97	0·955	3·53	0·936	3·86
0·18	0·999	0·34	0·997	0·67	0·987	1·23	0·973	1·59	0·956	1·73	0·938	1·65
0·20	0·999	0·09	0·997	0·16	0·987	0·21	0·974	0·09	0·957	−0·24	0·938	−0·76

It will be noted that there is a phase lag of the heat transfer behind the velocity fluctuation, except at the two highest frequencies (in the last two columns) for the highest Péclet number quoted, for which there is a phase advance.

TABLE 2

leading term, $2L(\beta)$, in C_{q0} would be modified, although only slightly for small values of β, in the next approximation. The effect on the terms in β^2 is likely to be considerable, so we shall confine attention here to the leading terms in the expressions for C_{q0} and C_{q1}. Actually the term involving β^2 in (31) is only about 7 % of the leading term for a Reynolds number of 1 in air ($\beta = 0{\cdot}09$), and it is an even smaller fraction for smaller Reynolds numbers. It is therefore certainly permissible to concentrate on the leading terms.

It will be convenient to introduce the quasi-steady value of the expression

$$C_{q1} = i\frac{8\beta}{h}[L(\beta) - L(\alpha\beta)],$$

obtained by letting the frequency tend to zero ($h \to 0$ and $\alpha \to 1$). This is given by

$$C_{q1}^{*} = 2L^2(\beta), \tag{33}$$

and we shall then write

$$\frac{C_{q1}}{C_{q1}^{*}} = i\,\frac{4\beta}{h}\,\frac{L(\beta)-L(\alpha\beta)}{L^2(\beta)} = m\,e^{-i\delta}, \tag{34}$$

where m is the magnification factor and δ the phase lag of the fluctuating component of the heat transfer compared with its quasi-steady value. Values of C_{q1}^{*} for a range of Péclet numbers are given in Table 1, and the values of m amd δ for various frequencies and for the same range of Péclet numbers are given in Table 2.

4. Sphere

Although it is not relevant to the hot-wire anemometer, the corresponding problem of fluctuating heat transfer from a warm sphere will now be briefly considered. With spherical polar co-ordinates r, θ, λ, there is no dependence on the azimuthal angle λ because of axial symmetry, and the required solution of (13) may be written as

$$g_0 = \sum_{m=0}^{\infty} a_m \chi_m(s)\, P_m(\cos\theta), \tag{35}$$

where the a_m are constants to be determined,

$$\chi_m(s) = (2m+1)\,(\pi/2s)^{\frac{1}{2}}\, K_{m+\frac{1}{2}}(s), \tag{36}$$

and P_m denotes the Legrendre polynomial of degree m. Since

$$e^{-s\cos\theta} = \sum_{m=0}^{\infty} (-1)^m\,(2m+1)\,(\pi/2s)^{\frac{1}{2}}\, I_{m+\frac{1}{2}}(s)\, P_m(\cos\theta),$$

the boundary condition corresponding to (18) gives

$$a_m = (-1)^m\,\frac{I_{m+\frac{1}{2}}(s_0)}{K_{m+\frac{1}{2}}(s_0)}. \tag{37}$$

The equation corresponding to (20) is

$$(\nabla^2 - \alpha^2 k^2)\, g_1 = 2k^2 \sum_{m=0}^{\infty} A_m \chi_m(s)\, P_m(\cos\theta), \tag{38}$$

where

$$A_m = (-1)^{m+1}\left[K'_{m+\frac{1}{2}}(s_0) + \frac{K_{m+\frac{1}{2}}(s_0)}{2s_0}\right][s_0 K_{m-\frac{1}{2}}(s_0)\, K_{m+\frac{1}{2}}(s_0)\, K_{m+\frac{3}{2}}(s_0)]^{-1}.$$

The required solution of (38), vanishing at the surface of the sphere and at infinity, is

$$g_1 = \frac{iP}{2h} \sum_{m=0}^{\infty} A_m \left[\chi_m(s) - \frac{\chi_m(s_0)}{\chi_m(\alpha s_0)}\,\chi_m(\alpha s)\right] P_m(\cos\theta). \tag{39}$$

Since

$$e^{s\cos\theta} P_m(\cos\theta) = \sum_{n=0}^{\infty} e_{mn}(s)\, P_n(\cos\theta),$$

where

$$e_{mn}(s) = (2n+1) \sum_{r=0}^{\infty} \frac{(2r)!\,(2m-2r)!\,(2n-2r)!}{(r!)^2\,(2m+2n-2r+1)!} \left[\frac{(m+n-r)!}{(m-r)!\,(n-r)!}\right]^2 \times (2m+2n-4r+1)\,(\pi/2s)^{\frac{1}{2}}\, I_{m+n-2r+\frac{1}{2}}(s),$$

it follows that

$$f_0 = \sum_{m=0}^{\infty} \sum_{n=0}^{\infty} a_m F_{mn}(s, s)\, P_n(\cos\theta),$$

where

$$F_{mn}(\xi, \eta) = \chi_m(\xi)\, e_{mn}(\eta), \tag{40}$$

and

$$f_1 = \frac{iP}{2h} \sum_{m=0}^{\infty} \sum_{n=0}^{\infty} A_m \left[F_{mn}(s, s) - \frac{\chi_m(s_0)}{\chi_m(\alpha s_0)} F_{mn}(\alpha s, s) \right] P_n(\cos\theta). \tag{41}$$

The heat flux from the surface of the sphere is

$$Q = -\int_0^{\pi} \lambda \left(\frac{\partial T}{\partial r} \right)_{r=a} 2\pi a^2 \sin\theta \, d\theta$$

and the Nusselt number, defined as

$$C_q = \frac{Q}{4\pi a^2 [\lambda (T_w - T_\infty)/2a]},$$

is given by

$$C_q = -ka \int_{-1}^{1} \left(\frac{\partial f}{\partial s} \right)_{s=s_0} d(\cos\theta).$$

$4h/P$	0·1	0·2	0·4	0·6	0·8	1·0
m	0·999	0·996	0·986	0·970	0·952	0·931
$\delta°$	1·43	2·85	5·59	8·15	10·49	12·62

TABLE 3

Hence

$$C_q = C_{q0} + \epsilon\, e^{i\omega t} C_{q1}, \tag{42}$$

where

$$C_{q0} = \frac{\pi}{s_0} \sum_{m=0}^{\infty} (2m+1)(-1)^m \frac{I_{m+\frac{1}{2}}(s_0)}{K_{m+\frac{1}{2}}(s_0)}, \tag{43}$$

and

$$C_{q1} = -\frac{i\pi P}{2h} \sum_{m=0}^{\infty} (2m+1) A_m I_{m+\frac{1}{2}}(s_0) K_{m+\frac{1}{2}}(s_0) \left[\frac{K'_{m+\frac{1}{2}}(s_0)}{K_{m+\frac{1}{2}}(s_0)} - \frac{\alpha K'_{m+\frac{1}{2}}(\alpha s_0)}{K_{m+\frac{1}{2}}(\alpha s_0)} \right]. \tag{44}$$

As before, we must restrict attention to small values of the arguments of the Bessel functions, and we obtain

$$C_{q0} = 2 + 4\beta + O(\beta^2), \tag{45}$$

$$C_{q1} = -\frac{2iP}{h}(\alpha - 1)\beta + O(\beta^2). \tag{46}$$

We have not included terms $O(\beta^2)$ because they are likely to be modified when the neglected convection terms are brought back into the energy equation. The quasi-steady value of C_{q1} is

$$C^*_{q1} = 4\beta,$$

and so

$$\frac{C_{q1}}{C^*_{q1}} = m\, e^{-i\delta} = -\frac{iP}{2h}(\alpha - 1).$$

This is a function of h/P only, and the values of m and δ for the same range of values of h/P as were used for the circular cylinder are given in Table 3.

REFERENCES

KAPLUN, S. 1957 *J. Math. Mech.* **6**, 595–603.

LAMB, SIR HORACE 1932 *Hydrodynamics*, 6th edition. Cambridge University Press.

WATSON, G. N. 1944 *Theory of Bessel Functions*, 2nd edition. Cambridge University Press.

On the motion of thin airfoils in fluids of finite electrical conductivity

By JAMES E. McCUNE
Cornell University, Ithaca, New York†

(Received 29 September 1958 and in revised form 4 May 1959)

A two-dimensional, small-perturbation theory for the steady motion of thin lifting airfoils in an incompressible conducting fluid, with the uniform applied magnetic field perpendicular to (and in the plane of) the undisturbed, uniform flow field, is described. The conductivity of the fluid is assumed to be such that the magnetic Reynolds number, R_m, of the flow is large but finite. Within this assumption, a theory based on superposition of sinusoidal modes is constructed and applied to some simple thin airfoil problems.

It is shown that with this particular field geometry the Alfvén wave mechanism is important in making possible very deep penetration into the flow field of currents and their associated vorticity. It is also shown that the current penetration for an airfoil is much larger than for a wavy wall of wavelength equal to the airfoil chord.

A value of $R_m = 5$ is found to be a good approximation to infinity in this study; in fact, use of the present technique for values of R_m of the order of unity is permissible. These results provide an indication of what is meant by 'large' magnetic Reynolds number in two-dimensional magneto-aerodynamics.

Introduction

In a recent paper Sears & Resler (1959) have developed basic small-perturbation theories for the interaction of the steady two-dimensional motion of an inviscid, incompressible fluid of large conductivity (i.e. large magnetic Reynolds number, R_m) with magnetic fields of two different orientations. They were concerned primarily with the case of infinite R_m; for that case they succeeded in determining the pressure distributions on perfectly insulating sinusoidal walls and thin airfoils when the applied magnetic field is either parallel or perpendicular to (and in the plane of) the undisturbed, uniform flow field. For easy reference we refer to these two orientations as 'aligned' or 'crossed'.

The extensive results obtained by Sears & Resler divide essentially into two parts, depending on the orientation of the applied magnetic field. In the case of aligned fields the basic irrotational flow pattern is unchanged if $R_m = \infty$; the essential new phenomenon is the appearance of surface currents that modify the values of the normal stresses acting on the flow boundaries, whether wavy wall or thin airfoil. These stresses remain in phase with the classical (no magnetic field) surface pressures, and no drag results from the magneto-aerodynamic interaction. When the magnetic Reynolds number is large but finite, on the other hand, the

† Now with Aeronautical Research Associates of Princeton, Inc.

surface currents diffuse into the flow field a distance proportional to $R_m^{-\frac{1}{2}}$ and a boundary layer of current appears. The stresses on the surface are unchanged so long as the 'boundary-layer' approximation holds, and again no drag is predicted. This last result enhances the importance, for aligned fields, of the infinite-conductivity theories.

The important phenomena when the applied magnetic field and undisturbed fluid velocity are mutually perpendicular are markedly different. For infinite R_m standing waves analogous to Mach waves appear, and these waves (which arise from the Alfvén mechanism) carry vorticity and current into the flow field. An important feature of the theory is the appearance of an irrotational elliptic part of the flow field in conjunction with the rotational part arising from the Alfvén mechanism. The pressures on the boundaries are modified from their classical values in the crossed-fields case in such a way that a net drag appears corresponding to the energy carried off by the Alfvén waves. When large but finite values of R_m are introduced, the current and vorticity waves become diffused as they move away from the body. The situation is then analogous to the viscous attenuation of sound waves (Rayleigh 1946; Lighthill 1956) rather than to boundary-layer phenomena.

Sears & Resler have not analysed the finite R_m case for crossed-fields except to show how sinusoidal waves decay. However, the pressures and forces acting on an insulating wavy wall are modified for crossed-fields by the introduction of finite values of R_m (Resler & McCune 1960); so it is important to investigate the extent to which the general infinite R_m theory of Sears & Resler must be modified in this case to allow calculation of significant aerodynamic quantities for finite values of R_m. It is of particular interest to investigate how far into the flow-field current waves actually penetrate for finite bodies (as contrasted with the infinite sinusoidal wall). The results of such a study can be used as a measure of the possible importance, for typical aerodynamic configurations, of electro-magnetic interaction with the flow field.

The present paper presents techniques applicable to linearized, incompressible magneto-aerodynamic problems involving a combination of the phenomena of Alfvén propagation and current diffusion set up by flows past bodies made of perfectly insulating material. The central concern of the paper is with the finite-conductivity magneto-aerodynamic flow fields of cylindrical bodies of finite chord, e.g. thin airfoils, and a procedure using Fourier synthesis of sinusoidal modes (in an approximate form valid for large R_m) is suggested.

As a basis for this approach, the exact sinusoidal solutions of the governing equations are described and relations between the rotational parts of the magnetic and velocity fields are developed for each mode. The solutions given are more general than those of Sears & Resler, since they hold for all R_m, but they are only a special case of more recent results (Resler & McCune 1960) which include effects of compressibility and arbitrary field orientation.

These sinusoidal modes, of course, can be used to obtain the flow past infinite sinusoidal walls; examples have been worked out in detail by Resler & McCune. In order to give a preliminary indication of the range of validity of the present large R_m approximation, exact results for the pressures on an infinite insulating

sinusoidal wall are quoted from the latter work and compared with results obtained for the same problem using the approximate form of the sinusoidal modes.

In the main portion of the paper a theory applicable to flows past thin airfoils, when the magnetic Reynolds number is large but finite, is developed for the crossed-fields configuration. As in the infinite-conductivity case, rotational and irrotational parts of the field appear. The technique used here is to construct the *rotational part* of the field by means of superposition of the appropriate sinusoidal modes and to relate this to the *irrotational part* through the boundary conditions at the insulating body. This procedure leads to the formulation of a boundary-value problem of mixed type (see, for example, equations (35*a*, *b*)), which provides the extension of the Sears–Resler theory to finite values of R_m. Both the rotational and irrotational parts of the field are modified for finite R_m.

The method, which is correct to order $(4\pi R_m)^{-1}$, is worked out in the present paper only for the lifting airfoil of zero thickness; the thickness problem can be treated by a completely analogous procedure. The cyclic constant of the elliptic field is determined in this paper by application of the Kutta condition, which requires that the pressure be continuous at the trailing edge of the airfoil.

One of the results of the theory is a practical estimate of the depth of penetration of the current into the flow field for values of R_m of the order of one or greater.

The linearized equations

The governing equations of magneto-aerodynamics have been discussed recently by several authors (see, for example, Cowling (1957) and Resler & Sears (1958)). Our present interest is in the form these equations take for steady, two-dimensional inviscid motion.

Let us denote dimensional quantities by ($\hat{}$). The assumption of two-dimensionality requires that the electric field have only a single component normal to the flow

$$\hat{\mathbf{E}} = (0, 0, \hat{E}), \tag{1}$$

whereas the condition of steady flow requires (Faraday's Law)

$$\operatorname{curl} \hat{\mathbf{E}} = 0. \tag{2}$$

Equations (1) and (2) together imply that $\hat{\mathbf{E}} = \hat{E}\mathbf{k}$ is constant throughout the flow field.

The governing equations can be linearized in accordance with the following conditions. The disturbance-free configuration consists of a uniform electrically conducting incompressible inviscid fluid stream of speed U in the presence of a uniform applied magnetic field of strength H_∞ oriented normal to the free-stream direction in the plane of the flow. In the absence of disturbances it is specified that *no currents flow*, thus implying that the constant value of the electric field is $-UH_\infty$. The electrical conductivity, σ, of the gas is considered a scalar and constant throughout the field, and displacement currents are neglected.

We write the velocity vector $\hat{\mathbf{q}} = (U + \hat{u}, \hat{v}, 0)$ and the magnetic-field vector $\hat{\mathbf{H}} = (\hat{h}_x, H_\infty + \hat{h}_y, 0)$ and assume

$$\frac{\hat{u}}{U}, \frac{\hat{v}}{U} \ll 1 \quad \text{and} \quad \frac{\hat{h}_x}{H_\infty}, \frac{\hat{h}_y}{H_\infty} \ll 1.$$

Under these conditions both the momentum equation and Ohm's Law can be linearized and written in dimensionless form

$$\frac{\partial \mathbf{q}}{\partial x} + \nabla p = \frac{1}{m^2}\left(\frac{\partial \mathbf{H}}{\partial y} - \nabla h_y\right), \tag{3}$$

$$\frac{\xi}{4\pi R_m} = u + h_y, \tag{4}$$

where p is the fluid pressure, ξ denotes the magnitude of curl $\mathbf{H} = (0, 0, \xi)$, and Ampère's Law has been used to replace the current by curl $\mathbf{H}$. Absolute electromagnetic units have been used and a magnetic permeability of unity (non-ferromagnetic materials) assumed throughout.

The dimensionless parameters† $R_m \equiv \sigma U L$ and $m \equiv U\sqrt{(4\pi\rho)}/H_\infty$ are respectively the magnetic Reynolds number and the ratio of the free-stream speed to the Alfvén speed (which might be called the 'magnetic Mach number'). Dimensional quantities, denoted by ($\hat{}$), are obtained from the dimensionless ones through the definitions

$$\left.\begin{aligned} &\hat{p} = \rho U^2 p, \quad \hat{\mathbf{q}} = U\mathbf{q}, \quad (\hat{x}, \hat{y}, \hat{z}) = L(x, y, z), \\ &\hat{\mathbf{H}} = H_\infty \mathbf{H}, \quad \hat{\mathbf{j}} = \sigma U H_\infty \mathbf{j}, \\ &\hat{\boldsymbol{\xi}} \equiv \operatorname{curl} \hat{\mathbf{H}} = \frac{H_\infty}{L} \operatorname{curl} \mathbf{H} \equiv \frac{H_\infty}{L}\boldsymbol{\xi}, \end{aligned}\right\} \tag{5}$$

where ρ is the mass density, $\hat{\mathbf{j}}$ is the current density, and L is some appropriate length for the given problem.

Equation (4) is available in such simple form only in two-dimensional cases where $\hat{\mathbf{E}}$ is constant and known. An alternative expression which is sometimes useful can be obtained by taking the curl of Ohm's Law, thus eliminating $\hat{\mathbf{E}}$ through equation (2). In linearized, dimensionless form the result is

$$\frac{\partial \mathbf{H}}{\partial x} - \frac{\partial \mathbf{q}}{\partial y} = \frac{1}{4\pi R_m}\nabla^2 \mathbf{H}. \tag{6}$$

This relation is correct for any (linearized) steady flow with the crossed-field orientation.

Taking the divergence of (3) yields

$$\nabla^2\left(p + \frac{1}{m^2}h_y\right) = 0 \quad \text{(for any value of } R_m\text{)}, \tag{7}$$

since div $\mathbf{H}$ and div $\mathbf{q}$ are zero. Finally, taking the curls of (3) and (6) and cross-differentiating, one finds (Sears & Resler 1959)

$$\frac{\partial^2 \xi}{\partial x^2} - \frac{1}{m^2}\frac{\partial^2 \xi}{\partial y^2} = \frac{1}{4\pi R_m}\nabla^2 \frac{\partial \xi}{\partial x} \tag{8}$$

and

$$\frac{\partial^2 \Omega}{\partial x^2} - \frac{1}{m^2}\frac{\partial^2 \Omega}{\partial y^2} = \frac{1}{4\pi m^2 R_m}\nabla^2 \frac{\partial \xi}{\partial y}, \tag{9}$$

where Ω is the magnitude of the curl of the velocity field. Note that if $R_m = \infty$, both ξ and Ω obey wave equations.

It is of interest to note that when R_m is large but finite, equation (8) can easily be put into a form analogous with the damped sound-wave equation first studied

† In the absolute e.m.u. system of units the conductivity has purely mechanical dimensions. The R_m defined here differs from that used by some authors by a factor of 4π.

by Stokes and recently analysed further by Lighthill (1956). (In the process, terms of order R_m^{-2} are neglected.) By noting that

$$\nabla^2 \frac{\partial \xi}{\partial x} = \frac{\partial}{\partial x} \nabla^2 \xi \quad \text{and that} \quad \frac{\partial^2 \xi}{\partial x^2} = \frac{1}{m^2} \frac{\partial^2 \xi}{\partial y} + O(R_m^{-1}),$$

we can write (8) in the iterative forms

$$\frac{\partial^2 \xi}{\partial x^2} - \frac{1}{m^2} \frac{\partial^2 \xi}{\partial y^2} \approx \frac{1}{4\pi R_m} (1 + m^{-2}) \frac{\partial^2 \xi}{\partial y^2 \, \partial x} \tag{10a}$$

$$\approx \frac{1}{4\pi R_m} (1 + m^2) \frac{\partial^3 \xi}{\partial x^3}. \tag{10b}$$

Equation (10a) is in the form of Lighthill's equations (31), p. 267.

The basic sinusoidal modes

In this section we shall develop the basic relationships between the sinusoidal modes of the velocity and magnetic fields needed for our subsequent Fourier synthesis method of treating finite-body problems.

Any of equations (8), (10a) or (10b) can be solved approximately for general flows in exactly the same way as in the treatment given by Lighthill. First, however, we may observe that equation (8) can be solved exactly for an elementary sinusoidal mode, yielding a solution, valid for any value of R_m, which takes the form

$$\xi_\lambda(x, y) = A_\lambda e^{i\lambda x} \exp\left[\mp \lambda m y \sqrt{\left\{ -\left(1 - \frac{i\lambda}{4\pi R_m}\right) \Big/ \left(1 + \frac{i\lambda m^2}{4\pi R_m}\right) \right\}} \right] \tag{11}$$

for $y \gtrless 0$. This expression is useful in making clear the behaviour of a sinusoidal current 'wave' for any value of R_m, large or small. It can in fact be used to construct the flow field for a wavy wall for all R_m (Resler & McCune 1960). We are primarily interested here, however, in the form assumed by equation (11) when R_m is large, since the superposition theory for flows past finite bodies is relatively simple only when the square root in (11) is expanded for either large or small R_m.

When $\lambda(m^2 + 1)/4\pi R_m$ is small compared with one,† the solution (11) takes the approximate form, for $y \gtrless 0$,

$$\xi_\lambda(x, y) \approx A_\lambda e^{i\lambda(x - my)} e^{\mp \lambda^2 \gamma y}, \tag{12}$$

where

$$\gamma \equiv \frac{m(m^2 + 1)}{8\pi R_m}$$

and the boundary condition of no incoming waves has been applied. This result is given by Sears & Resler and is clearly in the form of a damped propagating wave. It is also the approximate solution to either of equations (10a) or (10b) and is in the form given by Lighthill and others for a damped, plane sound wave.

† Note that this amounts to the specification of a 'cut-off' value for the wave number λ when expansions for large values of R_m are used. Such a restriction on λ arises from the fact that the large R_m approximation depends on the magnetic Reynolds number (based on wavelength) appropriate for each mode being large. This condition must always be violated for some sufficiently high mode, but it is not expected that such violations will lead to any important errors in practical aerodynamic problems (see the later discussion). Throughout this paper the parameter m is taken to be a quantity of order unity, wherever the large R_m approximation is used.

If R_m is based on the wavelength of a sinusoidal wall and λ is taken to correspond to the fundamental mode, then $\lambda = 2\pi$. Such a wave is damped to $1/e$ its value at the wall when y has the value

$$(\lambda^2\gamma)^{-1} = \frac{2R_m}{\pi m(m^2+1)}.$$

This is the damping distance for large R_m, obtained by Sears & Resler, which is appropriate for current waves set up by the motion of a conducting fluid past a sinusoidal wall.

Substitution of (11) into (9), and use of the boundary conditions at $y = \infty$, shows that for $y \geqslant 0$

$$\left.\begin{aligned} &\Omega_\lambda(x,y) = B_\lambda\, e^{i\lambda x}\exp\left[-\lambda my\sqrt{\left\{\left(\frac{i\lambda}{4\pi R_m}-1\right)\Big/\left(1+\frac{i\lambda m^2}{4\pi R_m}\right)\right\}}\right] \\ &\text{provided} \qquad B_\lambda = +\frac{i\sqrt{\left\{\left(\frac{i\lambda}{4\pi R_m}-1\right)\Big/\left(1+\frac{i\lambda m^2}{4\pi R_m}\right)\right\}}}{m}A_\lambda. \end{aligned}\right\} \tag{13}$$

This provides the essential connexion between the curls of the velocity and magnetic fields. Equations (13) can of course be expanded in an obvious way for large values of R_m, and they then take on a form analogous to equations (12), with

$$B_\lambda \approx -\frac{(m-i\lambda\gamma)}{m^2}A_\lambda. \tag{13a}$$

If we break up the perturbation fields into rotational and irrotational parts

$$\mathbf{v} \equiv (u,v) = \mathbf{v}_R + \nabla\phi_1,$$
$$\mathbf{h} \equiv (h_x, h_y) = \mathbf{h}_R + \nabla\phi_2,$$

and keep in mind that the magnetic and velocity fields are both divergence free, (11) and (13) can be integrated immediately to give the perturbation components in the upper half plane

$$\left.\begin{aligned} u_\lambda &= -\frac{m\sqrt{\left\{\left(\frac{i\lambda}{4\pi R_m}-1\right)\left(1+\frac{i\lambda m^2}{4\pi R_m}\right)\right\}}}{\lambda(1+m^2)}B_\lambda\, e^{i\lambda x}\exp\left[-\lambda my\sqrt{\frac{\frac{i\lambda}{4\pi R_m}-1}{1+\frac{i\lambda m^2}{4\pi R_m}}}\right]+\frac{\partial\phi_1}{\partial x}, \\ v_\lambda &= -\frac{i\left(1+\frac{i\lambda m^2}{4\pi R_m}\right)}{\lambda(1+m^2)}B_\lambda\, e^{i\lambda x}\exp\left[-\lambda my\sqrt{\frac{\frac{i\lambda}{4\pi R_m}-1}{1+\frac{i\lambda m^2}{4\pi R_m}}}\right]+\frac{\partial\phi_1}{\partial y}, \\ h_{x\lambda} &= -\frac{m\sqrt{\left\{\left(\frac{i\lambda}{4\pi R_m}-1\right)\left(1+\frac{i\lambda m^2}{4\pi R_m}\right)\right\}}}{\lambda(1+m^2)}A_\lambda\, e^{i\lambda x}\exp\left[-\lambda my\sqrt{\frac{\frac{i\lambda}{4\pi R_m}-1}{1+\frac{i\lambda m^2}{4\pi R_m}}}\right]+\frac{\partial\phi_2}{\partial x}, \\ h_{y\lambda} &= -\frac{i\left(1+\frac{i\lambda m^2}{4\pi R_m}\right)}{\lambda(1+m^2)}A_\lambda\, e^{i\lambda x}\exp\left[-\lambda my\sqrt{\frac{\frac{i\lambda}{4\pi R_m}-1}{1+\frac{i\lambda m^2}{4\pi R_m}}}\right]+\frac{\partial\phi_2}{\partial y}. \end{aligned}\right\} \tag{14}$$

provided $\nabla^2\phi_1 = \nabla^2\phi_2 = 0$. This step is analogous to the procedure used by Sears & Resler and amounts to a definition of the potentials ϕ_1 and ϕ_2.

The rotational parts of the velocity and magnetic fields are related for each mode through equations (13) and (14). The potentials ϕ_1 and ϕ_2 can also be related through the linearized Ohm's Law, equation (4), by observing that equality between rotational and irrotational parts of any equation must hold separately. Thus

$$\frac{\partial\phi_1}{\partial x} = -\frac{\partial\phi_2}{\partial y} \tag{15}$$

for all R_m. Furthermore, differentiation of (15) with respect to x, use of the fact that $\nabla^2\phi_1 = 0$, and subsequent integration with respect to y shows that

$$\frac{\partial\phi_1}{\partial y} = \frac{\partial\phi_2}{\partial x} + f(x) \tag{16}$$

and $f(x) = 0$ because of the boundary condition of uniform flow at $y = \infty$. Equations (15) and (16) are general and hold for any flow field with this field orientation. They were also given by Sears & Resler for $R_m = \infty$.

The wavy wall solution

Before turning to the application of the above results to general flow problems, let us look briefly at the effects of finite conductivity in modifying the forces acting on an infinite, perfectly insulating sinusoidal wall, specified by $Y(x) = \epsilon\cos 2\pi x$. These results (Resler & McCune 1960) are merely quoted here and are intended both as an illustration of the importance of finite conductivity for crossed-fields and as an indication of the error involved in approximating the solutions for large R_m.

Resler & McCune show for the crossed-fields case that the pressure on the surface of the wavy wall is given in general by (real part implied)

$$p(x,0^+) - p_\infty = \frac{-2\pi\epsilon\left[m^2\left(1+m\sqrt{\left|\left(\frac{i\lambda}{4\pi R_m}-1\right)\Big/\left(1+\frac{i\lambda m^2}{4\pi R_m}\right)\right|}\right)+2\right]}{m\left[m+(m^2+2)\sqrt{\left|\left(\frac{i\lambda}{4\pi R_m}-1\right)\Big/\left(1+\frac{i\lambda m^2}{4\pi R_m}\right)\right|}\right]} e^{2\pi i x} \tag{17}$$

or, for large R_m and m of order unity

$$p(x,0^+) - p_\infty = \frac{-2\pi\epsilon}{m(m-2i)}\left\{m^2 - 2i - 2 + \frac{(m-i)^2}{R_m(m-2i)}\right\} e^{2\pi i x} \tag{18}$$

correct to order R_m^{-1}.

It will be seen that the first term in brackets in (18) is the same as that obtained by Sears & Resler for $R_m = \infty$. The second term represents the first correction to the pressure for finite values of R_m.

A phase diagram comparing the real and imaginary parts of $(p-p_\infty)e^{-2\pi i x}/(-2\pi\epsilon)$ for various values of R_m ranging from 0 to ∞ is presented in figure 1. It will be seen that the effect of finite R_m is to shift the phase in such a way as to decrease the drag per wavelength for any m. In fact, for large R_m the drag per wavelength is given by

$$C_D \equiv \frac{\hat{D}}{\rho U_\infty^2 L} = \frac{4\pi^2\epsilon^2}{m(m^2+4)}\left\{2 - \frac{m(m^2+2)}{R_m(m^2+4)}\right\}. \tag{19}$$

Note that for $m = 1$ and $R_m = 5$ the correction is only 6%. Expression (19) is plotted against R_m in figure 2 for $m = 1$ and $m = 3$, and compared with the exact result obtained from (17).

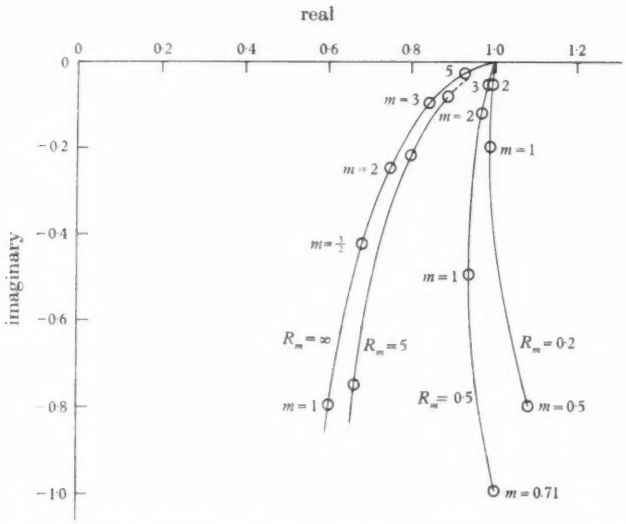

FIGURE 1. Phase diagram showing the pressure on a sinusoidal wall $Y = \epsilon \cos 2\pi x$, for crossed-fields and several values of $R_m (= \sigma UL)$ and $m (= U(4\pi\rho)^{\frac{1}{2}}/H_\infty)$. The diagram gives the real and imaginary parts of the quantity $[p(x, 0^+) - p_\infty]\, e^{-2\pi i x}/(-2\pi\epsilon)$; a negative imaginary part leads to positive drag.

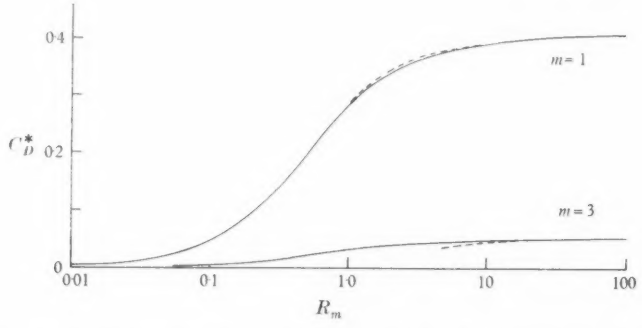

FIGURE 2. Drag per wavelength on the sinusoidal wall of figure 1. The quantity $C_D^* \equiv \hat{D}/(4\pi\rho U_\infty^2 L\epsilon^2)$ is plotted against R_m for the complete (all R_m) theory and compared with the present large R_m approximation. —, all R_m; - - - -, large R_m approximation.

It will be seen from figures 1 and 2 that for this simple case of the flow over a sinusoidal wall, a value of $R_m = 5$ is large enough to provide an acceptable approximation to infinity when m is near one; moreover, the large R_m approximation is successful near $R_m = 1$. We shall see subsequently that this result holds true also for certain typical thin airfoil problems.

Thin-airfoil theory

Use of Fourier synthesis

The results obtained above for sinusoidal modes can be used through Fourier synthesis to provide the basis for solution of any small-perturbation problem. In particular, it is useful to study the flow field associated with a lifting airfoil of small camber moving in a fluid of large but finite conductivity, in order to determine in that case the range of influence of the electro-magnetic body force.

With this in mind, and for the purposes of simplicity, we shall use the above results for the Fourier components in their approximate form for large R_m, correct to order R_m^{-1}. In view of the existence of a finite 'cut-off' value for the wave-number λ (see footnote p. 453) it will be necessary to assume that the airfoils with which we are concerned are so shaped that the higher Fourier components of the induced rotational fields are not too important. In other words, if

$$\xi(x, 0^+) = \int_{-\infty}^{\infty} A^+(\lambda)\, e^{i\lambda x}\, d\lambda \tag{20}$$

we shall generally require $A^+(\lambda)$ to vanish sufficiently strongly as $|\lambda| \to \infty$. This condition will be discussed further in a later section.

We shall introduce the notation y^+ and y^- to denote respectively the upper and lower half planes. Applying the condition that there are no incoming waves, we have from (12) the approximate relations

$$\left.\begin{aligned} \xi(x, y^+) &= \int_{-\infty}^{\infty} A^+(\lambda)\, e^{i\lambda(x - my)}\, e^{-\lambda^2 \gamma y}\, d\lambda, \\ \xi(x, y^-) &= \int_{-\infty}^{\infty} A^-(\lambda)\, e^{i\lambda(x + my)}\, e^{+\lambda^2 \gamma y}\, d\lambda. \end{aligned}\right\} \tag{21}$$

These relations can be reduced to an integration over the values of ξ on the x-axis through the use of Fourier inversion. In complete analogy with Lighthill's treatment of damped sound waves, we find

$$\left.\begin{aligned} \xi(x, y^+) &= \frac{1}{m^{\frac{3}{2}} \sqrt{\left(\frac{1}{2R_m}(1 + m^{-2})\, y\right)}} \int_{-\infty}^{\infty} \xi(u, 0^+) \exp\left[- \frac{\left(\frac{x-u}{m} - y\right)^2}{\frac{m}{2\pi R_m}(1 + m^{-2})\, y} \right] du, \\ \xi(x, y^-) &= \frac{1}{m^{\frac{3}{2}} \sqrt{\left(\frac{-1}{2R_m}(1 + m^{-2})\, y\right)}} \int_{-\infty}^{\infty} \xi(u, 0^+) \exp\left[+ \frac{\left(\frac{x-u}{m} - y\right)^2}{\frac{m}{2\pi R_m}(1 + m^{-2})\, y} \right] du. \end{aligned}\right\} \tag{22}$$

Thus, if the current density on the x-axis is known or can be determined, it is determined throughout the field.

Moreover, because the Fourier components of the *rotational parts* on the fields (u_R, v_R, h_{xR}, h_{yR}, as well as Ω and ξ) all have the same functional form, each quantity can be written for the upper and lower half planes exactly as in (22) with $\xi(u, 0)$ replaced in each case by the values of the quantity in question on the x-axis. Also, the Fourier transform of each rotational quantity can be related to

the Fourier transform of any other rotational quantity just as B_λ and A_λ were related in equation (13a). Consequently, knowledge of any one of the rotational quantities on the x-axis will determine all the others everywhere. We shall treat $v_R(x, 0^\pm)$ as the important quantity, because of its close connexion with the usual aerodynamic boundary condition at the airfoil.

The relations between the various Fourier transforms follow in a straightforward manner from the approximate form of equations (13) and (14) and their counterparts for $y < 0$. If we pair the functions and their transforms as indicated in table 1, then each of the functions listed obeys an equation like (20). Some of the important relations between the transforms that follow approximately from (13) and (14) are given in table 2, correct to order

$$\gamma = \frac{m(m^2+1)}{8\pi R_m}.$$

Function	$\xi(x, 0^\pm)$	$\Omega(x, 0^\pm)$	$h_{xR}(x, 0^\pm)$	$h_{yR}(x, 0^\pm)$	$u_R(x, 0^\pm)$	$v_R(x, 0^\pm)$
Transform	$A^\pm(\lambda)$	$B^\pm(\lambda)$	$C^\pm(\lambda)$	$D^\pm(\lambda)$	$E^\pm(\lambda)$	$F^\pm(\lambda)$

TABLE 1

$$B^\pm(\lambda) = \mp \frac{(m - i\lambda\gamma)}{m^2} A^\pm(\lambda) \tag{2.1}$$

$$B^\pm(\lambda) = [i\lambda(1+m^2) + 2\lambda^2 m\gamma] F^\pm(\lambda) \tag{2.2}$$

$$E^\pm(\lambda) = \pm (m - i\lambda\gamma) F^\pm(\lambda) \tag{2.3}$$

$$A^\pm(\lambda) = [i\lambda(1+m^2) + 2\lambda^2 m\gamma] D^\pm(\lambda) \tag{2.4}$$

$$C^\pm(\lambda) = \pm (m - i\lambda\gamma) D^\pm(\lambda) \tag{2.5}$$

$$A^\pm(\lambda) = \mp m \left[i\lambda(1+m^2) - \frac{\lambda^2\gamma}{m}(1-m^2) \right] F^\pm(\lambda) \tag{2.6}$$

$$D^\pm(\lambda) = \mp m \left(1 + \frac{i\lambda\gamma}{m}\right) F^\pm(\lambda) \tag{2.7}$$

$$C^\pm(\lambda) = -m^2 F^\pm(\lambda) \tag{2.8}$$

$$C^\pm(\lambda) = \mp m \left(1 + \frac{i\lambda\gamma}{m}\right) E^\pm(\lambda) \tag{2.9}$$

$$D^\pm(\lambda) = -m \left(1 + \frac{2i\lambda\gamma}{m}\right) E^\pm(\lambda) \tag{2.10}$$

TABLE 2

These results imply, for example, that

$$h_{xR}(x, 0^\pm) = -m^2 v_R(x, 0^\pm), \tag{23}$$

$$h_{yR}(x, 0^\pm) = \mp m \left[v_R(x, 0^\pm) + \frac{\gamma}{m} v_R'(x, 0^\pm) \right], \tag{24}$$

$$\xi(x, 0^\pm) = \mp m \left[(1+m^2) v_R'(x, 0^\pm) + \frac{\gamma}{m}(1-m^2) v_R''(x, 0^\pm) \right], \tag{25}$$

where the primes denote differentiation with respect to x at $y = 0^\pm$. Note that the symmetry properties of, say, v_R determine the symmetry properties of all the other rotational quantities.

Application of boundary conditions

We are now in a position to apply the boundary conditions appropriate to thin airfoils. For lifting airfoils of small camber and zero thickness we have as usual

$$v(x, 0^{\pm}) = Y'(x) = v_R(x, 0^{\pm}) + \left.\frac{\partial \phi_1}{\partial y}\right|_{y=0^{\pm}}$$

for
$$-\frac{c}{2L} \leqslant x \leqslant \frac{c}{2L}, \tag{26}$$

where c is the chord of the airfoil. We have further the conditions that both h_x and h_y must be continuous at $y = 0$†. Thus

$$h_{yR}(x, 0^+) - h_{yR}(x, 0^-) = -\left[\left.\frac{\partial \phi_2}{\partial y}\right|_{y=0^+} - \left.\frac{\partial \phi_2}{\partial y}\right|_{y=0^-}\right], \tag{27}$$

$$h_{xR}(x, 0^+) - h_{xR}(x, 0^-) = -\left[\left.\frac{\partial \phi_2}{\partial x}\right|_{y=0^+} - \left.\frac{\partial \phi_2}{\partial y}\right|_{y=0^-}\right]. \tag{28}$$

Substituting equation (23) into (28) we find

$$-m^2[v_R(x, 0^+) - v_R(x, 0^-)] = -\left[\left.\frac{\partial \phi_2}{\partial x}\right|_{y=0^+} - \left.\frac{\partial \phi_2}{\partial x}\right|_{y=0^-}\right] \tag{29}$$

Function	Symmetry in y	Function	Symmetry in y
v_R	Symm.	h_{yR}	Antisymm.
Ω	Symm.	u_R	Antisymm.
ξ	Antisymm.	ϕ_1	Antisymm.
h_{xR}	Symm.	ϕ_2	Symm.

TABLE 3

which, with (26), gives for all x

$$m^2\left[\left.\frac{\partial \phi_1}{\partial y}\right|_{y=0^+} - \left.\frac{\partial \phi_1}{\partial y}\right|_{y=0^-}\right] = -\left[\left.\frac{\partial \phi_2}{\partial x}\right|_{y=0^+} - \left.\frac{\partial \phi_2}{\partial x}\right|_{y=0^-}\right]. \tag{30}$$

Comparison of (30) with (16) shows that for all R_m

$$\left.\frac{\partial \phi_1}{\partial y}\right|_{y=0^+} - \left.\frac{\partial \phi_1}{\partial y}\right|_{y=0^-} = 0 \tag{31}$$

and consequently both v_R and $\partial \phi_2/\partial x$ are also continuous at $y = 0$. These results completely determine the symmetry of the problem; for example, the potential part of the flow field arises at most from a distribution of vortices over the airfoil, while the potential part of the magnetic field is due to a (fictitious) distribution of magnetic 'sources and sinks'. The symmetry is thus the same as found by Sears & Resler for $R_m = \infty$. The symmetry properties of the various quantities are listed in table 3.

Further information can be obtained by substituting (27) into Ohm's Law, equation (4): $u(x, 0^+) - u(x, 0^-) = (\xi(x, 0^+) - \xi(x, 0^-))/4\pi R_m$.

† No surface currents can exist, of course, for finite R_m in the steady state, since all currents tend to diffuse away from the boundaries. They do not exist, however, with the present field orientation, even in the limit of $R_m \to \infty$ (Sears & Resler 1959).

But in view of the symmetry properties listed in table 3 this implies

$$u(x, 0^{\pm}) = \frac{\xi(x, 0^{\pm})}{4\pi R_m}, \tag{32}$$

and also

$$h_y(x, 0^{+}) = 0 = h_y(x, 0^{-}). \tag{33}$$

The boundary-value problem for the potential flow

Equation (2.3) of table 2 implies $u_R(x, 0^{\pm}) = \pm m v_R(x, 0^{\pm}) \mp \gamma v'_R(x, 0^{\pm})$ and this result with (25) in (32) leads to a relation between $\partial\phi_1/\partial x|_{y=0^+}$ and $v_R(x, 0)$

$$\begin{aligned} \left.\frac{\partial \phi_1}{\partial x}\right|_{y=0^+} &= -\frac{m(m^2+1)}{4\pi R_m} v'_R(x, 0) - m v_R(x, 0) + \frac{m(m^2+1)}{8\pi R_m} v'_R(x, 0) \\ &= -m v_R(x, 0) - \gamma v'_R(x, 0) \end{aligned} \tag{34}$$

correct to order R_m^{-1}. Eliminating v_R with (26) and iterating in the resulting formula, one easily finds the alternative relations

$$\left.\frac{\partial \phi_1}{\partial x}\right|_{y=0^+} = m \left.\frac{\partial \phi_1}{\partial y}\right|_{y=0^+} - m\, Y'(x) + \gamma \left.\frac{\partial^2 \phi_1}{\partial y\, \partial x}\right|_{y=0^+} - \gamma\, Y''(x) + O(\gamma^2). \tag{35a}$$

$$\left.\frac{\partial \phi_1}{\partial x}\right|_{y=0} = m \frac{\partial \phi_1}{\partial y} - m\, Y'(x) + \frac{\gamma}{m} \left.\frac{\partial^2 \phi_1}{\partial x^2}\right|_{y=0^+} + O(\gamma^2) \tag{35b}$$

for

$$-\frac{c}{2L} \leqslant x \leqslant \frac{c}{2L},$$

either of which provides the necessary boundary conditions for the potential field when added to conditions of vanishing perturbations at infinity and the symmetry properties already determined. It will be seen later that while (35*b*) appears to be in a nicer form it is probably not uniformly valid. For most purposes (35*a*) will be more useful than (35*b*).

The first two terms in the right-hand side of equations (35) will be recognized as forming the potential-flow boundary condition for the infinite R_m case previously determined by Sears & Resler. The last terms in equation (35*a*) represent the first correction of the boundary condition for ϕ_1 due to the fact that R_m is finite. Thus, not only is the rotational part of the field modified when R_m is finite, but also the irrotational field is changed through the boundary condition.

Solution of the potential problem leads to a complete determination of the flow field (within the limitations already stated) since knowledge of $\partial\phi_1/\partial y$ determines v_R on the airfoil through the boundary condition (26). Moreover, v_R is zero off the airfoil (on the x-axis), as can be seen in the following manner: using the results of table 2 with equation (32), we can integrate the x-component of equation (3) on the x-axis to obtain

$$p(x, 0^{\pm}) - p_\infty = -\frac{m^2+1}{m^2} h_{yR}(x, 0^{\pm}) = \pm \frac{(m^2+1)}{m} v_R(x, 0) \pm \frac{\gamma}{m^2}(m^2+1)\, v'_R(x, 0) \tag{36}$$

correct to order R_m^{-1}. But the pressure perturbations must vanish on the x-axis off the airfoil from symmetry considerations, so $h_{yR}(x, 0^{\pm})$ and its derivatives must vanish off the airfoil. Furthermore, equation (2.7) of table 2 shows that

$$v_R(x, 0) = \mp \frac{1}{m} h_{yR}(x, 0^{\pm}) \pm \frac{\gamma}{m^2} h'_{yR}(x, 0^{\pm}) \tag{37}$$

again correct to R_m^{-1}. Consequently, v_R is known on the entire x-axis, and all rotational quantities, including the currents, are determined, once ϕ_1 is determined.

In addition, the pressure on the boundaries is immediately determined upon solution of the potential problem, since comparison of equations (36) and (34) shows that

$$p(x, 0^{\pm}) - p_\infty = -\frac{m^2+1}{m^2}\left.\frac{\partial \phi_1}{\partial x}\right|_{y=0^{\pm}}, \tag{38}$$

which also implies that

$$h_{yR}(x, 0^{\pm}) = \left.\frac{\partial \phi_1}{\partial x}\right|_{y=0^{\pm}}. \tag{39}$$

This last relation determines $\partial\phi_2/\partial y|_{y=0^{\pm}}$, in view of equation (33).

Note, finally, that the Kutta condition is satisfied, through equation (38), provided only that $\partial\phi_1/\partial x|_{y=0^+}$ is finite at the trailing edge.

Application to thin airfoils

(*a*) *Direct problem*

The potential-flow boundary condition (35*a*) presents a rather formidable boundary-value problem when only $Y'(x)$ is given, since it amounts to a differential equation relating potential derivatives of different order on the airfoil. For example, the solution due to Rott & Cheng (1954), available when $R_m = \infty$, no longer applies.

The theory of conjugate functions enables one to write (35*a*) as an integro-differential equation in $\partial\phi_1/\partial y|_{y=0^+}$

$$m\left.\frac{\partial \phi_1}{\partial y}\right|_{y=0^+} = \frac{1}{\pi}\sqrt{\left(\frac{(c/2L)-x}{(c/2L)+x}\right)}\,\mathscr{P}\int_{-c/2L}^{c/2L}\left.\frac{\partial \phi_1}{\partial y}\right|_{y=0^+}\sqrt{\left(\frac{(c/2L)+\zeta}{(c/2L)-\zeta}\right)}\frac{d\zeta}{x-\zeta} + m\,Y'(x) - \gamma\frac{\partial}{\partial x}\left[\left.\frac{\partial \phi_1}{\partial y}\right|_{y=0^+}\right] + \gamma\,Y''(x) \tag{40}$$

in which the Kutta condition has been applied. The symbol $\mathscr{P}$ denotes the Cauchy principal value. Solution of equation (40) is beyond the scope of the present paper and will be left for future research.

Another approach to the problem, which is somewhat more revealing at this early stage, is to use the Glauert series (Glauert 1926) appropriate for that family of flows wherein

$$\left.\frac{\partial \phi_1}{\partial y}\right|_{y=0^+} = -\sum_{n=0}^{\infty} B_n \cos n\theta; \quad \frac{2Lx}{c} = \cos\theta. \tag{41}$$

The Glauert theory shows that in such cases

$$\left.\frac{\partial \phi_1}{\partial x}\right|_{y=0^+} = B_0\frac{1-\cos\theta}{\sin\theta} + \sum_{n=1}^{\infty} B_n \sin n\theta \tag{42}$$

and it can be seen that this satisfies the Kutta condition at the trailing edge. Moreover, because of equation (38), the loading is

$$l(x) \equiv -4(p(x, 0^+) - p_\infty) = \frac{4(m^2+1)}{m^2}\left.\frac{\partial \phi_1}{\partial x}\right|_{y=0^+} = \frac{4(m^2+1)}{m^2}\left(B_0\frac{1-\cos\theta}{\sin\theta} + \sum_{n=1}^{\infty} B_n \sin n\theta\right) \tag{43}$$

and the lift coefficient becomes

$$C_l = \frac{\text{lift per unit span}}{\frac{1}{2}\rho U_\infty^2 c} = 2\pi\left(\frac{m^2+1}{m^2}\right)\{B_0 + \tfrac{1}{2}B_1\}. \tag{44}$$

It should be noted that the limit $m \to \infty$ gives the classical formula.

Unfortunately, these simple results cannot be taken too seriously, since the profile shapes that correspond to this family of solutions are quite unusual. The condition (35a) implies in this case that

$$Y'(x) + \frac{\gamma}{m}Y''(x) = -\frac{B_0}{m}\left\{\frac{1-\cos\theta}{\sin\theta} + m\right\} - \sum_{n=1}^{\infty} B_n\left\{\cos n\theta + \frac{1}{m}\sin n\theta + \frac{2L\gamma}{cm}\, n\frac{\sin n\theta}{\sin\theta}\right\}. \tag{45}$$

The profiles corresponding to (45) have singular slopes at the leading edge and singular curvatures at the leading and trailing edges, unless B_0 vanishes. Such geometrical details appear to be necessary in order to set up the family of flows satisfying the Glauert relations, but it is unlikely that real fluids, acting in the presence of boundary layers and unable to respond to detailed profile contours, would actually show the kind of behaviour indicated in (42).

It should be mentioned here that application of (35b) in replacing either (40) or (45) will result in generally more severe singularities at the leading edge (either in the flow field or in the profile shape) than those present when $R_m = \infty$. The iterative procedure used in obtaining (35b) from (35a) is consequently not uniformly valid and should be applied only with great care.

(*b*) *Indirect problem*

Equation (45) illustrates that even the indirect problem of aerodynamics, wherein the pressure is specified and the profile shape is required, is not necessarily simple. Specification of the pressure amounts to specification of $\partial\phi_1/\partial x|_{y=0^+}$ (equation (38)), and from this $\partial\phi_1/\partial y|_{y=0^+}$ can immediately be determined from the familiar relation

$$\left.\frac{\partial\phi_1}{\partial y}\right|_{y=0^+} = -\frac{1}{\pi}\mathscr{P}\int_{-c/2L}^{c/2L}\left.\frac{\partial\phi_1}{\partial x}\right|_{y=0^+}\frac{d\zeta}{x-\zeta}. \tag{46}$$

If $\partial\phi_1/\partial x|_{y=0^+}$ is not singular, this relation, along with the specified value of $\partial\phi_1/\partial x|_{y=0^+}$, can be substituted into (35b) to determine $Y'(x)$. If $\partial\phi_1/\partial x|_{y=0^+}$ is singular, (35a) must be used.

A simple example of the indirect problem for $R_m = \infty$ was given by Sears & Resler. They specified that the loading be elliptic (proportional to $\sin\theta$) and determined the corresponding profile shape. As an example of the use of the present theory, we may repeat their procedure for finite values of R_m.

If the loading is elliptic, only B_1 in the Glauert series is non-zero. Then (45) becomes

$$Y'(x) + \frac{\gamma}{m}Y''(x) = -B_1\left\{\cos\theta + \frac{1}{m}\sin\theta + \frac{2L\gamma}{mc}\right\}. \tag{47}$$

Hence

$$Y(x) = -B_1\left\{(x^2 - \tfrac{1}{4}) + \frac{x}{2m}\sqrt{(1-4x^2)} - \frac{1}{4m}\cos^{-1}2x - \frac{\gamma}{m^2}\sqrt{(1-4x^2)}\right\}, \tag{48}$$

where L has been identified with the airfoil chord, c, and the value of $Y(\frac{1}{2})$ has arbitrarily been put equal to zero. This airfoil shape has been plotted in figure 3 for several values of m and R_m, under the restriction that the magnitude of the loading be the same for each case.

The airfoil shapes shown in figure 3 for $m < \infty$ amount to airfoils of small camber at an angle of attack. The effect of the magnetic field, therefore, is to change the pressure distribution for a given airfoil from essentially that of a flat plate (with leading-edge singularity) to a case of 'shockless entry' with symmetrical loading. Consequently, the magnetic field has a strong (generally

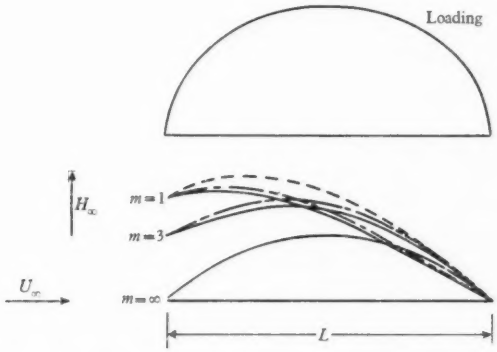

FIGURE 3. Airfoil camber lines producing an elliptic loading for various values of R_m and m. $m=\infty$ gives the classical result for all R_m; the curve $R_m = 1$ is included only for the case $m = 1$. The comparison is made for the same magnitude of the loading (cf. equation (43)). —, $R_m=\infty$ (Sears & Resler 1959); - - - - $R_m = 1$; —·—·, $R_m = 5$. $R_m=\sigma U_\infty L$.

favourable) effect on the boundary layer and provides a means of shifting the centre of pressure. However, it is clear that except for $m = \infty$ (zero magnetic-field strength) each airfoil is associated with a positive drag. This drag arises from wave energy carried away by the Alfvén mechanism; the effect of finite conductivity is to reduce the drag for the same loading.

It will again be noted, for $m = 1$, that $R_m = 5$ provides a good approximation to the results obtained by Sears & Resler at $R_m = \infty$. This conclusion holds for a wide range of m and is important in defining what we mean by large or infinite magnetic Reynolds numbers.

Current penetration

In order to determine the extent of the important magneto-aerodynamic interaction for an airfoil, let us use the present theory to compute the depth of penetration into the field of the current density. For this purpose, we choose a convenient form for the pressure distribution and use it, through equations (36) and (2.4), to determine a corresponding value of the current density on the airfoil. This will provide sufficient information, through equations (21) or (22), to determine approximately the current penetration into the field.

As an example, let us suppose that on the airfoil

$$p(x, 0^+) - p_\infty = P(1 - 4x^2) = -\frac{m^2+1}{m^2} h_{yR}(x, 0^+), \tag{49}$$

so that

$$\xi(x, 0^+) \approx (1+m^2) h'_{yR}(x, 0^+) = 8m^2 P x. \tag{50}$$

Thus,

$$\xi(x, y^+) \approx \frac{2\xi(\frac{1}{2}, 0^+)}{m^{\frac{3}{2}} \sqrt{\left(\frac{m^2+1}{2m^2 R_m} y\right)}} \int_{-\frac{1}{2}}^{\frac{1}{2}} u\, du \exp\left\{-\frac{(x-my-u)^2}{\frac{m(m^2+1)}{2\pi R_m} y}\right\} \tag{51}$$

from which it is easily recognized that the limit $R \to \infty$ is $2\xi(\frac{1}{2}, 0^+)(x - my)$, in agreement with Sears & Resler. Further, the right-hand side of equation (51) can be integrated exactly to give

$$\xi(x, y^+) \approx \xi(\tfrac{1}{2}, 0^+) \left\{ \sqrt{\frac{Ky}{\pi}} \left[\exp\left\{-\frac{(my - x + \frac{1}{2})^2}{Ky}\right\} - \exp\left\{-\frac{(my - x - \frac{1}{2})^2}{Ky}\right\} \right] \right.$$
$$\left. + (x - my) \left[\operatorname{erf}\left(\frac{\frac{1}{2} + my - x}{\sqrt{Ky}}\right) - \operatorname{erf}\left(\frac{-\frac{1}{2} + my - x}{\sqrt{Ky}}\right) \right] \right\}, \tag{52}$$

where

$$K \equiv \frac{m(m^2+1)}{2\pi R_m} = 4\gamma.$$

This expression has all the correct limits, since

$$\operatorname{erf}(x) \equiv \frac{2}{\sqrt{\pi}} \int_0^x e^{-t^2} dt \quad \text{and} \quad \operatorname{erf}(-\infty) = -\operatorname{erf}(\infty).$$

The distance in chord lengths (measured along the characteristic line $x - my = \frac{1}{2}$) for the current density to fall off to one-tenth its value at $y = 0^+$ is plotted versus R_m in figure 4. The current penetration is infinite if $R_m = \infty$ and still very large for finite R_m.

It is of interest that the current penetration is very much larger for the airfoil in question than for the wavy wall with a wavelength equal to the airfoil chord. In fact, it is easy to check that the sinusoidal mode that is damped by the same ratio at the same height has a wavelength equal to about twenty-five chords. This is related to the fact that the current waves set up by the airfoil diffuse outward from their characteristic lines at the same time that they diminish in intensity, so that an observer at a large height above the airfoil will measure appreciable current density for many chord lengths in the x-direction (see figure 4).

The appearance of the Alfvén mechanism, with its ability to carry currents and the associated vorticity deeply into the flow, renders the crossed-fields case more interesting than it might otherwise be. The large current penetration is in sharp contrast with the aligned-fields case (Sears & Resler 1959), where the Alfvén mechanism cannot penetrate the flow field, and with the small R_m case, where the Alfvén mechanism is not discernible for any field orientation. (In the latter case, the first-order currents are given directly by the fluid motion and the *applied* magnetic field, with the usual hydrodynamic flow pattern prevailing, and consequently the currents die out in about one chord length.)

The large R_m approximation—discussion of error

As mentioned previously, the large R_m approximation, when used in the context of Fourier synthesis, requires the special assumption that the higher harmonics of the rotational part of the flow field (and of the magnetic field) are not too important. It would be useful, therefore, to give an indication of how

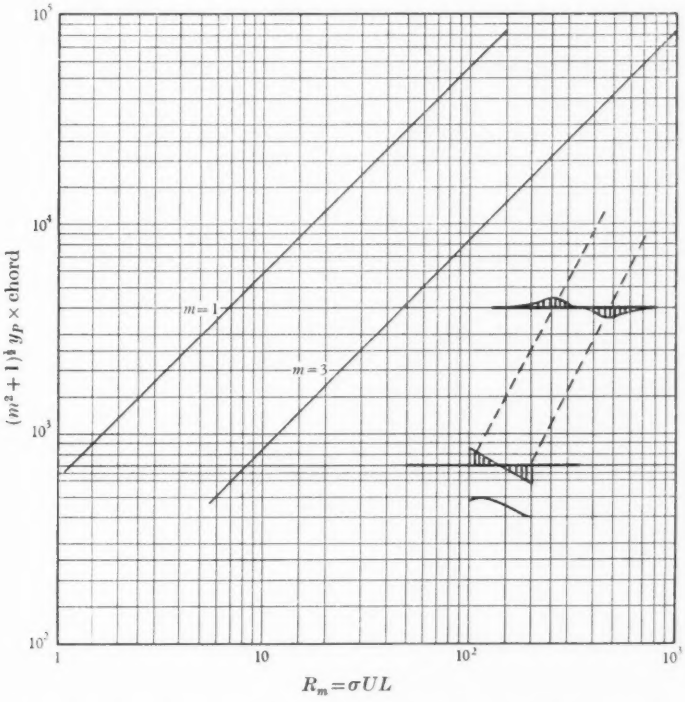

FIGURE 4. Current penetration into the flow field resulting from the Alfvén wave mechanism. The quantity $y_p(m^2+1)^{\frac{1}{2}}$ is the distance in chords, measured along characteristic lines, for the current density to fall off to 0·1 times its value at the airfoil. The inset figure illustrates the chordwise spread, as well as the decay in amplitude, of the current density generated by an airfoil of the shape shown.

rapidly the Fourier transforms occurring in any given problem should fall off for large $|\lambda|$. Any such indication will naturally suffer from a certain degree of arbitrariness, but it is hoped that the discussion given below will, nevertheless, be helpful.

We have at our disposal a clearly defined 'cut-off' value for the wave-number, $\lambda^* = 4\pi R_m/(m^2+1)$, with m explicitly assumed to be of order one. We shall consider the contribution of the Fourier transform for values of λ less than λ^* as an indication of the magnitude of a given quantity. We shall then require that the contribution made for values of λ greater than λ^* be

negligible in comparison with this magnitude. For this purpose we define in the upper half plane

$$M \equiv \int_0^{\lambda^*} F(\lambda)\, e^{i\lambda x} \exp\left[-\lambda m y \sqrt{\left\{\left(\frac{i\lambda}{4\pi R_m} - 1\right)\Big/\left(1 + \frac{i\lambda m^2}{4\pi R_m}\right)\right\}}\right] d\lambda,$$
$$\epsilon_T \equiv \int_{\lambda^*}^{\infty} F(\lambda)\, e^{i\lambda x} \exp\left[-\lambda m y \sqrt{\left\{\left(\frac{i\lambda}{4\pi R_m} - 1\right)\Big/\left(1 + \frac{i\lambda m^2}{4\pi R_m}\right)\right\}}\right] d\lambda. \tag{53}$$

In this approach to the problem there are really two independent considerations that arise. The first has to do simply with the convergence of the Fourier integrals involved. This is a standard problem and has nothing directly to do with the large R_m approximation itself. In order to simplify the following discussion we shall assume that we are dealing with a problem in which the most slowly convergent transforms (see table 2) are absolutely convergent.†

Since the large R_m approximation was introduced in this problem primarily to enable us to deduce the boundary conditions on the x-axis, our first concern is with the behaviour of ϵ_T and M as $y \to 0$. Under the assumption of absolute convergence it will generally be sufficient for the purposes of the large R_m approximation to require that the transform ($F(\lambda)$, say) has no maxima at values of λ greater than λ^* and that $|F(\lambda^*)| \ll |F(\lambda_0)|$, where λ_0 is some reference wave-number at which $|F|$ is at a maximum. To give a specific example, let us suppose that we have a transform of the form $A/[1 + (\lambda/\lambda_c)^n]$. In order for this to be absolutely convergent, $n > 1$, and hence $|F(\lambda^*)| \ll |F(0)|$ provided $\lambda^*/\lambda_c \gg 1$. For this example, at the point $x = 0$, $y = 0$, where the effect of the higher harmonics is greatest, we find the ratio of ϵ_T to M to be of the order

$$(\lambda_c/\lambda^*)^{n-1}.$$

Thus, in this example we simply require $\lambda^* \gg \lambda_c$.

Considerations similar to this can be applied for any given problem at $y = 0$ when the boundary conditions are given and the nature of the pertinent transforms has been determined. Often, however, since the value of the function itself will be known on the x-axis, only the behaviour of its transform for wave-numbers greater than λ^* need be determined so that ϵ_T can be compared directly with the function in that region.

It is also of interest to investigate the influence of the higher harmonics on the flow field as a whole, and in particular their comparative importance in the far field. For this purpose we note that, since $\lambda^* = m/2\gamma$,

$$|M| \geqslant \left| \int_0^{m/2\gamma} F(\lambda)\, e^{i\lambda(x - my)} \exp\left(-\frac{\lambda m y}{\sqrt{2}}\right) d\lambda \right|,$$
$$\epsilon_T \leqslant \int_{m/2\gamma}^{\infty} |F(\lambda)|\, e^{-\lambda y}\, d\lambda \tag{54}$$

† Of course, in practical problems it is not necessary that the Fourier integrals all be absolutely convergent; convergence *in the mean* is sufficient. However, in that case the discussion of the error associated with the large R_m approximation becomes more complicated. For example, ϵ_T does not exist at the point $x = 0$, $y = 0$ unless absolute convergence is assumed. The present discussion is limited to the assumption of absolute convergence for simplicity.

and hence

$$\frac{|\epsilon_T|}{|M|} \leqslant \frac{\int_{m/2\gamma}^{\infty} |F(\lambda)|\, e^{-\lambda y}\, dy}{\left| \int_0^{m/2\gamma} F(\lambda)\, e^{i\lambda(x-my)} \exp\left(-\frac{\lambda m y}{\sqrt{2}}\right) dy \right|} \equiv \mathscr{R}. \tag{55}$$

This is not the closest upper bound that might be constructed, but it has the advantage of being relatively easy to use.

For example, if we again consider Fourier transforms of the form $A/[1+(\lambda/\lambda_c)^n]$, the upper bound of the ratio given by (55) is of the order (for integer n and y not near zero)

$$\mathscr{R} \approx \frac{[(x-my)^2 + \frac{1}{2}(m^2y^2)]}{\lambda_c^{-n}(n-1)!} \times \frac{y^{n-1}\, E(\lambda^* y)}{\{[(my/\sqrt{2})\,(1-e^{-ay}\cos\lambda^*\bar{x}) + \bar{x}\, e^{-ay}\sin\lambda^* x]^2 + [\bar{x}(1-e^{ay}\cos\lambda^*\bar{x}) - (my/\sqrt{2})\, e^{-ay}\sin\lambda^*\bar{x}]^2\}^{\frac{1}{2}}}, \tag{56}$$

where $a = (m^2\sqrt{2}/4\gamma)$, $\bar{x} = (x-my)$ and $E(u)$ is the exponential integral,

$$E(u) \equiv \int_u^{\infty} \frac{e^{-t}\, dt}{t}.$$

It will be noted that $\mathscr{R}$ approaches zero exponentially as $y \to \infty$ for all n, and for any finite value of y it vanishes as $R_m \to \infty$. In particular, if $m = 1$, and $R_m = 3/\pi$, $\mathscr{R}$ is proportional to $e^{-6}/6(n-1)!$ at $y = 1$. Thus, at finite values of y the higher harmonics are automatically damped out rapidly due to the very nature of the rotational parts of the solution, and the large R_m approximation is good in the far field even for functions whose transforms are themselves rather slowly convergent.

Conclusions

We have shown that it is possible to compute, with the assumption that the magnetic Reynolds number R_m is large but finite, significant magneto-aerodynamic quantities for finite bodies immersed in an incompressible fluid stream in the presence of a uniform magnetic field which is perpendicular to the free stream and in the plane of the flow. To do this, the results of an exact calculation of the flow field of a small-amplitude wavy wall, valid for all R_m and m, have been used in approximate form to construct a thin airfoil theory for fluids of large but finite conductivity. The boundary-value problem for the irrotational part of the flow field has been determined, and the method for obtaining the pressure distribution on the airfoil and all rotational parts of the flow field once the boundary-value problem is solved has been given.

We have used the theory to solve the indirect problem of determining the airfoil shape associated with a given loading and have compared the results with those of Sears & Resler for $R_m = \infty$. In addition, we have studied for a particular example the depth of penetration into the flow field of the currents set up by the motion of an airfoil. As shown in figure 4, the depth of penetration of this current,

which is carried into the flow field by the Alfvén mechanism, is surprisingly large. Indeed, it is so large as to emphasize the need for further study of current penetration in practical cases, for example, when the magnetic field is non-uniform, or of finite extent.

Perhaps the most significant conclusion to be drawn from the present study is that a value of $R_m = 5$ is, in the cases studied, large enough to be a good approximation to infinity. Moreover, if the Fourier transforms of the pertinent quantities converge sufficiently rapidly, the present technique of expanding in reciprocal powers of R_m appears to be valid in the neighbourhood of $R_m = 1$. These results help to define what we mean by large magnetic Reynolds number in this area of magneto-aerodynamics.

REFERENCES

Cowling, T. G. 1957 *Magnetohydrodynamics.* London: Interscience.

Glauert, H. 1926 *Aerofoil and Airscrew Theory.* Cambridge University Press.

Lighthill, M. J. 1956 *Surveys in Mechanics* (ed. G. K. Batchelor and R. M. Davies). Cambridge University Press.

Rayleigh, Lord 1946 *Theory of Sound II*, 2nd ed. New York: Dover.

Resler, E. L., Jr. & McCune, J. E. 1960 *Rev. Mod. Phys.* (in the Press).

Resler, E. L., Jr. & Sears, W. R. 1958 *J. Aero. Sci.* **25**, 235.

Rott, N. & Cheng, H. K. 1954 *J. Rat. Mech. Anal.* **3**, 357.

Sears, W. R. & Resler, E. L., Jr. 1959 *J. Fluid Mech.* **5**, 257.

On the generation of surface waves by turbulent shear flows

By JOHN W. MILES
Department of Engineering, University of California, Los Angeles

(Received 24 March 1959, and in revised form 4 August 1959)

The model proposed by Phillips (1957) for the generation of water waves by the random fluctuations of normal pressure already present in a turbulent wind is generalized to include energy transfer associated with the interaction between surface wave and mean air flow (Miles 1957). It is found that this energy transfer may increase by an order of magnitude the surface displacements produced by a given distribution of pressure fluctuations in the principal stage of development.

1. Introduction

Two models for the generation of surface waves on a nearly inviscid liquid by turbulent winds have been developed recently by Phillips (1957) and Miles (1957). Both models are based on linearized equations of motion, both neglect direct interactions between surface waves and turbulent fluctuations, and both predict total energy-transfer to gravity waves in order-of-magnitude agreement with observation; however, their mechanisms are largely complementary.

The model proposed by Phillips assumes as its essential mechanism the direct action of turbulent fluctuations in aerodynamic pressure on the surface of the water, but neglects all interaction between air flow and surface wave. It is an *uncoupled* model in the sense that excitation is assumed to be independent of response. (See also Eckart (1953) for a similar but rather more artificial model.)

The model proposed by Miles neglects turbulent fluctuations (except as they enter indirectly through the prescription of the mean wind profile) and assumes as its essential mechanism the interaction between mean air flow and surface wave. It is a *coupled* model in the sense that excitation is assumed to be proportional to response, and it finds its antecedants in the classical problems of hydrodynamic stability (and also in the sheltering theory of Jeffreys—see Lamb 1945, §348).

There can be little doubt that both of the foregoing mechanisms are operative in some degree, with that of Phillips providing a broad-spectrum energy-input and that of Miles a frequency-selective feedback. (But we must bear in mind that the two mechanisms are independent only in our simplified model; in reality, the turbulent fluctuations must be affected by the wave motion. It also may be pertinent to observe that, according to Townsend (1956, §6.1), the structure of the largest eddies is determined by the stability of the mean profile.) Assuming linearity, such a feedback may be expected to augment the wave-growth initiated by the pressure fluctuations and lead to an exponential time-dependence, rather than the linear time-dependence (for the power spectral density) that

characterizes the original model proposed by Phillips. Non-linear effects, such as a reduction of the energy transfer from the mean flow (cf. Stuart 1958) to the longer waves and breaking of the shorter waves (Phillips 1958), would eventually alter this time-dependence, to be sure, but we remark that the amplitudes of the longest (also largest and fastest) waves are likely to be limited simply by the length of time that the wind blows.

We shall develop here a model that combines these two mechanisms and then seek to determine their relative importance. We consider first (in §2) the response $\eta(x,t)$ of a free surface to a pressure distribution $p_0(x,t)+p_1(x,t)$, where p_0 denotes a prescribed distribution and p_1 is linearly proportional to η_t; in the context of the preceding discussion, p_1 represents the aerodynamic pressure coupled with the wave motion, but we also may regard it as comprising other effects, such as viscous damping in the water. Eventually (in §3), we shall assume p_1 to be a stationary random function of (vector position) $\mathbf{x}$ and t and generalize to two-dimensional surface waves, but initially we shall find it expedient to consider the nearly-periodic function

$$p_0(x,t) = f(t)\,e^{ik(x-Vt)}, \qquad |\dot{f}/kVf| \ll 1, \tag{1.1a,b}$$

where $f(t)$ is a slowly varying function of time in the sense of (1.1*b*) and V denotes the convection speed. Following Phillips, we then shall focus attention on those (resonant) surface waves that have wave speeds $c = c(k)$ approximating the convection speed V and that may be expressed in the form

$$\eta(x,t) = a(t)\,e^{ik(x-ct)}, \qquad |\dot{a}/kca| \ll 1, \tag{1.2a,b}$$

where $a(t)$ also is a slowly varying function of time. (Assuming η in this form allows c to remain real, whereas in Miles (1957) it had to be assigned a small imaginary part.) After expressing $a(t)$ in terms of $f(t)$, we may extend the analysis to a two-dimensional disturbance, travelling at an angle α with respect to the convected pressure p_0, simply by writing†

$$V = \mathscr{U}(k)\cos\alpha, \tag{1.3}$$

where $\mathscr{U}(k)$ is the convection speed for the pressure fluctuation of wave-number k ($\mathscr{U} = \mathscr{U}_c$ in Phillips's notation). We then (in §3) may generalize our result to a stationary random p_0 with the aid of Fourier–Stieltjes integrals. These could have been introduced from the beginning, but carrying out the initial analysis in terms of nearly-periodic functions perhaps serves to bring out more simply the essential features of the *resonance mechanism* (discovered by Phillips) and the associated approximations.‡

Phillips considered two stages in the development of surface waves under random pressure: (*a*) an 'initial stage', during which the spectrum of the pressure fluctuations may be assumed to be independent of time, and (*b*) a 'principal stage' during which the relatively short waves that influence the wind profile may be

† This is essentially Squire's (1933) result. Alternatively, we may note that if

$$\eta = a(t)\exp\left[ik(x\cos\alpha + y\sin\alpha - ct)\right],$$

the phase velocity in the direction of the convected pressure is simply $c\sec\alpha$.

‡ I am indebted to the referee for this suggestion.

assumed to have achieved a statistical equilibrium and during which only the growth of the longer gravity waves need be considered. We shall give primary attention (in §4) to the principal stage, for it is only then that the interaction between mean flow and *gravity* waves could have developed sufficiently to be important; however, in order to substantiate this last statement, we shall cite (without derivation) the appropriate generalization of Phillips's result for the angular spectrum during the initial stage.

Having combined the two mechanisms of energy transfer in §§2 to 4, we shall develop in §5 an expression for the energy transfer from the mean flow in terms of a Reynolds stress, following a suggestion by Lin (private communication). We then shall show that the energy transfer from the mean flow may be of dominant importance for a significant portion of the gravity-wave spectrum.

2. Resonant surface waves excited by convected pressure

Let $\eta(x,t)$ be the displacement of the free surface of a liquid of density ρ_w that is subjected to a pressure $p(x,t)$, and let p exhibit the x-dependence e^{ikx}. The equation of motion for small disturbances then may be put in the form

$$(\rho_w/k)\,\eta_{tt}+(\rho_w g+Tk^2)\,\eta = -p, \tag{2.1}$$

where ρ_w/k is the effective mass per unit area for an irrotational motion of the liquid, and g denotes the acceleration of gravity and T the surface tension. We do *not* use the moving reference frame adopted by Phillips, but otherwise (2.1) is equivalent to P(2.11). (Here and subsequently, equations from Phillips (1957) will be denoted by P( ), where ( ) contains the equation number.) If $p = 0$, (2.1) has free-surface-wave solutions of the form (1.2a) with $a(t)$ = const. and

$$c^2 = gk^{-1}+(T/\rho_w)\,k. \tag{2.2}$$

Now let us assume

$$p(x,t) = p_0(x,t)+p_1(x,t), \qquad p_1 = -\zeta\rho_w c\eta_t, \tag{2.3a, b}$$

where p_0 is prescribed by (1.1a, b) and ζ is a small but otherwise arbitrary constant. Substituting (1.1a) and (2.3a, b) in (2.1) and dividing through by ρ_w/k, we then obtain

$$\eta_{tt}-\zeta kc\eta_t+k^2c^2\eta = -(k/\rho_w)f(t)\,e^{ik(x-Vt)}. \tag{2.4}$$

We observe that the complementary solutions to (2.4) are of the form (1.2a) with $a^2(t) = e^{\zeta kct}$, and ζ may be interpreted as the fractional increase in mean energy per radian-cycle according to

$$\zeta = (kc\bar{E})^{-1}(\partial\bar{E}/\partial t), \tag{2.5}$$

where $\bar{E}$ denotes the mean (over an integral number of cycles or wavelengths) energy of the surface wave; $|\zeta| \ll 1$ then implies that $\bar{E}$ must be a slowly varying function of time in the sense of (1.1b) and (1.2b).

We may express the solution of (2.4), subject to the initial conditions $\eta = \eta_t = 0$ at $t = 0$, as

$$\eta(x,t) = \frac{e^{ik(x-Vt)}}{2i\rho_w c}\int_0^t e^{m(t-\tau)}[e^{ik(V-c)(t-\tau)}-e^{ik(V+c)(t-\tau)}]f(\tau)\,d\tau, \tag{2.6}$$

where

$$m = \tfrac{1}{2}\zeta kc \ll 1. \tag{2.7}$$

We now invoke our hypotheses that $f(t)$ is a slowly varying function of time and that $V \doteq c$; then, after several cycles ($kct \gg 1$), the contribution of the term in $V-c$ will be much more important than that in $V+c$,† and we obtain the *resonance approximation*

$$\eta(x,t) \doteq \frac{e^{ik(x-Vt)}}{2i\rho_w c}\int_0^t \exp\{[m+ik(V-c)](t-\tau)\}f(\tau)\,d\tau, \tag{2.8a}$$

if

$$V \doteq c. \tag{2.8b}$$

Comparing (2.8a) to (1.2a), we obtain

$$a(t) = \frac{e^{mt}}{2i\rho_w c}\int_0^t \exp\{-[m+ik(V-c)]\tau\}f(\tau)\,d\tau. \tag{2.9}$$

We observe that, subject to the restrictions (1.1b), (2.7) and (2.8b), $a(t)$ must be a slowly varying function of time, as anticipated in (1.2b).

3. Response of free surface to random pressure

Following Phillips, we now suppose the pressure acting on the free surface to have the stochastic form

$$p_0(\mathbf{x},t) = \int \exp[i\mathbf{k}.(\mathbf{x}-\mathbf{U}t)]\,\mathrm{d}\varpi(\mathbf{k},t), \tag{3.1}$$

where $\mathbf{x}$ denotes vector position on the free surface, $\mathbf{k}$ is a (two-dimensional) vector wave-number of magnitude k (Phillips used κ where we use k), $\mathbf{U}(k)$ the convection velocity of that differential component of p_0 having the wave-number k, and the integral is of the Fourier–Stieltjes type. We also define α as the angle between $\mathbf{U}$ (which is assumed to have a fixed direction, namely, that of the wind) and the wave-front normal of a given component of $\eta(\mathbf{x},t)$ (see (3.2) below); we then may regard k and α as the polar (spectral) co-ordinates of $\mathbf{k}$. These definitions correspond to those adopted by Phillips, but we again emphasize that we have not used his moving reference frame, so that where he writes $\mathbf{x}$ we write $\mathbf{x}-\mathbf{U}t$; this avoids any possible difficulties associated with the fact that, in general, the convection speed $\mathscr{U}$ depends on k.

Corresponding to (3.1), we may assume the free-surface response to have the form

$$\eta(\mathbf{x},t) = \int \exp[i\mathbf{k}.(\mathbf{x}-\mathbf{U}t)]\,dA(\mathbf{k},t). \tag{3.2}$$

Comparing (3.1) and (3.2) with (1.1a) and (1.2a) and regarding $d\varpi(\mathbf{k},t)$ as the counterpart of $f(t)$, the corresponding counterpart of $a(t)$ is

$$\exp[i(kc-\mathbf{k}.\mathbf{U})t]\,dA(\mathbf{k},t).$$

Identifying V with $\mathscr{U}\cos\alpha$, as in (1.3), we then may generalize the resonance approximation (2.8a) according to

$$dA(\mathbf{k},t) = \frac{1}{2i\rho_w c}\int_0^t \exp\{[m+ik(V-c)](t-\tau)\}\,d\varpi(\mathbf{k},\tau)\,d\tau \tag{3.3a}$$

if

$$V = \mathscr{U}(k)\cos\alpha \doteq c(k). \tag{3.3b}$$

† The argument here is essentially similar to that invoked in Kelvin's stationary-phase approximation. Alternatively, taking the Laplace transform of (2.6) and allowing the transform parameter to tend to zero (corresponding to $kct \gg 1$) reveals that the respective integrals are proportional to $[m^2+k^2(V-c)^2]^{-\frac{1}{2}}$ and $[m^2+k^2(V+c)^2]^{-\frac{1}{2}}$.

Still following Phillips, we now introduce the amplitude spectrum

$$\Phi(\mathbf{k},t) = \frac{\overline{dA(\mathbf{k},t)\,dA^*(\mathbf{k},t)}}{dk_1\,dk_2}, \tag{3.4}$$

where the asterisk denotes the complex conjugate, the bar implies an ensemble (or equivalent) average, and $dk_1\,dk_2\,(=k\,dk\,d\alpha)$ is the element of area in the $\mathbf{k}$-plane. Similarly, we introduce the pressure spectrum

$$\Pi(\mathbf{k},t) = \frac{\overline{d\varpi(\mathbf{k},t')\,d\varpi^*(\mathbf{k},t+t')}}{dk_1\,dk_2}, \tag{3.5}$$

which is a function of the time separation t. Substituting (3.3a) in (3.4) then yields

$$\Phi(\mathbf{k},t) = \frac{1}{4\rho_w^2 c^2}\int_0^t\int_0^t \exp\left[m(2t-\tau-\tau')+ik(V-c)(\tau'-\tau)\right] \times \frac{\overline{d\varpi(\mathbf{k},\tau)\,d\varpi^*(\mathbf{k},\tau')}}{dk_1\,dk_2}\,d\tau\,d\tau' \tag{3.6a}$$

$$= \frac{1}{4\rho_w^2 c^2}\int_0^t\int_0^t \exp\left[m(2t-\tau-\tau')+ik(V-c)(\tau'-\tau)\right]\Pi(\mathbf{k},\tau-\tau')\,d\tau\,d\tau', \tag{3.6b}$$

where (3.6b) follows from (3.6a) in accordance with (3.5). Introducing $\tau+\tau'$ and $\tau-\tau'$ as new variables of integration, noting that $\Pi(\mathbf{k},t)$ is an even function of t, carrying out the $\tau+\tau'$ integration, and then replacing the dummy variable $\tau-\tau'$ by τ, we obtain

$$\Phi(\mathbf{k},t) = \frac{e^{mt}}{2\rho_w^2 c^2 m}\int_0^t \sinh\left[m(t-\tau)\right]\cos\left[k(V-c)\,\tau\right]\Pi(\mathbf{k},\tau)\,d\tau. \tag{3.7}$$

We emphasize that the result (3.7) is valid only over that portion of the k-spectrum for which (3.3b) may be considered a satisfactory approximation.

4. The principal stage; gravity waves

We consider now what Phillips has termed the principal stage of development, in which t is assumed to exceed the development time of $d\varpi(\mathbf{k},t)$. This implies that the relatively short waves that influence the mean velocity profile have achieved (a statistical) equilibrium and that only the growth of the longer gravity waves need be considered.

We consider first the asymptotic approximation of the integral in (3.7). Let

$$g_1(t) = \int_0^t g_2(\tau)\sinh\left[m(t-\tau)\right]d\tau, \qquad g_2(\tau) = \Pi(\mathbf{k},\tau)\cos\left[k(V-c)\,\tau\right], \tag{4.1a,b}$$

and let capitals denote Laplace transforms according to

$$G(s) = \int_0^\infty e^{-st}g(t)\,dt. \tag{4.2}$$

Transforming (4.1a) with the aid of the convolution theorem, we obtain

$$G_1(s) = m(s^2-m^2)^{-1}G_2(s). \tag{4.3}$$

We then may obtain the (first term in the) asymptotic approximation to $g(t)$ for $t \gg T$, where T denotes the time scale of $g_2(t)$, simply by setting $s = 0$ in $G_2(s)$; on the other hand, we have *not* assumed $mt \gg 1$ and therefore do not approximate $s^2 - m^2$ by $-m^2$. It follows that

$$g_1(t) \sim G_2(0) \sinh(mt) = \sinh(mt) \int_0^\infty g_2(\tau)\, d\tau, \tag{4.4}$$

whence we obtain from (3.7)

$$\Phi(\mathbf{k}, t) \sim \frac{F(t,m)}{2\rho_w^2 c^2} \int_0^\infty \Pi(\mathbf{k}, \tau) \cos[k(V-c)\tau]\, d\tau \tag{4.5a}$$

$$= (2\rho_w^2 c^2)^{-1} F(t,m)\, \Pi(\mathbf{k}, 0)\, \theta(\mathbf{k}, c \sec\alpha - \mathscr{U}), \tag{4.5b}$$

where

$$F(t,m) = (2m)^{-1}(e^{2mt} - 1), \tag{4.6}$$

and θ denotes the integral time-scale of the pressure fluctuations (as defined by Phillips).

Expanding (4.6) according to

$$F(t,m) = t + mt^2 + \ldots \quad (mt \to 0), \tag{4.7}$$

we observe that (4.5*a*) reduces to P(4.3) as $mt \to 0$ provided that the resonance approximation (which implies neglecting $\cos[k(V+c)\tau]$ relative to $\cos[k(V-c)\tau]$ in the integral) is invoked in P(4.3) and a minor error therein is corrected by multiplying it by $\sqrt{2}$.†

We conclude from equations (4.5) to (4.7) that the relative importance of energy transfer through the direct action of the pressure fluctuations and energy transfer through the interaction between surface wave and mean flow depends (within the assumptions implicit in our model) only on the size of mt relative to unity. In particular, the shape of Φ *vs* k is independent of t if $mt \ll 1$, but otherwise it is not.

We also note that if Π is assumed to be independent of $\tau - \tau'$ in (3.7), as in the initial stage considered by Phillips, and (following Phillips) the angular spectrum $\Psi(\alpha)$ is defined according to

$$\overline{\eta^2} = \iint \Phi k\, dk\, d\alpha = \int_0^{\alpha_{cr}} \Psi(\alpha)\, d\alpha, \tag{4.8}$$

where

$$\alpha_{cr} = \cos^{-1}(c_{\min}/\mathscr{U}) = \cos^{-1}(4gT/\rho\mathscr{U}^4)^{\frac{1}{4}}, \tag{4.9}$$

then the time-dependent factor in Ψ, which was simply t in Phillips's result, also becomes $F(t,m)$ for the present model.

5. Energy transfer from the mean flow

We turn now to the calculation of ζ, as defined by (2.5). Assuming that the motion is two-dimensional and inviscid, it is known that the rate at which energy is transferred from the mean flow to the disturbance is given by (Lin 1955, equations (4.5.1, 2))

$$\frac{\partial \overline{E}}{\partial t} = -\rho \iint (\overline{uv})\, \overline{u}_y\, dx\, dy, \tag{5.1}$$

† Phillips also has found that P(4.3) *et seq.* for Φ require the correction factor $\sqrt{2}$ (private communication).

where u and v denote the x- and y-components of velocity and ρ the density. Assuming the flow to consist of a small disturbance with respect to the parallel shear flow $U(y)$, we may take $\overline{u} = U(y)$. We also assume the small disturbance to exhibit the x-dependence e^{ikx}, as in (1.2a), and take mean values over x. The Reynolds stress in (5.1) then may be evaluated according to (Lin 1954)†

$$-\rho_a \overline{uv} = -\rho_a(\pi U_c''/kU_c')\,\overline{v_c^2} \quad y < y_c, \tag{5.2a}$$

$$= 0 \qquad\qquad\qquad\qquad y > y_c, \tag{5.2b}$$

where the subscript c implies evaluation at the critical layer defined by

$$U(y_c) = c \quad (\alpha = 0), \tag{5.3a}$$

or, anticipating the extension to obliquely moving waves,

$$U(y_c)\cos\alpha = c. \tag{5.3b}$$

Substituting (5.2a, b) in (5.1) and taking the mean value over x, we obtain

$$\left(\overline{\frac{\partial E}{\partial t}}\right) = -\rho_a \int_0^{y_c} (\overline{uv})U'(y)\,dy = -\rho_a c(\pi U_c''/kU_c')\,\overline{v_c^2}. \tag{5.4}$$

The mean kinetic and potential energies for the surface wave of (1.2) are equal if $a(t)$ is constant and approximately equal if $a(t)$ is slowly varying in the sense of (1.2b); accordingly, the mean total energy is given by

$$\overline{E} = \rho_w k^{-1}\overline{\eta_i^2}. \tag{5.5}$$

Substituting (5.4) and (5.5) in (2.5), we obtain

$$\zeta = -s(\pi U_c''/kU_c')\,(\overline{v_c^2}/\overline{\eta_i^2}), \tag{5.6}$$

where

$$s = \rho_a/\rho_w. \tag{5.7}$$

The calculation of $\overline{v_c^2}/\overline{\eta_i^2}$, the ratio of the mean-square velocity at the inner critical layer to the mean-square velocity of the surface wave, requires the solution of the inviscid Orr–Sommerfeld equation. Only a rough, integral approximation was given originally by Miles (1957), but the equation has since been integrated numerically (Conte & Miles 1959) for the logarithmic profile

$$U(y) = U_1 \log(y/z_0), \qquad U_1 = U_*/\kappa, \tag{5.8a, b}$$

where U_* denotes Prandtl's shearing-stress velocity, κ ($\doteqdot 0{\cdot}4$) Karman's constant, and z_0 the effective roughness parameter. Both the approximate and direct (numerical) integrations of the differential equation lead to the conclusion that if the parameter β is introduced according to

$$\zeta = s(U_1\cos\alpha/c)^2\beta, \tag{5.9}$$

where U_1/c is replaced by $U_1\cos\alpha/c$ to allow for oblique waves, then

$$\beta \doteqdot \beta(ky_c) \quad (ky_0 < ky_c < 2), \tag{5.10}$$

† The neglect of viscosity in calculating the Reynolds stress can be justified (as an approximation) only if $U_c''/U_c' < 0$, corresponding to positive energy-transfer; otherwise, the inviscid solution may not be significant for mathematically small but physically finite values of the viscosity.

where y_0 denotes the lower limit of validity for the logarithmic profile. Within the indicated range for ky_c, β does not depend on the parameter kz_0,† which enters only indirectly through the relation between ky_c and $c/U_1\cos\alpha$; for gravity waves this relation may be placed in the form (from (5.3*b*) and (5.8*a*))

$$ky_c = \Omega(U_1\cos\alpha/c)^2\exp(c/U_1\cos\alpha), \tag{5.11a}$$

where

$$\Omega = gz_0/U_1^2\cos^2\alpha. \tag{5.11b}$$

The numerical results for β are plotted in figures 1 and 2, with Ω appearing as the family parameter in the latter. We emphasize that, since β is proportional to the profile curvature $U''(y_c)$, the assumption of a logarithmic profile may lead to appreciable error even though the approximation to $U(y)$ is close; this is especially so for the lower portion of the profile.

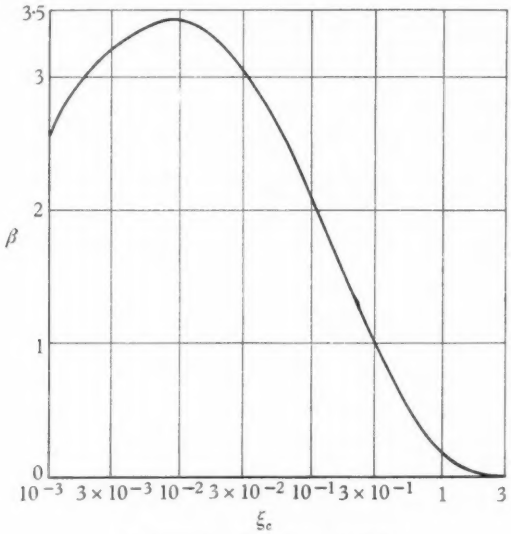

FIGURE 1. β *vs* ky_c; see (5.9).

Returning now to the results of § 4, we shall consider possible values of $F(t, m)$, as defined in (4.5) and (4.6). Letting

$$k = g/c^2 \tag{5.12}$$

on the assumption of gravity waves and evaluating ζ from (5.9), we obtain

$$2mt = \zeta kct = s\beta(U_1\cos\alpha/c)^2(gt/c). \tag{5.13}$$

Referring to the data cited from Sverdrup & Munk by Phillips in his figure 6, and assuming that the convection speed $\mathscr{U}$ for gravity waves can be approximated by the anemometer speed U and that the latter is given approximately by

$$U = 9U_1, \tag{5.14}$$

† The referee has suggested that, similarly, $\Pi = \rho_a^2U_1^4k^{-2}P(ky_c, \alpha)$, where the dependence of P on α is much less 'dramatic' than its dependence on ky_c. This suggestion might simplify the evaluation of the integrals in (3.7) and (4.5), but it still remains to determine P.

as for wind speeds of the order of 10 m/sec at an elevation (of the anemometer) of 10 m and $\Omega \doteqdot 10^{-2}$, we present some representative calculations in table 1. We also add that calculations carried out for the initial stage lead to the conclusion $mt \ll 1$ for all t and k for which the pressure spectrum may be considered independent of t and for which energy transfer from the mean flow exceeds that dissipated by viscosity in the water (which may be included by adding the negative increment $-2\nu_w k^2$ to m, where ν_w is the kinematic viscosity of water (Stokes 1850)).

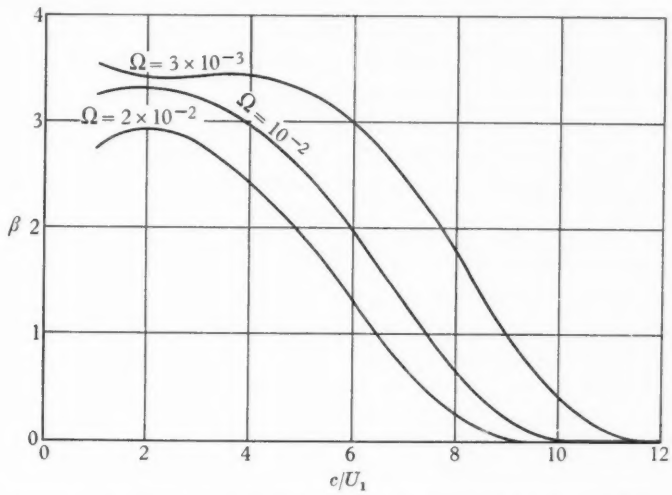

FIGURE 2. β *vs* c/U_1; $\Omega = gz_0/U_1^2$; U_1 must be replaced by $U_1 \cos\alpha$ if $\alpha \neq 0$.

gt/U	c/U	α	β	ζkct	$t^{-1}F(t, m)$
10^5	1	0°	0·19	0·28	1·14
10^5	0·5	0°	2·8	33	10^{13}
10^5	0·5	45°	1·1	6·5	10^2
10^4	0·5	0°	2·8	3·3	8

TABLE 1. Representative calculations based on (5.13) and (4.6) with $\rho_a/\rho_w = 1{\cdot}2 \times 10^{-3}$ and $\Omega = 10^{-2}\sec^2\alpha$. The values of β have been obtained from figure 2.

It seems obvious from the values of $F(t, m)$ indicated in table 1 that the inclusion of energy transfer from the mean flow yields a total energy-transfer to the surface waves that is likely to be much greater than that predicted (in its absence) by P(4.13); on the other hand, we recall that the rate of energy transfer from the mean flow to a *prescribed spectrum of surface waves* appears to be in order-of-magnitude agreement with observation (Miles 1959). The fact that P(4.13) gives order-of-magnitude agreement with observation then suggests that at least one of the approximations invoked by Phillips might be appreciably in error. Of these approximations, perhaps the most uncertain are those leading to his estimate of root-mean-square pressure fluctuation as $(\overline{p^2})^{\frac{1}{2}} \doteqdot 0{\cdot}6(\frac{1}{2}\rho_a U^2)$. This is

roughly an order of magnitude larger than the values estimated by Eckart (1953), but in the absence of actual measurements the question must be regarded as open.†

It might be objected, to be sure, that the very large values of ζkct indicated in table 1 imply that the assumption of small disturbances cannot remain valid. It is entirely possible, however, that linearized theory does give the right order of magnitude for the energy transfer from the mean flow (even though there might be some non-linear reduction thereof) and that non-linear effects are dominant only in the dissipative mechanism. Such an interpretation is supported by the agreement with observation cited above (Miles 1959).

Another objection that may be lodged against our model (although not for the values of c/U in table 1) is that, for wind speeds of the order of 10 m/sec, there must be a significant portion of the gravity-wave spectrum for which y_c is so small that the logarithmic profile cannot remain valid. It remains true, nevertheless, that in the absence of viscosity some energy will be transferred from the mean flow to the surface waves if $U_c''/U_c' < 0$, as is evident from (5.4); moreover, the inclusion of viscosity (in the air) in the calculation actually can *increase* this energy transfer (see Benjamin 1959; Miles 1959). It also is likely that appreciable energy could be transferred through 'sheltering'—i.e. form drag, involving a flow that alternately separates from and reattaches to the wave crests (Lamb 1945, §348).

6. Conclusions

We conclude that energy transfer associated with interaction between surface waves and mean air flow in the excitation of these waves by prescribed, random fluctuations of normal pressure may increase the total energy-transfer by an order of magnitude, at least under those conditions for which non-linear effects may be neglected. We emphasize, however, that a decisive assessment of our results depends on a more precise determination of the pressure fluctuations than any presently available.

REFERENCES

BENJAMIN, T. BROOKE 1959 *J. Fluid Mech.* **6**, 161.
CONTE, S. & MILES, J. W. 1959 *J. Soc. Indust. Appl. Math.* (in the Press).
ECKART, C. 1953 *J. Appl. Phys.* **24**, 1485.
LAMB, H. 1945 *Hydrodynamics.* New York: Dover.
LIN, C. C. 1954 *Proc. Nat. Acad. Sci.* **40**, 741.
LIN, C. C. 1955 *The Theory of Hydrodynamic Stability.* Cambridge University Press.
MILES, J. W. 1957 *J. Fluid Mech.* **3**, 185.
MILES, J. W. 1959 *J. Fluid Mech.* **6**, 568.
PHILLIPS, O. M. 1957 *J. Fluid Mech.* **2**, 417.
PHILLIPS, O. M. 1958 *J. Fluid Mech.* **4**, 426.
SQUIRE, H. B. 1933 *Proc. Roy. Soc.* A, **142**, 621.
STOKES, G. G. 1850 *Trans. Camb. Phil. Soc.* **9**, 8; Papers **3**, 71.
STUART, J. T. 1958 *J. Fluid Mech.* **4**, 1.
TOWNSEND, A. A. 1956 *The Structure of Turbulent Shear Flow.* Cambridge University Press.

† Phillips also has concluded that his estimate of $(\overline{p^2})^{\frac{1}{2}}$ was too large (private communication).

REVIEWS

Liquid Helium. By K. R. Atkins. Cambridge University Press, 1959. 312 pp. 60*s*.

Reading this book has reminded the reviewer that, although the raw material of fluid mechanics should be real fluids occurring in nature, he and many like him reserve the term 'real fluid' for fluids with a Newtonian viscosity. Good practical reasons for this narrow view of reality are easily found—two such fluids, air and water, are cheap and easily obtained, and the equations of motion are not too complicated—but it is useful to be reminded of the existence of other kinds of fluid. Much of Prof. Atkins's book is concerned with liquid helium II, which is a real fluid with most remarkable properties. It is difficult to believe that first observation of the behaviour of this liquid produced anything but bewilderment, and it is an interesting experience to read of the theoretical and experimental work that has led to a coherent account of the bulk properties of this unique liquid.

The basis of the phenomenonological theory of the properties of liquid helium II is the assumption of Tisza and of Landau that it is a mixture of two fluids, the normal component and the superfluid, which interpenetrate freely and are capable of independent movement. The normal component has an ordinary Newtonian viscosity (of order 10^{-5} poise) and carries with it all the entropy of the liquid, but the superfluid possesses neither viscosity nor entropy. The proportions of the two components varies with temperature, the fraction of the normal liquid decreasing from unity at the λ-point to zero at 0 °K. Besides accounting for the anomalous flow properties and for the thermomechanical effects that make such spectacular demonstrations, Tisza showed that the above assumption implies the existence of a second mode of sound propagation in which counterflow of the two components takes place without change of density and the discovery of this 'second sound' has placed the two-fluid theory in a very strong position.

The absence of viscosity in the superfluid might suggest that this is the perfect fluid of classical hydrodynamics but the simple experiment of rotating a beaker of liquid helium and observing the shape of the free surface shows that, unlike a perfect fluid, the superfluid is capable of taking up rotation. The explanation is that vorticity of the superfluid is concentrated in *quantized* vortex-lines of strength h/m (m is the mass of a helium atom) and that these can be generated at the walls of the container if sufficient energy is available in the flow. In the steady state, the lines are uniformly distributed through the liquid and the macroscopic appearance is that of a fluid in uniform rotation. Further evidence for the existence of quantized vortex-lines is provided by measurements of the attenuation of second-sound passing through a volume of liquid helium II in steady rotation, and by the approximate agreement between observed critical velocities of flow and the values calculated assuming that the flow can only lose energy if it has sufficient energy to form at least one vortex-line.

This leads to what is for me the most intriguing problem in the hydrodynamics of liquid helium II, the properties and nature of the turbulent flow in the superfluid. There is little doubt that flows with velocities above the critical value are in fact turbulent and that this turbulent motion is shared by the superfluid, but consideration of the mechanics of turbulent flow in a fluid with concentrated vorticity and a 'quantum' viscosity raises some new problems. A substantial beginning has been made by Vinen, who has used the technique of measuring the attenuation of second sound to study the growth and decay of vortex-lines in a turbulent flow produced by a heat current. He suggests that, when vortex-lines approach closely, they may pinch off small vortex-rings of atomic dimensions, so forming a thermal excitation (a roton) which is part of the normal liquid, and he has obtained a satisfactory description of the decay of the turbulence using results from the study of homogeneous turbulence. This is a plausible mechanism for the dissipation of the energy of the turbulent motion and, like ordinary viscosity, is most effective at destroying small-scale components of the turbulent motion. It would be an interesting problem to modify the ordinary treatment of turbulent flow in channels by taking into account the special qualities of this mode of energy dissipation and to compare the results with the observations of supercritical flow.

This is only one example of the problems which appear to require for their solution familiarity with fluid mechanics and with the structure of liquid helium, and I hope that hydrodynamicists will read this book and perhaps assist with the study of this fluid. As a very small contribution, I should like to point out that the statement on p. 191 (that flow of a normal liquid between rotating cylinders with the inner cylinder stationary cannot become turbulent at any velocity) is wrong, as was shown experimentally by G. I. Taylor (*Proc. Roy. Soc.* A, **157**, 1936, 546). The laminar flow is stable to infinitesimal axisymmetric disturbances, but there are other kinds of disturbance, one of which is apparently amplified when the Reynolds number is large.

There is much more in this book than the elucidation of the flow properties of liquid helium II, including of course discussion of the fundamental reasons why superfluidity exists in helium of mass 4 and not in other isotopes or other rare gases, but I do not feel qualified to discuss these sections. I shall only say that they, like the remainder of the book, appear comprehensive, clearly expressed and, considering the bulk of the work described, easy to read. To me at least, it has provided a most interesting introduction to this subject.

A. A. Townsend

THE QUÉRE TITRATOR

has wide applications in recording physico-chemical processes

The Quére Titrator is a precision instrument for recording titrations accurately. Equipped with an automatically variable recording table to suit the gradient of the curve, it permits the rate of advance to be reduced when the rate of change increases. Reagent flow is controlled by the table mechanism and by changing the jet of the syringe, the volume being represented by the abscissa of the graph and the state of mixture by the ordinate. The circle method determines accurately the end points of titration. *The circuits permit all kinds of potentiometric titrations and with special attachments it is possible to perform conductimetric or polarised-electrode titrations.*

- **PHOTOMETRY** The Quére strip photometer attachment is provided with filters and a vacuum type photocell giving accurate and stable readings.
- **USING A LIQUID MEDIUM** photometric attachment to this Recorder allows any photocolourimetric titration, recording photometric variations instead of equivalent points.
- **INTEGRATION** The Recorder automatically integrates the curve as it is traced. The results are entered on the axis of the ordinate of the curve by means of an electric pen marking 'tens' and 'units'.
- **RECORDING TIME FUNCTIONS** The Titrator is fitted with a zero drift correcting circuit using an automatic potentiometer. To make accurate measurements it is necessary only to check the zero periodically; the instrument itself will then introduce the necessary corrections.

Write for fully illustrated and descriptive leaflet

Tinsley

H. TINSLEY & CO. LTD.

Werndee Hall, South Norwood, London, S.E.25

Telephone: ADDiscombe 6046-8

JSP 5719

JOURNAL OF FLUID MECHANICS

Volume 7, Part 3 March 1960

CONTENTS

Interaction of a shock wave with a mixture region
by N. RILEY *page* 321

Centrifugal waves
by O. M. PHILLIPS 340

The impact of a water wedge on a wall
by E. CUMBERBATCH 353

Temperature fluctuations in the atmospheric boundary layer
by C. H. B. PRIESTLEY 375

An experiment on the stability of hypersonic laminar boundary layers
by ANTHONY DEMETRIADES 385

Measurements of the effect of molecular diffusivity in turbulent diffusion
by WILLIAM R. MICKELSEN 397

An empirical torque relation for supercritical flow between rotating cylinders
by R. J. DONNELLY and N. J. SIMON 401

A comparison between buoyant vortex rings and vortex pairs
by J. S. TURNER 419

The stability of free boundary layers between two uniform streams
by T. TATSUMI and K. GOTOH 433

A note on fluctuating heat transfer at small Péclet numbers
by C. R. ILLINGWORTH 442

On the motion of thin airfoils in fluids of finite electrical conductivity
by JAMES E. MCCUNE 449

On the generation of surface waves by turbulent shear flows
by JOHN W. MILES 469

REVIEWS
Liquid Helium 479

Printed in Great Britain at the University Press, Cambridge
(Brooke Crutchley, University Printer)